Physik-Department

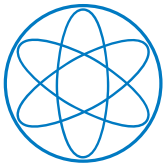

Study of 2π and 3π resonances in diffractively produced $\pi^-\pi^-\pi^+$

Untersuchung von 2π- und 3π-Resonanzen in diffraktiv produzierten $\pi^-\pi^-\pi^+$

Kumulative Habilitationsschrift
zur Erlangung der *Venia Legendi*

eingereicht am
Fachbereich Physik
der Technischen Universität München
von

Dr. rer. nat. Boris Grube

September 2018

Technische Universität
München

Contents

Synopsis

Just as the electromagnetic force binds electrons and nuclei into atoms, the strong force binds quarks into hadrons. In the Standard Model of particle physics, both forces are described by quantum field theories, i.e., quantum electrodynamics (QED) and quantum chromodynamics (QCD), with photons and gluons as mediators. A remarkable feature of QCD, which sets it apart from QED, is the fact that not only the quarks but also the gluons carry the charges of the strong interaction. Therefore, the gluons can self-interact. At low energies, this leads to the phenomenon of confinement, i.e., the entrapment of quarks and gluons into composite hadrons. Unfortunately, the QCD equations cannot be directly solved in the confinement regime because of the strong coupling of quarks and gluons. The quantitative understanding of how confinement arises from QCD is one of the last open questions of the Standard Model.

In an analog way as studying the excitation spectrum of atoms has lead to an understanding of the electromagnetic force and eventually to QED, studying the excitation spectrum of hadrons deepens our understanding of how quarks and gluons behave at low energies. According to the constituent quark model, the simplest hadrons are the mesons, which are made of a quark and an antiquark, i.e., $q\bar{q}$. However, in addition to ordinary $q\bar{q}$ states, QCD in principle allows meson-like states that are made, for example, out of four quarks, out of a $q\bar{q}$ pair plus an excited gluon field, or even states that are made entirely out of gluons. These "exotic" states should appear as supernumerary states in the hadron spectrum or mix with nearby conventional $q\bar{q}$ states with the same quantum numbers. Unambiguous proof for the existence of exotic states would be the experimental observation of mesons with quantum numbers that are forbidden for $q\bar{q}$. A particular class of manifestly exotic mesons are those with so-called spin-exotic quantum numbers, i.e., with quantum-number combinations $J^{PC} = 0^{+-}$, 1^{-+}, 2^{+-}, 3^{-+}, ... of spin J, parity P, and charge conjugation C that are forbidden for $q\bar{q}$ states in the non-relativistic limit.

The search for exotic mesons is a global effort with various experiments exploring different parts of the meson spectrum. The excitation spectrum of light-quark mesons, which consist of up, down, or strange quarks, is particularly interesting. Over the last decades, the light-meson spectrum has been studied extensively by many experiments. Many states are already identified and for most of them masses, widths, and decay modes are well-known. However, experimental information is often scarce or even non-existent especially for higher excited meson states. Most of these states lie in the mass region around and above $2\,\mathrm{GeV}/c^2$. Furthermore, experiments reported evidence for light-meson states with spin-exotic $J^{PC} = 1^{-+}$ quantum numbers, the so-called π_1 states. Interestingly, numerical ab-initio calculations of QCD (lattice QCD) have recently predicted a set of exotic states with excited gluon fields in the mass region around $2\,\mathrm{GeV}/c^2$, with the lightest one having spin-exotic quantum numbers of $J^{PC} = 1^{-+}$. However, the resonance interpretation

of the experimentally observed π_1 signals is debated controversially in the community. Hence these states require further confirmation.

The COMPASS experiment is a multi-purpose fixed-target experiment at the CERN Super Proton Synchrotron (SPS). One of its goals is to measure the light-meson spectrum with high precision, in particular to explore the $2\,\mathrm{GeV}/c^2$ mass region and to search for supernumerary states and exotic mesons. At COMPASS, excited light mesons are produced in inelastic scattering reactions of high-energy pion or kaon beams on proton or nuclear targets. The produced excited mesons decay via the strong interaction into final states of two or more lighter mesons, e.g., π, η, η', or K. The excited mesons hence appear in the reaction as intermediate states with very short lifetimes of the order of $10^{-23}\,\mathrm{sec}$. Such particles are called resonances and are characterized e.g., by their mass, width, J^{PC} quantum numbers, and decay modes. Due to the short life times of the resonances, their identification and the measurement of their parameters has to be based solely on the measured kinematic distribution of the final-state particles that reach the detector. This requires an elaborate method called partial-wave analysis (PWA), which decomposes the data into partial-wave amplitudes that correspond to well-defined J^{PC} quantum numbers and decay modes. Resonances appear typically as peak structures in the squared magnitudes, i.e., the intensities, of these amplitudes, which are accompanied by changes of the phase of the amplitude by approximately 180°.

The COMPASS experiment has recorded world-leading datasets for several final states. The largest dataset was acquired for the reaction $\pi^- + p \to \pi^-\pi^-\pi^+ + p$ and consists of 46×10^6 events. This dataset is at least an order of magnitude larger than any dataset from previous experiments and allows to study the spectrum of isovector mesons in unprecedented detail. This cumulative habilitation thesis reports on results from the analysis of this dataset based on the following three articles, which have been co-authored by the author of this thesis.

[H1] C. Adolph *et al.*, [COMPASS Collaboration], "Observation of a New Narrow Axial-Vector Meson $a_1(1420)$," *Phys. Rev. Lett.* **115** (2015) 082001, arXiv:1501.05732 [hep-ex].

[H2] C. Adolph *et al.*, [COMPASS Collaboration], "Resonance production and $\pi\pi$ S-wave in $\pi^- + p \to \pi^-\pi^-\pi^+ + p_{\mathrm{recoil}}$ at $190\,\mathrm{GeV}/c$," *Phys. Rev. D* **95** (2017) 032004, arXiv:1509.00992 [hep-ex], supplemental material at http://journals.aps.org/prd/supplemental/10.1103/PhysRevD.95.032004.

[H3] M. Aghasyan *et al.*, [COMPASS Collaboration], "Light isovector resonances in $\pi^- p \to \pi^-\pi^-\pi^+ p$ at $190\,\mathrm{GeV}/c$," *Phys. Rev. D* **98** (2018) 092003, arXiv:1802.05913 [hep-ex], supplemental material at https://journals.aps.org/prd/supplemental/10.1103/PhysRevD.98.092003.

The three articles report on results from the so far most comprehensive and detailed partial-wave analysis of the 3π final state. Employing the isobar model, which describes the decay of the intermediate states to $\pi^-\pi^-\pi^+$ as a chain of two successive two-body decays, we decompose the data into partial-wave amplitudes with well-defined quantum numbers and decay chains. For this we use the so far largest PWA model consisting of 88 partial waves. We perform the partial-wave decomposition in 100 bins of the three-pion mass, $0.5 < m_{3\pi} < 2.5\,\mathrm{GeV}/c^2$, and simultaneously in 11 bins of the reduced squared four-momentum, $0.1 < t' < 1.0\,(\mathrm{GeV}/c)^2$, that is transferred from the beam to the target particle.

We present detailed studies of selected 3π partial waves with $J^{PC} = 0^{-+}$, 1^{++}, 2^{++}, 2^{-+}, 4^{++}, and spin-exotic 1^{-+} quantum numbers. In addition, we present the results of a novel method to extract from the data the dynamical amplitude of the $\pi^-\pi^+$ subsystem with $J^{PC} = 0^{++}$ quantum numbers in various 3π partial waves as a function of $m_{\pi^-\pi^+}$, $m_{3\pi}$, and t'. This method not only significantly reduces the model dependence of the PWA results but it in addition allows us to study $\pi^-\pi^+$ resonances that appear in the $\pi^-\pi^-\pi^+$ decays and their possible distortion due to interactions among the final-state pions. Using this method, we observe for the first time the decay modes $\pi(1800) \to f_0(1500)\,\pi \to 3\pi$, $\pi_2(1880) \to f_0(980)\,\pi \to 3\pi$, and $\pi_2(1880) \to f_0(1500)\,\pi \to 3\pi$.

In order to identify resonances in the extracted partial-wave amplitudes and to measure their parameters, we performed the so far most comprehensive resonance-model fit using Breit-Wigner amplitudes. The resonance model simultaneously describes a subset of 14 selected waves using 11 isovector light-meson resonances. We measure the masses and widths of these resonances. The model contains the well-known resonances $\pi(1800)$, $a_1(1260)$, $a_2(1320)$, $\pi_2(1670)$, $\pi_2(1880)$, and $a_4(2040)$. It also includes the excited states $a_1(1640)$, $a_2(1700)$, and $\pi_2(2005)$. In addition, the model includes the disputed spin-exotic $\pi_1(1600)$. We confirm its existence and its decay mode into $\rho(770)\,\pi$. With the results from our analysis, we can also reconcile the seemingly contradictory observations from previous experiments that puzzled the community for a long time. We trace back the observed contradictions to artificial structures that are induced by too limited PWA models, which were employed in some previous analyses, and to the fact that the $\pi_1(1600)$ signal is accompanied by non-resonant background with a strongly t'-dependent intensity so that the $\pi_1(1600)$ dominates only in the region $t' \gtrsim 0.5\,(\mathrm{GeV}/c)^2$ that was not considered in some previous analyses.

In our analysis we also have discovered a new and unexpected resonance-like signal with $J^{PC} = 1^{++}$ quantum numbers, the $a_1(1420)$. We observe it as a narrow peak in the $f_0(980)\,\pi$ decay mode. The data are well described by a Breit-Wigner amplitude with a mass of $1411\,^{+4}_{-5}\,\mathrm{MeV}/c^2$ and a width of $161\,^{+11}_{-14}\,\mathrm{MeV}/c^2$. If interpreted as a genuine resonance, the $a_1(1420)$ would be a supernumerary state and a candidate for a four-quark state. However, the peculiar properties of the $a_1(1420)$ indicate that it might not be a resonance but could be an effect in the rescattering of daughter particles from the decay of the $a_1(1260)$ ground state. Such effects may also explain some of the exotic-meson signals observed in the heavy-quark sector.

In a novel approach, we extract the dependence of the resonance amplitudes on t' from the data. The t' dependences contain information about the production mechanism, which can be used to verify and improve models. We find that for most resonances the t' dependences of the intensities differs distinctly from those of the non-resonant background components. In our approach, this improves the separation of the resonances from the non-resonant background components.

In this thesis, we attempt to supplement the articles [H1–H3] by a broader introduction into the subject of meson spectroscopy in Chapter 1. In Secs. 1.1 to 1.3, we discuss the relation of QCD and meson spectroscopy. We introduce in Sec. 1.4 the quark model as the basis for the understanding of the meson spectrum. Section 1.6 contains a discussion of the specifics of the light-meson spectrum. We introduce the concept of a particle resonance, present theoretical predictions for the light-meson spectrum with a particular focus on results from numerical ab-initio calculations of QCD (lattice QCD), and discuss exotic mesons. The measured reaction and the COMPASS experiment are briefly introduced in

Secs. 2.1 and 2.2, respectively. In Sec. 2.3, we describe the event selection and discuss basic kinematic distributions. Since the discussion of the analysis method in the articles [H1–H3] is necessarily somewhat compressed and fragmented, we attempt in Chapter 3 a more coherent and detailed derivation of the formulae and methods starting from first principles. The concrete models that were used to analyze the data are presented in Sec. 4.1. Selected results are discussed in Sec. 4.2. We conclude in Chapter 5 and also give an outlook on possible future research.

Chapter 1

Introduction

1.1 The theory of strong interaction

Our current understanding of nature is that all interactions between matter particles can be reduced to four fundamental interactions: gravitational, electromagnetic, weak, and strong. The latter three interactions are described by the Standard Model of particle physics using relativistic quantum gauge field theories.

In the Standard Model, quantum chromodynamics (QCD) describes the strong interaction of quarks and gluons. The quarks are massive point-like spin-1/2 elementary constituents of matter (fermions), whereas the gluons are massless spin-1 exchange particles that mediate the strong interaction (gauge bosons). Both, quarks and gluons, carry charges of the strong interaction. In QCD, there are $N_c = 3$ kinds of these so-called "color" charges: "red", "green", and "blue", which are conserved in all physical processes. The theory of strong interaction is perfectly symmetric with respect to the three colors, i.e., it is invariant under local gauge transformations of the Lie symmetry group SU(3) in color space.[a] Using the principle of minimal coupling, one can construct the QCD Lagrangian density that is invariant under $\mathrm{SU}(3)_{\mathrm{color}}$ gauge transformations (see, e.g., Ref. [1]),[b]

$$\mathcal{L}_{\mathrm{QCD}} = \sum_{\substack{f=\{u,d,c,\\ s,t,b\}}} \sum_{k,l=1}^{N_c} \bar{q}_{f,k} \left[i\,\gamma^\mu\,(D_\mu)_{kl} - m_f\,\delta_{kl} \right] q_{f,l} - \frac{1}{4} \sum_{a=1}^{N_c^2-1} G_a^{\mu\nu}\,G_{\mu\nu}^a, \tag{1.1}$$

where $q_{f,k}(x)$ are the spinors of the quark fields, which have one of the six known flavors $f =$ "up" (u), "down" (d), "charm" (c), "strange" (s), "top" (t), or "bottom" (b). Each quark flavor comes in three colors, which means that the quark spinors are grouped into fundamental $\mathrm{SU}(3)_{\mathrm{color}}$ triplet representations with color index k. The γ^μ are the Dirac matrices, the m_f the quark masses, and $(D_\mu)_{kl}$ is the gauge covariant derivative, which is given by

$$(D_\mu)_{kl} = \partial_\mu\,\delta_{kl} + i\,g_s \sum_{a=1}^{N_c^2-1} \frac{\lambda_{kl}^a}{2}\,A_\mu^a(x). \tag{1.2}$$

[a] The special unitary group $\mathrm{SU}(N)$ is the non-abelian Lie group that is represented by $N \times N$ unitary matrices with unit determinant.

[b] In this chapter, we use natural units, where $\hbar = c = 1$.

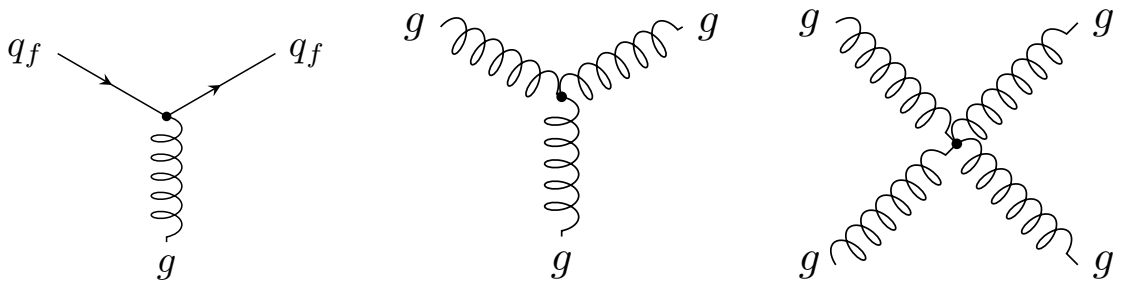

Figure 1.1: The fundamental Feynman vertices of QCD.

Here, g_s is the coupling constant of the strong interaction and the $A^a_\mu(x)$ are the gluon gauge fields. There are $N_c^2 - 1 = 8$ kinds of gluons.[c] The λ^a_{kl} are the eight 3×3 Gell-Mann matrices, which are the generators of the SU(3) group. The gauge invariant gluon field-strength tensor $G^a_{\mu\nu}$ in Eq. (1.1) is given by

$$G^a_{\mu\nu} = \partial_\mu A^a_\nu(x) - \partial_\nu A^a_\mu(x) - g_s \sum_{b,c=1}^{N_c^2-1} f_{abc}\, A^b_\mu(x)\, A^c_\nu(x). \tag{1.3}$$

The real-valued factors f_{abc} are the so-called structure constants of the SU(3) group, which close the SU(3) Lie algebra via the commutator relation

$$\left[\frac{\lambda^a_{kl}}{2}, \frac{\lambda^b_{kl}}{2}\right] = i \sum_{c=1}^{N_c^2-1} f_{abc}\, \frac{\lambda^c_{kl}}{2}. \tag{1.4}$$

As it is evident from Eqs. (1.1) to (1.4), QCD has only seven fundamental parameters that need to be determined by experiment: the coupling constant g_s and the six quark masses m_f.

Due to the non-abelian structure of the $\mathrm{SU(3)_{color}}$ gauge group, the Lagrangian in Eq. (1.1) contains not only terms that describe the coupling of quarks and gluons, i.e., terms of the form

$$g_s\, \bar{q}_{f,k}\, \gamma^\mu\, \lambda^a_{kl}\, q_{f,l}\, A^a_\mu,$$

but in addition terms of the form

$$g_s\, f_{abc}\, (\partial^\mu A^{\nu,a})\, A^b_\mu\, A^c_\nu \qquad \text{and} \qquad g_s^2\, f_{abc}\, f_{ade}\, A^{\mu,b}\, A^{\nu,c}\, A^d_\mu\, A^e_\nu$$

that describe the couplings of three and four gluons, respectively. Hence the Feynman rules for QCD include three fundamental types of interaction: (i) a quark may absorb or emit a gluon (see Fig. 1.1(a)), (ii) a gluon may absorb or emit a gluon (see Fig. 1.1(b)), and (iii) four gluons may interact directly (see Fig. 1.1(c)).

The self-interaction of the gluons has important consequences for the behavior of the strong interaction. In quantum field theories, the coupling "constant" actually depends

[c] The gluons carry color and anticolor charges. In $\mathrm{SU(3)_{color}}$, there are eight such combinations that belong to the adjoint octet representation and are given by the Gell-Mann matrices. The ninth combination, $(r\bar{r} + g\bar{g} + b\bar{b})/\sqrt{3}$, is a color-singlet, which is unphysical (see Sec. 1.2).

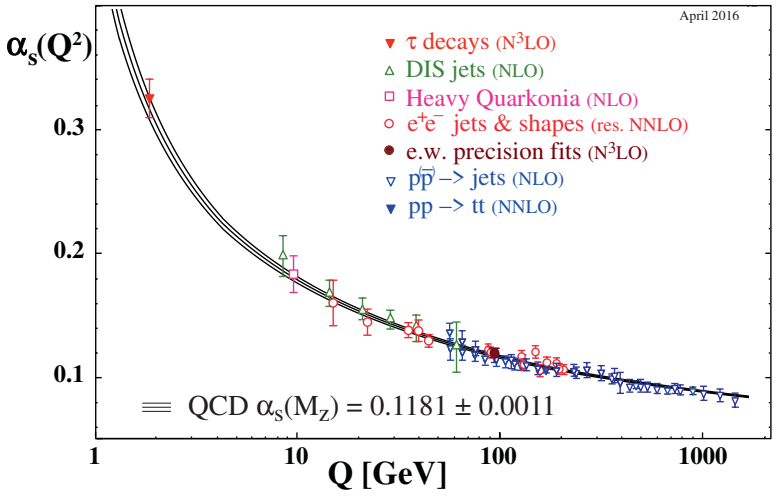

Figure 1.2: World data on α_s as a function of the energy scale Q overlaid by the theory prediction for $\alpha_s(Q^2)$. From Ref. [1].

on the energy scale μ of the physical process under consideration. This is called *running coupling*. In QCD, the self-interaction of the gluons determines the running of the strong coupling constant g_s, which is given by [2, 3]

$$\alpha_s(\mu^2) \equiv \frac{g_s^2(\mu^2)}{4\pi} \approx \frac{1}{\beta_0 \ln(\mu^2/\Lambda^2_{\mathrm{QCD}})}. \tag{1.5}$$

Here, α_s is the QCD equivalent to the fine-structure constant of the electromagnetic interaction, $\beta_0 = (33 - n_f)/(12\pi)$ depends on the number n_f of quark flavors that are considered light, i.e., for which $m_f \ll \mu$, and $\Lambda_{\mathrm{QCD}} \approx 200\,\mathrm{MeV}$ is the QCD scale parameter. The coupling $g_s(\mu^2)$ can be thought of as the dimensionless version of the effective strong charge that a quark carries.

For processes that are characterized by a transferred four-momentum Q, the effective strength of the strong interaction in that process is given by $\alpha_s(Q^2)$. Figure 1.2 shows that QCD is in excellent agreement with the world data on $\alpha_s(Q^2)$. It also shows that α_s becomes much smaller than one in "hard processes", i.e., in reactions with $Q \gg \Lambda_{\mathrm{QCD}}$. This is the regime of so-called weak coupling or *asymptotic freedom*. In this regime, the QCD field equations can be solved approximately by applying perturbation theory, i.e., by expanding them in a truncated power series in α_s. Perturbative QCD has been rigorously tested at high-energy accelerators and was confirmed to describe strong-interaction phenomena up to the highest energies available today at the Large Hadron Collider (LHC) at CERN [1]. The LHC measurements of the Higgs boson and the search for physics beyond the Standard Model critically depend on our understanding of production mechanisms and backgrounds, which are calculated using perturbative QCD.

1.2 Confinement

The second crucial consequence of the gluon self-interaction is the phenomenon called *confinement*. The confinement hypothesis states that no free colored states exist in nature. Hence all asymptotic states of QCD have to be color-neutral, i.e., singlet states that are

invariant under $\mathrm{SU}(3)_{\mathrm{color}}$ transformations. Consequently, it is impossible to observe free quarks or gluons. They are always confined into *hadrons*, i.e., into color-neutral composite particles that are bound states of quarks and gluons.[d]

Qualitatively, the phenomenon of confinement can be understood by considering two static elementary color charges, i.e., a heavy quark and a heavy antiquark, separated in space by a distance r. According to the Heisenberg uncertainty principle, the separation r of the quark-antiquark pair is inversely proportional to the transferred four-momentum Q. Hence the coupling strength of the strong interaction depends on r via Eq. (1.5). The coupling is weak at small distances (corresponding to large energies) and strong at large distances (corresponding to small energies). Neglecting the effect of light quarks, the interaction of the quark-antiquark pair can be described by an effective static potential. A popular ansatz is the so-called Cornell potential [5],

$$V(r) = -\frac{a}{r} + kr, \tag{1.6}$$

which consists of two parts. The first term is proportional to $1/r$ and represents a Coulomb-like potential, which corresponds to one-gluon exchange between the quark and the antiquark.[e] This term dominates at small separations $r \ll 1/\Lambda_{\mathrm{QCD}} \approx 1\,\mathrm{fm}$.[f] In this region, the coupling is weak and the color field is a dipole field with field lines spreading out in space, analogous to an electric dipole field. Hence the force between the quark-antiquark pair decreases with $1/r^2$. For large separations $r \gg 1/\Lambda_{\mathrm{QCD}}$,[g] the coupling and therefore the gluon self-interaction becomes strong. This leads to a rearrangement of the color-field lines between the quarks into so-called color strings or flux tubes (see Fig. 1.3(a)). The potential of such a string with tension $k \approx 1\,\mathrm{GeV/fm}$ is described by the second term in Eq. (1.6), which is proportional to r. This corresponds to a constant force between the quark-antiquark pair. This term prevents a complete separation of the quark-antiquark pair because this would require an infinite amount of energy. It is hence this term that makes the potential confining. In the real world, increasing r increases the energy stored in the gluon string until this energy becomes large enough to produce another quark-antiquark pair from the vacuum leading to a breaking of the gluon string. So instead of producing two isolated color charges, two color-neutral quark-antiquark pairs each bound by gluons are produced. As shown in Fig. 1.3(b), numerical simulations of the QCD Lagrangian that ignore light-quark contributions (so-called quenched approximation; see Sec. 1.6.2.2) confirm the Cornell potential.

Confinement leads to the curious situation that the actual fundamental degrees of freedom of QCD, the quarks and gluons, are not directly observable. The experimentally observable asymptotic states of any QCD scattering process will always be color-singlet hadrons. While the confinement hypothesis is experimentally well established, it is not fully understood on a theoretical level [8]. The reason for this is again the running of the QCD coupling in Eq. (1.5). At low energies of the order of Λ_{QCD}, which correspond to large distances of the order of 1 fm, $\alpha_s(Q^2)$ becomes close to or larger than one, so that

[d] The term "hadron" to designate strongly interacting composite particles was coined 1962 by L. B. Okun [4]. It was derived from the Greek ἀδρός (hadrós) meaning "stout, thick" and was chosen to contrast the term "lepton" that is used to designate elementary particles that do not participate in strong interactions and that was derived from the Greek λεπτός (leptós) meaning "fine, small, thin".

[e] This is analogous to the Coulomb potential of the electromagnetic interaction between two point charges, which corresponds to one-photon exchange in quantum electrodynamics.

[f] This corresponds to $Q \gg \Lambda_{\mathrm{QCD}}$.

[g] This corresponds to $Q \ll \Lambda_{\mathrm{QCD}}$.

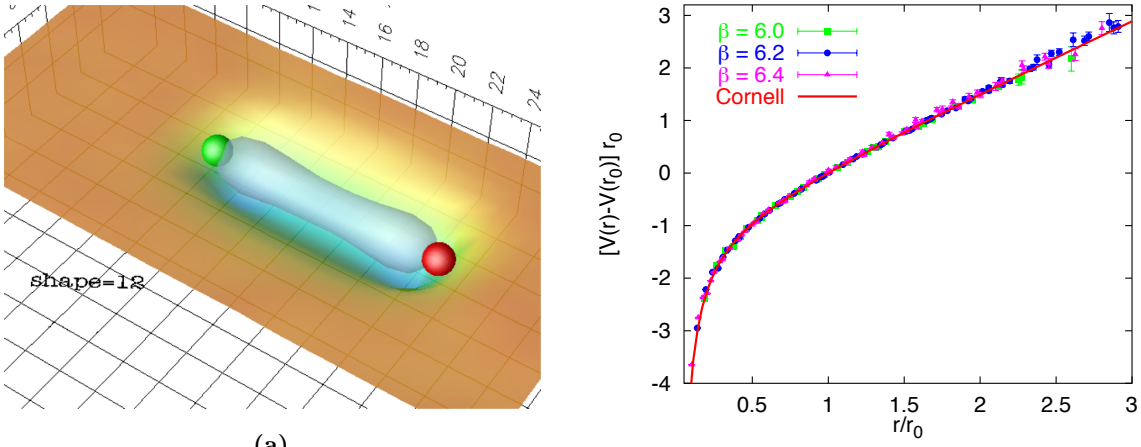

(a) (b)

Figure 1.3: Results of numerical simulations of the QCD Lagrangian for a pair of a heavy quark and a heavy antiquark ignoring contributions from light quarks (see Sec. 1.6.2.2). (a) shows a visualization of the gluon string that forms between the quark and the antiquark, which are represented by the spheres. From Ref. [6]. (b) shows the effective potential between the quark-antiquark pair as a function of their separation r from numerical simulations (points) overlaid with the Cornell potential from Eq. (1.6) (red curve). From Ref. [7].

the strong interaction becomes highly non-linear. Therefore, the perturbative expansion in α_s breaks down and cannot be used anymore to solve the field equations. This realm of the strong interaction is called *non-perturbative QCD*. Because of the non-perturbative nature of QCD, we are unable to perform analytic ab-initio calculations even for simple static properties of hadrons such as their masses. Up to now, all attempts to construct an analytic proof of color confinement in any non-abelian gauge theory were unsuccessful. The confinement problem remains one of the last open questions of the Standard Model and one of the biggest challenges in theoretical particle physics.[h]

A solution of the confinement problem would not only greatly enhance our understanding of the Standard Model and of hadron physics in particular, but might also be a key for constructing an extension to the Standard Model. Some proposed extensions, like Technicolor [10] or composite Higgs models [11], introduce new non-abelian and hence confining gauge interactions and face challenges similar to non-perturbative QCD.

1.3 Non-perturbative QCD and hadron spectroscopy

Hadrons are a direct consequence of confinement and reflect the workings of QCD at low energies. Hence their properties are tightly related to the confinement mechanism. The most fundamental static property of a hadron is its mass. Usually, bound states of particles have a mass that is smaller than the sum of their constituent's masses. This is due to the binding energy and is known as the "mass defect", which can be observed, for example, in nuclei and—on a much smaller scale—also in atoms. Hadrons, however, behave fundamentally different.

[h] Finding a proof for confinement is actually one of the seven Millennium Prize Problems posed by the Clay Mathematics Institute and is endowed with a prize money of 10^6 USD [9].

The most important hadrons are the proton and the neutron. They are made of up and down quarks with only small contributions from the heavier quarks. The up and down quarks have masses of $m_u = 2.2\,^{+0.6}_{-0.4}\,\text{MeV}$ and $m_d = 4.7\,^{+0.5}_{-0.4}\,\text{MeV}$[i] that are, however, much smaller than the nucleon mass of about $m_N = 938.9\,\text{MeV}$ [13].[j] In order to quantify the contribution of the up and down quark masses to the nucleon mass, we express the nucleon mass in terms of the nucleon matrix element [14]:

$$m_N = \frac{1}{2m_N}\,\langle N(p)|\theta^\mu_\mu|N(p)\rangle\,. \tag{1.7}$$

Here, $|N(p)\rangle$ represents a nucleon state with four-momentum p and θ^μ_μ is the trace of the QCD energy-momentum tensor, which in leading order in α_s is given by

$$\theta^\mu_\mu = \sum_{f=\{u,d,s\}} m_f\,\bar\psi_f\,\psi_f - \frac{9\alpha_s}{4\pi}\,\text{tr}\big(G^{\mu\nu}\,G_{\mu\nu}\big)\,, \tag{1.8}$$

where we have considered only the three lightest quark flavors. The ψ_f are color triplets of quark spinors, $G^{\mu\nu} \equiv \sum_{a=1}^{N_c^2-1} G^{\mu\nu}_a\,\lambda_a/2$, and the trace is taken over the 3×3 color matrices. The second term containing the square of the gluon field tensor is called the *QCD trace anomaly*. It represents the contribution of the gluon fields to the nucleon mass.

The contribution of the up and down quarks is represented by the so-called *pion-nucleon sigma term*,

$$\sigma_N = \frac{1}{2m_N}\,\langle N(p)|m_u\,\bar\psi_u\,\psi_u + m_d\,\bar\psi_d\,\psi_d|N(p)\rangle\,. \tag{1.9}$$

It has a value of $\sigma_N = 45 \pm 8\,\text{MeV}$ [15, 16], which corresponds to the value by which the nucleon mass would be lowered, if up and down quarks were massless. This means that although the nucleon is made of up and down quarks, the mass of these constituents contributes only a small fraction to the nucleon mass. It turns out that also the contribution from the strange quarks is small. Therefore, QCD generates massive hadrons from nearly massless constituents. According to Eqs. (1.7) and (1.8), the bulk part of the nucleon mass must hence come from the trace anomaly. This means that the nucleon mass is of dynamical origin, i.e., it is generated by the strong confining forces. Therefore, mass and size of the nucleon are determined by the interaction of the gluons with each other and by the relativistic kinetic energy of the light quarks.[k]

This means that although the discovery of the Higgs particle at the LHC [18, 19] has proven that we understand the mechanism that generates the masses of the Standard Model particles including the quarks, we do not yet understand quantitatively the origin of the hadron masses. This is in particular true for the masses of protons and neutrons, which make up all visible matter in the universe.

[i] Since quarks cannot be free, the definition of quark masses is actually highly non-trivial (see, e.g., Ref. [12] for details). The masses given here are the so-called *current quark masses* that enter the QCD Lagrangian in Eq. (1.1) and are calculated in a particular renormalization scheme ($\overline{\text{MS}}$) at a renormalization scale of 2 GeV [13].

[j] The nucleon mass is defined as the arithmetic average of the masses of proton and neutron.

[k] An additional key ingredient is the spontaneous breaking of the chiral symmetry of the QCD Lagrangian. Chiral symmetry is describes the fact that in the limit of massless light quarks, left- and right-handed quark fields decouple from each other in the QCD Lagrangian in Eq. (1.1). In addition to the spontaneous breaking, chiral symmetry is slightly broken explicitly by the small masses of up, down, and strange quarks. For more details see, e.g., Ref. [17].

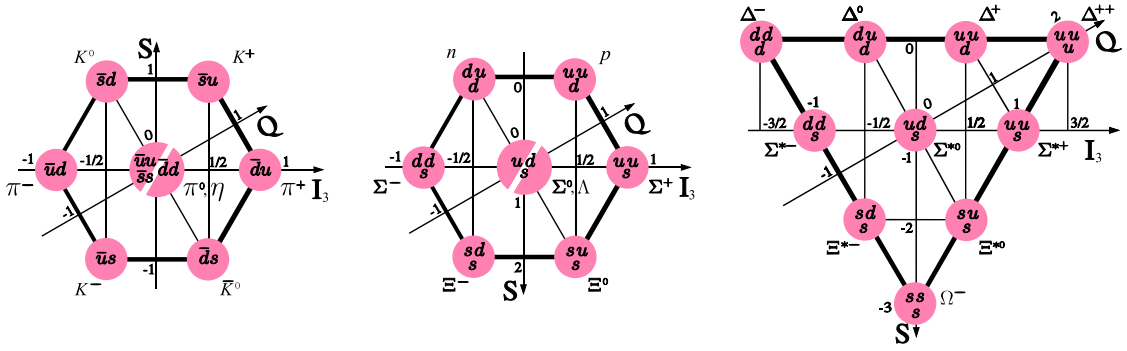

(a) (b) (c)

Figure 1.4: $SU(3)_{\text{flavor}}$ multiplets for hadrons made of up, down, and strange quarks: (a) octet of ground-state mesons with spin zero and negative parity, (b) octet of ground-state baryons with spin 1/2 and positive parity, and (c) decuplet of ground-state baryons with spin 3/2 and positive parity. Q is the charge, S the strangeness, and I_3 the z-component of the isospin. From Refs. [25–27].

In an analog way as studying the excitation spectrum of atoms has lead to an understanding of the electromagnetic force and eventually to QED, a precise measurement of the rich excitation spectrum of hadrons and of hadron decays provides valuable input to theory and phenomenology and helps to improve our understanding of how quarks and gluons behave at low energies. Today, the study of the hadron spectrum is a global effort with experiments at all major particle-physics facilities exploring different parts of these spectra. The ultimate goal is to prove that QCD is the correct theory also at low-energies and that it is able to describe all the complex properties of hadrons.

1.4 The constituent quark model

Hadrons can be subdivided into two classes: *mesons*, which have integer spin and are hence bosons, and *baryons*, which have half-integer spin and are hence fermions. In the 1950s and 1960s, many new hadrons were found in experiments. At that time, it was not yet clear that hadrons are composite objects and they were hence colloquially referred to as the "particle zoo". It was therefore a big leap forward when M. Gell-Mann [20] and Y. Ne'eman [21] independently found that the hadrons known at that time could be organized into representations of an SU(3) symmetry group: the mesons form an octet (see Fig. 1.4(a)); the baryons an octet and a decuplet (see Figs. 1.4(b) and 1.4(c)).[l] This finding led M. Gell-Mann [22] and G. Zweig [23, 24] independently to propose the existence of fundamental spin-1/2 particles that Gell-Mann named "quarks" and Zweig named "aces" and that come in three flavors: up, down, and strange. In this model, a meson is a bound state of a quark q and an antiquark $\bar{q}$, i.e., $|q\bar{q}\rangle$; baryons are bound states of three quarks, i.e., $|qqq\rangle$.[m] The quark model therefore reduces the large number of observed hadrons to three fundamental building blocks.

[l] Gell-Mann called this classification scheme the "Eightfold Way" inspired by the Noble Eightfold Path of Buddhism.

[m] Here, q stands for u, d, or s and, unless specified otherwise, the various q or $\bar{q}$ in a state may represent different flavors.

In the simplest form of the quark model, the *constituent quark model*, the quarks are interpreted as effective particles, which determine the quantum numbers of the hadron. The quarks are "dressed" by a surrounding cloud of gluons and virtual quark-antiquark pairs, which is taken into account in the form of an effective constituent quark mass that is much larger than the current quark mass in the QCD Lagrangian in Eq. (1.1). This means constituent quarks are not point-like, but are extended objects with internal structure. The mass of a hadron is given by the sum of the constituent quark masses, if we assume that the constituent quarks are at rest and non-interacting, except for a color-magnetic spin-spin interaction. This interaction gives a contribution to the hadron mass that can be calculated analogously to the electromagnetic hyperfine interaction of the electron and proton spins in a hydrogen atom. The up and down quarks have a constituent mass of about one third of the proton mass. Strange quarks are about 150 MeV heavier. Due to the similar masses of the constituents quarks, the masses of the hadrons in the same $\mathrm{SU}(3)_{\mathrm{flavor}}$ multiplet are also similar and their differences are in most cases well explained by the heavier strange quark(s). Given its simplicity, the constituent quark model reproduces the masses of ground-state baryons and mesons already astonishingly well (see, e.g., Refs. [28, 29]).

Today, we know that there are six quark flavors: u, d, c, s, t, and b. With the exception of the top quark, which decays too quickly via the weak interaction, quarks of all flavors form hadrons. By including the charm quark one can extend the flavor symmetry to $\mathrm{SU}(4)_{\mathrm{flavor}}$. However, this symmetry is strongly broken due to the much heavier charm quark. This breaking becomes even stronger when one extends the symmetry to $\mathrm{SU}(5)_{\mathrm{flavor}}$ by also including the bottom quark. Nevertheless, these symmetries are useful to classify hadrons.

1.5 Light mesons

In this work, we study light mesons, i.e., $|q\bar{q}\,'\rangle$ states,[n] that are made of u, d, and s quarks and are hence organized in $\mathrm{SU}(3)_{\mathrm{flavor}}$ multiplets. Light mesons are characterized by their spin J, the parity eigenvalue P of their wave function, their isospin I, the z-component I_z of the isospin, and their strangeness [30].

For $|q\bar{q}\rangle$ states, i.e., states of a quark and its own antiquark, in addition the charge conjugation quantum number C is defined. For mesons with $I_z = 0$, i.e., neutral mesons, and for charged mesons without strangeness, the charge conjugation operator $\hat{C}$ can be generalized to the G-parity operator $\hat{G}$ via

$$\hat{G} \equiv \hat{C}\, e^{i\pi\, I_y}. \tag{1.10}$$

Hence G-parity is the combination of charge conjugation and a rotation by 180° about the y-axis in isospin space. The latter is equivalent to a sign flip of I_z, which corresponds to a sign flip of the electrical charge. This undoes the sign flip of the charge caused by the charge conjugation operator. Therefore, the members of an isospin triplet, such as (π^-, π^0, π^+), are eigenstates of $\hat{G}$ with eigenvalue

$$G = C\,(-1)^I. \tag{1.11}$$

That all members of the isospin triplet have the same G-parity reflects the fact that the strong interaction does not care about the electrical charge and hence cannot distinguish

[n] In this section, we explicitly distinguish $|q\bar{q}\rangle$ mesons that consist of a quark and its own antiquark and $|q\bar{q}\,'\rangle$ mesons that consist of a quark and an antiquark of different flavors.

between the differently charged states. For charged states, it is often customary in the literature to quote the C-parity of the neutral partner in the isospin triplet instead of the G-parity. We follow this convention here as well.

In the constituent quark model, the quantum numbers of a meson are given by the quantum numbers of the $q\bar{q}'$ pair. The spins of the quark and the antiquark can couple to a total intrinsic spin of $S = 0$ (quark spins anti-parallel) or 1 (quark spins parallel). The total intrinsic spin couples with the relative orbital angular momentum L between the quark and the antiquark to the total spin J of the meson, so that

$$|L - S| \leq J \leq L + S. \tag{1.12}$$

The parity of a $|q\bar{q}'\rangle$ state is

$$P = (-1)^{L+1}, \tag{1.13}$$

where the factor $(-1)^L$ represents the parity of the spatial wave function of an orbital-angular-momentum eigenstate. The additional factor of -1 comes from the intrinsic parity of a fermion-antifermion pair.[o] Applying the charge conjugation operator to a $|q\bar{q}\rangle$ state, one can show that the C-parity of this state is

$$C = (-1)^{L+S}. \tag{1.14}$$

Therefore, S, L, and J define the J^{PC} quantum numbers of a meson via Eqs. (1.13) and (1.14). Using Eq. (1.11), it follows that

$$G = (-1)^{L+S+I}. \tag{1.15}$$

In addition to L, which characterizes orbital excitations of the $q\bar{q}'$ pair, the principal quantum number

$$n \equiv n_r + 1. \tag{1.16}$$

characterizes the radial excitation of the two-particle system. Here, n_r is the radial quantum number, which is equal to the number of nodes in the radial wave function.[p] To define a $|q\bar{q}'\rangle$ state one commonly uses the term symbol $n\,^{2S+1}L_J$, where L is represented by capital letters, i.e., $L = S, P, D, F, \ldots$.

The light mesons are grouped into $\mathrm{SU}(3)_{\mathrm{flavor}}$ multiplets. For each term symbol, i.e., each combination of n and J^{PC}, there exist a flavor singlet and a flavor octet. Together, they are referred to as an $\mathrm{SU}(3)_{\mathrm{flavor}}$ *nonet*. For example, the octet for the $1\,^1S_0$ states with $J^P = 0^-$ and—where defined—$C = +1$ and $G = -1$ is shown in Fig. 1.4(a). The corresponding singlet state is the $\eta'(958)$. According to the Particle Data Group (PDG), the $\mathrm{SU}(3)_{\mathrm{flavor}}$ nonets for the first radial and orbital excitations are fairly well established [30]. They are listed in Table 1.1 with the exception of the scalar mesons with $J^{PC} = 0^{++}$ because their assignment is unclear. In fact, the light scalar nonet with $a_0(980)$, $K_0^*(800)$, $f_0(980)$, and $f_0(500)$ might even belong to a completely different class of meson states, which goes beyond the simple $|q\bar{q}'\rangle$ picture of the quark model. This will be discussed further in Sec. 1.6.3.

[o] One can show from the Dirac equation that fermions and antifermions must have opposite intrinsic parity.

[p] Note that the definition of the principal quantum number in Eq. (1.16) differs from the one used in atomic physics, where

$$n \equiv n_r + L + 1. \tag{1.17}$$

Table 1.1: Assignment of light-meson states to quark-model $q\bar{q}'$ $\mathrm{SU}(3)_{\mathrm{flavor}}$ nonets according to the PDG [30]. The two last columns list the physical $I = 0$ states. The $\mathrm{SU}(3)_{\mathrm{flavor}}$ singlet and octet states with $I = 0$ have the same quantum numbers and therefore mix. The mixing leads to two physical states, of which in most cases one is dominated by $s\bar{s}$ and the other by $u\bar{u}$ and $d\bar{d}$. The latter is therefore lighter. Since the kaons are neither C- nor G-parity eigenstates, kaon states of different nonets may mix. This is known to be the case for the kaon states in the $J^{PC} = 1^{+-}$ and 1^{++} nonets: K_{1A} and K_{1B} are nearly equal mixtures of $K_1(1270)$ and $K_1(1400)$. Also, the kaon states in the $J^{PC} = 2^{-+}$ and 2^{--} nonets mix. The $1\,^3D_1$, $1\,^3D_2$, and $1\,^3F_4$ nonets are still incomplete.

n	L	S	J^{PC}	Term symbol	$I = 1$	$I = 1/2$	$I = 0$	$I = 0$
1	0	0	0^{-+}	$1\,^1S_0$	π	K	η	$\eta'(958)$
		1	1^{--}	$1\,^3S_1$	$\rho(770)$	$K^*(892)$	$\phi(1020)$	$\omega(782)$
	1	0	1^{+-}	$1\,^1P_1$	$b_1(1235)$	K_{1B}	$h_1(1380)$	$h_1(1170)$
		1	1^{++}	$1\,^3P_1$	$a_1(1260)$	K_{1A}	$f_1(1420)$	$f_1(1285)$
		1	2^{++}	$1\,^3P_2$	$a_2(1320)$	$K_2^*(1430)$	$f_2'(1525)$	$f_2(1270)$
	2	0	2^{-+}	$1\,^1D_2$	$\pi_2(1670)$	$K_2(1770)$	$\eta_2(1870)$	$\eta_2(1645)$
		1	1^{--}	$1\,^3D_1$	$\rho(1700)$	$K^*(1680)$		$\omega(1650)$
		1	2^{--}	$1\,^3D_2$		$K_2(1820)$		
		1	3^{--}	$1\,^3D_3$	$\rho_3(1690)$	$K_3^*(1780)$	$\phi_3(1850)$	$\omega_3(1670)$
	3	1	4^{++}	$1\,^3F_4$	$a_4(2040)$	$K_4^*(2045)$		$f_4(2050)$
2	0	0	0^{-+}	$2\,^1S_0$	$\pi(1300)$	$K(1460)$	$\eta(1475)$	$\eta(1295)$
		1	1^{--}	$2\,^3S_1$	$\rho(1450)$	$K^*(1410)$	$\phi(1680)$	$\omega(1420)$

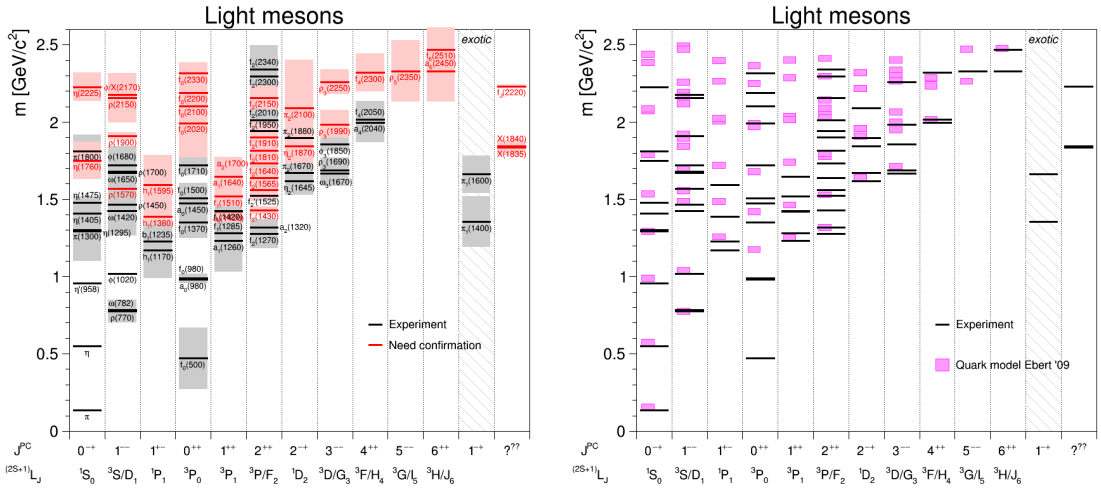

(a) **(b)**

Figure 1.5: (a) World data on the spectrum of non-strange light mesons as collected by the PDG [31]. The meson states are sorted by their J^{PC} quantum numbers. Horizontal lines represent the masses of the states, shaded boxes their widths. The black lines and gray boxes indicate states that are considered established by the PDG; red lines and red shaded boxes indicate states that need confirmation. (b) Comparison of the measured light-meson masses (black lines) with the masses of $|q\bar{q}'\rangle$ states as calculated in a relativistic quark model [32] (magenta boxes). Both figures from Ref. [33].

1.6 The spectrum of non-strange light mesons

In this work, we study the spectrum of light mesons with zero strangeness. The spectrum of these mesons has been studied for many decades by many experiments. Therefore, many states are already known and for many of them also their masses, widths and decay modes are known rather well as is illustrated in Fig. 1.5(a). Most light mesons decay via the strong interaction and hence have substantial widths of the order of 100 MeV. For higher-excited mesons, with masses of about 2 GeV or larger, many states are disputed or need confirmation (see Fig. 1.5(a)). This mass region is referred to as the "light-meson frontier". The identification of resonances in this mass region is challenging because states usually become broader with increasing mass. Together with the increasing density of states, this leads to overlapping and mixing of states with the same quantum numbers, which makes the identification of states more difficult.

1.6.1 Resonances

As mentioned above, most light mesons decay via the strong interaction into lighter hadrons and have therefore very short life times of the order of 10^{-23} sec. Such particles are called *resonances* [34]. Resonances are not directly detectable in an experiment. Only those daughter particles from their decays that are stable with respect to the strong and electromagnetic interactions will reach the detector. These so-called *quasi-stable particles* are often pions and kaons. Resonances—from here on represented by X—may appear in three kinds of processes: (i) *formation experiments* of the form $a + b \to X \to h_1 + \ldots + h_n$ (see Fig. 1.6(a)), where a and b are the colliding particles and the h_i are the measured

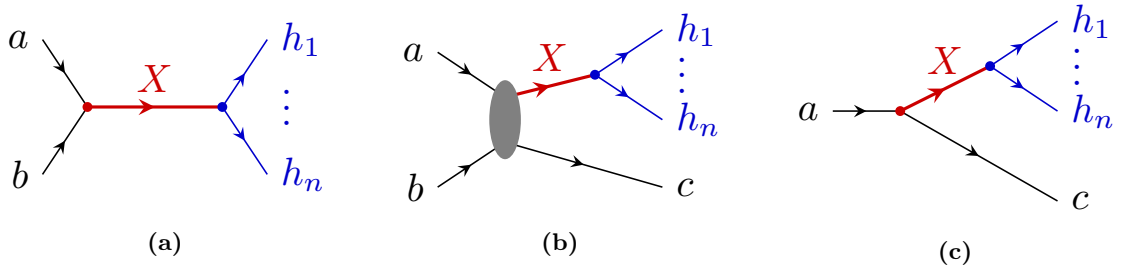

Figure 1.6: Three kinds of processes, in which a resonance X can be produced: (a) formation experiment, (b) production experiment, and (c) particle decay.

final-state hadrons that X decays into, (ii) *production experiments* of the form $a+b \to X+c$ with $X \to h_1 + \ldots + h_n$ (see Fig. 1.6(b)), where c represent one or more spectator particles, and (iii) *decays* of the form $a \to X + c$ with $X \to h_1 + \ldots + h_n$ (see Fig. 1.6(c)).

In formation experiments, the resonance is formed by the two colliding particles as an intermediate state. The invariant mass m_X of X is given by the center-of-mass energy $\sqrt{s}$ of the collision, where s is the Mandelstam variable defined as

$$s \equiv (p_a + p_b)^2 \,, \tag{1.18}$$

with p_i being the four-momentum of particle i. This process is also called s-channel scattering. The initial state fixes not only the mass of X but also the quantum numbers of X. Hence formation experiments provide a well-controlled environment, but one can often study only a limited set of states. The study of resonances in particle decays has similar limitations,[q] although one has in principle a larger choice of initial states.

Production experiments impose the least constraints on the produced resonances. The quantum numbers of X are only limited by the conversation laws of the interaction. Although s is often fixed, the center-of-mass energy is shared between X and the recoil particle c. Hence an m_X range from the kinematic threshold at $\sum_{i=1}^{n} m_{h_i}$ up to $\sqrt{s} - m_c$ can be probed. At high center-of-mass energies, production processes are dominated by the exchange of virtual (quasi)particles, so-called t-channel exchange. In addition to the variable s, the inelastic scattering process is characterized by the squared four-momentum t that is transferred by the exchange particle. This Mandelstam variable is defined as

$$t \equiv (p_a - p_X)^2 = (p_c - p_b)^2 \,. \tag{1.19}$$

In t-channel exchange processes, t has always negative values. It is convenient to introduce the positive definite reduced squared four-momentum transfer t', which is defined as

$$t' \equiv |t| - |t|_{\text{min}}. \tag{1.20}$$

Here, $|t|_{\text{min}}$ is the minimum absolute value of t required to produce the (X, c) system.[r]

[q] Here, $m_X^2 = (p_a - p_c)^2$.

[r] In the laboratory frame,

$$|t|_{\text{min}} \approx \left(\frac{m_X^2 - m_a^2}{2|\vec{p}_a|} \right)^2 . \tag{1.21}$$

In the simplest case, resonances appear as enhancements of the scattering cross section or the decay rate as a function of m_X. This is analogous to a driven harmonic oscillator, for which the energy transfer becomes maximal at the resonance frequency. The analogy can be taken even further: the phase difference between the oscillator and the driving force grows with increasing frequency from zero at low frequencies, over 90° at the resonance frequency up to 180° at very high frequencies. In particle physics, the quantum mechanical probability amplitude of a resonance exhibits a similar behavior as a function of m_X. This m_X dependence of the resonance phase is called *phase motion*.

In addition to their mass m_0, resonances are characterized by their total width Γ_0, which is related via the Heisenberg uncertainty principle to the mean lifetime τ of the resonance, i.e.,

$$\tau = \frac{1}{\Gamma_0}. \tag{1.22}$$

1.6.1.1 Resonance amplitudes

The simplest approximation for the amplitude of an isolated narrow resonance far above kinematic thresholds is the *relativistic Breit-Wigner amplitude* [35]. It has the form[s]

$$\Delta^{\mathrm{BW}}(m_X; m_0, \Gamma_0) = \frac{m_0\,\Gamma_0}{m_0^2 - m_X^2 - i\,m_0\,\Gamma_0} \tag{1.23}$$

and can be thought of as the propagator of an unstable particle with nominal mass m_0 and total width Γ_0. Figure 1.7(a) shows the intensity, i.e., $\left|\Delta^{\mathrm{BW}}(m_X)\right|^2$, of a Breit-Wigner amplitude for a fictitious resonance. The intensity distribution exhibits the typical resonance peak at m_0 with a width given by Γ_0. Figure 1.7(b) shows the corresponding rising phase motion $\arg\left[\Delta^{\mathrm{BW}}(m_X)\right]$ which crosses 90° at m_0. The Breit-Wigner amplitude in Eq. (1.23) can also be visualized in the complex plane as shown in Fig. 1.7(c). In such *Argand diagrams*, a resonance appears as counter-clockwise circular structure.

For resonances with larger widths, a better approximation to the physical amplitude is

$$\Delta^{\mathrm{BW}}(m_X; m_0, \Gamma_0) = \frac{m_0\,\Gamma_0}{m_0^2 - m_X^2 - i\,m_0\,\Gamma_{\mathrm{tot}}(m_X)} \tag{1.24}$$

with the *mass-dependent total width*

$$\Gamma_{\mathrm{tot}}(m_X) = \sum_i^{\substack{\text{decay}\\ \text{modes}}} \Gamma_i \,\frac{q_i}{m_X}\,\frac{m_0}{q_{i,0}}\,\frac{F_{L_i}^2(q_i)}{F_{L_i}^2(q_{i,0})}, \tag{1.25}$$

which takes into account the opening of the phase space for the decay into the daughter particles across the resonance width. The total width is given by the sum of the phase-space volumes of all decay modes i of the resonance X, weighted by their partial widths Γ_i. In Eq. (1.25), it is assumed that all decay modes of X are two-body decays that are characterized by a relative orbital angular momentum L_i between the two daughter particles.

[s] The numerator in Eq. (1.23) depends on the normalization, which we have chosen such that $\Delta^{\mathrm{BW}}(m_0) = +i$.

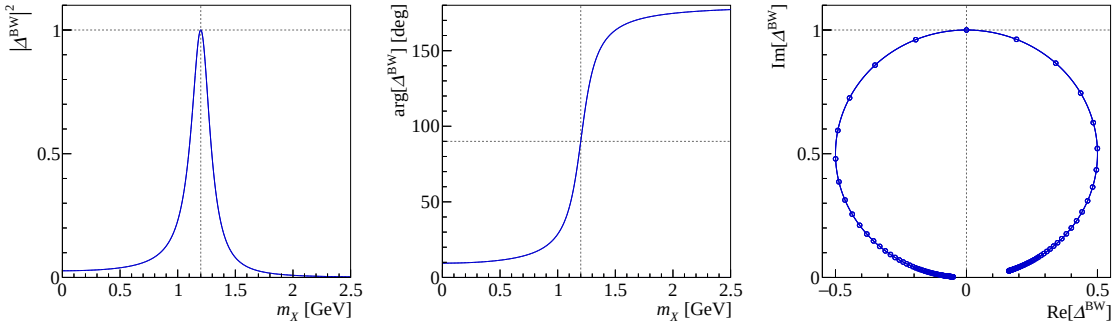

(a) **(b)** **(c)**

Figure 1.7: Example of a relativistic Breit-Wigner amplitude with constant width as in Eq. (1.23) for a fictitious resonance with a mass of $m_0 = 1200\,\mathrm{MeV}$ and a total width of $\Gamma_0 = 200\,\mathrm{MeV}$. The amplitude is normalized such that it is $+i$ at the resonance mass. (a) shows the intensity, i.e., the absolute value squared of the amplitude, (b) the phase of the amplitude, and (c) the Argand diagram of the amplitude. The points in (c) are spaced equidistantly in m_X by 20 MeV and m_X increases in counter-clockwise direction from 0 to 2.5 GeV.

The two-body phase-space volume is given by q_i/m_X, where q_i is the magnitude of the *two-body breakup momentum* in the X rest frame as given by

$$\begin{aligned} |\vec{q}_i|^2 &\equiv q_i^2(m_X; m_{i,1}, m_{i,2}) \\ &= \frac{\left[m_X^2 - (m_{i,1} + m_{i,2})^2\right]\left[m_X^2 - (m_{i,1} - m_{i,2})^2\right]}{4m_X^2}. \end{aligned} \tag{1.26}$$

Here, $m_{i,1}$ and $m_{i,2}$ are the masses of the daughter particles for decay mode i.

Since in Eq. (1.25) $q_{i,0} \equiv q_i(m_0)$, the mass-dependent width is normalized such that

$$\Gamma_{\mathrm{tot}}(m_0) = \sum_{i}^{\substack{\text{decay}\\ \text{modes}}} \Gamma_i. \tag{1.27}$$

The *Blatt-Weisskopf centrifugal-barrier factors* $F_{L_i}(q_i)$ that appear in Eq. (1.25) take into account the barrier effect caused by the orbital angular momentum L_i in the two-body decay. The maximum L_i in a decay is limited by the magnitude of the linear breakup momentum q_i and the impact parameter between the daughters that is typically assumed to be given by the range of the strong interaction, which is about 1 fm. This corresponds via the Heisenberg uncertainty relation to a range parameter of $q_R \approx 200\,\mathrm{MeV}$. At small m_X, i.e., small q_i, it is difficult to generate the orbital angular momentum in the decay. Close to threshold, the decay rate is therefore proportional to the product of the two-body phase-space factor q_i/m_X and the centrifugal-barrier factor $q_i^{2L_i}$. However, for larger m_X, i.e., larger q_i, the $q_i^{2L_i}$ factor would lead to unphysical growth of the decay rate and hence needs to be damped. A phenomenological parametrization of the barrier factors in terms of spherical Hankel functions of the first kind was derived by Blatt and Weisskopf [36]. The barrier factors are usually written as functions of $z_i(m_X) \equiv \left[q_i(m_X)/q_R\right]^2$ and often the parametrization of von Hippel and Quigg [37] is used. It is customary to normalize the barrier factor such that $F_{L_i}(z_i) = 1$ at $z_i = 1$. For the lowest values of L_i, the barrier

factors read[t]

$$F_0^2(z_i) = 1, \quad F_1^2(z_i) = \frac{2z_i}{z_i + 1}, \quad \text{and} \quad F_2^2(z_i) = \frac{13z_i^2}{z_i^2 + 3z_i + 9}. \tag{1.28}$$

Although we assume in Eq. (1.25) that the daughter particles of the two-body decays are stable, this parametrization is often also applied to cases where at least one of the daughter particles is unstable. Such two-body approximations neglect the effect of the finite width(s) of the unstable daughter particle(s).[u]

The simple Breit-Wigner parametrizations in Eqs. (1.23) and (1.24) have further limitations [34]. Using a sum of Breit-Wigner amplitudes to describe the total amplitude of a set of resonances with the same quantum numbers is a good approximation only if the resonances are well-separated so that they have little overlap. Otherwise unitarity, i.e., the conservation of probability, may be violated (see also the paragraph below). For resonances with multiple decay modes, Breit-Wigner parametrizations do also not take into account coupled-channel effects caused by unitarity constraints. These effects may become large when the kinematic thresholds of one or more of these decay modes are in the mass range of the resonance. In practice, the limitations discussed above render Breit-Wigner parameters model- and process-dependent.

In principle, strong-interaction scattering and decay processes are described by the S-matrix, which is a unitary operator that connects the sets of asymptotically free particle states of the initial and the final state of a reaction [34, 38]. The elements of the S-matrix are related to the scattering amplitudes. The S-matrix is constrained by unitarity, crossing symmetry, and analyticity, where the latter is a consequence of causality. This means that scattering amplitudes must be analytic functions in the complex plane of the Mandelstam variable s. These functions may have branch cuts that are caused by the opening of scattering channels with increasing s and poles that are caused either by bound states or by resonances. The location of a resonance pole in the complex s plane and the residue of that pole represent the actual universal resonance properties, which one wants to extract from data. However, the construction of amplitudes that describe multi-body decays of hadrons and that fulfill all S-matrix constraints is a formidable task and has so far only been achieved in a few cases.

If the threshold of a decay channel is close to the resonance, the next best approximation beyond the Breit-Wigner amplitude is usually the Flatté parametrization [39]. More general approaches for the parametrization of resonance amplitudes that respect at least analyticity and two-body unitarity, such as K-matrix approaches [40, 41] are usually more difficult to employ. One of the difficulties is that the data from a single decay channel are often insufficient to estimate all parameter values reliably from the data.

Unfortunately, it turns out that a resonance pole is not uniquely defined by an intensity peak with an associated phase motion of about 180°. Under special circumstances, scattering amplitudes may have singularities that exhibit the same experimental signature without being related to resonances. A possible example is the $a_1(1420)$ signal, which could be the logarithmic singularity of a triangle diagram in a rescattering process of the daughter particles [42, 43]. This is discussed further in Sec. 4.2.4.

[t] A list of barrier factors for orbital angular momenta up to $L = 6$ can be found, for example, in eqs. (33) through (39) in Ref. [H2].

[u] Note that Eqs. (1.25) and (1.26) are not a good approximation anymore if subthreshold contributions are important, i.e., if the decay of X proceeds via the low-mass tail(s) of the unstable daughter particle(s).

1.6.2 Theoretical predictions

As discussed in Sec. 1.2, most properties of hadrons cannot be directly calculated from the QCD Lagrangian in Eq. (1.1) due to the non-perturbative nature of QCD. In the past, various QCD-inspired models have been developed to predict the spectrum and the decays of light mesons (see, e.g., Refs. [44, 45] and references therein). In Sec. 1.6.2.1, we discuss, as an example, a recent quark-model calculation.

In recent years, numerical ab-initio methods based on the simulation of the QCD Lagrangian on a discretized space-time lattice have made tremendous progress. These so-called lattice QCD calculations are now able to make predictions for light-meson spectra and for two-body scattering processes. The status of these calculations is discussed in Sec. 1.6.2.2.

1.6.2.1 Quark-model calculations

Due to the small masses of the up, down, and strange quarks, they move at highly relativistic velocities within hadrons. Therefore, simple static potential models, such as the Cornell potential in Eq. (1.6), are not good approximations anymore. There are several quark models that incorporate relativistic effects. A recent example from Ref. [32] is shown in Fig. 1.5(b). For most of the lower-lying states, the calculation is in fair agreement with the data. In the 2 GeV region, many states are predicted by the model that have not yet been found by experiments. Interestingly, the model fails to reproduce the low-lying scalar states with $J^{PC} = 0^{++}$. They will be discussed in Sec. 1.6.3 below.

1.6.2.2 Lattice QCD results

Lattice QCD is presently the only available rigorous ab-initio method that can consistently describe the physics of binding and decay of hadrons [46–48]. It is a form of lattice gauge theory as proposed by K. G. Wilson in Ref. [49], where calculations are performed in a discretized Euclidean space-time using a hypercubic lattice with lattice spacing a. The lattice spacing leads to a momentum cut-off $\propto 1/a$ (ultraviolet regularization). In lattice QCD, the quark fields are placed at the lattice sites, while the gluon gauge fields are defined on the links that connect neighboring sites.

The calculations are performed using Monte Carlo techniques, i.e., by sampling possible configurations of the quark and gluon fields according to the probability given by the QCD Lagrangian. This requires large computational resources provided only by supercomputers. Because of the employed Monte Carlo approach, only a finite number of configurations can be considered. This leads to statistical uncertainties of the lattice QCD results. To limit the computational cost, the calculations are often performed using heavier up and down quarks than in nature. This drastically reduces the number of virtual quark-antiquark loops that have to be taken into account. The up and down quark masses are commonly expressed in terms of the resulting pion mass.

In lattice QCD calculations, the extend of the space-time lattice is necessarily finite. Many calculations use asymmetric lattices with N_s lattice points in the three spatial directions and N_t points in the temporal direction.[v] The sizes of the space-time box are hence $L_s = aN_s$ and $L_t = aN_t$, where often $L_t \geq 2L_s$ is chosen to give excited-state

[v] In some cases, also different lattice spacings are chosen for the spatial and temporal directions.

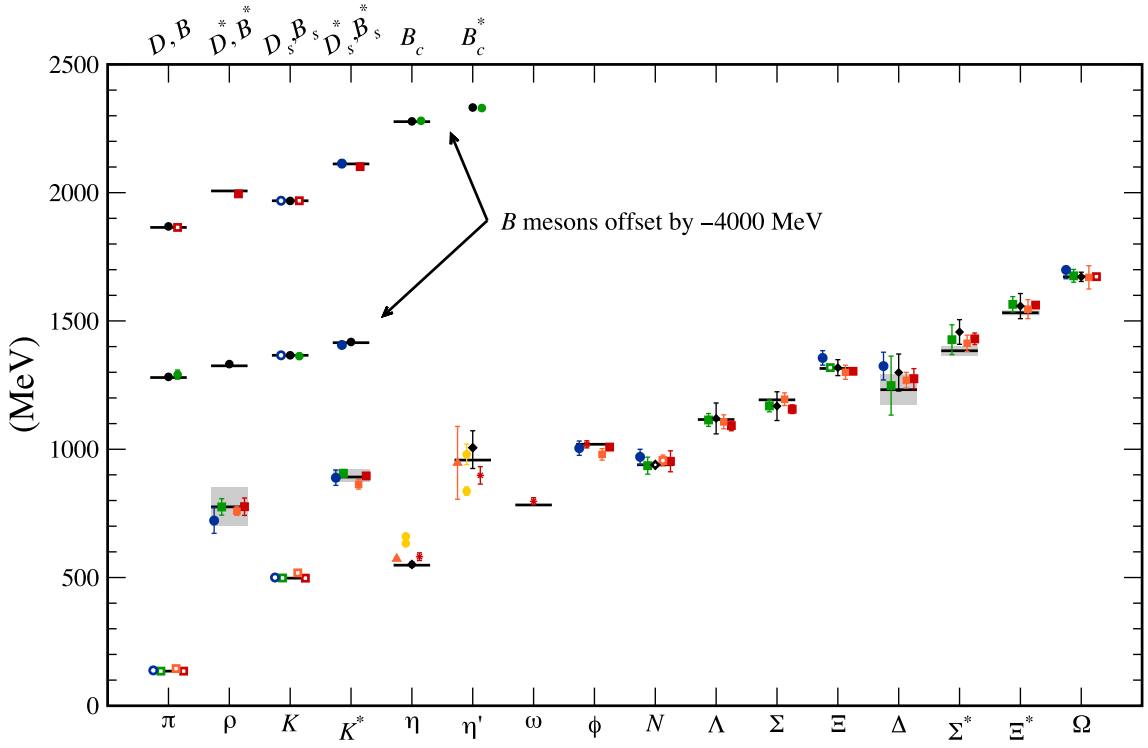

Figure 1.8: Spectrum of meson and baryon states that correspond to orbital and radial ground states. The black horizontal lines represent the experimentally measured masses, the gray boxes the measured widths. The masses of the bottom-flavored mesons have been shifted down by 4000 MeV. The points represent lattice QCD results from various groups. Open symbols indicate those hadron masses that were used to fix parameters in the calculation. Figure by A. S. Kronfeld; from Ref. [30]; earlier version in Ref. [54].

contributions time to decay. Hence the dominant systematic effects introduced by the lattice are due to its finite spatial volume and its discrete nature.

In order to obtain physical results, several limits have to be taken: (i) the *continuum limit*, i.e., the extrapolation to $a \to 0$, (ii) the *infinite-volume limit*, i.e., the extrapolation to $L_s \to \infty$, and (iii) the *physical quark-mass limit*, i.e., the extrapolation to physical quark masses. Many present lattice calculations are already performed directly at or very close to the physical values of the quark masses (see, e.g., Ref. [50]), so that the latter extrapolation becomes less of an issue. Unfortunately, this is not yet the case for lattice QCD calculations of excited hadron resonances as will be discussed further below.

Lattice QCD calculations have shown that QCD confines color [51–53] (see Fig. 1.3). The method was also used successfully to calculate various hadron properties. As an example, Fig. 1.8 shows the current lattice QCD results on the masses of ground-state hadrons. The results match the experimental values with impressive precision. This is a highly non-trivial result and shows that QCD indeed seems to be the correct theory also at low energies.

Compared to the ground-state hadrons, lattice QCD studies of the excitation spectrum of hadronic states are still performed further away from the physical point. However, tremendous progress has been made in the development of methods in order to extract

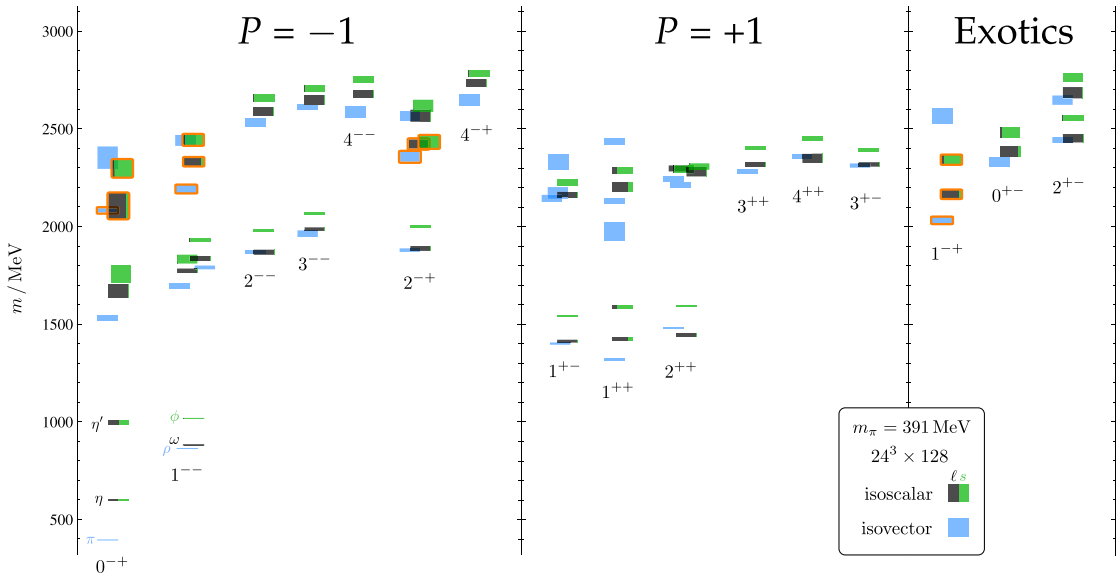

Figure 1.9: Spectrum of light non-strange isoscalar (blue boxes) and isovector mesons (green/black boxes) from a lattice QCD calculation performed on a $24^3 \times 128$ lattice with a spatial lattice spacing of 0.12 fm and a temporal lattice spacing of 0.034 fm using unphysical up and down quark masses that correspond to a pion mass of 391 MeV. The height of the boxes corresponds to the statistical uncertainty of the estimated masses. For the isoscalar states, the mixing contribution from up and down quarks is indicated by the black areas, the contribution from strange quarks by the green areas. Boxes outlined with orange represent the lightest states that have a large chromomagnetic component in their wave function. They can be interpreted as the lightest hybrid-meson supermultiplet. From Ref. [55].

towers of highly excited states and to determine their inner structure (see, e.g., Ref. [48] and references therein). The cubic lattice breaks the rotational invariance of space and hence makes the identification of the spin of states more difficult. It was found that with a sufficiently fine lattice spacing the effects of the reduced rotational symmetry of a cubic lattice can be overcome. By correlating meson operators with definite continuum spin with the irreducible representations of cubic rotations, it is possible to make spin assignments from lattice QCD simulations with a single lattice spacing. Another key improvement was the development of variational methods so that a large base of operators can be used in order to reliably extract many excited states and to probe their internal structure.

Figure 1.9 shows the spectrum of light non-strange mesons from the lattice QCD calculation in Ref. [55]. The spectrum is qualitatively similar to the one predicted by quark models (see, e.g., Fig. 1.5(b)), but lattice QCD predicts also the existence of exotic non-$q\bar{q}$ states that are discussed in Sec. 1.6.3. The extracted masses of the states depend on the pion mass used in the calculation. The lowest pion mass used in Ref. [55] was 391 MeV, which is still quite far away from the physical point. Since the simulation did not include multi-hadron operators, the extracted states are quasi-stable and their masses are in general not identical to the resonance masses. For the same reason, the calculation cannot predict widths and decay modes of the states. For this, one still has to rely on models for most of the states.

Lattice QCD calculations are performed by applying periodic spatial boundary conditions

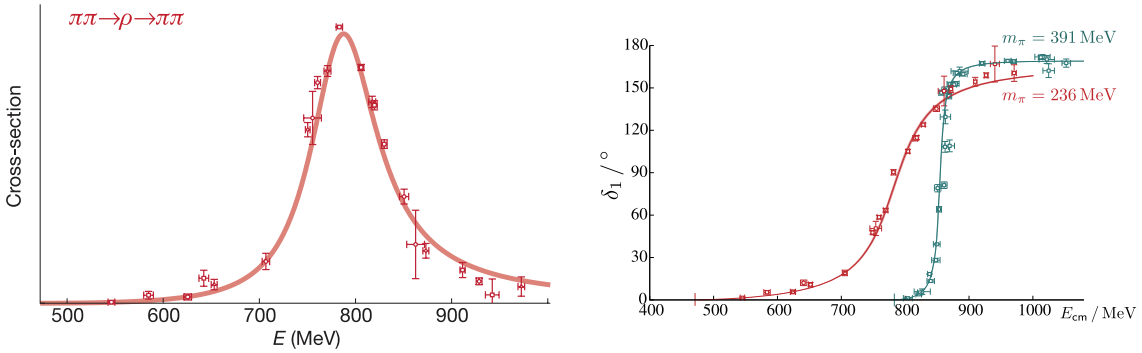

(a) **(b)**

Figure 1.10: Intensity and phase shift of the elastic $\pi\pi$ P-wave amplitude with isospin $I = 1$ as a function of the $\pi\pi$ center-of-mass energy. The points represent lattice QCD results; the curves fits of Breit-Wigner amplitudes. (a) shows the results for a pion mass of 236 MeV. In (b), the blue points and curve are for a pion mass of 391 MeV; the red points and curve for a pion mass of 236 MeV. (a) from Ref. [59], (b) from Ref. [58].

to the quark and gluon fields. This means that within the cube of finite volume L_s^3, free particles can only have discrete three-momenta $\vec{p} = (2\pi/L_s)\,(n_x, n_y, n_z)$ with integer n_i. Hence in scattering processes, multi-hadron states are limited to a discrete spectrum of states, which are the energies of the eigenstates of the QCD Hamiltonian in a finite box. The simplest case is the decay of a state into two (quasi-)stable particles, e.g., two pions. The energies of the two-particle state depend on the interactions between these particles. By inverting this relation, one can extract information about scattering amplitudes, e.g., scattering phase shifts, from the volume dependence of the discrete spectrum in a finite volume. This idea goes back to M. Lüscher [56, 57] and it was developed into a general method to calculate scattering amplitudes for all possible $2 \to 2$ scattering processes of mesons by including hadron-hadron operators that, for example, represent $\pi\pi$ or $K\overline{K}$ systems with defined momenta of the particles (see Ref. [48] and references therein). The resonances, which may appear in these scattering processes, are extracted by analytic continuation of the scattering amplitude into the complex s plane, where the resonances appear as poles (see discussion in Sec. 1.6.1.1). Figure 1.10 shows, as an example, intensity and phase shift of the $\pi\pi$ P-wave with isospin $I = 1$ from lattice QCD simulations performed at two values of the pion mass [58]. The data clearly exhibit an intensity peak and a 180° phase motion that is characteristic for a resonance, which is in this case the ρ. With decreasing pion mass, the ρ mass decreases toward its physical mass and the widths increases because of the increasing phase-space volume.

The lattice calculations of scattering amplitudes performed so far were mostly of exploratory nature and were hence performed at rather large pion masses. Unfortunately, performing these kind of calculations closer to the physical point is not only a question of computational cost. With decreasing pion mass also the thresholds for three- and four-hadron channels decrease. In particular highly excited states couple strongly to multi-hadron final states. However, the current method is not applicable to these channels. A complete finite-volume formalism for three or even more particles would therefore be a major breakthrough for the calculation of masses and decay modes of hadron resonances. Such a formalism is already in the developmental stage (see Ref. [48] and references therein).

1.6.3 Exotic mesons

As discussed in Sec. 1.4, the quark model describes mesons as $|q\bar{q}\rangle$ states grouped into $\mathrm{SU}(N)_{\mathrm{flavor}}$ multiplets.[w] However, a quark-antiquark pair is not the only mesonic color-singlet configuration that one can construct. Hence non-$q\bar{q}$ meson states could exist, which for historic reasons are generally referred to as *exotic states*. One such exotic configuration would be multi-quark states.[x] Mesons could be constructed, for example, from $|qq\bar{q}\bar{q}\rangle$ configurations, where the quarks could be arranged as compact diquark-antidiquark states, $|(qq)(\bar{q}\bar{q})\rangle$, which are called *tetraquarks*, or as bound states of two ordinary mesons, $|(q\bar{q})(q\bar{q})\rangle$, which are called *molecules*. In a similar way, one could imagine $|qqq\bar{q}\bar{q}\bar{q}\rangle$ configurations, e.g., in the form of bound states of a baryon and an antibaryon, so-called *baryonium* states. Since the quarks in hadrons are bound by gluon fields, QCD suggests that excited gluonic field configurations could contribute to the quantum numbers of meson states. Such states would be called *hybrids*. An important feature of QCD is the self-interaction of gluons. Consequently, states that are made of bound gluons and that do not contain constituent quarks could exist. Such states would be called *glueballs*.

Although the above classification scheme seems rather clear and simple, in nature the different forms of hadronic matter are not necessarily realized as separate states. The different configurations actually represent states in a Fock-space expansion and a physical meson is in general a complicated object that can be represented as a linear combination of different configurations all having the same set of quantum numbers. The contributions of these different configurations are in principle determined by QCD, but are difficult to calculate due to the non-perturbative nature of QCD. Also experimentally, the disentanglement of such configuration mixings is a daunting task. Therefore, current efforts focus on identifying the leading configuration in the observed states.

The additional exotic configurations should—if they exist—lead to an overpopulation of states in certain mass regions, i.e., to *supernumerary states* that exist in addition to the ordinary $|q\bar{q}\rangle$ nonet states. From an experimental point of view, such supernumerary meson states can be divided into three categories: (i) *flavor-exotic states* that have flavor quantum numbers, such as isospin $I > 1$ or strangeness $|S| > 1$, that are forbidden for ordinary $|q\bar{q}\rangle$ states, (ii) *spin-exotic states* that have combinations of quantum numbers $J^{PC} = 0^{--}$, $(\mathrm{even})^{+-}$, or $(\mathrm{odd})^{-+}$ that do not fulfill Eqs. (1.12) to (1.14) and are hence forbidden for $|q\bar{q}\rangle$ states,[y] and (iii) *crypto-exotic states* that have quantum numbers of ordinary $|q\bar{q}\rangle$ states. Finding a flavor-exotic or spin-exotic meson would be a clear proof for a non-$q\bar{q}$ configuration. Crypto-exotic states are, however, much harder to identify, because they will in general mix with nearby ordinary $|q\bar{q}\rangle$ states. They can only be identified by studying their production and decay modes in detail.

For several decades, various experiments have searched for evidence for exotic forms of hadronic matter. The so far clearest evidence has been found in the heavy-quark sector. Currently, there are two established charmonium-like states, the $Z_c(3900)$ and the $Z_c(4430)$ [60], that carry electric charge and are therefore flavor exotic. The minimal quark

[w] In this section, we switch back to the simplified notation introduced in Sec. 1.4, where $|q\bar{q}\rangle$ represents any quark flavor combination allowed by the $\mathrm{SU}(N)_{\mathrm{flavor}}$ symmetry.

[x] This idea is actually as old as the quark model itself and was already pointed out by Gell-Mann in Ref. [22] where he states: "Baryons can now be constructed from quarks by using the combinations (qqq), $(qqqq\bar{q})$, etc., while mesons are made out of $(q\bar{q})$, $(qq\bar{q}\bar{q})$, etc."

[y] We use here the convention introduced in Sec. 1.5 to quote the C-parity of the neutral partner in the isospin triplet instead of the G-parity.

content of these states consists of a $c\bar{c}$ pair and a $q\bar{q}$ pair of u and d quarks with isospin $I = 1$. The Z_c states are hence candidates for tetraquark or molecular states. Analogous exotic charged states containing a $b\bar{b}$ pair, the $Z_b(10610)$ and the $Z_b(10650)$, have been found in the bottomonium spectrum [60].

In the light-meson sector, the experimental situation is more complicated. This has been the subject of several recent review articles [44, 45, 59–66]. Although a number of candidates for multi-quark states, hybrids, and glueballs has been found, their interpretation as exotic states or as resonances is discussed controversially and alternative explanations could not yet be ruled out. One of the reasons for this is that in contrast to heavy mesons, excited light mesons have in general large widths and may overlap (see discussion above), which makes them experimentally more difficult to identify.

Interestingly, already the $J^P = 0^+$ ground-state mesons $a_0(980)$, $f_0(980)$, $f_0(500)$ (or σ), and $K^*(800)$ (or κ) exhibit some unusual properties that contradict their interpretation as $|q\bar{q}\rangle$ states. In the constituent quark model, these states would correspond to states with $n = 1$ and $S = L = 1$. The $f_0(500)$ would be an isoscalar $(u\bar{u} + d\bar{d})/\sqrt{2}$ state, the $a_0(980)$ an isovector $(u\bar{u} - d\bar{d})/\sqrt{2}$ state, and the isoscalar $f_0(980)$ would consist mainly of $s\bar{s}$. However, such an assignment is in conflict with the observed mass degeneracy of $a_0(980)$ and $f_0(980)$. Due to its dominant $s\bar{s}$ content, the $f_0(980)$ should be heavier than the $a_0(980)$, as is the case for the vector mesons, where the $\phi(1020)$ is significantly heavier than the $\rho(770)$. The $f_0(500)$ is extremely light and broad and until recently its existence as a resonant state was even questioned. Also here the mass is in contradiction with the quark-model expectation, where the masses of the $a_0(980)$ and the $f_0(500)$ should be more similar, like in the case of $\rho(770)$ and $\omega(782)$. The observed mass pattern can actually be explained, if the light scalar mesons are tetraquarks or molecules or a mixture of both [61], which would make them crypto-exotic. An interpretation as $K\overline{K}$ molecules, could, for example, explain the mass degeneracy of $a_0(980)$ and $f_0(980)$, the closeness of their masses to the $K\overline{K}$ threshold, and therefore their relatively small widths. However, not all data seem to agree with this model [60].

Although there are no known flavor-exotic light mesons, there are candidates for spin-exotic light mesons [44, 45, 60, 63]. As discussed above, finding a spin-exotic state would be unambiguous proof for the existence of non-$q\bar{q}$ states.[z] The currently known spin-exotic candidates are all isovectors with $J^{PC} = 1^{-+}$ quantum numbers. Hence these states cannot be glueballs, but they could be hybrids or multi-quark states. The candidates are pion-like objects with spin 1 and are hence denoted π_1 according to the PDG convention. There are three spin-exotic candidates: $\pi_1(1400)$, $\pi_1(1600)$, and $\pi_1(2015)$. However, the resonance interpretation of the observed signals is discussed controversially. Out of these states, the $\pi_1(1600)$ is currently the best established one.

Various model calculations predict that spin-exotic states exist, but do not agree on the mass of the lightest spin-exotic state [45, 63]. The predicted masses range from 1.0 to 2.3 GeV. Nevertheless most models predict that the lightest spin-exotic state has $J^{PC} = 1^{-+}$ quantum numbers. This is confirmed by lattice QCD calculations (see Sec. 1.6.2.2 and Fig. 1.9). The mass estimates from these calculations are still limited by a number of systematic effects. Currently, the main limitations result from the fact that the calculations are performed at unphysically large pion masses and that the states are treated as quasi-stable. The predicted masses for the lightest $J^{PC} = 1^{-+}$ state vary between

[z] However, once found, the determination of their inner structure will be a much more difficult task.

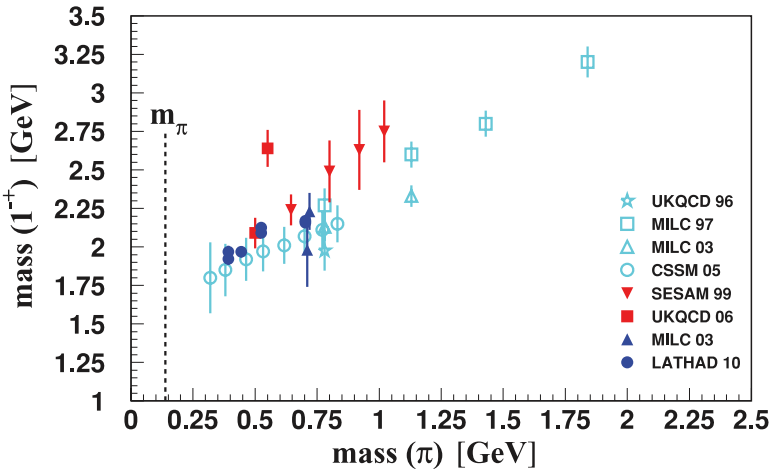

Figure 1.11: Mass of the lightest isovector state with $J^{PC} = 1^{-+}$ from various lattice QCD calculations as a function of the pion mass used in the calculation. The open symbols indicate quenched calculations, where internal $q\bar{q}$ loops are neglected, filled symbols indicate dynamical calculations, where these loops are included. From Ref. [63].

about 1.8 and 2.1 GeV. However, these masses depend on the value of the pion mass that was chosen to perform the lattice QCD calculation. This is illustrated in Fig. 1.11, which shows the mass of the lightest isovector state with $J^{PC} = 1^{-+}$ from various lattice QCD calculations, which were performed at different pion masses. Unfortunately, the current lattice QCD results are too far away from the physical point in order to perform a controlled extrapolation.

Lattice QCD predicts a whole supermultiplet of hybrid states with 0^{-+}, 1^{--}, 2^{-+}, and 1^{-+} quantum numbers [55] (boxes outlined with orange in Fig. 1.9), where the first three are quantum numbers of ordinary $|q\bar{q}\rangle$ states. Each J^{PC} combination corresponds to a nonet of meson states. The states contain excited gluon fields with $J^{PC} = 1^{+-}$ and have masses in the range between 2.1 and 2.4 GeV, about 1.3 GeV heavier than the lightest 1^{--} state. A similar pattern is found for charmed hybrid mesons. This leads the authors of Ref. [59] to propose this as a new rule to construct hybrid mesons.

Although lattice QCD predicts the existence of spin-exotic and hybrid states, it cannot yet predict the widths and decay modes of these objects. Currently, this can only be done using models. Detailed calculations have been performed, for example, by Page, Swanson, and Szczepaniak [67]. For an isovector hybrid state with 1^{-+} quantum numbers and a mass of 1.6 GeV, such as the $\pi_1(1600)$, they predict the following partial widths:

Channel	$\rho(770)\,\pi$	$b_1(1235)\,\pi$	$f_1(1285)\,\pi$	$\eta(1295)\,\pi$	$K\,K^*(892)$
$\boldsymbol{\Gamma_{\text{channel}}}$ **[MeV]**	9	24	5	2	0.8

The decays into $\eta(548)\,\pi$, $\eta'(958)\,\pi$, $f_2(1270)\,\pi$, and $\rho(770)\,\omega(782)$ are predicted to have negligible partial widths.

In this work, we focus on the $\rho(770)\,\pi$ decay mode. According to the above prediction, this channel has the second largest branching fraction. Since the $\rho(770)$ decays practically exclusively into 2π, the $\pi_1(1600)$ should appear in 3π final states. Experimentally, the easiest 3π final state to measure is $\pi^-\pi^-\pi^+$. For this final state, the COMPASS experiment

has acquired a world-leading data sample that is about an order of magnitude larger than any other existing data set (see Sec. 2.3) and therefore allows to study the resonance content of the $\pi^-\pi^-\pi^+$ system in unprecedented detail (see Chapter 4). The $\rho(770)\,\pi$ decay mode is also interesting because previous analyses of this channel arrived at seemingly contradictory conclusions concerning the existence of the $\pi_1(1600)$ resonance. The resolution of this controversy by the results of the analysis of the COMPASS data that is presented in Sec. 4.2.5.1.

Chapter 2

Diffractive $\pi^-\pi^-\pi^+$ production at the COMPASS experiment

2.1 Light-meson production in pion diffraction

As discussed in Sec. 1.6.1, excited light mesons can be produced in various processes. In this work, we study pion-induced t-channel exchange processes of the form

$$\pi + p \to X + p \qquad \text{with} \qquad X \to h_1 + \ldots + h_n, \tag{2.1}$$

which are mediated by the strong interaction. In these processes, the beam pion is excited to an intermediate state X via the strong interaction with the target proton. The squared four-momentum t that is transferred from the beam to the target particle has typically small absolute values below $1\,(\mathrm{GeV}/c)^2$ (see Sec. 2.3.2).[a] Therefore, the exchange particle is not able to resolve the inner structure of the proton and the scattering at the target vertex is elastic and coherent.[b] Such reactions are also referred to as *soft* or *peripheral scattering*. The intermediate states X are very short-lived and dissociate via the strong interaction into n-body final states of lighter hadrons h_i, which consist in most cases of π, K, η, or $\eta'(958)$. The whole reaction is pictured in Fig. 2.1.

The inelastic strong-interaction scattering subprocess $\pi + p \to X + p$ can be described using Regge theory [38, 68–70]. Regge theory exploits the crossing symmetry of scattering amplitudes and relates physical resonances that appear in s-channel scattering to exchange particles that mediate the residual strong interaction between color-neutral hadrons. If one plots the spins of meson resonances against their squared masses, which correspond to positive values of t, the resonances fall approximately on straight lines

$$\alpha(t) = \alpha_0 + \alpha' t, \tag{2.2}$$

which are called Regge trajectories. This means that $\alpha(m^2_{\text{meson}}) = J_{\text{meson}}$. Figure 2.2 shows such a Chew-Frautschi plot for light mesons.

In Regge theory, the scattering amplitudes are considered as functions of the spin, where the spin is not restricted to integer values but is a complex-valued variable. In this approach,

[a] From here on, we switch to SI units.

[b] That the target proton remains intact is ensured by the applied event selection criteria (see Secs. 2.2.2 and 2.3.1), which suppress events where also the target proton is excited, e.g., into an N^* resonance.

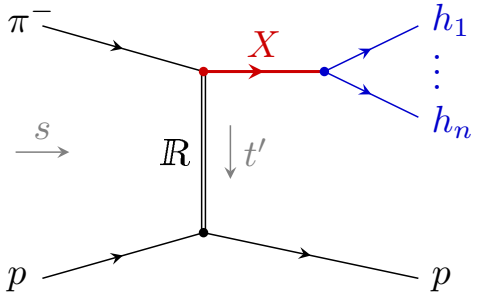

Figure 2.1: Production of an intermediate state X by excitation of a beam pion via exchange of a Reggeon $\mathbb{R}$ with a target proton. The intermediate state decays into an n-body final state of hadrons, $h_1, \ldots, h_n$.

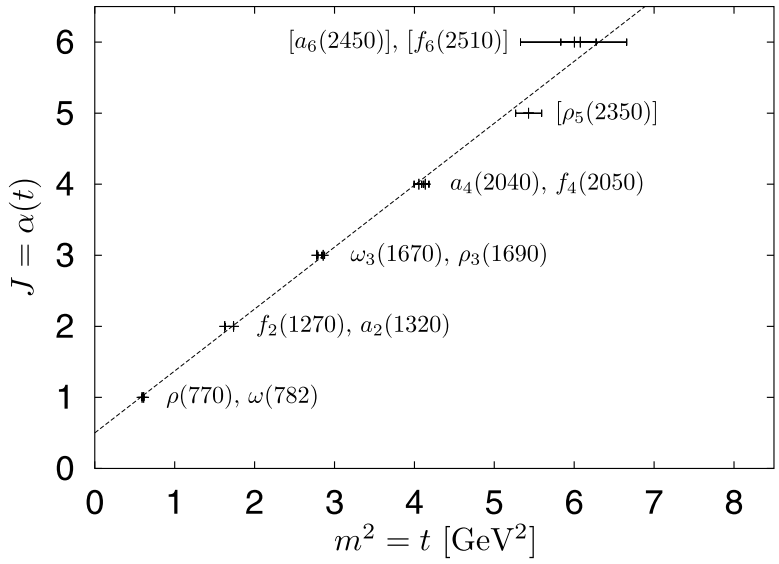

Figure 2.2: Chew-Frautschi plot: the spins J of light mesons are plotted against the squared meson masses, which correspond to positive values of t. Meson states enclosed in square brackets are states that are not yet considered as established by the PDG [13]. The meson states lie on four degenerate Regge trajectories, the ρ, ω, f, and a trajectories, that are approximately given by $\alpha(t) = 0.5 + 0.9\,(\mathrm{GeV}/c)^{-2}\,t$ (dashed line). From Ref. [70].

physical meson states correspond to poles of the scattering amplitude in the complex spin plane. The t-channel reactions are described as exchanges of quasi-particles with variable spin $\alpha(t)$, where the Regge trajectories $\alpha(t)$ are extrapolated to negative values of t. These quasi-particles are called *Reggeons* ($\mathbb{R}$). Hence the Regge trajectories connect the s-channel scattering at low energies, where $t = m^2 > 0$, with the t-channel exchange reactions at high energies, where $t < 0$.

In the Regge approach, the scattering amplitude $\mathcal{A}(s,t)$ for a given Regge trajectory is proportional to $s^{\alpha(t)}$. The total cross section is given via the optical theorem by the imaginary part of the forward scattering amplitude, i.e.,

$$\sigma_{\text{tot}} \propto \frac{1}{s} \operatorname{Im}\big[\mathcal{A}(s, t=0)\big] \propto s^{\alpha_0 - 1}. \tag{2.3}$$

This means, that if $\alpha_0 < 1$ the cross section decreases with increasing s. This is true for all known Regge trajectories that correspond to physical meson states. However, experimentally the hadron-hadron cross sections is found to rise slowly with s. In order to explain this rise of the cross section, V. N. Gribov proposed the so-called Pomeron trajectory, which has $\alpha_0 > 1$ [69]. Hence the Pomeron trajectory dominates the cross section at large center-of-mass energies. The first Regge pole of the Pomeron trajectory would correspond to a flavorless hadron with $J^{PC} = 2^{++}$ and a mass of about $1.9\,\text{GeV}/c^2$. However, up to now no physical meson resonance could be associated with the Pomeron trajectory beyond doubt. It is also speculated that the Pomeron trajectory could be related to glueballs.

The Reggeon that corresponds to the Pomeron trajectory is called *Pomeron* ($\mathbb{P}$) and has the same quantum numbers as the vacuum state.[c] High-energy hadron scattering processes that are mediated by Pomeron exchange are also called *diffractive scattering*.[d] From previous experiments, diffractive reactions are known to produce a rich spectrum of resonances in the intermediate state X. Since the Pomeron has vacuum quantum numbers, the flavor quantum numbers of the beam particle remain unchanged in diffractive scattering processes. This means that the produced intermediate state X has the same isospin and strangeness quantum numbers and, where applicable, the same C- and G-parity as the beam particle. For a pion beam, this means that in diffractive reactions only isovector states with $I^G = 1^-$ quantum numbers, which correspond to positive C-parity of the neutral member in the isospin triplet, can be produced. This limits the meson states that may appear as X to the families of a_J mesons with $I^G\,J^{PC} = 1^-\,J^{++}$ quantum numbers and π_J mesons with $1^-\,J^{-+}$ quantum numbers. Table 2.1 lists all currently known mesons with $I^G = 1^-$.

2.2 The COMPASS experiment

The COmmon Muon and Proton Apparatus for Structure and Spectroscopy (COMPASS) is a multi-purpose fixed-target experiment at the CERN Super Proton Synchrotron (SPS). One of the goals of the COMPASS experiment is the high-precision measurement of the light-meson spectrum. In this section, we briefly describe the experimental setup, which is shown schematically in Fig. 2.3. More details can be found in Refs. [71, 72].

[c] The Pomeron was named after I. Pomeranchuk.

[d] The name originates from the resemblance of hadronic scattering processes with diffraction of light waves by a black disk, where t is basically equivalent to the scattering angle. For both phenomena, the measured intensity is characterized by a dominant forward peak, the diffraction peak, that is accompanied by a series of symmetric minima and maxima at values of t and the scattering angle, respectively, that depend on the size of the object that the beam scatters off.

Table 2.1: Known isovector resonances with $I^G = 1^-$ quantum numbers in the mass region below 2.1 GeV/c^2 and their parameters as given by the PDG [31]. The PDG distinguishes between well-known "established states", "states omitted from summary table" that are less well-known, and "further states" that still require confirmation. From Ref. [H2].

Particle	J^{PC}	**Mass [MeV/c^2]**	**Width [MeV/c^2]**
		Established states	
$a_0(980)$	0^{++}	980 ± 20	50 to 100
$a_1(1260)$	1^{++}	1230 ± 40	250 to 600
$a_2(1320)$	2^{++}	$1318.3^{+0.5}_{-0.6}$	107 ± 5
$a_0(1450)$	0^{++}	1474 ± 19	265 ± 13
$a_4(2040)$	4^{++}	1996^{+10}_{-9}	255^{+28}_{-24}
$\pi(1300)$	0^{-+}	1300 ± 100	200 to 600
$\pi_1(1400)$	1^{-+}	1354 ± 25	330 ± 35
$\pi_1(1600)$	1^{-+}	1662^{+8}_{-9}	241 ± 40
$\pi_2(1670)$	2^{-+}	1672.2 ± 3.0	260 ± 9
$\pi(1800)$	0^{-+}	1812 ± 12	208 ± 12
$\pi_2(1880)$	2^{-+}	1895 ± 16	235 ± 34
		States omitted from summary table	
$a_1(1640)$	1^{++}	1647 ± 22	254 ± 27
$a_2(1700)$	2^{++}	1732 ± 16	194 ± 40
$\pi_2(2100)$	2^{-+}	2090 ± 29	625 ± 50
		Further states	
$a_3(1875)$	3^{++}	$1874 \pm 43 \pm 96$	$385 \pm 121 \pm 114$
$a_1(1930)$	1^{++}	1930^{+30}_{-70}	155 ± 45
$a_2(1950)$	2^{++}	1950^{+30}_{-70}	180^{+30}_{-70}
$a_2(1990)$	2^{++}	$2050 \pm 10 \pm 40$ $2003 \pm 10 \pm 19$	$190 \pm 22 \pm 100$ $249 \pm 23 \pm 32$
$a_0(2020)$	0^{++}	2025 ± 30	330 ± 75
$a_2(2030)$	2^{++}	2030 ± 20	205 ± 30
$a_3(2030)$	3^{++}	2031 ± 12	150 ± 18
$a_1(2095)$	1^{++}	$2096 \pm 17 \pm 121$	$451 \pm 41 \pm 81$
$\pi_2(2005)$	2^{-+}	$1974 \pm 14 \pm 83$ 2005 ± 15	$341 \pm 61 \pm 139$ 200 ± 40
$\pi_1(2015)$	1^{-+}	$2014 \pm 20 \pm 16$ $2001 \pm 30 \pm 92$	$230 \pm 32 \pm 73$ $333 \pm 52 \pm 49$
$\pi(2070)$	0^{-+}	2070 ± 35	310^{+100}_{-50}
$X(1775)$	$?^{-+}$	1763 ± 20 1787 ± 18	192 ± 60 118 ± 60
$X(2000)$	$?^{?+}$	1964 ± 35 ~ 2100 2214 ± 15 2080 ± 40	225 ± 50 ~ 500 355 ± 21 340 ± 80

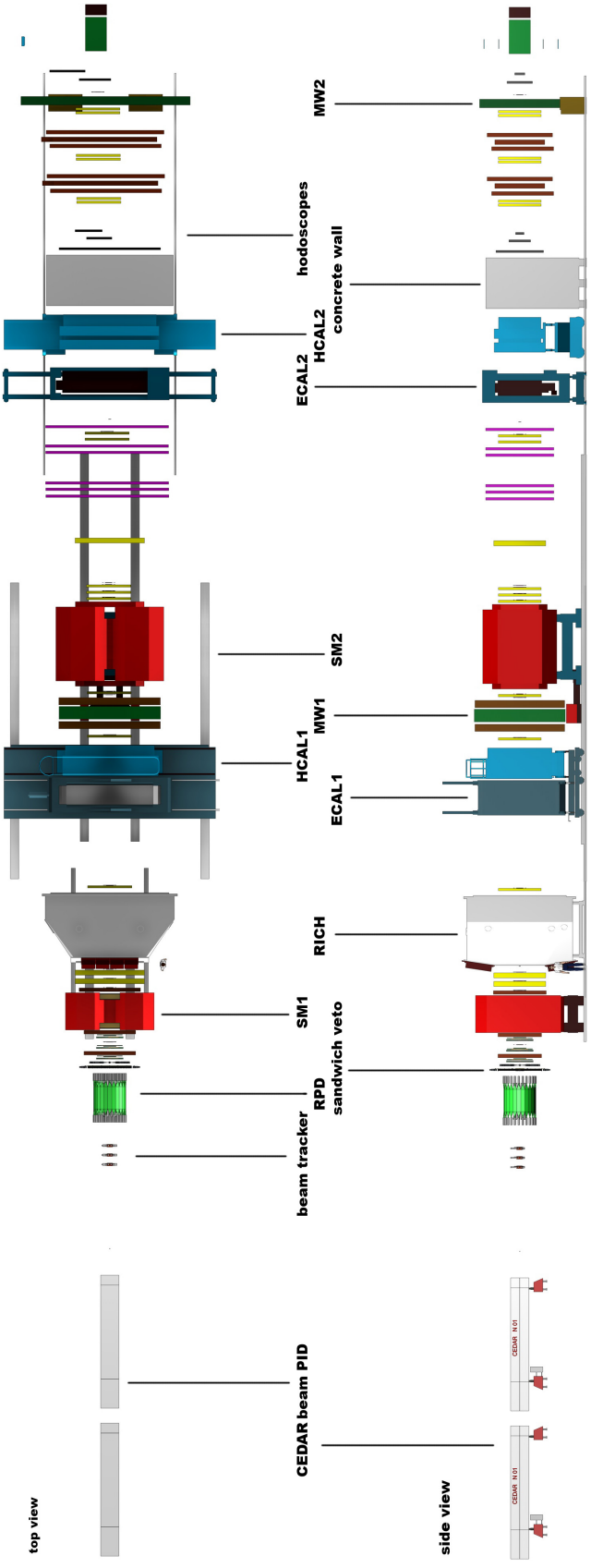

Figure 2.3: Schematic view of the COMPASS experimental setup.

2.2.1 Beam and target

At COMPASS, excited light mesons are produced using positively or negatively charged secondary hadron beams with a momentum of 190 GeV/c and an intensity of up to 10^7 particles per second. The secondary hadron beams are produced by shooting the high-intensity 400 GeV/c proton beam delivered by the SPS onto a 50 cm long production target made of beryllium. The produced secondary hadrons are momentum-selected by magnetic filters and transported via the M2 beam line to the COMPASS target, which is located approximately 1.1 km downstream of the production target.

The positively charged hadron beam consists of 74.6 % p, 24.0 % π^+, and 1.4 % K^+ at the COMPASS target; the negatively charged one of 96.8 % π^-, 2.4 % K^-, and 0.8 % $\bar{p}$. The beam particles are identified by a pair of differential Cherenkov counters (CEDAR) that are placed in the beam line upstream of the COMPASS target. In this work, we study diffractive reactions that are induced by the π^- component of the negatively charged hadron beam. The direction of the beam particles is precisely measured by several planes of silicon micro-strip detectors mounted upstream of the COMPASS target.

We use as target either a 40 cm long cylindrical Mylar cell filled with liquid hydrogen or disks and foils made of nickel, tungsten, or lead. In this work, we only consider data taken with the liquid-hydrogen target. The target is surrounded by two concentric barrels of scintillator slats. This recoil-proton detector (RPD) measures the slow protons that are emitted from the target under large angles between about 50° and 90° with respect to the beam direction. The RPD can only detect recoil protons with a momentum of at least 270 MeV/c because of the energy loss that the recoil protons suffer in the target walls and the inner scintillator barrel. This translates into a minimum detectable reduced squared four-momentum transfer t' of approximately 0.07 GeV/c^2.

2.2.2 Trigger

Diffractive-dissociation events of the reaction (2.1) are selected by a minimum-bias trigger. In order to make sure that a beam particle has entered the target, the trigger requires signals in a scintillating-fiber detector and a small scintillator disk, both placed upstream of the target. The trigger requires in addition a signal from a recoil proton in the RPD to ensure that a scattering has occurred. A scintillator/iron sampling detector, the so-called Sandwich Veto, is placed downstream of the target and detects produced particles that are emitted outside of the wide angular acceptance of the spectrometer of ±180 mrad. The trigger uses the Sandwich Veto to discard events that contain such particles. In addition, events with non-interacting beam particles are discarded by the trigger based on conicident signals in two scintillator disks that are placed along the nominal beam trajectory 25 m and 33 m downstream of the target.

2.2.3 Forward magnetic spectrometer

In contrast to the recoil proton, the daughter particles of the intermediate state X in reaction (2.1) are strongly Lorentz-boosted and are hence emitted under small angles with respect to the beam axis. These forward-going final-state particles are measured by a high-resolution two-stage magnetic spectrometer.

The position of the primary interaction vertex is precisely determined by several planes

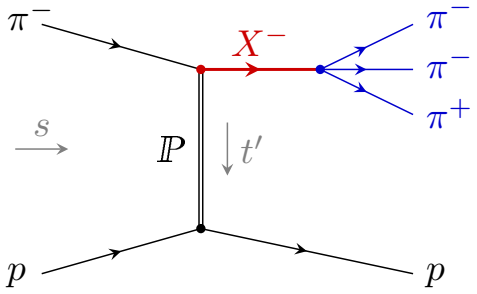

Figure 2.4: Diffractive production of an intermediate state X^- on a proton target and dissociation of X^- into the $\pi^-\pi^-\pi^+$ final state.

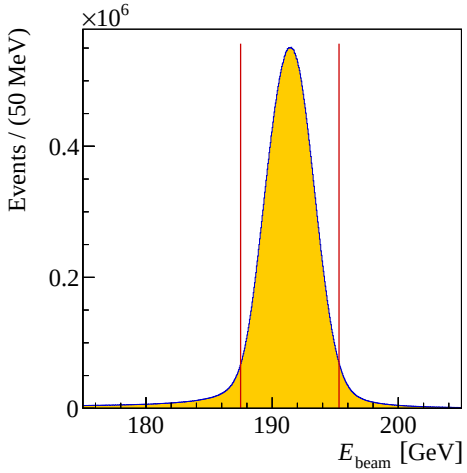

Figure 2.5: Distribution of the reconstructed beam energy after all selection cuts. The vertical red lines indicate the accepted range. From Ref. [H2].

of silicon micro-strip detectors mounted downstream of the COMPASS target. The first spectrometer stage uses the SM1 dipole magnet that has a field integral of 1.0 Tm and measures charged particles with lower momenta starting from about 1 GeV/c. The second spectrometer stage uses the SM2 dipole magnet that has a larger field integral of 4.4 Tm and covers the high-momentum range. Both spectrometer stages are equipped with tracking detectors and with electromagnetic and hadronic calorimeters. This setup provides a high momentum resolution of $\sigma_p/p < 0.5\,\%$ for momenta $p > 5\,\text{GeV}/c$ and a large and uniform acceptance for charged as well as neutral particles over a wide kinematic range. The first spectrometer stage is in addition equipped with a ring-imaging Cherenkov detector (RICH) that can separate pions and kaons in the momentum range from about 10 to 50 GeV/c.

2.3 The COMPASS $\pi^-\pi^-\pi^+$ data

In this work, we study the diffractive production of the $\pi^-\pi^-\pi^+$ final state on a liquid-hydrogen target in great detail. This means we study the inelastic scattering reaction

$$\pi^- + p \to X^- + p \qquad \text{with} \qquad X^- \to \pi^-\pi^-\pi^+, \tag{2.4}$$

which is pictured in Fig. 2.4. In this section, we briefly summarize the selection criteria that are applied to the triggered events (see Sec. 2.2.2) and characterize the selected data. Further details can be found in Refs. [73, H2].

2.3.1 Event selection

We perform an exclusive measurement of reaction (2.4), i.e., we reconstruct all incoming and outgoing particles. To this end, we select events that have exactly one incoming beam pion, exactly one reconstructed recoil proton in the RPD, and exactly three forward-going

charged particles that emerge from a primary interaction vertex and that have charges that add up to -1. The position of the primary vertex is confined to the volume of the liquid-hydrogen in the target. The three forward-going particles are assumed to be pions. We ensure momentum conservation by requiring that the momentum of the recoil proton is back-to-back with the total momentum of the three forward-going particles in the plane transverse to the beam. This reduces contaminations from processes, where also the target proton is excited to short-lived N^* states. Another measure for the exclusivity is the reconstructed beam energy E_{beam}, which is the energy sum of the three forward-going particles corrected for the target recoil. Figure 2.5 shows the E_{beam} distribution after all selection cuts. The dominant peak around the nominal beam energy corresponds to exclusive events that are selected by requiring E_{beam} to be within $\pm 3.78\,\text{GeV}$ around the peak position, which corresponds to two standard deviations. Contaminations from non-exclusive background events are at the percent level.

Small contributions from other background processes are suppressed by further cuts. Using the information from the CEDAR detectors, it is ensured that the beam particle is a pion. This removes background from diffractive dissociation of beam kaons, such as $K^- + p \to K^-\pi^-\pi^+ + p$. Background from final-state kaon pairs, i.e., from $\pi^- + p \to \pi^- K^- K^+ + p$, is suppressed by using the RICH information. Contaminations from central-production reactions $\pi^- + p \to \pi^-_{\text{fast}} + \pi^-\pi^+ + p$, which do not have a well-defined intermediate three-body state (see also discussion in Sec. 3.3.7), are reduced by removing events that have an outgoing π^- with a momentum close to the beam momentum.

After all cuts, the data sample contains 46×10^6 events in the analyzed kinematic range of the three-pion invariant mass $0.5 < m_{3\pi} < 2.5\,\text{GeV}/c^2$ and of the reduced squared four-momentum transfer $0.1 < t' < 1.0\,(\text{GeV}/c)^2$. The lower bound of the t' range is given by the acceptance of the RPD (see Sec. 2.2.1) and the upper bound by the decrease of the number of events with increasing t'.

2.3.2 Kinematic distributions

The distributions of selected kinematic variables are shown in Fig. 2.6. The invariant mass distribution of the produced $\pi^-\pi^-\pi^+$ system exhibits structures that correspond to the well-known resonances $a_1(1260)$, $a_2(1320)$, and $\pi_2(1670)$ (see Table 2.1). Also the invariant mass distribution of the $\pi^-\pi^+$ subsystem shows enhancements that correspond to the well-known resonances $\rho(770)$, $f_0(980)$, $f_2(1270)$, and $\rho_3(1690)$. Figure 2.6(c) shows that the structures in the three-pion mass spectrum are correlated with those in the $\pi^-\pi^+$ mass spectrum. This is an important input for the construction of the physical model that we use to analyze the data (see Secs. 3.2 and 4.1.1). The t' distribution is steeply falling with increasing t' and exhibits an approximately exponential behavior.

An important property of the data is that the $m_{3\pi}$ and t' distributions are correlated. This is illustrated in Fig. 2.7. Figures 2.7(a) and 2.7(b) show how the $m_{3\pi}$ spectrum changes with t'. Whereas at low t', the $a_1(1260)$ peak is dominant and only a small $a_2(1320)$ peak is visible, the relative intensities of the peaks are inverted at high t'. Conversely, the t' distribution depends strongly on $m_{3\pi}$ as is illustrated in Figs. 2.7(c) and 2.7(d). The observation, that resonance signals may have different dependences on t' has motivated us to explicitly take into account this t' dependence in the construction of the analysis model. This will be explained in detail in Chapter 3.

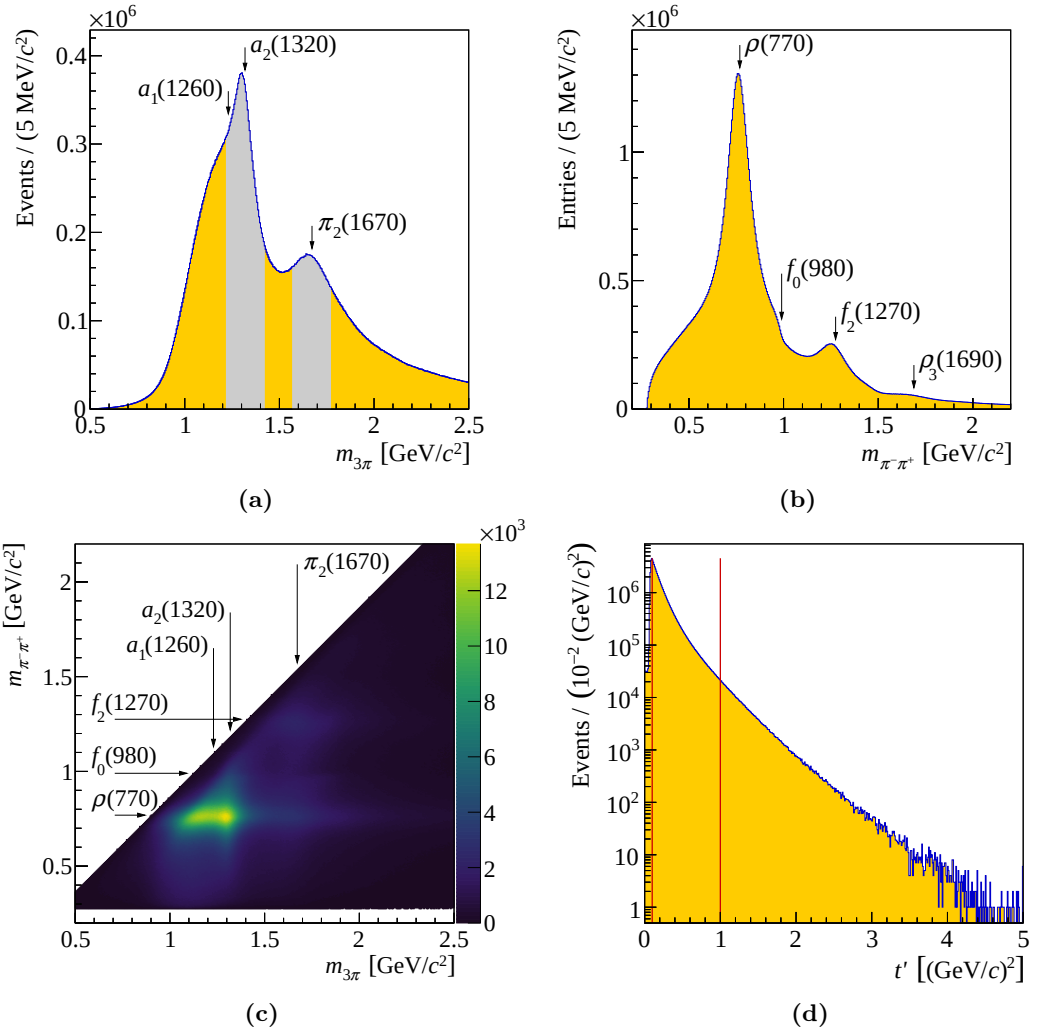

Figure 2.6: Kinematic distributions of the event sample after all selection cuts: (a) $\pi^-\pi^-\pi^+$ invariant mass spectrum in the analyzed range, (b) invariant mass distribution of the $\pi^-\pi^+$ subsystem (two entries per event), (c) correlation of the $\pi^-\pi^-\pi^+$ and $\pi^-\pi^+$ mass (two entries per event), and (d) t' distribution with vertical lines indicating the analyzed range. The labels indicate the position of major 3π and 2π resonances, the gray shaded areas in (a) indicate the mass regions used to generate the Dalitz plots in Fig. 3.3. From Ref. [H2].

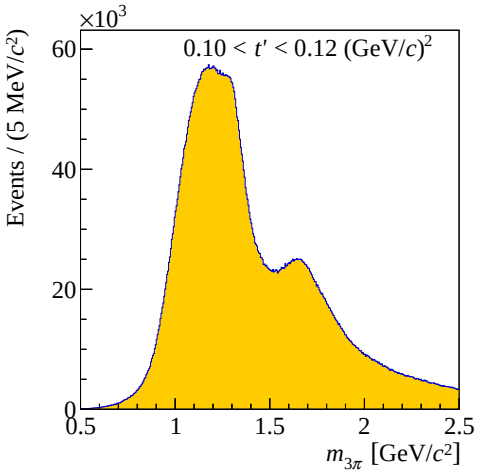

(a) $m_{3\pi}$ spectrum for low values of t'.

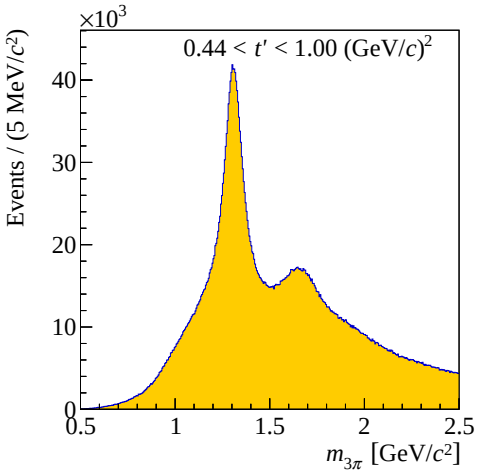

(b) $m_{3\pi}$ spectrum for high values of t'.

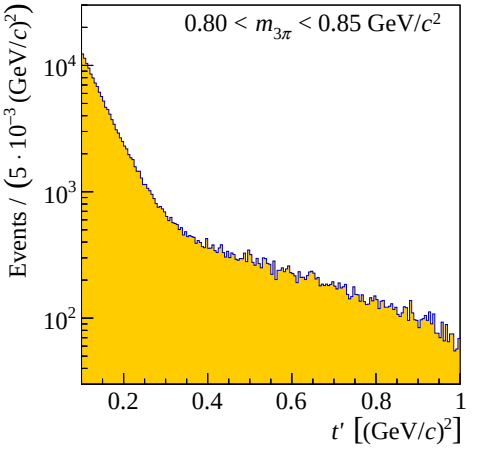

(c) t' spectrum for low values of $m_{3\pi}$.

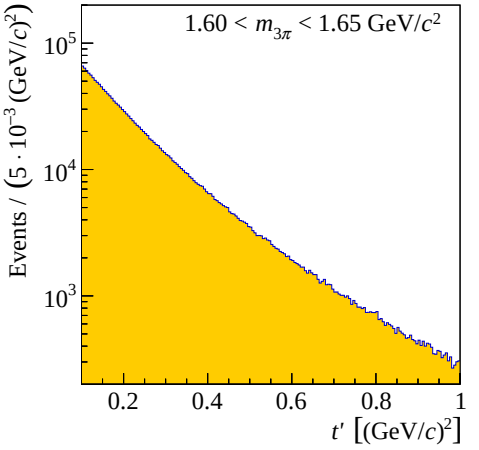

(d) t' spectrum for medium values of $m_{3\pi}$.

Figure 2.7: The t' dependence of the measured $\pi^-\pi^-\pi^+$ invariant mass spectrum and vice versa. From Ref. [H2].

Chapter 3

The method of partial-wave analysis

The 3π invariant mass distribution shown in Fig. 2.6(a) already shows structures from known 3π resonances that are produced as intermediate states in the diffractive scattering reaction (2.4). However, the information in the invariant mass spectrum alone is not sufficient to identify resonances, to determine their quantum numbers, and to measure their parameters. In order to extract this information from the data, we employ a method called partial-wave analysis (PWA) that exploits the full information contained in the measured multi-dimensional kinematic distribution of the final-state particles.

The technique of partial-wave analysis (PWA) of three-body mesonic final states goes back to the early works from the 1960s in Refs. [74–82]. The application of this method to the 3π system was pioneered by G. Ascoli *et al.* in Refs. [83, 84]. In this chapter, we give a brief summary of the main aspects of the PWA method and of the extensions that we developed. More detailed derivations and discussions can be found in Refs. [85–94, H2, H3] and the references therein.

3.1 Parametrization of the scattering cross section

In this work, we consider inelastic scattering reactions of the form

$$a + b \to (1 + 2 + 3) + c. \tag{3.1}$$

The cross section for such a reaction is [95]

$$\mathrm{d}\sigma_{a+b\to(1+2+3)+c} = \frac{1}{4\sqrt{(p_a \cdot p_b)^2 - m_a^2\, m_b^2}} \left|\mathcal{M}_{fi}\right|^2 \mathrm{d}\varphi_4(p_a + p_b; p_1, p_2, p_3, p_c). \tag{3.2}$$

Here, the p_i are the four-momenta and the m_i the masses of the particles. The Lorentz-invariant transition matrix element from the initial to the final state is represented by $\mathcal{M}_{fi}$.[a] The differential Lorentz-invariant four-body phase-space element of the final-state particles is represented by $\mathrm{d}\varphi_4$.

At high center-of-mass energies, the three-body final state $(1 + 2 + 3)$ in reaction (3.1) is produced via t-channel exchange. Assuming that the three-body intermediate states

[a] In order to simplify notation, the term $|\mathcal{M}_{fi}|^2$ is assumed to include the incoherent averaging and summation over the spin states of the initial- and the final-state particles, respectively.

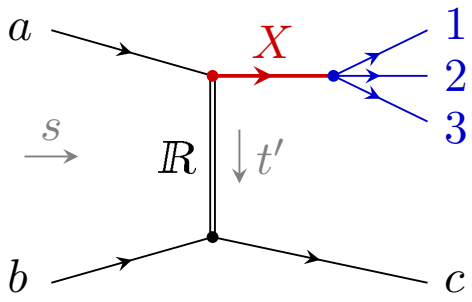

Figure 3.1: Production of an intermediate state X in a t-channel exchange reaction and dissociation of X into a three-body final state.

are dominated by resonances, we can subdivide reaction (3.1) into two subprocesses: (i) an inelastic two-body scattering reaction $a + b \to X + c$ and (ii) the subsequent decay of particle X into the three-body final state, $X \to 1 + 2 + 3$. This is shown in Fig. 3.1. Subprocess (i) is described in terms of the three-body invariant mass m_X,[b] the squared center-of-mass energy s (see Eq. (1.18)), and the reduced squared four-momentum transfer t' (see Eq. (1.20)).

Analogous to the subdivision of the scattering process, we split the phase space of the four outgoing particles into a two-body phase space for the particles X and c and a three-body phase space for the decay $X \to 1 + 2 + 3$. The latter one is given by[c]

$$\mathrm{d}\varphi_3(p_X; p_1, p_2, p_3) = (2\pi)^4 \, \delta^{(4)}\Big(p_X - \sum_{i=1}^{3} p_i\Big) \prod_{i=1}^{3} \frac{\mathrm{d}^3 p_i}{(2\pi)^3 \, 2E_i}. \tag{3.3}$$

Splitting the phase space and using Eq. (1.20) brings Eq. (3.2) in the form

$$\mathrm{d}\sigma_{a+b\to(1+2+3)+c} = \frac{1}{16\pi} \frac{1}{\big[s - (m_a + m_b)^2\big]\big[s - (m_a - m_b)^2\big]} \times \big|\mathcal{M}_{fi}\big|^2 \, \mathrm{d}t' \, \frac{2m_X}{2\pi} \, \mathrm{d}m_X \, \mathrm{d}\varphi_3(p_X; p_1, p_2, p_3). \tag{3.4}$$

Here, we have expressed the flux factor in terms of s and the two-body phase space of the (X, c) system in terms of t'. We also have used the fact that for an unpolarized reaction, $\mathcal{M}_{fi}$ is independent of the azimuthal angle of X about the beam axis in the center-of-mass frame of the reaction $a + b \to X + c$.

In the following, we assume that the center-of-mass energy $\sqrt{s}$ of the scattering reaction is fixed[d] and we omit the s dependence from all formulas. The kinematic distribution of the final-state particles depends on m_X, t', and a set of five additional phase-space variables represented by τ.[e] These phase-space variables fully describe the three-body decay and will be defined in Sec. 3.2.1.

[b] For the $\pi^-\pi^-\pi^+$ final state, $m_X = m_{3\pi}$.

[c] We slightly deviate from the convention used in Ref. [95] by including the factor $(2\pi)^4$ into the phase-space element.

[d] This is, for example, the case in a fixed-target experiment, where p_a and p_b are constant.

[e] The three four-momenta of the final-state particles have 12 components. The components are constrained by the three known masses of the final-state particles and by four equations, which are given by four-momentum conservation and the known four-momentum of X.

The intensity distribution of the events that are produced in reaction (3.1) is

$$\begin{aligned}\mathcal{I}(m_X, t', \tau) &\equiv \frac{\mathrm{d}N}{\mathrm{d}m_X\ \mathrm{d}t'\ \mathrm{d}\varphi_3(m_X, \tau)} \propto \frac{\mathrm{d}\sigma_{a+b\to(1+2+3)+c}}{\mathrm{d}m_X\ \mathrm{d}t'\ \mathrm{d}\varphi_3(m_X, \tau)} \\ &\propto m_X\ \left|\mathcal{M}_{fi}(m_X, t', \tau)\right|^2 , \end{aligned} \tag{3.5}$$

where N is the number of produced events. On the right-hand side of Eq. (3.5), all constant factors have been dropped. It is worth noting that, since $\mathcal{I}$ is differential in the Lorentz-invariant three-body phase-space element, it is independent of the particular choice of the phase-space variables τ.[f] The intensity $\mathcal{I}$ essentially represents the deviation of the kinematic distribution of the produced final-state particles from a pure phase-space distribution. It is therefore a direct measure for $\left|\mathcal{M}_{fi}(m_X, t', \tau)\right|^2$.

3.2 Model for the intensity distribution

In order to derive a model for the intensity distribution in Eq. (3.5), we assume that the diffractive-dissociation process is dominated by intermediate resonances X. Since resonance production and decay are independent, we factorize the amplitude for a particular X into two parts: (i) the *transition amplitude* $\widetilde{\mathcal{T}}_i(m_X, t')$ that describes the production and propagation of a state X with a set of quantum numbers given by

$$i \equiv \left\{I^G, J^{PC}, M\right\}, \tag{3.7}$$

where M is the projection of the spin J on the chosen quantization axis, and (ii) the *decay amplitude* $\widetilde{\Psi}_{i,j}(m_X, \tau)$ that describes the decay of X into a particular three-body final state that is indexed by j.

In contrast to the transition amplitude, which is *a priori* unknown, the decay amplitude is calculable using the *isobar model* [87, 88]. In this model, the X decay is described as a chain of successive two-body decays via additional intermediate resonances, the so-called *isobars* ξ, which appear in the two-body subsystems of the three-body final state.[g] Without loss of generality, the isobar decay chain of X is given by $X \to \xi + 3$ and $\xi \to 1 + 2$ (see Fig. 3.2). Particle 3 is called *bachelor particle*. The isobar model also assumes that the daughter particles of the two-body decays do not interact with each other, i.e., final-state interactions are neglected.

Our $\pi^-\pi^-\pi^+$ data support the assumption that the two-body subsystems are dominated by resonances as is shown in Fig. 3.3 in the form of Dalitz plots.[h] If the pions in the $\pi^-\pi^+$ subsystems would be uncorrelated, the events would be distributed uniformly in the Dalitz plot. However, the data exhibit clear structures that correspond to decays that proceed via $\xi = \rho(770)$, $f_0(980)$, or $f_2(1270)$ as intermediate $\pi^-\pi^+$ resonances.

[f] The Lorentz-invariant phase-space element can be written as

$$\mathrm{d}\varphi_3(m_X, \tau) = \rho_3(m_X, \tau)\ \mathrm{d}\tau, \tag{3.6}$$

where $\rho_3(m_X, \tau)$ represents the density of points in the phase space expressed in the variables m_X and τ. Hence $\rho_3(m_X, \tau)$ is the Jacobian corresponding to the particular choice of the phase-space variables τ.

[g] The usage of the term "isobar" for the intermediate states has historical reasons. The isobar model was first introduced by Lindenbaum and Sternheimer in Ref. [96] to describe excited intermediate nucleon resonances, which were termed "isobars" in analogy to nuclear physics.

[h] Also Fig. 2.6(b) indicates the presence of $\pi^-\pi^+$ isobar resonances in the $\pi^-\pi^-\pi^+$ final state.

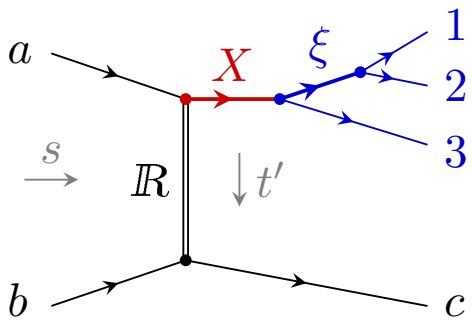

Figure 3.2: Production of an intermediate state X in a t-channel exchange reaction and decay of X into a three-body final state via a two-body isobar resonance ξ.

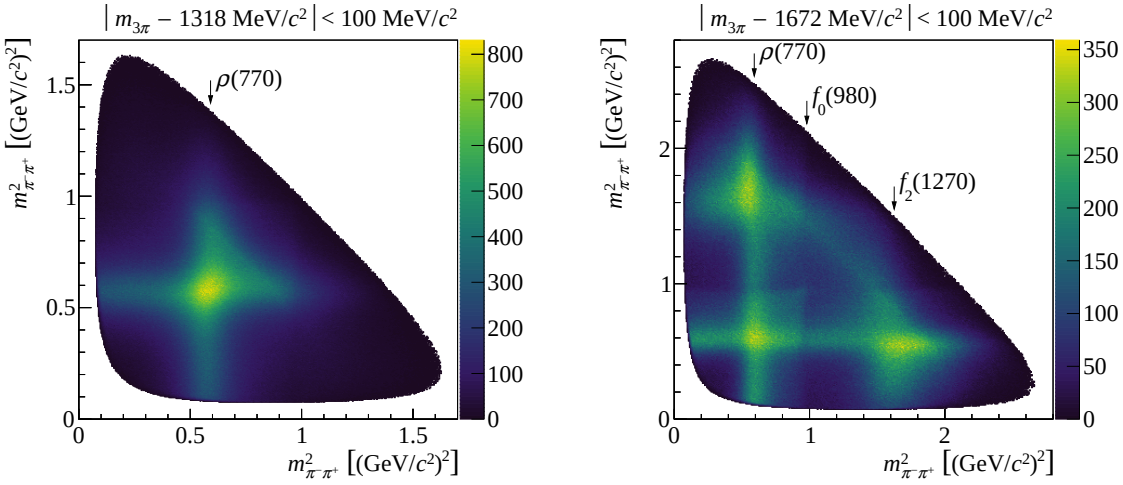

(a) **(b)**

Figure 3.3: Dalitz plots for two 100 MeV/c^2 wide 3π mass regions: (a) around the $a_2(1320)$, (b) around the $\pi_2(1670)$. The used 3π mass regions are indicated by gray shaded areas in Fig. 2.6(a). In (a), the $a_1(1260)$ and $a_2(1320)$ are the dominant 3π resonances and their decay into $\rho(770)\,\pi$ is clearly visible. The $\pi_2(1670)$ region exhibits $\rho(770)\,\pi$, $f_0(980)\,\pi$, and $f_2(1270)\,\pi$ decay modes.

From here on, we assume that the final-state particles of the X decay are spinless particles, e.g., π, K, η, or $\eta'(958)$. In this case, the isobar decay chain is completely defined by the isobar resonance ξ and the relative orbital angular momentum L between ξ and the third daughter particle. Therefore, the index j that defines the X decay is given by

$$j \equiv \{\xi, L\}\,. \tag{3.8}$$

For convenience, we introduce the index a that summarizes all information required to calculate the decay amplitude:

$$a \equiv \{i, j\} = \left\{I^G, J^{PC}, M; \xi, L\right\}. \tag{3.9}$$

A particular index a represents a *partial wave* and $|\widetilde{\Psi}_a(m_X, \tau)|^2$ represents the five-dimensional kinematic τ distribution of the final-state particles for this partial wave for a given value of m_X.[i]

In diffractive-dissociation reactions, the possible quantum numbers for X are limited only by the conservation laws of the strong interaction (see Sec. 2.1) and hence a rich spectrum of states X with various J^P quantum numbers is produced. In addition, the states X may decay via various ξ and L. As a result, usually many partial-wave amplitudes contribute to the intensity. The X and the isobars appear as intermediate states and are thus not directly measurable, while the initial- and final-state particles are the same for all partial waves. Therefore, the partial-wave amplitudes interfere with each other and hence have to be added coherently. Consequently, the model for the intensity distribution in Eq. (3.5) can be written as

$$\mathcal{I}(m_X, t', \tau) = \left| \sum_{a \equiv \{i,j\}}^{N_\text{waves}} \widetilde{\mathcal{T}}_i(m_X, t')\, \widetilde{\Psi}_a(m_X, \tau) \right|^2. \tag{3.10}$$

Here, N_waves is the number of partial waves included in the model.

The transition amplitudes $\widetilde{\mathcal{T}}_i(m_X, t')$ in our model are *a priori* unknown. Therefore, a two-stage approach is commonly used to analyze the data. In the first analysis stage, which is often called *partial-wave decomposition* or *mass-independent fit*, we make as little assumptions as possible about the intermediate states X. The goal of this first analysis stage is to extract the set $\left\{\widetilde{\mathcal{T}}_i(m_X, t')\right\}$ from the data. This is possible because we can calculate the decay amplitudes $\widetilde{\Psi}_a(m_X, \tau)$ for a given value of m_X using the isobar model.[j] Since the dependence of the transition amplitudes on m_X and t' is unknown, the partial-wave decomposition is performed independently in narrow (m_X, t') cells. This yields binned approximations to the $\widetilde{\mathcal{T}}_i(m_X, t')$ and is explained in detail in Sec. 3.3. Because of the binning approach, the first analysis stage makes no assumptions about the three-body resonance content of the partial waves. Based on the isobar model for the three-body decay of X, the data are decomposed into partial-wave amplitudes with well-defined quantum numbers that are given by the partial-wave index a as defined in Eq. (3.9). One may think of the partial-wave decomposition as merely a transformation of the data from four-momentum space of the final-state particles into the space of transition amplitudes. This yields a

[i] Depending on the context, the partial-wave index a has two meanings. It either represents directly the set of quantum numbers that define a partial-wave amplitude as in Eq. (3.9) or it enumerates all waves consecutively, i.e., a is an integer that uniquely identifies a specific partial wave as in Eq. (3.10).

[j] As will be discussed in Sec. 3.3, this is true only up to unknown complex factors.

representation of the data in terms of intensities and relative phases of the transition amplitudes that allows for a direct interpretation in terms of resonances.

In the second analysis stage, which is often called *resonance-model fit* or *mass-dependent fit*, we construct a model that describes the m_X and t' dependence of a selected subset of transition amplitudes in terms of resonant and non-resonant components. This is explained in Sec. 3.4. It is important to note that the resonance-model fit does not have to describe *all* transition amplitudes that are extracted from the data, but may focus on selected partial waves. This is in particular important for the analysis of high-energy scattering reactions, where often sizable non-resonant components contribute to the analyzed reaction. These non-resonant contributions project into all partial-wave amplitudes and often dominate the intensity of high-spin waves. Such waves are only important to describe the data but are uninteresting when it comes to extracting resonances. They are therefore not included in the resonance-model fit.

3.2.1 Parametrization of the decay amplitudes

In the isobar model, the three-body decay of X is described as a chain of two consecutive two-body decays. Consequently, the fundamental building block for the construction of the decay amplitude $\widetilde{\Psi}_a$ in Eq. (3.10) is the two-body decay amplitude $\mathcal{A}_r^{J_r\,M_r}$, which describes the propagation of a resonance r with spin J_r and spin projection M_r with respect to a chosen quantization axis and the decay of r into particles 1 and 2. The two-body decay amplitude can be calculated in the r rest frame using the helicity formalism [85, 91, 97, 98]. The two daughter particles have spins $J_{1,2}$ and are described in the helicity basis, where the quantization axes are the directions of the momenta of particles 1 and 2, respectively. In the r rest frame, the momenta of particles 1 and 2 are by definition back to back and have a fixed magnitude given by Eq. (1.26). Therefore, the kinematics of the decay of particle r is completely defined by the polar angle ϑ_r and the azimuthal angle ϕ_r of the momentum of one of the daughter particles.

The two-body decay amplitude factorizes into an angular and a dynamical part.[k] The angular part is given by first principles and is completely defined by the angular-momentum quantum numbers of the particles. The dynamical part describes the dependence of the amplitude on the invariant mass m_r of the $(1, 2)$ system and needs to be modeled. It can be factorized further into three parts: (i) an amplitude $\Delta_r(m_r)$ that describes the propagation of the decaying r, e.g., a Breit-Wigner amplitude as in Eqs. (1.24) and (1.25), (ii) a barrier factor $F_{L_r}(m_r)$ that describes the effect of the centrifugal barrier due to the orbital angular momentum L_r between the two daughter particles (see Eq. (1.28)), and (iii) an unknown complex-valued coupling $\alpha_{r\to 1+2}$ that describes strength and phase of the decay mode. We assume $\alpha_{r\to 1+2}$ to be independent of any kinematic variables. The parametrization for the

[k] This is analogous to the case of a two-particle system in a central potential, where the two-body wave function can be factorized into an angular part that is completely determined by the angular-momentum quantum numbers and a radial part that depends on the shape of the potential.

two-body decay amplitudes hence reads

$$\begin{aligned}\mathcal{A}_r^{J_r\,M_r\,L_r\,S_r}(m_r,\vartheta_r,\phi_r) = \underbrace{\sqrt{\frac{2L_r+1}{4\pi}}}_{\text{normalization}} \overbrace{\underbrace{\Delta_r(m_r)}_{\substack{\text{propagator}\\\text{term}}}\ \underbrace{F_{L_r}(m_r)}_{\substack{\text{barrier}\\\text{factor}}}\ \underbrace{\alpha_{r\to 1+2}}_{\text{coupling}}}^{\text{dynamical part}} \\ \times \sum_{\lambda_1,\lambda_2} \overbrace{(J_1\,\lambda_1\ J_2\,{-\lambda_2}\,|\,S_r\,\lambda)\,(L_r\,0\ S_r\,\lambda\,|\,J_r\,\lambda_r)\,D^{J_r\,*}_{M_r\,\lambda_r}(\phi_r,\vartheta_r,0)}^{\text{angular part}} \\ \times \underbrace{\mathcal{A}_1^{J_1\,\lambda_1\,L_1\,S_1}(m_1,\vartheta_1,\phi_1)}_{\substack{\text{two-body decay}\\\text{amplitude of particle 1}}} \underbrace{\mathcal{A}_2^{J_2\,\lambda_2\,L_2\,S_2}(m_2,\vartheta_2,\phi_2)}_{\substack{\text{two-body decay}\\\text{amplitude of particle 2}}}. \end{aligned} \tag{3.11}$$

The angular part contains two Clebsch-Gordan coefficients: one for the coupling of the spins of the two daughter particles to the total intrinsic spin S_r and one for the coupling of L_r and S_r to J_r. The two Clebsch-Gordan coefficients define the spin projection λ of the $(1,2)$ system and the spin projection λ_r of r using the direction of particle 1 as the quantization axis:

$$\lambda_r = \lambda = \lambda_1 - \lambda_2. \tag{3.12}$$

Since the orbital angular momentum L_r in the decay is by construction perpendicular to the momenta of particles 1 and 2, it has no projection onto the helicity quantization axis. The coherent summation over all allowed daughter helicities in Eq. (3.11) is performed only in the case, where particle 1 or 2 or both appear as intermediate states in the decay chain of X.

The Wigner D-function [99–101] that appears in Eq. (3.11) represents the transformation property of a spin state $|J,M\rangle$ under an arbitrary active rotation $\hat{\mathcal{R}}$, which is defined by the three Euler angles α, β, and γ. Since the $|J,M\rangle$ basis is complete, the rotated state can be expressed as a linear combination of the basis states:

$$\begin{aligned}\hat{\mathcal{R}}(\alpha,\beta,\gamma)\,|J,M\rangle &= \overbrace{\sum_{M'=-J}^{+J} |J,M'\rangle\,\langle J,M'|}^{=\mathbb{1}}\,\hat{\mathcal{R}}(\alpha,\beta,\gamma)\,|J,M\rangle \\ &= \sum_{M'=-J}^{+J} \underbrace{D^J_{M'\,M}(\alpha,\beta,\gamma)}_{\equiv\, D^J_{M'\,M}(\alpha,\beta,\gamma)}\,|J,M'\rangle\,. \end{aligned} \tag{3.13}$$

The amplitude $\mathcal{A}_i^{J_i\,\lambda_i\,L_i\,S_i}$ that appears in Eq. (3.11) represents the decay amplitude of the daughter particle i if it is unstable as well. In this case, the daughter particle appears as an isobar in the decay chain and its decay amplitude has the same form as Eq. (3.11). In case the daughter particle is a stable final-state particle, the corresponding amplitude is unity.

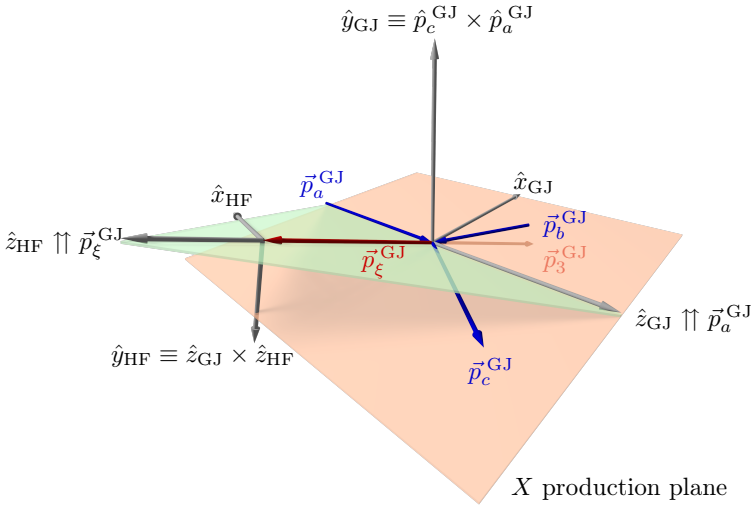

Figure 3.4: Definition of the Gottfried-Jackson (GJ) and helicity (HF) reference frames for the reaction $a + b \to X + c$ with $X \to \xi + 3$. Here, a is the beam, b the target, and c the recoil particle. Unit vectors are indicated by a circumflex. Adapted from Ref. [H2].

3.2.1.1 Coordinate systems

The angles that describe the two-body decays in the X decay chain and that enter the Wigner D-function in Eq. (3.11) are defined in the respective rest frames of the parent particles using right-handed coordinate systems. For high-energy scattering reactions with target particle b at rest in the laboratory frame, beam particle a, and target recoil c, the decay of X is usually described in the Gottfried-Jackson (GJ) frame. In this reference frame, the direction of the beam particle defines the z_{GJ} axis and the y_{GJ} axis is given by the normal of the production plane, i.e., $\hat{y}_{\mathrm{GJ}} \propto \hat{p}_a^{\,\mathrm{lab}} \times \hat{p}_X^{\,\mathrm{lab}} \propto \hat{p}_c^{\,\mathrm{GJ}} \times \hat{p}_a^{\,\mathrm{GJ}}$, where unit vectors are indicated by a circumflex. Since in the GJ frame X is at rest, the momenta of the isobar ξ and the bachelor particle 3 are back to back. Thus the angular distribution is described by the polar angle ϑ_{GJ} and the azimuthal angle ϕ_{GJ} of one of the daughter particles. The choice of the analyzer is a question of convention. Here, we use the isobar as the analyzer for the X decay.

The decay of an isobar resonance is described in the helicity reference frame (HF), which is constructed by boosting from the X rest frame into the isobar rest frame. The HF coordinate system is defined by taking the z_{HF} axis along the original direction of motion of the isobar, i.e., opposite to the direction of motion of X in the isobar rest frame, and $\hat{y}_{\mathrm{HF}} \propto \hat{z}_{\mathrm{GJ}} \times \hat{z}_{\mathrm{HF}}$. In the helicity frame, the two daughter particles of the isobar are emitted back to back, so that the angular distribution is described by the polar angle ϑ_{HF} and the azimuthal angle ϕ_{HF} of one of the daughters. Again, the choice of the analyzer is a question of convention. Here, we use the positive particle as the analyzer for the ξ decay.

Figure 3.4 illustrates the definition of the Gottfried-Jackson and helicity reference frames for the decay $X \to \xi + 3$.

3.2.1.2 Examples for decay amplitudes

Decay into two spinless final-state particles The simplest example is the decay of X into a two-body final state of spinless particles, $X \to 1 + 2$.[1] In this case, the amplitude $\widetilde{\Psi}_a(m_X, \vartheta_{\text{GJ}}, \phi_{\text{GJ}})$ for the X decay is given by Eq. (3.11) with $r = X$ and $\mathcal{A}_1 = \mathcal{A}_2 = 1$. In addition, we have to take into account that the (unknown) propagator term $\Delta_X(m_X)$ for X is already contained in the transition amplitudes $\widetilde{\mathcal{T}}_i(m_X, t')$ in Eq. (3.10). With $J_1 = J_2 = 0$ and hence $\lambda_1 = \lambda_2 = 0$, the decay amplitude reads

$$\begin{aligned}\widetilde{\Psi}_a(m_X, \vartheta_{\text{GJ}}, \phi_{\text{GJ}}) = \sqrt{\frac{2L_X + 1}{4\pi}}\, F_{L_X}(m_X)\, \alpha_{X\to 1+2} \\ \times (0\,0\;0\,0\,|\,S_X\,\lambda)\,(L_X\,0\;S_X\,\lambda\,|\,J\,\lambda_X)\, D^{J*}_{M\,\lambda_X}(\phi_{\text{GJ}}, \vartheta_{\text{GJ}}, 0). \quad (3.14)\end{aligned}$$

The only non-vanishing Clebsch-Gordan coefficients are the ones for which the total spin S_X of the $(1, 2)$ system and its spin projection λ are both zero and as a consequence, $\lambda_X = \lambda = 0$ and $J = L_X$. Since $\lambda_X = 0$, the Wigner D-function reduces to the spherical harmonics Y^M_J according to

$$D^J_{M\,0}(\phi_{\text{GJ}}, \vartheta_{\text{GJ}}, 0) = \sqrt{\frac{4\pi}{2J + 1}}\, Y^{M*}_J(\vartheta_{\text{GJ}}, \phi_{\text{GJ}}). \quad (3.15)$$

Therefore, Eq. (3.14) simplifies to

$$\widetilde{\Psi}_a(m_X, \vartheta_{\text{GJ}}, \phi_{\text{GJ}}) = F_J(m_X)\, \alpha_{X\to 1+2}\, Y^M_J(\vartheta_{\text{GJ}}, \phi_{\text{GJ}}). \quad (3.16)$$

Decay into three spinless final-state particles For decays of X into three final-state particles, i.e., $X \to \xi + 3$ with $\xi \to 1 + 2$, the decay amplitude $\widetilde{\Psi}_a(m_X, \tau)$ is calculated by recursive application of Eq. (3.11):

$$\begin{aligned}\widetilde{\Psi}_a(m_X, \overbrace{\vartheta_{\text{GJ}}, \phi_{\text{GJ}}, m_\xi, \vartheta_{\text{HF}}, \phi_{\text{HF}}}^{\equiv \tau}) = \sqrt{\frac{2L + 1}{4\pi}}\, F_L(m_X)\, \alpha_{X\to\xi+3} \\ \times \sum_{\lambda_\xi} \overbrace{(J_\xi\,\lambda_\xi\;0\,0\,|\,S\,\lambda_X)}^{=\delta_{J_\xi S}\,\delta_{\lambda_\xi\lambda_X}} (L\,0\;S\,\lambda_X\,|\,J\,\lambda_X)\, D^{J*}_{M\,\lambda_X}(\phi_{\text{GJ}}, \vartheta_{\text{GJ}}, 0) \\ \times \underbrace{\Delta_\xi(m_\xi)\, F_{J_\xi}(m_\xi)\, \alpha_{\xi\to 1+2}\, Y^{\lambda_\xi}_{J_\xi}(\vartheta_{\text{HF}}, \phi_{\text{HF}})}. \quad (3.17) \\ = \mathcal{A}^{J_\xi\,\lambda_\xi\,L_\xi\,S_\xi}_\xi(m_\xi, \vartheta_{\text{HF}}, \phi_{\text{HF}}) \text{ as given by Eq. (3.11)}\end{aligned}$$

The first part of the decay amplitude describes the decay $X \to \xi + 3$ and corresponds to the amplitude $\mathcal{A}^{J\,M\,L\,S}_X(m_X, \vartheta_{\text{GJ}}, \phi_{\text{GJ}})$ as given by Eq. (3.11), with the only difference that the (unknown) propagator term $\Delta_X(m_X)$ for X does not appear here since it is already contained in the transition amplitudes $\widetilde{\mathcal{T}}_i(m_X, t')$ in Eq. (3.10). In Eq. (3.17), λ_ξ is the helicity of ξ in the Gottfried-Jackson rest frame of X. Since $J_3 = 0$ and hence $\lambda_3 = 0$, the total spin S of the $(\xi, 3)$ system is given by J_ξ and the sum λ_X of the helicities of particles ξ and 3 is equal to λ_ξ. The second part of Eq. (3.17) describes the decay $\xi \to 1 + 2$. Since

[1] This could be, for example, $X^- \to \pi^-\eta$ or $\pi^-\eta'$, where η and η' are considered as quasi-stable particles.

both final-state particles are spinless, the same arguments apply as for the decay $X \to 1+2$ discussed in the paragraph above. Equation (3.17) can thus be simplified to

$$\begin{aligned}\widetilde{\Psi}_a(m_X, \vartheta_{\text{GJ}}, \phi_{\text{GJ}}, m_\xi, \vartheta_{\text{HF}}, \phi_{\text{HF}}) \\ = \sqrt{\frac{2L+1}{4\pi}}\, F_L(m_X)\, \alpha_{X\to\xi+3}\, \Delta_\xi(m_\xi)\, F_{J_\xi}(m_\xi)\, \alpha_{\xi\to 1+2} \\ \times \sum_{\lambda_\xi} (L\,0\; J_\xi\, \lambda_\xi \,|\, J\, \lambda_\xi)\, D^{J*}_{M\,\lambda_\xi}(\phi_{\text{GJ}}, \vartheta_{\text{GJ}}, 0)\, Y^{\lambda_\xi}_{J_\xi}(\vartheta_{\text{HF}}, \phi_{\text{HF}}). \end{aligned} \tag{3.18}$$

3.2.1.3 Symmetrization of the decay amplitude

If the three-body final state contains indistinguishable particles, the decay amplitude has to be symmetrized accordingly. For mesonic final states, the decay amplitude has to be totally symmetric under exchange of any of the indistinguishable final-state particles (Bose symmetry). The symmetrized decay amplitude is constructed by summing the amplitudes for all permutations of the indistinguishable final-state particles.

The $\pi^-\pi^-\pi^+$ final state considered here contains two indistinguishable π^-. Hence the Bose symmetrized decay amplitude is

$$\widetilde{\Psi}^{\text{sym}}_a = \frac{1}{\sqrt{2}} \left[\widetilde{\Psi}_a(m_X, \tau_{13}) + \widetilde{\Psi}_a(m_X, \tau_{23})\right] \tag{3.19}$$

with $\widetilde{\Psi}_a(m_X, \tau)$ given by Eq. (3.18). Here, τ_{13} and τ_{23} are the two sets of phase-space variables that correspond to the two possible $\pi^-\pi^+$ combinations in the $\pi^-_1\pi^-_2\pi^+_3$ system. To simplify notation, we redefine $\widetilde{\Psi}_a(m_X, \tau)$ to always represent the Bose-symmetrized decay amplitude in the remaining text.

3.3 Stage I: partial-wave decomposition

The decomposition of the data into partial-waves with well-defined quantum numbers and isobar decay chains constitutes the first stage of the analysis. In this stage, the m_X and t' dependence of the unknown transition amplitudes $\widetilde{\mathcal{T}}_i$ in Eq. (3.10) is extracted from the data by subdividing the data sample into narrow bins in these two kinematic variables. We assume that the bins in m_X and t' are narrow enough, such that we can in good approximation neglect the m_X and t' dependence in a given (m_X, t') cell. Hence in this cell, the intensity distribution in Eq. (3.10) is a function only of the five phase-space variables represented by τ. The other two kinematic variables, m_X and t', appear as constant parameters:

$$\mathcal{I}(\tau; m_X, t') = \left| \sum_{a\equiv\{i,j\}}^{N_{\text{waves}}} \widetilde{\mathcal{T}}_i(m_X, t')\, \widetilde{\Psi}_a(\tau; m_X) \right|^2. \tag{3.20}$$

This binned approach does not make any assumptions about the three-body resonance content of the transition amplitudes. In addition, the kinematic cells are statistically independent so that the partial-wave decomposition can be performed in parallel. A caveat of the binning approach is that the method introduces a large number of free parameters—the values of the transition amplitudes in each (m_X, t') cell—that need to be determined from data. For that reason, it is only applicable to sufficiently large data sets.

The decay amplitudes $\widetilde{\Psi}_a$ as given by Eqs. (3.18) and (3.19) contain unknown complex-valued couplings $\alpha_{X\to\xi+3}$ and $\alpha_{\xi\to 1+2}$. Assuming that these couplings do not depend on any of the phase-space variables, they can be pulled out of each two-body decay amplitude so that

$$\widetilde{\Psi}_a(\tau; m_X) \equiv \underbrace{\alpha_{X\to\xi+3}\,\alpha_{\xi\to 1+2}}_{\equiv\,\alpha_a}\,\overline{\Psi}_a(\tau; m_X). \tag{3.21}$$

Assuming that we know the propagator terms for all isobars precisely, the decay amplitudes $\overline{\Psi}_a(\tau; m_X)$ defined in Eq. (3.21) are calculable and do not contain any free parameters. The unknown α_a are absorbed into the transition amplitudes via the redefinition

$$\overline{\mathcal{T}}_a(m_X, t') \equiv \alpha_a\,\widetilde{\mathcal{T}}_i(m_X, t'). \tag{3.22}$$

Note that the $\overline{\mathcal{T}}_a$ now depend not only on the set i of the X quantum numbers as defined in Eq. (3.7), but also on the decay mode j defined in Eq. (3.8). The model for the intensity distribution in an (m_X, t') cell therefore reads

$$\mathcal{I}(\tau; m_X, t') = \left| \sum_a^{N_\text{waves}} \overline{\mathcal{T}}_a(m_X, t')\,\overline{\Psi}_a(\tau; m_X) \right|^2. \tag{3.23}$$

In the following, we consider the intensity always in a given (m_X, t') cell and hence leave off the m_X and t' parameters from the formulas in order to simplify notation.

The PWA model in Equation (3.23) still needs to be modified and extended in order to take into account (i) possible background contributions, (ii) the spin states of the target and recoil particles, and (iii) parity conservation in the strong-interaction scattering process.

3.3.1 Background contributions

The analyzed data are usually contaminated by misreconstructed or partially reconstructed events that are similar to the signal process and hence fulfill the event selection criteria. We model this background by a distribution that is isotropic in phase space. Therefore, these events have a constant probability density over all phase-space elements. In order to account for such events, we incoherently add a component to Eq. (3.23), the so-called *flat wave*. The corresponding decay amplitude $\overline{\Psi}_\text{flat}$ is constant and without loss of generality we set $\overline{\Psi}_\text{flat} \equiv 1$ so that

$$\mathcal{I}(\tau) = \left| \sum_a^{N_\text{waves}} \overline{\mathcal{T}}_a\,\overline{\Psi}_a(\tau) \right|^2 + \left|\overline{\mathcal{T}}_\text{flat}\right|^2. \tag{3.24}$$

Since only the intensity of the flat wave enters in Eq. (3.24), the phase of this wave is immeasurable. Thus $\overline{\mathcal{T}}_\text{flat}$ is chosen to be real-valued.

Background contributions from other processes, e.g., from non-resonant components, for which the final-state particles are correlated and are hence distributed anisotropically in phases space, do not contribute strongly to the flat wave and usually contaminate the other waves in the PWA model. These contributions have to be taken into account in the resonance-model fit, which constitutes the second stage of the analysis (see Sec. 3.4).

3.3.2 Spin-density matrix and rank

The data analyzed here were taken using a proton target. Since the target protons are unpolarized and the beam pions are spinless, $|\mathcal{M}_{fi}|^2$ in Eq. (3.4) includes averaging over the two spin states of the target proton and summation over the two spin states of the recoiling proton. Due to parity conservation and rotational invariance, the scattering amplitude depends only on the relative orientation of the spin states of the target and the recoil proton. Thus the cross section consists of two incoherent parts: one for spin-flip at the target vertex, one for spin-non-flip. Additional incoherent terms may arise if the target proton is excited in the scattering process. Also performing the partial-wave decomposition over wide t' ranges may lead to effective incoherence, if the transition amplitudes have different dependences on t'. Furthermore, multiple exchange processes might contribute to the scattering process, which may lead to additional incoherence.

A way to include these incoherences in the PWA model in Eq. (3.24) is the introduction of an additional index r for the transition amplitudes that is summed over incoherently:

$$\mathcal{I}(\tau) = \sum_{r=1}^{N_r} \left| \sum_{a}^{N_\text{waves}} \overline{\mathcal{T}}_a^r \, \overline{\Psi}_a(\tau) \right|^2 + \left| \overline{\mathcal{T}}_\text{flat} \right|^2 \tag{3.25}$$

$$= \sum_{a,b}^{N_\text{waves}} \overline{\Psi}_a(\tau) \underbrace{\left[\sum_{r=1}^{N_r} \overline{\mathcal{T}}_a^r \, \overline{\mathcal{T}}_b^{r*} \right]}_{\equiv \, \overline{\varrho}_{ab}} \overline{\Psi}_b^*(\tau) + \left| \overline{\mathcal{T}}_\text{flat} \right|^2. \tag{3.26}$$

In Eq. (3.26), we introduce the Hermitian and positive-semidefinite spin-density matrix $\overline{\varrho}_{ab}$ that completely describes the intermediate state X in terms of combinations of pure quantum states. The elements of the spin-density matrix represent the actually measurable observables. The number N_r of transition amplitudes per partial wave corresponds to the rank of the spin-density matrix. For most reactions, N_r is significantly smaller than the mathematically allowed maximum, which is given by the dimension of the spin-density matrix, i.e., N_waves.[m] We employ the parametrization of Chung and Trueman [102] for the spin-density matrix, which reduces the number of free real-valued parameters that need to be determined from the data to the minimum, which is $N_r \, (2N_\text{waves} - N_r)$.

Assuming a single production mechanism and neglecting other sources of incoherence, the maximum rank of the spin-density matrix for X in the scattering process $\pi + p \to X + p$ is $N_r = 2$. This corresponds to spin-flip and spin-non-flip processes at the target vertex as discussed above. It is worth noting that the spins of the target and recoil particles define only the *maximum* rank of the spin-density matrix. Depending on the scattering process and the data sample, a lower rank might be sufficient to describe the data. Diffractive scattering of spinless beam particles off nucleons is known to be dominated by spin-non-flip processes [103]. Hence for these processe, a rank-1 spin-density matrix yields a satisfactory description of the data, if other sources for incoherence like target excitations or integration over large t' intervals are avoided.

[m] Since the spin-density matrix is Hermitian and positive-semidefinite, it is diagonalizable and has real-valued eigenvalues. Of these eigenvalues, N_r are positive and $N_\text{waves} - N_r$ are zero.

3.3.3 Parity conservation and reflectivity

For all we know, the strong interaction conserves parity. A convenient way of including parity conservation into the PWA model in Eq. (3.26) is to consider the scattering subprocess $a+b \to X+c$ in the so-called *reflectivity basis* [102]. If this process is parity conserving, the scattering amplitude should be invariant under space inversion. Such a parity transformation flips the directions of the particle momenta. Since the four particles lie in the production plane, this can be undone by performing, in addition to the space inversion, a rotation by 180° about the production plane normal. The combined transformation is represented by the reflectivity operator Π_y and corresponds to a reflection through the production plane, which leaves the momenta of those particles that lie in that plane unchanged.

In the Gottfried-Jackson frame defined in Sec. 3.2.1.1, the state X with spin J, intrinsic parity P, and spin projection M transforms under the reflectivity operator Π_y as follows

$$\Pi_y \left| J^P, M \right\rangle = P\,(-1)^{J-M} \left| J^P, -M \right\rangle . \tag{3.27}$$

We can therefore construct eigenstates to Π_y by linear combination of canonical states with spin projections of opposite sign:

$$\left| J^P, M^\varepsilon \right\rangle \equiv \mathcal{N}_M \Big[\left| J^P, M \right\rangle - \varepsilon \underbrace{P\,(-1)^{J-M} \left| J^P, -M \right\rangle}_{= \Pi_y \left| J^P, M \right\rangle} \Big], \tag{3.28}$$

where we choose the normalization factor to be

$$\mathcal{N}_M = \begin{cases} 1/\sqrt{2} & \text{for } M > 0, \\ 1/2 & \text{for } M = 0, \\ 0 & \text{for } M < 0. \end{cases} \tag{3.29}$$

This choice ensures that in the reflectivity basis the multiplicity $2J+1$ of the spin state remains unchanged. The reflectivity eigenstate defined in Eq. (3.28) is characterized by the spin-projection quantum number M and the eigenvalue ε^* of the reflectivity operator, i.e.,

$$\Pi_y \left| J^P, M^\varepsilon \right\rangle = \varepsilon^* \left| J^P, M^\varepsilon \right\rangle \tag{3.30}$$

The *reflectivity* ε is ± 1 for bosons.[n] According to Eq. (3.29), there are no states with $M < 0$ in the reflectivity basis. States with spin projection $M = 0$ vanish, if $\varepsilon = P\,(-1)^J$. Hence for a given J^P, there exists only one state with $\varepsilon = P\,(-1)^{J+1}$ and $M = 0$. For each $M > 0$, two states with $\varepsilon = \pm 1$ exist, so that in total the multiplicity of the spin state is $2J+1$, as in the canonical basis.

Using Eq. (3.28), we can define the rotation function for the reflectivity eigenstates:

$$\begin{aligned} {}^{\varepsilon}D^J_{M'\,M}(\alpha,\beta,\gamma) &\equiv \left\langle J^P, M'^{\varepsilon} \right| \hat{\mathcal{R}}(\alpha,\beta,\gamma) \left| J^P, M \right\rangle \\ &= \mathcal{N}_M \Big[\left\langle J^P, M \right| \hat{\mathcal{R}} \left| J^P, M \right\rangle - \varepsilon^*\, P\,(-1)^{J-M} \left\langle J^P, -M \right| \hat{\mathcal{R}} \left| J^P, M \right\rangle \Big] \\ &= \mathcal{N}_M \Big[D^J_{M'\,M}(\alpha,\beta,\gamma) - \varepsilon^*\, P\,(-1)^{J-M}\, D^J_{-M'\,M}(\alpha,\beta,\gamma) \Big]. \end{aligned} \tag{3.31}$$

[n] The reflectivity is $\pm i$ for fermions.

Although these functions are not a representation of the rotation group, they still have properties similar to those of the fundamental D-functions. In particular, they form an orthogonal function system. In order to calculate the X decay amplitude in the reflectivity basis, the Wigner D-function $D^{J}_{M\,\lambda_X}(\phi_{\text{GJ}}, \vartheta_{\text{GJ}}, 0)$ in Eq. (3.18) is replaced by Eq. (3.31).

Describing the spin state of X in the reflectivity basis also changes the structure of the spin-density matrix. In order to fully define a wave in the reflectivity basis, we have to specify in addition to the wave index a, which contains the spin-projection quantum number $0 \leq M \leq J$ (see Eq. (3.9)), also the reflectivity quantum number $\varepsilon = \pm 1$. Analogous to the definition of the spin-density matrix in Eq. (3.26), where $-J \leq M \leq +J$, we can write the spin-density matrix in the reflectivity basis:

$$\overline{\varrho}^{\varepsilon\varepsilon'}_{ab} = \sum_{r=1}^{N_r} \overline{\mathcal{T}}^{r\varepsilon}_{a}\, \overline{\mathcal{T}}^{r\varepsilon'*}_{b}. \tag{3.32}$$

It is important to note that $\overline{\varrho}^{\varepsilon\varepsilon'}_{ab}$ has the same number of elements as $\overline{\varrho}_{ab}$ in Eq. (3.26).

It is shown in Ref. [102] that due to parity conservation and rotational invariance, the spin-density matrix assumes a block-diagonal form with respect to ε in the reflectivity basis, i.e.,

$$\overline{\varrho}^{\varepsilon\varepsilon'}_{ab} = \begin{pmatrix} \overline{\varrho}^{++}_{ab} & 0 \\ 0 & \overline{\varrho}^{--}_{ab} \end{pmatrix}. \tag{3.33}$$

This means that all interference terms of transition amplitudes with opposite reflectivity quantum numbers are zero. In the reflectivity basis, the PWA model in Eq. (3.26) can therefore be written as

$$\begin{aligned} \mathcal{I}(\tau) &= \sum_{\varepsilon=\pm 1} \sum_{r=1}^{N_r} \left| \sum_{a}^{N_{\text{waves}}} \overline{\mathcal{T}}^{r\varepsilon}_{a}\, \overline{\Psi}^{\varepsilon}_{a}(\tau) \right|^2 + \left| \overline{\mathcal{T}}_{\text{flat}} \right|^2 \\ &= \sum_{\varepsilon=\pm 1} \sum_{a,b}^{N_{\text{waves}}} \overline{\Psi}^{\varepsilon}_{a}(\tau)\, \overline{\varrho}^{\varepsilon}_{ab}\, \overline{\Psi}^{\varepsilon *}_{b}(\tau) + \left| \overline{\mathcal{T}}_{\text{flat}} \right|^2 \end{aligned} \tag{3.34}$$

with

$$\overline{\varrho}^{\varepsilon}_{ab} \equiv \overline{\varrho}^{\varepsilon\varepsilon}_{ab} = \sum_{r=1}^{N_r} \overline{\mathcal{T}}^{r\varepsilon}_{a}\, \overline{\mathcal{T}}^{r\varepsilon *}_{b}. \tag{3.35}$$

In Eq. (3.34), $\overline{\Psi}^{\varepsilon}_{a}$ is the decay amplitude in the reflectivity basis, where the Wigner D-function for the X decay is replaced by Eq. (3.31).

Up to this point, we just transformed from one complete set of states to another. The formulation in the reflectivity basis in Eqs. (3.33) and (3.35) is completely equivalent to the formulation in the canonical basis in Eq. (3.26). An important advantage of the formulation in the reflectivity basis is that in the high-energy limit the reflectivity quantum number of X corresponds to the naturality of the exchange particle in the scattering process [104, 105].[o] The naturality η of a quantum state is defined as

$$\eta \equiv P\,(-1)^{J}. \tag{3.36}$$

[o] The relative sign between the two terms in Eq. (3.28) was chosen accordingly.

For historical reasons, a state is said to have *natural parity* if $\eta = +1$, i.e., $P = (-1)^J$, and *unnatural parity* if $\eta = -1$, i.e., $P = (-1)^{J+1}$.

Scattering processes of hadrons at high energies, such as the ones studied here, are dominated by Pomeron exchange. Since the Pomeron has positive naturality, partial-wave amplitudes with $\varepsilon = -1$ that correspond to unnatural-parity exchange are suppressed. As a consequence, PWA models for these reactions require much less waves with negative than with positive reflectivity in order to describe the data. Therefore, the dimension of $\overline{\varrho}_{ab}^{\varepsilon=-1}$ in the PWA model is much smaller than that of $\overline{\varrho}_{ab}^{\varepsilon=+1}$. This corresponds to a reduced number of free parameters of the PWA model. The different number of waves in the two reflectivity sectors are taken into account by the replacement

$$N_{\text{waves}} \to N_{\text{waves}}^{\varepsilon}. \tag{3.37}$$

Due to the correspondence of the reflectivity to different exchange particles and hence different production mechanisms, also the effective rank N_r of the spin-density matrix may be different for the two values of ε. We include this in the PWA model of Eq. (3.34) by the replacement

$$N_r \to N_r^{\varepsilon}. \tag{3.38}$$

3.3.4 Normalization

An important technical issue is the normalization of the transition and decay amplitudes. A consistent normalization allows us to extract yields of resonances and to compare the transition amplitudes of different waves in a PWA model as well as across different analyses and experiments.

In order to derive a normalization scheme, we go back to the definition of the intensity $\mathcal{I}$ in Eq. (3.5) as the number of produced events per unit in m_X, t', and three-body phase-space volume. By integrating $\mathcal{I}$ over the volume of the three-body phase space of the final-state particles, we get the density of produced events as a function of m_X and t':

$$\frac{\mathrm{d}N}{\mathrm{d}m_X\ \mathrm{d}t'} = \int \mathrm{d}\varphi_3(\tau; m_X)\, \mathcal{I}(\tau; m_X, t'). \tag{3.39}$$

Integrating Eq. (3.39) over the (m_X, t') cell, in which the partial-wave decomposition is performed, yields the number of events in that (m_X, t') cell as predicted by the model:

$$N_{\text{pred}}(m_X, t') = \int\limits_{m_{X,1}}^{m_{X,2}} \mathrm{d}\widetilde{m}_X \int\limits_{t'_1}^{t'_2} \mathrm{d}\widetilde{t'} \frac{\mathrm{d}N}{\mathrm{d}\widetilde{m}_X\ \mathrm{d}\widetilde{t'}}. \tag{3.40}$$

Here, $(m_{X,1}, t'_1)$ and $(m_{X,2}, t'_2)$ define the borders of the (m_X, t') cell. In our binned analysis approach, we neglect the m_X and t' dependence of $\mathrm{d}N/(\mathrm{d}m_X\ \mathrm{d}t')$ within the (m_X, t') cell, so that the integration in Eq. (3.40) is trivial.

We define the normalization of the intensity by demanding

$$\begin{aligned} N_{\text{pred}}(m_X, t') &= \int \mathrm{d}\varphi_3(\tau; m_X)\, \mathcal{I}(\tau; m_X, t') \\ &= \sum_{\varepsilon=\pm 1} \Bigg\{ \sum_{a}^{N^{\varepsilon}_{\text{waves}}} \sum_{r=1}^{N^{\varepsilon}_{r}} \left| \overline{\mathcal{T}}^{r\varepsilon}_{a}(m_X, t') \right|^2 \int \mathrm{d}\varphi_3(\tau; m_X) \left| \overline{\Psi}^{\varepsilon}_{a}(\tau; m_X) \right|^2 \\ &\quad + \sum_{a,b;a<b}^{N^{\varepsilon}_{\text{waves}}} 2\,\mathrm{Re}\Bigg[\sum_{r=1}^{N^{\varepsilon}_{r}} \overline{\mathcal{T}}^{r\varepsilon}_{a}(m_X, t')\, \overline{\mathcal{T}}^{r\varepsilon *}_{b}(m_X, t') \\ &\quad \times \int \mathrm{d}\varphi_3(\tau; m_X)\, \overline{\Psi}^{\varepsilon}_{a}(\tau; m_X)\, \overline{\Psi}^{\varepsilon *}_{b}(\tau; m_X) \Bigg] \Bigg\} + \left| \overline{\mathcal{T}}_{\text{flat}}(m_X, t') \right|^2 \int \mathrm{d}\varphi_3(\tau; m_X). \end{aligned} \tag{3.41}$$

Here, we have absorbed the m_X and t' bin widths into the normalization factor. We also have used Eqs. (3.34) and (3.37) to (3.39).

Equation (3.41) fixes the unit of $\mathcal{I}$ to number of events predicted by the model. However, it still leaves room for an arbitrary factor that can be shifted between the transition and decay amplitudes. In order to also fix the unit of the transition amplitudes, we normalize the decay amplitudes to the diagonal elements of the so-called *integral matrix*

$$I^{\varepsilon}_{ab}(m_X) \equiv \int \mathrm{d}\varphi_3(\tau; m_X)\, \overline{\Psi}^{\varepsilon}_{a}(\tau; m_X)\, \overline{\Psi}^{\varepsilon *}_{b}(\tau; m_X). \tag{3.42}$$

The normalized decay amplitudes are hence defined by

$$\Psi^{\varepsilon}_{a}(\tau; m_X) \equiv \frac{\overline{\Psi}^{\varepsilon}_{a}(\tau; m_X)}{\sqrt{I^{\varepsilon}_{aa}(m_X)}}. \tag{3.43}$$

In order to leave N_{pred} in Eq. (3.41) unchanged, the transition amplitudes are normalized according to

$$\mathcal{T}^{r\varepsilon}_{a}(m_X, t') \equiv \sqrt{I^{\varepsilon}_{aa}(m_X)}\, \overline{\mathcal{T}}^{r\varepsilon}_{a}(m_X, t'). \tag{3.44}$$

Expressing Eq. (3.41) in terms of the normalized spin-density matrix elements

$$\varrho^{\varepsilon}_{ab}(m_X, t') = \sum_{r=1}^{N^{\varepsilon}_{r}} \mathcal{T}^{r\varepsilon}_{a}(m_X, t')\, \mathcal{T}^{r\varepsilon *}_{b}(m_X, t') \tag{3.45}$$

yields

$$\begin{aligned} N_{\text{pred}}(m_X, t') = \sum_{\varepsilon=\pm 1} \Bigg\{ & \sum_{a}^{N^{\varepsilon}_{\text{waves}}} \underbrace{\varrho^{\varepsilon}_{aa}(m_X, t')}_{\text{intensities}} \\ & + \sum_{a,b;a<b}^{N^{\varepsilon}_{\text{waves}}} \underbrace{2\,\mathrm{Re}\left[\varrho^{\varepsilon}_{ab}(m_X, t') \frac{I^{\varepsilon}_{ab}(m_X)}{\sqrt{I^{\varepsilon}_{aa}(m_X)\, I^{\varepsilon}_{bb}(m_X)}} \right]}_{\text{overlaps}} \Bigg\} + \left| \mathcal{T}_{\text{flat}}(m_X, t') \right|^2. \end{aligned} \tag{3.46}$$

This equation provides an interpretation for the normalized spin-density matrix elements. The diagonal elements $\varrho^{\varepsilon}_{aa}$ are the *partial-wave intensities*, i.e., the expected number of events in wave a with reflectivity ε.[p] The off-diagonal elements $\varrho^{\varepsilon}_{ab}$, which contain information about the relative phase between waves a and b, contribute to the so-called *overlaps*, which are the number of events originating from the interference between waves a and b with reflectivity ε (see also Sec. 3.3.6).

Using the normalized transition and decay amplitudes, the final formula for the intensity reads

$$\begin{aligned}\mathcal{I}(\tau; m_X, t') &= \sum_{\varepsilon=\pm1} \sum_{r=1}^{N_r^{\varepsilon}} \left| \sum_{a}^{N_{\text{waves}}^{\varepsilon}} \mathcal{T}_a^{r\varepsilon}(m_X, t')\, \Psi_a^{\varepsilon}(\tau; m_X) \right|^2 + |\mathcal{T}_{\text{flat}}(m_X, t')|^2 \\ &= \sum_{\varepsilon=\pm1} \sum_{a,b}^{N_{\text{waves}}^{\varepsilon}} \Psi_a^{\varepsilon}(\tau; m_X)\, \varrho^{\varepsilon}_{ab}(m_X, t')\, \Psi_b^{\varepsilon *}(\tau; m_X) + |\mathcal{T}_{\text{flat}}(m_X, t')|^2.\end{aligned} \tag{3.47}$$

3.3.5 Unbinned extended maximum likelihood fit

The maximum likelihood method is used to estimate unknown parameter values of a statistical model by maximizing the likelihood function $\mathcal{L}$, which is the joint probability density of the data set given the parameter values [106]. For a given data set $\vec{x} \equiv (x_1, \ldots, x_N)^T$ of N independent random variables[q] that follow the same probability density function $f(x; \vec{\theta})$ with m parameters $\vec{\theta} \equiv (\theta_1, \ldots, \theta_m)^T$ with unknown values, the likelihood function is

$$\mathcal{L}(\vec{\theta}; \vec{x}) = \prod_{k=1}^{N} f(x_k; \vec{\theta}). \tag{3.48}$$

The maximum likelihood estimate $\hat{\vec{\theta}}$ for the parameters is given by those parameter values that maximize the likelihood function, i.e.,

$$\hat{\vec{\theta}} = \arg\max_{\vec{\theta}} \mathcal{L}(\vec{\theta}; \vec{x}). \tag{3.49}$$

In the above equation, $\mathcal{L}$ is a function of $\vec{\theta}$ for a given, i.e., fixed, $\vec{x}$. It is important to note that although for given $\vec{\theta}$, $\mathcal{L}$ is the probability density function of $\vec{x}$, $\mathcal{L}$ is in general *not* the probability density function of $\vec{\theta}$ for given $\vec{x}$. In other words, maximizing the probability to observe the data with respect to $\vec{\theta}$ as expressed in Eq. (3.49) does not necessarily yield the most probable parameter values. Also, $\mathcal{L}$ does not need to be normalized with respect to $\vec{\theta}$. An advantage of the maximum likelihood method is that Eq. (3.49) does not require any binning of the data. Therefore, the method is applicable also to high-dimensional data, where binned approaches quickly become prohibitively expensive in terms of computational resources. This is already the case for the analysis of three-body final states, since the kinematic phase-space distribution in a (m_X, t') cell is five-dimensional.

[p] For an experiment with acceptance different from unity, this corresponds to the acceptance-corrected number of events (see Sec. 3.3.5).

[q] Depending in the measurement, these variables may in turn be vectors in a higher-dimensional data space. In our case, the x_k would correspond to the measured phase-space variables τ_k of an event k.

If the number N of data points is not predetermined but is a result of the measurement and hence a random variable, the maximum likelihood principle can be extended. In the case of counting experiments, events are produced randomly in time with constant average rates and hence the number of events follows the Poisson distribution with the expected number of events λ. For this case, the extended likelihood function is

$$\mathcal{L}_{\text{ext}}(\vec{\theta}, \lambda; \vec{x}, N) = \underbrace{\frac{\lambda^N \, e^{-\lambda}}{N!}}_{\substack{\text{Poisson} \\ \text{distribution}}} \underbrace{\prod_{k=1}^{N} f(x_k; \vec{\theta})}_{= \mathcal{L}(\vec{\theta}; \vec{x})}. \tag{3.50}$$

This approach was first proposed by Fermi and is discussed in more detail in Refs. [107–109]. In Ref. [109], it is shown that the extended maximum likelihood estimator inherits the desired asymptotic properties of consistency, unbiasedness, and efficiency from the maximum likelihood estimator in Eq. (3.49).

We apply the extended maximum likelihood method to partial-wave analysis in order to estimate the values of the transition amplitudes $\{\mathcal{T}_a^{r\varepsilon}\}$ in our PWA model for the intensity distribution in Eq. (3.47). This approach has been pioneered by Ascoli *et al.* [83, 84]. The partial-wave decomposition is performed independently in (m_X, t') cells and we neglect the dependence of the intensity on m_X and t' in each cell. In order to simplify notation, we from here on consider a specific (m_X, t') cell and leave off the m_X and t' dependence in the formulas below.

Within a given (m_X, t') cell, our model in Eq. (3.47) describes the five-dimensional τ distribution of the produced events, i.e., the events a hypothetical perfect detector with unit acceptance would measure. In practice, the *acceptance* ϵ of the detector setup[r] is smaller than unity and depends on the kinematic variables m_X, t', and τ.[s] To obtain a model for the actual intensity distribution measured by the detector, we have to weight Eq. (3.47) by the detector acceptance. By normalizing this model and using Eq. (3.6), we get the probability density function of the measured events in τ space, i.e.,

$$f(\tau; \{\mathcal{T}_a^{r\varepsilon}\}) = \frac{\rho_3(\tau)\, \epsilon(\tau)\, \mathcal{I}(\tau; \{\mathcal{T}_a^{r\varepsilon}\})}{\int \mathrm{d}\tau' \, \rho_3(\tau')\, \epsilon(\tau')\, \mathcal{I}(\tau'; \{\mathcal{T}_a^{r\varepsilon}\})} \quad \text{such that} \quad \int \mathrm{d}\tau \, f(\tau; \{\mathcal{T}_a^{r\varepsilon}\}) = 1. \tag{3.51}$$

The intensity distribution $\mathcal{I}$ is normalized via Eqs. (3.41) and (3.46) such that it is given in units of number of produced events. Therefore, the normalization integral in the denominator of Eq. (3.51) corresponds to the number $\overline{N}$ of events that are expected to be measured by the detector:

$$\overline{N}(\{\mathcal{T}_a^{r\varepsilon}\}) = \int \mathrm{d}\tau \, \rho_3(\tau)\, \epsilon(\tau)\, \mathcal{I}(\tau; \{\mathcal{T}_a^{r\varepsilon}\}). \tag{3.52}$$

Using Eqs. (3.51) and (3.52), we can construct the extended likelihood function for our PWA model analogous to Eq. (3.50):

$$\mathcal{L}_{\text{ext}}(\{\mathcal{T}_a^{r\varepsilon}\}; \{\tau_k\}, N) = \frac{\overline{N}^N \, e^{-\overline{N}}}{N!} \prod_{k=1}^{N} \frac{\rho_3(\tau_k)\, \epsilon(\tau_k)\, \mathcal{I}(\tau_k; \{\mathcal{T}_a^{r\varepsilon}\})}{\int \mathrm{d}\tau \, \rho_3(\tau)\, \epsilon(\tau)\, \mathcal{I}(\tau; \{\mathcal{T}_a^{r\varepsilon}\})}. \tag{3.53}$$

[r] The term acceptance is used here in a broad sense and includes all effects that affect the detection efficiency such as the geometry of the detector setup and the efficiencies of the detectors, of the reconstruction, and of the event selection.

[s] Depending on the detector setup, the acceptance might depend on additional kinematic variables. Here, ϵ represents the acceptance integrated over all these additional variables.

In order to find the maximum likelihood estimate for the set $\{\mathcal{T}_a^{r\varepsilon}\}$ of the transition amplitudes, we have to maximize Eq. (3.53) with respect to these parameters. Since the value of the likelihood function at the maximum is irrelevant for the parameter estimation, we can simplify the expression for $\mathcal{L}_{\text{ext}}$ by dropping all constant factors that do not depend on the transition amplitudes. It is also convenient to consider the logarithm of $\mathcal{L}_{\text{ext}}$. Since the logarithm is a strictly monotonous function, it leaves the position of the maximum of $\mathcal{L}_{\text{ext}}$ in the space of the transition amplitudes unchanged. However, the logarithm converts the product over the measured events into a sum and makes the expression hence numerically easier to treat. Using Eqs. (3.47) and (3.52), we arrive at the final expression of the likelihood function that is maximized in order to estimate the transition amplitudes

$$
\begin{aligned}
&\ln \mathcal{L}_{\text{ext}}(\{\mathcal{T}_a^{r\varepsilon}\};\{\tau_k\},N) \\
&= \sum_{k=1}^{N} \ln \mathcal{I}(\tau_k;\{\mathcal{T}_a^{r\varepsilon}\}) - \overline{N}(\{\mathcal{T}_a^{r\varepsilon}\}) \\
&= \sum_{k=1}^{N} \ln \left[\sum_{\varepsilon=\pm 1} \sum_{r=1}^{N_r^\varepsilon} \left| \sum_{a}^{N_{\text{waves}}^\varepsilon} \mathcal{T}_a^{r\varepsilon}\, \Psi_a^\varepsilon(\tau_k) \right|^2 + |\mathcal{T}_{\text{flat}}|^2 \right] \\
&\quad - \sum_{\varepsilon=\pm 1} \sum_{r=1}^{N_r^\varepsilon} \sum_{a,b}^{N_{\text{waves}}^\varepsilon} \mathcal{T}_a^{r\varepsilon}\, \mathcal{T}_b^{r\varepsilon *} \underbrace{\int \mathrm{d}\tau\, \rho_3(\tau)\, \epsilon(\tau)\, \Psi_a^\varepsilon(\tau)\, \Psi_a^{\varepsilon *}(\tau)}_{\equiv\, {}^{\text{acc}}I_{ab}^\varepsilon} - |\mathcal{T}_{\text{flat}}|^2 \underbrace{\int \mathrm{d}\tau\, \rho_3(\tau)\, \epsilon(\tau)}_{\equiv\, {}^{\text{acc}}I_{\text{flat}}}.
\end{aligned}
\tag{3.54}
$$

Since the transition amplitudes are not a function of τ, they can be pulled out of the normalization integral. In Eq. (3.54), this leads to an integral matrix ${}^{\text{acc}}I_{ab}^\varepsilon$ that is similar to the integral matrix I_{ab}^ε in Eq. (3.42). The difference between the two is that in ${}^{\text{acc}}I_{ab}^\varepsilon$ the integration is performed over the accepted phase space. If the decay amplitudes do not contain any free fit parameters, we can calculate the decay amplitudes as well as the integral matrices I_{ab}^ε and ${}^{\text{acc}}I_{ab}^\varepsilon$ using Monte Carlo integration techniques before maximizing the likelihood function. Since in particular the integral matrices are computationally very expensive, this reduces the time to compute the likelihood function by several orders of magnitude. It is only due to this fact that the maximization procedure becomes actually feasible in terms of computational resources. However, allowing no free parameters in the decay amplitudes is a severe limitation and source of important systematic uncertainties. This is discussed further in Sec. 3.3.7. This also means that in particular the dynamical amplitudes of all isobars in the model have to be known. In Sec. 3.3.8 we discuss a novel method that circumvents most of these issues.

3.3.6 Observables

The spin-density matrices ϱ_{ab}^ε, which are extracted from the data by maximizing the likelihood function in Eq. (3.54) in the (m_X, t') cells, contain all information obtainable about the intermediate states X. Based on $\varrho_{ab}^\varepsilon(m_X, t')$, we can define a number of observables that are useful to characterize the result of a partial-wave decomposition and to search for resonance signals.

In Eq. (3.46), we defined the number of produced events $N_{\text{pred}}(m_X, t')$ that the model predicts for the given (m_X, t') cell. This number can be expressed in terms of the *partial-wave*

intensities,

$$\text{int}_a^\varepsilon(m_X, t') \equiv \varrho_{aa}^\varepsilon(m_X, t') = \sum_{r=1}^{N_r^\varepsilon} \left|\mathcal{T}_a^{r\varepsilon}(m_X, t')\right|^2, \tag{3.55}$$

and the *overlaps*,

$$\text{ovl}_{ab}^\varepsilon(m_X, t') \equiv 2\,\text{Re}\left[\varrho_{ab}^\varepsilon(m_X, t')\,\frac{I_{ab}^\varepsilon(m_X)}{\sqrt{I_{aa}^\varepsilon(m_X)\,I_{bb}^\varepsilon(m_X)}}\right], \tag{3.56}$$

of all pairs of waves, i.e.,

$$N_\text{pred}(m_X, t') = \sum_{\varepsilon=\pm1}\left\{\sum_a^{N_\text{waves}^\varepsilon} \text{int}_a^\varepsilon(m_X, t') + \sum_{a,b;a<b}^{N_\text{waves}^\varepsilon} \text{ovl}_{ab}^\varepsilon(m_X, t')\right\} + \text{int}_\text{flat}(m_X, t'). \tag{3.57}$$

It is often useful to limit the sums in Eq. (3.57) to a selected subset $\mathbb{S}$ of partial waves. In this case, Eq. (3.57) yields the number of produced events $N_\text{pred}^\mathbb{S}$ in these waves in the given (m_X, t') cell. This number takes into account all mutual interference terms of the waves in $\mathbb{S}$. For example, it is often interesting to calculate the number of events in subsets of waves that have the same $J^{PC}\,M^\varepsilon$ quantum numbers but different decay chains. Studying these so-called *spin totals* as a function of m_X and/or t' often better reveals possible resonance signals because statistical fluctuations are reduced.

The partial-wave intensities in Eq. (3.55) correspond to the diagonal elements of the spin-density matrix. Due to the chosen normalization (see Secs. 3.3.4 and 3.3.5), the intensities are given in terms of number of produced events in wave a with reflectivity ε. If a resonance is present in a partial wave, the m_X dependence of the intensity of this waves often exhibits a Breit-Wigner-shaped peak similar to the one shown in Fig. 1.7(a).

The contribution of an individual partial wave to the data sample is often quantified by the *relative intensity*, which is defined as the ratio of the partial-wave intensity $\text{int}_a^\varepsilon(m_X, t')$ in Eq. (3.55) and the total number of produced events $N_\text{pred}(m_X, t')$ in Eq. (3.57).[t] Often, the relative intensity is calculated by summing both quantities over the same m_X and/or t' range:

$$\text{relint}_a^\varepsilon \equiv \frac{\sum_{m_X\text{ bins}}\sum_{t'\text{ bins}} \text{int}_a^\varepsilon(m_X, t')}{\sum_{m_X\text{ bins}}\sum_{t'\text{ bins}} N_\text{pred}(m_X, t')}. \tag{3.58}$$

Although the relative intensity of a given wave includes—where applicable—the effect of self-interference due to Bose symmetrization (see Sec. 3.2.1.3), it does *not* include the interference effects of this wave with any of the other waves, i.e., the overlaps. Consequently, the relative intensities of all waves in the PWA model will in general not sum to unity. The difference of this sum from unity is a measure for the overall strength of the interference in the model.

[t] The relative intensities are equivalent to the *fit fractions* often quoted for Dalitz-plot analyses.

Another important observable is the relative phase $\Delta\phi^{\varepsilon}_{ab}(m_X, t')$ between two waves a and b with reflectivity ε. It is given by the corresponding off-diagonal element of the spin-density matrix:

$$\Delta\phi^{\varepsilon}_{ab}(m_X, t') \equiv \arg\big[\varrho^{\varepsilon}_{ab}(m_X, t')\big], \tag{3.59}$$

i.e.,

$$\varrho^{\varepsilon}_{ab}(m_X, t') = \big|\varrho^{\varepsilon}_{ab}(m_X, t')\big|\, e^{i\,\Delta\phi^{\varepsilon}_{ab}(m_X, t')}.$$

Note that for $N^{\varepsilon}_r = 1$, i.e., full coherence of all partial waves,

$$\Delta\phi^{\varepsilon}_{ab}(m_X, t') = \arg\big[\mathcal{T}^{\varepsilon}_a(m_X, t')\big] - \arg\big[\mathcal{T}^{\varepsilon}_b(m_X, t')\big]. \tag{3.60}$$

If a resonance is present in a partial wave, the phase relative to a second wave that has no resonance grows with rising m_X by about 180° across the resonance, i.e., the partial wave exhibits a phase motion.[u] Figure 1.7(b) shows, as an example, the phase motion of a Breit-Wigner resonance.

It is important to note that although the overlap $\text{ovl}^{\varepsilon}_{ab}$ between two waves may be zero because of the orthogonality of the decay amplitudes, the corresponding off-diagonal element $\varrho^{\varepsilon}_{ab}$ of the spin-density matrix in general does not vanish. Therefore, the two waves still have a well-defined phase, which characterizes their interference. Since the spin-density matrix has a block-diagonal structure with respect to the reflectivity, partial-wave amplitudes with opposite ε do not interfere. Thus relative phases between such waves are undefined.

3.3.7 Discussion of the partial-wave analysis model

The PWA model presented in Secs. 3.2 and 3.3 makes a number of assumptions that have practical consequences. Here, we focus on those aspects that are most relevant for the interpretation of the results that will be presented in Chapter 4. Further details are discussed, e.g., in Ref. [87].

An important practical issue is the truncation of the partial-wave expansion in Eq. (3.47), i.e., the decision which waves to include in the PWA model and which ones to leave out. Although the quantum numbers of the most dominantly produced intermediate states X may be known from previous experiments, in situations where the analyzed data set is about an order of magnitude larger than any of the existing ones—like it is the case for the COMPASS $\pi^-\pi^-\pi^+$ data—this knowledge is not sufficient to construct a realistic PWA model.

In contrast to s-channel processes, where the maximum spin of the intermediate state is limited by the breakup momentum and therefore by the center-of-mass energy, in high-energy t-channel exchange processes in principle arbitrarily high spins can be produced. Even though the production of intermediate states is expected to be suppressed with increasing spin, there is no clear cut-off. This problem is aggravated by contributions from non-resonant processes. Irreducible and interfering contributions from these processes are often contained in the data. For t-channel exchange processes, the largest non-resonant contributions come from so-called double-Regge exchange processes. Figure 3.5 shows

[u] If the second wave also contains a resonance, the phase motion might be reduced or even completely compensated if the two resonances have similar masses and widths.

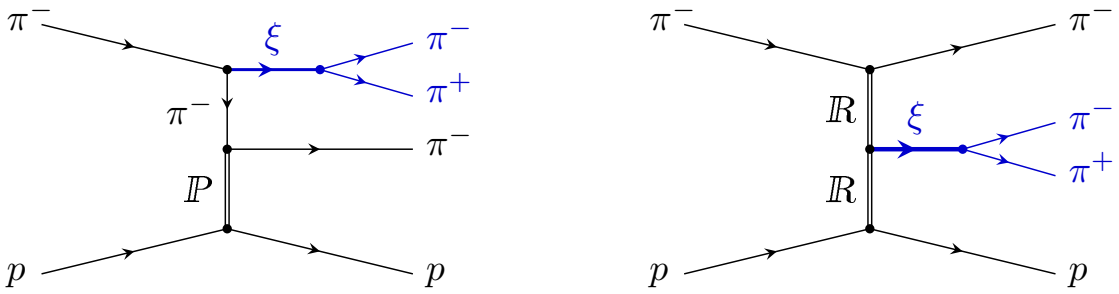

(a) **(b)**

Figure 3.5: Examples for irreducible non-resonant contributions to diffractive production of 3π on a proton target. (a) Process proposed by R. T. Deck [110], where the beam pion dissociates into a $\pi^-\pi^+$ isobar ξ and a bachelor π^-, followed by diffractive scattering of the π^- off the target proton. (b) Central production, where the beam and target particles scatter elastically via exchange of Reggeons, which fuse to produce a $\pi^-\pi^+$ system.

two examples for such processes, the *Deck process* and the *central production* process, for $\pi^-\pi^-\pi^+$ production. Since in these processes, no 3π intermediate states with well-defined quantum numbers appear, the non-resonant contributions project into all partial waves. Some high-spin partial waves are even dominated by non-resonant contributions. Such waves are important in order to describe the data but are uninteresting when it comes to extracting resonances. So, in addition to estimating the transition amplitudes from the data as described in Sec. 3.3.5, one also needs to determine the set $\{a\}$ of partial waves that enters in Eq. (3.47) from the data. The analysis problem hence turns into a more difficult model-selection problem, which is complicated by the correlations of the partial-wave amplitudes due to their mutual interference.

Another important ingredient of the PWA model that is part of the model-selection problem is the set of isobar resonances. Although signals in the invariant mass distributions of the respective subsystems of the final-state particles help to identify the contributing isobars (see, e.g., Fig. 2.6(b)), this information is in some cases not enough to unambiguously identify all isobars.[v] As explained in Sec. 3.3.5, the decay amplitudes must not have any free parameters because otherwise the computation of the likelihood function becomes very expensive. Thus we do not only have to decide which isobar resonances to include in the PWA model but also which parametrizations and resonance parameters describe them best. The model building hence requires input from other measurements. In most cases, the dynamical amplitudes of the isobar resonances are approximated by Breit-Wigner amplitudes as in Eqs. (1.24) and (1.25) and the PDG world averages are used for the resonance parameters. However, for some isobar resonances, the parameters are not precisely known and/or it is unclear which parametrization to use for the dynamical amplitude. For example, the isoscalar resonances with $J^{PC} = 0^{++}$ quantum numbers, i.e., the f_0 states, that appear in the $\pi^-\pi^+$ subsystems of the $\pi^-\pi^-\pi^+$ final state are notoriously difficult to describe. When analyzing high-precision data, the issue is exacerbated by possible effects from final-state interactions, which may distort the effective dynamical amplitudes of the isobar resonances.

[v] For example, some isobar resonances have different quantum numbers but similar resonance parameters and therefore may appear as indistinguishable peaks in the invariant mass distribution. In addition, broad isobars and/or isobars that contribute only weakly to the data are difficult to find in the invariant mass distribution.

The limitation of the conventional PWA approach to parameter-free decay amplitudes makes it very difficult to implement and test models that take into account such effects. A crude way of checking, whether the used parameters of the isobar resonances deviate from the data, are so-called likelihood scans. In this method, one performs several PWA fits with different values of selected isobar parameters and compares the maximum values of the likelihood function for each parameter set. Using the asymptotic normality of the maximum of the likelihood function in terms of the resonance parameters, one can estimate isobar parameters that better fit the data. However, this method is practical only for a few free parameters [111]. A more model-independent approach that is able to extract the amplitudes of subsystems with well-defined quantum numbers from the data is presented in Sec. 3.3.8.

Another issue that complicates the wave-set selection is the non-orthogonality of some partial-wave amplitudes. Since the Wigner D-functions that are contained in the decay amplitudes in Eqs. (3.18) and (3.19) are orthogonal, the off-diagonal elements of the phase-space integral matrix I^{ε}_{ab} in Eq. (3.42) vanish, i.e., the amplitudes are orthogonal, unless the waves a and b have the same $J^{PC}\,M^{\varepsilon}$ quantum numbers. In the latter case, amplitudes may not be orthogonal. A simple example would be two waves that have isobars with the same $J^{PC}\,M^{\varepsilon}$ quantum numbers and the same orbital angular momentum between the isobar and the bachelor pion, such as $1^{++}\,0^{+}\,f_0(980)\,\pi$ and $f_0(1500)\pi$ P-waves. A measure for the non-orthogonality are the normalized off-diagonal elements of the integral matrix in Eq. (3.42):

$$ {}^{\text{norm}}I^{\varepsilon}_{ab}(m_X) \equiv \frac{I^{\varepsilon}_{ab}(m_X)}{\sqrt{I^{\varepsilon}_{aa}(m_X)}\,\sqrt{I^{\varepsilon}_{bb}(m_X)}}. \tag{3.61} $$

This matrix is actually a Gram matrix for the scalar product between two partial-wave amplitudes that is represented by the phase-space integral in Eq. (3.42). If the magnitude of an off-diagonal element of ${}^{\text{norm}}I^{\varepsilon}_{ab}$ would be unity, this would mean that the corresponding partial-wave amplitudes are mathematically indistinguishable, i.e., linearly dependent. A PWA model containing such a pair of waves would be ill-defined and would lead to unphysical fit results for the corresponding waves. In practice, due to the finiteness of the measured data set, such distinguishability issues may already arise for waves that have $\left|{}^{\text{norm}}I^{\varepsilon}_{ab}\right|$ close to unity. This is usually the case for wave sets that include excited states of isobars. At low m_X, i.e., well below the nominal masses of a ground-state isobar and its radial excitation, the dynamical amplitudes of the two isobar resonances are nearly constant and hence very similar. In this case, waves with the same quantum numbers have large $\left|{}^{\text{norm}}I^{\varepsilon}_{ab}\right|$. This is a general problem that always appears when an isobar and its radial excitation are included in the PWA model. In order to resolve the arising ambiguities, one usually makes the PWA model discontinuous in m_X, i.e., one introduces m_X thresholds, below which certain waves are excluded from the PWA model. This means, in practice one would exclude waves with radially excited isobars at low masses. Thus we have to determine the wave set in principle for each m_X bin individually. This also takes into account the different sizes of the data samples in the various m_X bins.[w]

Up to now, the wave-set selection was performed "by hand", i.e., by starting with a larger wave set that is constructed based on previous experiments and educated guess and then removing step-by-step waves with small intensities. Although for many waves the

[w] In principle the wave set also depends on t' because waves with spin projections $M > 0$ are suppressed toward low t' (see Sec. 3.4.2).

results are satisfactory (as will be shown in Chapter 4), this approach has a number of caveats and limitations. For large data sets that usually require large wave sets, it is not a well-defined procedure and is hence prone to observer bias and difficult to document and reproduce. It is also often very time consuming. In addition, systematic uncertainties due to the choice of the wave set are difficult to estimate reliably.

A more systematic approach that is currently under study is the *regularization* of the log-likelihood function in Eq. (3.54). This means that one adds an additional regularization term to the log-likelihood function that introduces additional constraints on the fit parameters, i.e.,

$$\ln \widetilde{\mathcal{L}}(\{\mathcal{T}_a^{r\varepsilon}\}) = \ln \mathcal{L}_{\text{ext}}(\{\mathcal{T}_a^{r\varepsilon}\}) + \ln \mathcal{L}_{\text{reg}}(\{\mathcal{T}_a^{r\varepsilon}\}). \tag{3.62}$$

The idea is to perform the maximization of the regularized log-likelihood function $\ln \widetilde{\mathcal{L}}(\{\mathcal{T}_a^{r\varepsilon}\})$ using a large, systematically constructed set of all possible partial waves up to a cut-off criterion and to choose the regularization term $\ln \mathcal{L}_{\text{reg}}(\{\mathcal{T}_a^{r\varepsilon}\})$ such that partial-wave amplitudes that are statistically consistent with zero are suppressed, while partial-wave amplitudes far away from zero are influenced only negligibly. This way, one could determine from the data the smallest wave set that describes the data well.

Up to now several such approaches were studied using Monte Carlo pseudodata with known partial-wave content. The authors of Ref. [112] applied the so-called LASSO method,[x] where $\mathcal{L}_{\text{reg}}$ has Laplacian form in $\left|\mathcal{T}_a^{r\varepsilon}\right|$, so that

$$\ln \mathcal{L}_{\text{reg}}(\{\mathcal{T}_a^{r\varepsilon}\}) = -\lambda \sum_{\varepsilon=\pm 1} \sum_{r=1}^{N_r^\varepsilon} \sum_{a}^{N_{\text{waves}}^\varepsilon} \left|\mathcal{T}_a^{r\varepsilon}\right|. \tag{3.63}$$

This effectively suppresses partial waves with small intensities but also biases partial waves with large intensities. We studied independently the regularization using a Cauchy form in $\left|\mathcal{T}_a^{r\varepsilon}\right|$ for $\mathcal{L}_{\text{reg}}$ [114–116], i.e.,

$$\ln \mathcal{L}_{\text{reg}}(\{\mathcal{T}_a^{r\varepsilon}\}) = -\sum_{\varepsilon=\pm 1} \sum_{r=1}^{N_r^\varepsilon} \sum_{a}^{N_{\text{waves}}^\varepsilon} \ln \left[1 + \frac{\left|\mathcal{T}_a^{r\varepsilon}\right|^2}{\Gamma^2}\right]. \tag{3.64}$$

This term pulls the amplitudes of partial waves with small intensities toward zero, but leaves the waves with large intensities nearly unaffected.

Both regularization approaches give promising results when applied to Monte Carlo pseudodata. The application to real data is currently under study. A general problem is that the regularization terms have parameters, i.e., λ in Eq. (3.63) and Γ in Eq. (3.64) that need to be defined. Reference [112] proposes to apply information criteria in order to find the optimum values for these parameters, but more studies are needed to verify that these criteria are applicable. Currently, the regularization of the likelihood function seems to be a promising approach. The method makes the wave-set selection reproducible and the bias that is introduced by the regularization term explicit. By applying different regularization terms and parameter values, one can study the wave-set dependence of the PWA result. The method makes it also possible to study, for example, the dependence of the PWA result on the set of isobars, on the parametrizations of the dynamical amplitudes of the isobar resonances, and on the inclusion of partial waves with higher spin. Such studies are usually not practical when selecting the wave set "by hand".

[x] LASSO stands for "least absolute shrinkage and selection operator" and is a regularization method that was first proposed by R. Tibshirani in Ref. [113].

3.3.8 Freed-isobar partial-wave analysis

As discussed in Sec. 3.3.5, in the conventional PWA method the decay amplitudes must not have any free parameters, otherwise the computation of the likelihood function would become too expensive. Consequently, the choice of the parametrizations and parameters of the dynamical amplitudes of the isobar resonances induces significant systematic uncertainties that are difficult to estimate (see also Sec. 3.3.7). In order to circumvent these limitations and render the analysis less model-dependent, we developed the novel so-called freed-isobar PWA method, which was inspired by the so-called model-independent partial-wave analysis method developed by the authors of Ref. [117] in order to study three-body decays of heavy mesons. Here, we briefly sketch the method for a rank-1 spin-density matrix based on the $\pi^-\pi^-\pi^+$ final state. More details can be found in Refs. [94, 118, H2].

The conventional PWA model uses fixed parametrizations for the dynamical amplitude $\Delta_\xi(m_\xi)$ of the $\pi^-\pi^+$ isobar resonances ξ in order to calculate the decay amplitude in Eq. (3.18). To simplify notation, we assume that m_X is constant and omit all constant and m_X-dependent factors that are irrelevant because of the normalization in Eq. (3.43). Hence we rewrite Eq. (3.18) as

$$\Psi_a^\varepsilon(\vartheta_{\text{GJ}}, \phi_{\text{GJ}}, m_\xi, \vartheta_{\text{HF}}, \phi_{\text{HF}}) = \Delta_\xi(m_\xi)\, F_{J_\xi}(m_\xi)\, \mathcal{K}_a^\varepsilon(\Omega_{\text{GJ}}, \Omega_{\text{HF}}). \tag{3.65}$$

Here, the $\Delta_\xi(m_\xi)$ is the dynamical amplitude of ξ and $F_{J_\xi}(m_\xi)$ is the centrifugal-barrier factor for the ξ decay. The amplitude $\mathcal{K}_a^\varepsilon(\Omega_{\text{GJ}}, \Omega_{\text{HF}})$ collects all terms that depend on the angles $\Omega_{\text{GJ}} \equiv (\cos\vartheta_{\text{GJ}}, \phi_{\text{GJ}})$ in the Gottfried-Jackson frame and the angles $\Omega_{\text{HF}} \equiv (\cos\vartheta_{\text{HF}}, \phi_{\text{HF}})$ in the helicity frame. Taking into account the Bose symmetrization of the two π^- in the final state according to Eq. (3.19), the decay amplitude in a particular m_X bin is

$$\begin{aligned}\Psi_a^\varepsilon(\tau_{13}, \tau_{23}) = \frac{1}{\sqrt{2}} \Big[&\Delta_\xi(m_{13})\, F_{J_\xi}(m_{13})\, \mathcal{K}_a^\varepsilon(\Omega_{13}^{\text{GJ}}, \Omega_{13}^{\text{HF}}) \\ &+ \Delta_\xi(m_{23})\, F_{J_\xi}(m_{23})\, \mathcal{K}_a^\varepsilon(\Omega_{23}^{\text{GJ}}, \Omega_{23}^{\text{HF}}) \Big].\end{aligned} \tag{3.66}$$

The two terms in this equation represent the two possible $\pi^-\pi^+$ combinations of the $\pi_1^-\pi_2^-\pi_3^+$ system. The index a defined in Eq. (3.9) represents the full set of quantum numbers of the 3π partial wave, which includes the quantum numbers of the $\pi^-\pi^+$ subsystem ξ.

In our novel *freed-isobar method*, we replace the fixed parametrizations for $\Delta_\xi(m_\xi)$ by a set of piecewise constant amplitudes that fully cover the allowed mass range for m_ξ, i.e.,

$$\Delta_a^\varepsilon(m_\xi) = \sum_k^{m_\xi \text{ bins}} \mathcal{T}_{a,k}^\varepsilon\, \Pi_{k,\xi}(m_\xi), \tag{3.67}$$

where the index k runs over the $\pi^-\pi^+$ mass bins. The m_ξ bins are defined by sets of window functions $\{\Pi_{k,\xi}(m_\xi)\}$ that are non-zero only in a narrow m_ξ interval given by the bin borders $\{m_{\xi,k}\}$:

$$\Pi_{k,\xi}(m_\xi) = \begin{cases} 1 & \text{if } m_{\xi,k} \leq m_\xi < m_{\xi,k+1}, \\ 0 & \text{otherwise.} \end{cases} \tag{3.68}$$

Here, the bin width $\delta m_\xi = m_{\xi,k+1} - m_{\xi,k}$ may depend on the mass region of the $\pi^-\pi^+$ system. The $\{\mathcal{T}_{a,k}^\varepsilon\}$ are a set of unknown complex numbers that together determine

the freed-isobar amplitude $\Delta_a^\varepsilon(m_\xi)$. This approach is conceptually similar to the binning already performed in m_X and t'. Note that $\Delta_a^\varepsilon(m_\xi)$ depends on the 3π partial-wave index a and the reflectivity ε, i.e., the model permits different freed-isobar amplitudes for different intermediate states X^-. This is in contrast to the conventional PWA approach, where the *same* isobar parametrization is used in all partial-wave amplitudes, where this isobar appears. Since the analysis is performed independently in (m_X, t') cells, the freed-isobar amplitude is also allowed to change as a function of m_X and t'.

For a given (m_X, t') cell, the model for the intensity in Eq. (3.47) contains terms of the form[y]

$$\begin{aligned}\mathcal{T}_a^\varepsilon \, \Psi_a^\varepsilon(\tau_{13}, \tau_{23}) = \mathcal{T}_a^\varepsilon \Bigg\{ \Bigg[\sum_k^{m_\xi \text{ bins}} \mathscr{T}_{a,k} \, \Pi_{k,\xi}(m_{13}) \Bigg] \, F_{J_\xi}(m_{13}) \, \mathcal{K}_a^\varepsilon(\Omega_{13}^{\text{GJ}}, \Omega_{13}^{\text{HF}}) \\ + \Bigg[\sum_k^{m_\xi \text{ bins}} \mathscr{T}_{a,k} \, \Pi_{k,\xi}(m_{23}) \Bigg] \, F_{J_\xi}(m_{23}) \, \mathcal{K}_a^\varepsilon(\Omega_{23}^{\text{GJ}}, \Omega_{23}^{\text{HF}}) \Bigg\},\end{aligned} \tag{3.69}$$

where we have used Eqs. (3.66) and (3.67). We absorb the unknown amplitudes $\mathscr{T}_{a,k}^\varepsilon$ into the transition amplitude $\mathcal{T}_a^\varepsilon$ via the redefinition

$$\mathcal{T}_{a,k}^\varepsilon \equiv \mathcal{T}_a^\varepsilon \, \mathscr{T}_{a,k}^\varepsilon. \tag{3.70}$$

Note that now the transition amplitudes also depend on the m_ξ bin index k. Using this equation, we can write the intensity as

$$\mathcal{I}(\tau) = \sum_{\varepsilon=\pm 1} \left| \sum_a^{N_{\text{waves}}^\varepsilon} \sum_k^{m_\xi \text{ bins}} \mathcal{T}_{a,k}^\varepsilon \, \Psi_{a,k}^\varepsilon(\tau_{13}, \tau_{23}) \right|^2 + |\mathcal{T}_{\text{flat}}|^2, \tag{3.71}$$

where

$$\begin{aligned}\Psi_{a,k}^\varepsilon(\tau_{13}, \tau_{23}) \equiv F_{J_\xi}(m_{13}) \, \mathcal{K}_a^\varepsilon(\Omega_{13}^{\text{GJ}}, \Omega_{13}^{\text{HF}}) \, \Pi_{k,\xi}(m_{13}) \\ + F_{J_\xi}(m_{23}) \, \mathcal{K}_a^\varepsilon(\Omega_{23}^{\text{GJ}}, \Omega_{23}^{\text{HF}}) \, \Pi_{k,\xi}(m_{23}).\end{aligned} \tag{3.72}$$

The additional coherent sum over the m_ξ bin index k in Eq. (3.71) appears in the same way as the sum over the partial-wave index a. This means that each m_ξ mass bin k can be treated like an independent partial wave. Thus by defining a new freed-isobar partial-wave index $\widetilde{a} \equiv \{a, k\}$, Eq. (3.71) becomes mathematically equivalent to Eq. (3.47). This means that exactly the same maximum likelihood fit procedure as described in Sec. 3.3.5 can be employed to determine the $\{\mathcal{T}_{a,k}^\varepsilon\}$. This also includes the pre-calculation of the integral matrices of the decay amplitudes. It is actually this fact that makes the freed-isobar approach practically applicable, while allowing free parameters in the dynamical isobar amplitudes is usually prohibitively expensive. Depending on how many decay amplitudes are parametrized using the freed-isobar amplitude in Eq. (3.67) and how many m_ξ bins are used for the freed-isobar amplitudes, the computation cost for a freed-isobar PWA grows only moderately by less than an order of magnitude.

Performing such a freed-isobar PWA in (m_X, t') cells, yields transition amplitudes $\mathcal{T}_a^\varepsilon(m_X, t', m_\xi)$ that now depend not only on m_X and t' but also on m_ξ. According to

[y] Since we are considering a rank-1 spin-density matrix, we leave off the rank index r.

Eq. (3.70), a freed-isobar transition amplitude contains information on the 3π system as well as on the $\pi^-\pi^+$ subsystem. For each freed-isobar wave and each (m_X, t') cell, the method yields an Argand diagram ranging in m_ξ from $2m_\pi$ to $m_X - m_\pi$. It is important to note that by parametrizing the m_ξ dependence of the decay amplitude for a wave a by Eq. (3.67), we do not make any assumptions about the resonance content of the $\pi^-\pi^+$ subsystem. The freed-isobar PWA allows us to determine from the data the overall amplitude of all $\pi^-\pi^+$ intermediate states with given J^{PC} quantum numbers in the 3π partial wave defined by a. This amplitude hence includes all $\pi^-\pi^+$ resonances, potential non-resonant contributions, as well as distortions due to final-state interactions. The reduced model dependence of the freed-isobar method and the additional information about the $\pi^-\pi^+$ subsystem come at the price of a considerably larger number of fit parameters compared to the conventional PWA. Thus even for large data sets, the freed-isobar approach can only be applied to a subset of the partial waves in the PWA model. For the other partial waves, the conventional fixed isobar parametrizations are used.

An additional complication arises if a freed-isobar PWA model contains more than one freed-isobar partial wave with the same $J^{PC}\,M^\varepsilon$ quantum numbers. In this case, mathematical ambiguities, so-called zero modes, may arise at the amplitude level. How to identify and resolve these ambiguities is described in Refs. [94, 118].

3.4 Stage II: resonance-model fit

The first analysis stage, i.e., the partial-wave decomposition of the data as described in Sec. 3.3, yields as a result the spin-density matrices ϱ^ε_{ab} in the (m_X, t') cells. This set of spin-density matrices is the input for the second analysis stage, where we want to identify 3π resonances that contribute to certain partial-wave amplitudes and determine their parameters. To this end, we formulate a model $\widehat{\varrho}^\varepsilon_{ab}(m_X, t')$[z] that describes the dependence of the spin-density matrix elements on m_X and t' in terms of resonant and non-resonant components. The parameters and yields of the resonances included in the model are determined by a fit to the measured spin-density matrices. In this *resonance-model fit*, which is also sometimes referred to as *mass-dependent fit*, we exploit that resonances have a characteristic signature. In the simplest case, they appear as Breit-Wigner-shaped peaks in the partial-wave intensities that are accompanied by 180° phase motions relative to non-resonating waves (see Sec. 1.6.1 and Fig. 1.7). In reality, this simple picture often does not hold. The behavior of the spin-density matrix elements is usually more complicated because multiple resonances, e.g., ground state plus radially excited states, may appear in a given partial wave. In general, the resonances overlap and interfere so that resonance peaks might shift, disappear, or—in the case of destructive interference—might even turn into dips in the intensity distribution. In diffractive dissociation reactions, this interference pattern is further complicated by additional coherent contributions from non-resonant processes like the Deck effect or central production (see Sec. 3.3.7 and Fig. 3.5). The different t' dependences of these contributions lead to t'-dependent interference patterns. Hence in many cases, the information from partial-wave intensities alone is insufficient to extract resonances and their parameters reliably from the data. It is therefore a great advantage that the partial-wave decomposition is performed at the amplitude level because the parameters of the resonances are constrained not only by the measured intensities of

[z] In the following text, modeled quantities are distinguished from their measured counterparts by a hat ("$\widehat{\ }$").

the partial waves but also by their mutual interference terms. This greatly improves the sensitivity for potential resonance signals.

When searching for resonance signals in the partial-wave amplitudes, one has to take into account that similar to the resonance peaks in the intensity distributions also the phase motions are distorted by the presence of other resonances. If, for example, waves a and b with reflectivity ε each contain a resonance, the rising motion of their relative phase $\Delta\phi^{\varepsilon}_{ab}(m_X)$ (see Eq. (3.59) and Fig. 1.7(b)) due to the resonance in a may be compensated partly by the falling motion due to the resonance in b. In the extreme case when the two resonances have similar parameters, this cancellation may become nearly complete. It is therefore often difficult to observe undisturbed phase motions of resonances. This effect is particularly pronounced in the high-mass regions, where broad excited states appear in most or even all waves in the resonance-model fit.

An advantage of the two-stage analysis approach is that the resonance model does not need to describe all partial-wave amplitudes that are included in the PWA model. The representation of the data in terms of the spin-density matrix allows us to model only selected matrix elements. Usually, one selects a subset of waves and models all elements of the corresponding spin-density submatrix. This is an important point for the $\pi^-\pi^-\pi^+$ final state analyzed here. As is discussed in Sec. 4.1, the wave set used for the partial-wave decomposition is so large that a simultaneous description off all partial waves by a resonance model would be practically impossible.

3.4.1 Resonance model

The spin-density matrix elements are given via by the transition amplitudes $\{\mathcal{T}^{r\varepsilon}_a(m_X, t')\}$ (see Eq. (3.45)), which are the actual fit parameters in the PWA fit described in Sec. 3.3.5. The transition amplitudes describe the production and propagation of the intermediate states X with quantum numbers defined by the wave index a and the reflectivity ε. A transition amplitude may contain contributions from several resonances and from non-resonant processes. All these *wave components* may interfere. Consequently, their amplitudes have to be summed coherently. If we assume that resonances dominate the transition amplitudes, we can exploit the fact that for a resonance production and propagation are independent. We can hence factorize the amplitude that describes a resonance that is represented by an index k in a partial wave defined by a and ε into two parts: (i) an amplitude $\widetilde{\mathcal{C}}^{r\varepsilon}_{ki}(m_X, t')$ that describes the production of resonance k with quantum numbers defined by i (see Eq. (3.7)) and ε and (ii) a dynamical amplitude $\Delta_k(m_X)$ that describes the propagation of resonance k. Using this ansatz, we can formulate the model for the transition amplitudes:

$$\widehat{\mathcal{T}}^{r\varepsilon}_a(m_X, t') = \sqrt{m_X}\,\sqrt{I^{\varepsilon}_{aa}(m_X)}\,\alpha^k_a \sum_{k\,\in\,\mathbb{S}_a} \widetilde{\mathcal{C}}^{r\varepsilon}_{ki}(m_X, t')\,\Delta_k(m_X;\zeta_k). \tag{3.73}$$

Here, the factor $\sqrt{m_X}$ is due to the splitting of the four-body phase space of the final-state particles (see Eq. (3.5)). The diagonal element I^{ε}_{aa} of the integral matrix of the decay amplitudes (see Eq. (3.42)) appears because of the chosen normalization of the transition amplitudes in Eq. (3.44). The factor α^k_a is the product of the unknown couplings at the two-body decay vertices as defined in Eq. (3.21) and appears due to Eq. (3.22). Note that this product of couplings now also depends on the wave component index k. The amplitudes of the wave components are summed coherently. The same wave component k, e.g., a resonance, may appear in several waves. Hence the sum in Eq. (3.73) runs over

the set $\mathbb{S}_a$ of those wave components that we assume to appear in wave a. The dynamical amplitudes each depend on a set of *shape parameters* that we denote by ζ_k. For example, in the case of a Breit-Wigner resonance, ζ_k represents mass and width of that resonance. It is important to note that the dynamical amplitudes and their shape parameters do not depend on the partial-wave index a. Hence if a wave component Δ_k appears in several partial waves, which, e.g., represent different decay modes of a resonance, the same shape parameters ζ_k, e.g., mass and width of this resonance, are used in these waves.

Usually, the amplitudes $\widetilde{\mathcal{C}}^{r\varepsilon}_{ki}(m_X, t')$ that describe the production of wave component k in Eq. (3.73) are only partly known. Using Regge theory (see Sec. 2.1), one can calculate an approximate amplitude $\mathcal{P}^{\varepsilon}(m_X, t')$ that at least models the average production probability of an intermediate state with mass m_X as a function of t'. Hence this amplitude does not depend on the wave index a, but it depends in the most general case on the reflectivity ε. This is because different values of ε correspond to different exchange particles. In a simple approach based on Ref. [119], the production probability is given by

$$|\mathcal{P}^{\varepsilon}(m_X, t')|^2 \approx \left[\frac{s}{m_X^2}\right]^{2\alpha_{\mathbb{P}}(t')-1}, \tag{3.74}$$

where the Pomeron trajectory $\alpha_{\mathbb{P}}(t')$ is based on the values from Refs. [120, 121]:

$$\alpha_{\mathbb{P}}(t') = 1.2 - 0.26\,(\text{GeV}/c)^{-2}\,t'. \tag{3.75}$$

More details can be found in Sec. IV A 3 in Ref. [H3].

The unknown details of the beam-Reggeon vertex, i.e., the t' dependence of the production strength and phase of wave component k in wave a with reflectivity ε, are factorized into so-called *coupling amplitudes* $\mathcal{C}^{r\varepsilon}_{ka}(t')$, which also absorbs the unknown α^k_a in Eq. (3.73). The coupling amplitudes therefore depend not only on r, ε, and the X quantum numbers i but also on the isobar decay chain. Together with $\mathcal{P}^{\varepsilon}(m_X, t')$, they describe the production of the wave components.

The dynamical amplitudes of the non-resonant wave components depend in the most general case also on r and ε and may have an explicit t' dependence. The reason for this will become clear in the discussion of the parametrization of the non-resonant components below. With these definitions, the resonance model for the transition amplitudes reads

$$\widehat{\mathcal{T}}^{r\varepsilon}_a(m_X, t') = \sqrt{m_X}\,\sqrt{I^{\varepsilon}_{aa}(m_X)}\,\mathcal{P}^{\varepsilon}(m_X, t') \sum_{k\,\in\,\mathbb{S}_a} \mathcal{C}^{r\varepsilon}_{ka}(t')\,\Delta^{r\varepsilon}_k(m_X, t'; \zeta^{r\varepsilon}_k). \tag{3.76}$$

Currently, theoretical models are not detailed enough in order to parametrize the t' dependence of the coupling amplitudes $\mathcal{C}^{r\varepsilon}_{ka}(t')$ in Eq. (3.76). Therefore, binned approximations of these t' dependences are extracted from the data by fitting the resonance model to all t' bins simultaneously and leaving the values of each $\mathcal{C}^{r\varepsilon}_{ka}$ in each t' bin as free parameters to be determined by the fit. The resonance model hence parametrizes mostly the m_X dependence of the spin-density matrix, but is model-independent with respect to the t' dependence in the sense that the amplitude of each component in each wave is allowed to have a different t' dependence. In this approach, the resonant and non-resonant wave components can be better disentangled because their amplitudes have usually different dependences on t'. The caveat of such a t'-resolved resonance-model fit is the large number of free parameters.

Assuming factorization of production, propagation, and decay of the intermediate 3π resonances, the dynamical amplitudes $\Delta_k^{\mathrm{R}}(m_X;\zeta_k^{\mathrm{R}})$ of the resonances should be independent of r, ε, and t'. The latter constraint is built into the model by using the same resonance shape parameters ζ_k^{R}, i.e., masses and widths of resonances, across all t' bins. Only strength and phase of each resonance component can be chosen freely by the fit in each t' bin in the form of the coupling amplitudes $\mathcal{C}_{ka}^{r\varepsilon}(t')$. Since the t' dependence of the amplitude of a resonant component is determined by the production mechanism, factorization of production and decay means that for a given spin projection M^{ε} the t' dependence of the amplitude should be the same in different decay modes of that resonance. This can be exploited to reduce the number of free parameters by fixing the t' dependence of the amplitude of resonance k in wave b, which is represented by $\mathcal{C}_{kb}^{r\varepsilon}(t')$, to the t' dependence of that resonance in wave a:[aa]

$$\mathcal{C}_{kb}^{r\varepsilon}(t') \;= {}_b\mathcal{B}_{ka}^{\varepsilon}\, \mathcal{C}_{ka}^{r\varepsilon}(t'). \tag{3.77}$$

The t'-independent complex-valued proportionality factors ${}_b\mathcal{B}_{ka}^{\varepsilon}$, which are determined by the fit, are called *branching amplitudes* and encode the relative strength and phase of the two decay modes a and b of resonance k.

The dynamical amplitudes of the resonance components are often parametrized using Breit-Wigner amplitudes as in Eq. (1.24). The parametrization used for the mass-dependent total width $\Gamma_{k,\mathrm{tot}}(m_X)$ depends on how well the decay modes of the resonance are known. If the branching fractions are known sufficiently well, often the two-body approximation in Eq. (1.25) is employed. In special cases, also more elaborate parametrizations are used (see, e.g., Sec. IV A 1 in Ref. [H3]). If the branching fractions of a resonance are not well-known or even unknown, usually the fixed-width approximation in Eq. (1.23) is used.

The dynamical amplitudes of the non-resonant components are in general not well known so that empirical parametrizations are employed, which are often developed in a data-driven approach. In general, we cannot assume factorization of production and decay and Eq. (3.77) does not hold for the non-resonant components. Hence one usually includes for each wave a separate non-resonant component. Consequently, the dynamical amplitude of a non-resonant component may depend on the reflectivity ε. In the most general case, the non-resonant terms may also have incoherent components so that the dynamical amplitude also depends on the rank index r. A common property of the employed parametrizations for these dynamical amplitudes is that their phase does not depend on m_X. Inspired by Ref. [122], in many analyses a Gaussian in the two-body breakup momentum q_a (see Eq. (1.26)) of the X decay in wave a is used, i.e.,[ab]

$$\begin{aligned}{}^{\mathrm{NR}}\Delta_k^{r\varepsilon}(m_X;\underbrace{b, c_0}) &= \left[\frac{m_X - m_{\mathrm{thr}}}{m_{\mathrm{norm}}}\right]^{b} e^{-c_0\, q_a^2(m_X)}. \\ &\equiv {}^{\mathrm{NR}}\zeta_k^{r\varepsilon}\end{aligned} \tag{3.78}$$

Here, we have added a term in square brackets, which approximates the phase-space opening with m_{thr} set to a value around the kinematic threshold at $3m_\pi$ and m_{norm} usually set to $1\,\mathrm{GeV}/c^2$. If we would use Eq. (1.26) to calculate q_a, we would neglect the width of the isobar that appears in wave a. Since the non-resonant components usually extend

[aa] The waves a and b must have the same $J^{PC}\,M^{\varepsilon}$ quantum numbers. If more than two waves in the resonance-model fit fulfill this criterion, always the same reference wave a is used in Eq. (3.77). Usually, the wave that corresponds to the most dominant decay chain of resonance k is chosen as the reference wave a.

[ab] To simplify notation, we omit the indices k, r, and ε from the shape parameters.

below the nominal threshold of the $X \to \xi + 3$ decay, Eq. (1.26) is not applicable and more advanced parametrizations have to be used (see, e.g., Sec. IV A 2 in Ref. [H3]). In general, the shape of the m_X distribution of a non-resonant component may change with t' so that the dynamical amplitude may have an explicit t' dependence. In such cases, it was found that an extension of Eq. (3.78) of the form

$$^{\text{NR}}\Delta_k^{r\varepsilon}(m_X, t'; \underbrace{b, c_0, c_1, c_2}_{\equiv\, ^{\text{NR}}\zeta_k^{r\varepsilon}}) = \left[\frac{m_X - m_{\text{thr}}}{m_{\text{norm}}}\right]^b e^{-\left(c_0 + c_1\, t' + c_2\, t'^2\right) q_a^2(m_X)} \tag{3.79}$$

yields a better description of the data.

3.4.2 t'-dependent observables

Since the resonance-model fit is performed simultaneously in several t' bins, we can extract the t' dependence of production strength and phase for each wave component in the model. This information is contained in the coupling amplitudes $\mathcal{C}_{ka}^{r\varepsilon}(t')$.

From the intensity of partial wave a with reflectivity ε as defined in Eq. (3.55), we can derive an expression for the intensity $\text{int}_{ka}^{\varepsilon}$ of wave component k predicted by the model in Eq. (3.76) for a given (m_X, t') cell:[ac]

$$\text{int}_{ka}^{\varepsilon}(m_X, t') \equiv m_X\, I_{aa}^{\varepsilon}(m_X) \left|\mathcal{P}^{\varepsilon}(m_X, t')\right|^2 \sum_{r=1}^{N_r^{\varepsilon}} \left|\mathcal{C}_{ka}^{r\varepsilon}(t')\right|^2 \left|\Delta_k^{r\varepsilon}(m_X, t'; \zeta_k^{r\varepsilon})\right|^2, \tag{3.80}$$

By integrating this intensity over the full m_X range under consideration, we get the t' *spectrum* of wave component k:

$$\begin{aligned}\mathcal{I}_{ka}^{\varepsilon}(t') &= \frac{\mathrm{d}N_{ka}^{\varepsilon}}{\mathrm{d}t'} \\ &= \frac{1}{\Delta t'} \sum_{r=1}^{N_r^{\varepsilon}} \left|\mathcal{C}_{ka}^{r\varepsilon}(t')\right|^2 \int_{m_{\text{min}}}^{m_{\text{max}}} \mathrm{d}m_X\, I_{aa}^{\varepsilon}(m_X)\, m_X \left|\mathcal{P}^{\varepsilon}(m_X, t')\right|^2 \left|\Delta_k^{r\varepsilon}(m_X, t'; \zeta_k^{r\varepsilon})\right|^2.\end{aligned} \tag{3.81}$$

Here, we divide by the t' bin width $\Delta t'$ in order to take into account the non-equidistant t' binning. The m_X integration range $[m_{\text{min}}, m_{\text{max}}]$ is usually given by the fit range that is used for the given partial wave.

In diffractive reactions, the t' spectra of most wave components exhibit an approximately exponential decrease with increasing t' in the range $t' \lesssim 1\,(\text{GeV}/c)^2$. This behavior can be explained in the framework of Regge theory [38, 123]. The t' spectra of partial-wave amplitudes with a spin projection of $M \neq 0$ along the beam direction are modified by an additional factor $(t')^{|M|}$. This factor is given by the forward limit of the Wigner D-functions [124] and suppresses the intensity toward small t'. We therefore parametrize the t' spectra by the model

$$\widehat{\mathcal{I}}_{ka}^{\varepsilon}(t'; A_{ka}^{\varepsilon}, b_{ka}^{\varepsilon}) = A_{ka}^{\varepsilon} \cdot \left(t'\right)^{|M|} \cdot e^{-b_{ka}^{\varepsilon}\, t'}. \tag{3.82}$$

[ac] Note that as discussed in Sec. 3.3.4, $\text{int}_{ka}^{\varepsilon}(m_X, t')$ represents the number of events integrated over the given (m_X, t') cell.

This parametrization has two free real-valued parameters: the magnitude parameter A^{ε}_{ka} and the *slope parameter* b^{ε}_{ka}. The parameters are estimated by performing a χ^2 fit, where the model function $\widehat{\mathcal{I}}^{\varepsilon}_{ka}(t')$ is integrated over each t' bin and compared to the measured value $\mathcal{I}^{\varepsilon}_{ka}(t')$ in Eq. (3.81).

In addition to the t' spectrum, we can also extract the relative phase between the coupling amplitudes of wave component k in wave a and wave component l in wave b,

$$\Delta\phi^{\varepsilon}_{ka,lb}(t') \equiv \arg\left[\sum_{r=1}^{N^{\varepsilon}_r} \mathcal{C}^{r\varepsilon}_{ka}(t')\,\mathcal{C}^{r\varepsilon *}_{lb}(t')\right]. \tag{3.83}$$

This is similar to Eq. (3.59). The quantity $\Delta\phi^{\varepsilon}_{ka,lb}$ is called *coupling phase*. Note that for a rank-1 spin-density matrix, i.e., full coherence of all partial waves,

$$\Delta\phi^{\varepsilon}_{ka,lb}(t') = \arg\big[\mathcal{C}^{\varepsilon}_{ka}(t')\big] - \arg\big[\mathcal{C}^{\varepsilon}_{lb}(t')\big]. \tag{3.84}$$

If the coupling amplitudes of a resonance in different decay modes are constrained via Eq. (3.77), the corresponding coupling phases are by definition independent of t' and are given by $\arg[{}_b\mathcal{B}^{\varepsilon}_{ka}]$. The interpretation of the value of a coupling phase is complicated by the fact that the coupling amplitude is the product of the actual production amplitude of the wave component and of α^k_a, which is in turn the product of the complex-valued couplings that appear at the two-body decay vertices in the three-body isobar decay chain of wave a (see Eq. (3.21)). The coupling phases of resonances are expected to be approximately independent of t', if a single production mechanism dominates. This is in general not true for non-resonant components, which are produced by different mechanisms. Relative to resonances, the coupling phases of the non-resonant components usually change with t'. This leads in general to a t'-dependent interference pattern, which often causes a t'-dependent shift of resonance peaks especially for waves with large non-resonant components. Hence changes of the shape of the measured m_X distribution of the intensity of a partial-wave amplitude with t' are a sign of contributions from non-resonant components.

3.4.3 Fit method

We construct the model for the spin-density submatrix of the selected waves using Eqs. (3.45) and (3.76):

$$\begin{aligned}
\widehat{\varrho}^{\varepsilon}_{ab}(m_X, t') &= \sum_{r=1}^{N^{\varepsilon}_r} \widehat{\mathcal{T}}^{r\varepsilon}_{a}(m_X, t')\,\widehat{\mathcal{T}}^{r\varepsilon *}_{b}(m_X, t') \\
&= m_X \sqrt{I^{\varepsilon}_{aa}(m_X)\,I^{\varepsilon}_{bb}(m_X)}\,\big|\mathcal{P}^{\varepsilon}(m_X, t')\big|^2 \\
&\quad \times \sum_{r=1}^{N^{\varepsilon}_r} \left[\sum_{k\,\in\,\mathbb{S}_a} \mathcal{C}^{r\varepsilon}_{ka}(t')\,\Delta^{r\varepsilon}_{k}(m_X, t'; \zeta^{r\varepsilon}_{k})\right] \left[\sum_{l\,\in\,\mathbb{S}_b} \mathcal{C}^{r\varepsilon}_{lb}(t')\,\Delta^{r\varepsilon}_{l}(m_X, t'; \zeta^{r\varepsilon}_{l})\right]^{*}.
\end{aligned} \tag{3.85}$$

The parameters of the resonance model, i.e., the set of coupling amplitudes $\{\mathcal{C}^{r\varepsilon}_{ka}(t')\}$ and the set of shape parameters $\{\zeta^{r\varepsilon}_{k}\}$, are estimated by fitting the model $\widehat{\varrho}^{\varepsilon}_{ab}(m_X, t')$ to the spin-density matrices that are measured in the (m_X, t') cells (see Sec. 3.3). In order to do this, we represent the Hermitian spin-density matrix by a real-valued matrix $\Lambda^{\varepsilon}_{ab}(m_X, t')$ of

the same dimension. The elements of $\Lambda^{\varepsilon}_{ab}$ are defined by the upper triangular part of the spin-density matrix:

$$\Lambda^{\varepsilon}_{ab}(m_X, t') \equiv \begin{cases} \mathrm{Re}\big[\varrho^{\varepsilon}_{ab}(m_X, t')\big] & \text{for } a < b, \\ \mathrm{Im}\big[\varrho^{\varepsilon}_{ba}(m_X, t')\big] & \text{for } a > b, \\ \varrho^{\varepsilon}_{aa}(m_X, t') & \text{for } a = b. \end{cases} \tag{3.86}$$

This means that the upper off-diagonal elements of $\Lambda^{\varepsilon}_{ab}$ are the real parts of the interference terms, the lower off-diagonal elements are the imaginary parts of the interference terms, and the diagonal elements are the partial-wave intensities. In an analogous way, we define $\widehat{\Lambda}^{\varepsilon}_{ab}(m_X, t')$ for our resonance model in Eq. (3.85).

In order to quantify the deviation of the resonance model $\widehat{\Lambda}^{\varepsilon}_{ab}(m_X, t')$ from the measured data $\Lambda^{\varepsilon}_{ab}(m_X, t')$, we sum the squared Pearson's residuals [125] of all matrix elements for all (m_X, t') cells:

$$\chi^2 = \sum_{\varepsilon=\pm1} \sum_{a,b}^{N^{\varepsilon}_{\text{waves}}} \sum^{t' \text{ bins}} \sum^{(m_X \text{ bins})_{ab}} \left[\frac{\Lambda^{\varepsilon}_{ab}(m_X, t') - \widehat{\Lambda}^{\varepsilon}_{ab}(m_X, t')}{\sigma^{\varepsilon}_{ab}(m_X, t')} \right]^2 . \tag{3.87}$$

Here, $N^{\varepsilon}_{\text{waves}}$ is the number of partial waves with reflectivity ε that are included in the fit model and $\sigma^{\varepsilon}_{ab}(m_X, t')$ is the statistical uncertainty of the matrix element $\Lambda^{\varepsilon}_{ab}(m_X, t')$ as determined by the partial-wave decomposition performed in the first analysis step (see Sec. 3.3). The sum in Eq. (3.87) runs over all t' bins and those m_X bins that lie within the chosen fit ranges. For the off-diagonal interference terms $\Lambda^{\varepsilon}_{ab}$, the m_X ranges are given by the intersections of the fit ranges for the intensities of waves a and b. The best estimate for the model parameters is determined by minimizing the χ^2 function using the MIGRAD algorithm of the MINUIT program [126, 127].[ad]

It is important to note that although we use the notation χ^2 for the minimized quantity in Eq. (3.87), the minimum of Eq. (3.87) does in general not follow a χ^2 distribution. This means that the expectation value of the minimum is not the number of degrees of freedom (n.d.f.). Also the deviation of the minimum from the n.d.f. is not directly interpretable as an absolute measure for the goodness of fit. This is because we assume in Eq. (3.87) that the elements of $\Lambda^{\varepsilon}_{ab}(m_X, t')$ are all statistically independent. Although this assumption is true for matrix elements from different m_X or t' bins, it is in general not true for matrix elements within a given (m_X, t') cell. They could be correlated due to statistical correlations of the transition amplitudes in the PWA fit. In principle, these correlations are known because in the partial-wave decomposition also the covariance matrix of the transition amplitudes is estimated. However, the propagation of this information to the covariance matrix of the elements of $\Lambda^{\varepsilon}_{ab}$ is not well defined. This is because the spin-density matrix has more free real-valued parameters than the set of transition amplitudes. In a (m_X, t') cell, the resonance-model fit minimizes the distance of the model to $\big([N^{\varepsilon=+1}_{\text{waves}}]^2 + [N^{\varepsilon=-1}_{\text{waves}}]^2\big)$ data points, which are the elements of $\Lambda^{\varepsilon}_{ab}$. In contrast, the set of transition amplitudes from the partial-wave decomposition represents only $\big(N_r^{\varepsilon=+1}\,[2N^{\varepsilon=+1}_{\text{waves}} - N_r^{\varepsilon=+1}] + N_r^{\varepsilon=-1}\,[2N^{\varepsilon=-1}_{\text{waves}} - N_r^{\varepsilon=-1}]\big)$ data

[ad] For high-precision data, the resonance model usually is not able to reproduce all details of the data. The residual deviations of the model from the data often induce a multi-modal behavior of the minimization procedure. Reference [H3] discusses strategies on how to resolve the multi-modality in order to obtain the best physical solution.

points (see Sec. 3.3.2).[ae] For a rank-1 spin-density matrix, this actually leads to analytical relations among the spin-density matrix elements of waves a, b, c, and d of the form

$$\varrho_{ab}\,\varrho_{cd} = \varrho_{ad}\,\varrho_{cb}, \tag{3.88}$$

which are not taken into account by Eq. (3.87).[af]

3.4.4 Discussion of the resonance model

In Sec. 1.6.1, we have already discussed the limitations and caveats of parametrizing amplitudes using sum of Breit-Wigner amplitudes. Another potential issue of our model, which introduces additional model and process dependence, is the decomposition of the partial-wave amplitudes into a sum of resonant and non-resonant components, which is not unique [34]. In principle, this decomposition would be constrained by unitarity, which is, however, not taken into account here. Due to the absence of realistic theoretical models, the parametrizations employed for the non-resonant wave components are only phenomenological (see Eqs. (3.78) and (3.79)). Also, the model assumption that the phase of a non-resonant amplitude is independent of m_X may not be well justified especially for cases where these amplitudes exhibit pronounced peaks in their intensity distribution. Although the parameters of the non-resonant components are nuisance parameters of the analysis, the choice of the parametrizations for the non-resonant components turns out to be one of the dominant sources of systematic uncertainty.

A striking advantage of the resonance model employed here is its simplicity, both from a conceptual and computational point of view. The results can also be compared directly to previous analyses of diffractive meson production that employed similar models. Some of the potential issues mentioned above are expected to be mitigated by our approach of simultaneously fitting multiple t' bins while forcing the resonance parameters to be the same across all t' bins. This puts strong constraints on the resonant and non-resonant wave components. Additional constraints that help to reduce systematic effects come from including as many decay modes of a resonance as possible into the resonance-model fit. Fitting a large spin-density submatrix with many waves with well-defined resonance signals has a similar effect. This is mainly because the resonance-model fit takes into account the whole spin-density submatrix with all interference terms. The number of these interference terms grows with the size of the spin-density submatrix squared. Hence the statistic in Eq. (3.87) that is employed to estimate the fit parameters effectively gives more weight to the interference terms than to the intensities. In practice, this often helps to stabilize the fit as the model tends to reproduce the phase motions usually more accurately than the intensities.

[ae] Only in the case of maximum rank, i.e., for $N_r^\varepsilon = N_{\text{waves}}^\varepsilon$, the set of transition amplitudes has the same number of real-valued parameters as Λ_{ab}^ε.

[af] For the case of a rank-1 spin-density matrix, Appendix C in Ref. [H3] provides formulations of χ^2 that correctly take into account all correlations. However, it turns out that for the analysis of the $\pi^-\pi^-\pi^+$ data these χ^2 formulations do not yield sensible fit results, because the resonance model has difficulties describing all details of the intensity distribution of the dominant wave, which has extremely small statistical uncertainties. See also discussion in Sec. 3.4.4 and Ref. [H3].

Chapter 4

Analysis results for the $\pi^-\pi^-\pi^+$ final state

In this chapter, we present selected results of the analysis of the COMPASS data on the diffractive dissociation reaction $\pi^- + p \to \pi^-\pi^-\pi^+ + p$ (see Sec. 2.3). We first introduce in Sec. 4.1 the analysis models that are employed for the partial-wave decomposition (first analysis stage; see Sec. 3.3) and for the resonance-model fit (second analysis stage; see Sec. 3.4). In Sec. 4.2, we present selected results from both analysis stages. The focus lies primarily on resonances that are candidates for exotic states, in particular hybrid states. A more comprehensive discussions of the results can be found in Refs. [H2, H3].

Due to the large data sample of 46×10^6 exclusive events, statistical uncertainties are negligible compared to systematic uncertainties. For this reason, we will not quote statistical uncertainties on the parameters obtained from the resonance-model fit. In order to identify partial waves, we use the shorthand notation $J^{PC}\, M^{\varepsilon}\, \xi\, \pi\, L$, where L is given in spectroscopic notation, i.e., $L = S, P, D, F, \ldots$, in the text below.

4.1 Analysis models

4.1.1 Stage I: partial-wave decomposition

The goal of the first analysis stage is to find a PWA model that describes the data well. As discussed in Sec. 3.3.7, the development of an optimal PWA model is a non-trivial and challenging task. Since the COMPASS $\pi^-\pi^-\pi^+$ data sample is about an order of magnitude larger than any data sample from previous experiments, the PWA model has to be significantly more detailed in order to achieve a good description of the data.

The main basis for constructing a wave set is to determine the set of isobars that appear in the data and to choose their parametrizations. Since there are no known resonances in the flavor-exotic $\pi^-\pi^-$ channel, which has $I = 2$, we choose to include only $\pi^-\pi^+$ isobar resonances in the PWA model. From the $\pi^-\pi^+$ mass spectrum in Fig. 2.6(b) and the Dalitz plots in Fig. 3.3, we can already infer that we have to include $\rho(770)$, $f_0(980)$, and $f_2(1270)$. The slight enhancement at about $m_{\pi^-\pi^+} = 1.7\,\mathrm{GeV}/c^2$ could be due to $\rho_3(1690)$, $\rho(1700)$, or $f_0(1710)$. From previous experiments (see, e.g., Ref. [128]) it is known that the $\rho_3(1690)$ appears in the $\pi^-\pi^+$ subsystem of diffractively produced 3π final states. Due to ambiguities of the partial-wave amplitudes that may arise when the PWA model contains

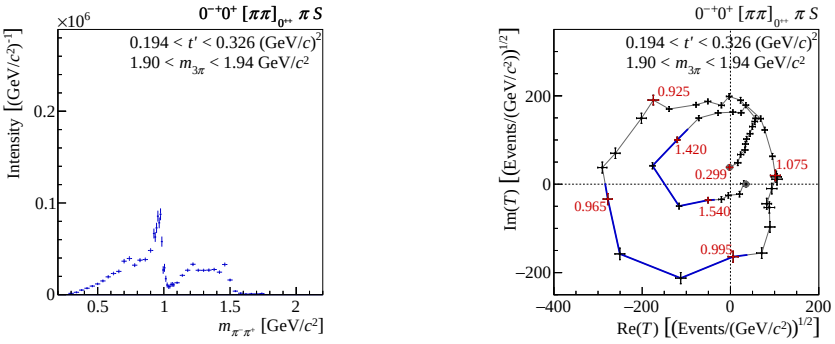

(a) **(b)**

Figure 4.1: Freed-isobar amplitude for $J^{PC} = 0^{++}$ isobars, denoted $[\pi\pi]_{0^{++}}$, in the 0^{-+} $0^+\,[\pi\pi]_{0^{++}}\,\pi\,S$ wave in a $(m_{3\pi}, t')$ cell. (a) shows the intensity as a function of $m_{\pi^-\pi^+}$, (b) the Argand diagram of the amplitude. The crosses with error bars are the result of the PWA fit. The numbers in the Argand diagram are the corresponding $m_{\pi^-\pi^+}$ values. The data points are connected by lines to indicate the order. The line segments highlighted in blue correspond to the $m_{\pi^-\pi^+}$ ranges around the $f_0(980)$ from 960 to 1000 MeV/c^2 and around the $f_0(1500)$ from 1400 to 1560 MeV/c^2. The 2π mass is binned in 10 MeV/c^2 wide intervals around the $f_0(980)$ and in 40 MeV/c^2 wide intervals elsewhere. The phase of the Argand diagram is fixed by the $1^{++}\,0^+\,\rho(770)\,\pi\,S$ wave. From Ref. [H2].

radially excited isobar resonances (see Sec. 3.3.7), we include neither the $\rho(1700)$ nor the $f_0(1710)$.

We confirm that the $f_0(1710)$ does not contribute significantly to the data by performing a freed-isobar analysis as described in Sec. 3.3.8 [H2]. In this analysis, we extract the dynamical isobar amplitude for $J^{PC} = 0^{++}$ isobars in selected 3π partial waves. Figure 4.1 shows, as an example, the dynamical isobar amplitude in the 3π partial wave with 0^{-+} quantum numbers. In the $f_0(1710)$ region, the amplitude vanishes. The Argand diagram in Fig. 4.1(b) shows that, in addition to the large circular structure that corresponds to the $f_0(980)$, there is a second circular structure that corresponds to the $f_0(1500)$. The intensity distribution in Fig. 4.1(a) exhibits a shoulder below the narrow $f_0(980)$ peak. This low-mass shoulder is mostly due to the $f_0(500)$, which is also known as σ. This state is extremely broad and is hence not well described by a Breit-Wigner amplitude. We describe the $f_0(500)$ effectively by modifying a parametrization that was developed to describe the amplitude of the $\pi\pi$ S-wave in $\pi\pi$ scattering [129] (see Sec. IV A in Ref. [H2] for details). In the text below, we denote this isobar amplitude by $[\pi\pi]_S$. Interestingly, we do not observe any signal of the $f_0(1370)$ in any of the extracted dynamical amplitudes for 0^{++} isobars. This is surprising since the PDG lists the $f_0(1370)$ as decaying into $\pi\pi$. Thus our finding adds to the controversy that surrounds the $f_0(1370)$. Preliminary studies with an extended PWA model that frees in addition to the dynamical amplitudes of 0^{++} isobars also those of isobars with 1^{--} and 2^{++} quantum numbers suggest that the data might contain small contributions from excited ρ and f_2 states [130]. In the PWA model used here, these contributions are ignored. We therefore arrive at a set of six isobars that we include in the PWA model. They are listed together with their $I^G\,J^{PC}$ quantum numbers and the employed parametrizations in Table 4.1.

Based on this set of six isobars, the number of possible partial waves is largely determined by the maximum allowed spin J of X^- and the maximum allowed orbital angular

Table 4.1: List of isobars that are used to construct the wave set for the PWA model. For more details see Ref. [H2].

Isobar resonance	$[\pi\pi]_S$	$\rho(770)$	$f_0(980)$	$f_2(1270)$	$f_0(1500)$	$\rho_3(1690)$
$\boldsymbol{I^G\,J^{PC}}$	$0^+\,0^{++}$	$1^+\,1^{--}$	$0^+\,0^{++}$	$0^+\,2^{++}$	$0^+\,0^{++}$	$1^+\,3^{--}$
Parametrization	$\pi\pi$ S-wave	Breit-Wigner	Flatté	Breit-Wigner	Breit-Wigner	Breit-Wigner

momentum L in the decay of the X^- to the isobar and the bachelor π^-. We have constructed a set of 128 waves, which—in accordance with Pomeron dominance—includes mainly positive-reflectivity waves with spin $J \leq 6$, orbital angular momentum $L \leq 6$, and spin projection $M = 0$, 1, and 2. Based on a PWA with this wave set, we have derived a smaller wave set by eliminating structureless waves with relative intensities below approximately 10^{-3} in an iterative process [73]. This yields a set of 88 partial waves that are used for the partial-wave decomposition. The 88-wave set is listed in Table 4.2 and consists of 80 waves with reflectivity $\varepsilon = +1$, seven waves with $\varepsilon = -1$, and one non-interfering flat wave representing three uncorrelated pions. This is the by far largest wave set used up to now in an analysis of the 3π final state. In order to avoid ambiguities between partial-wave amplitudes (see Sec. 3.3.7), we have to exclude 27 waves in the low-$m_{3\pi}$ region. The corresponding $m_{3\pi}$ thresholds were carefully tuned and are listed in Table 4.2.

Although the result of the freed-isobar PWA indicates an $f_0(1500)$ isobar in the 0^{-+} and 2^{-+} partial waves, the 88-wave set of the conventional PWA contains only a single wave with the $f_0(1500)$ isobar, i.e., the $0^{-+}\,0^+\,f_0(1500)\,\pi\,S$ wave. The reason for this is that the inclusion of several waves with $f_0(1500)\,\pi$ decay modes tends to destabilize the PWA fit. As discussed in Sec. 3.3.7, this is because for $m_{3\pi} \lesssim 1.7\,\text{GeV}/c^2$, the decay amplitudes of waves with $f_0(1500)$ isobar become similar to those with $[\pi\pi]_S$ or $f_0(980)$ isobars. This is much less of an issue for the waves with $[\pi\pi]_S$ and $f_0(980)$ isobars. Due to the narrowness of the $f_0(980)$, the corresponding partial-wave amplitudes are sufficiently different from those with the $[\pi\pi]_S$ isobar.

Using the 88-wave PWA model, the partial-wave decomposition is performed independently in 100 equidistant $m_{3\pi}$ bins in the range $0.5 < m_{3\pi} < 2.5\,\text{GeV}/c^2$. Each $m_{3\pi}$ bin is subdivided further into 11 non-equidistant t' bins, which are listed in Table 4.3. For each of the resulting 1100 $(m_{3\pi}, t')$ cells, an independent PWA fit is performed. Due to the fine binning in t', a rank-1 spin-density submatrix for the positive-reflectivity waves, i.e., $N^{\varepsilon=+1}_{\text{waves}} = 1$ is sufficient to describe the data. This corresponds to full coherence of all partial waves with $\varepsilon = +1$. For the negative-reflectivity waves, a rank-2 spin-density submatrix, i.e., $N^{\varepsilon=-1}_{\text{waves}} = 2$, describes the data best.

As already mentioned above, we also performed a freed-isobar PWA where we replace seven 3π partial waves with $J^{PC}\,M^{\varepsilon} = 0^{-+}\,0^+$, $1^{++}\,0^+$, and $2^{-+}\,0^+$ quantum numbers and fixed parametrizations of the $[\pi\pi]_S$, $f_0(980)$, and $f_0(1500)$ isobars by three partial waves: $0^{-+}\,0^+\,[\pi\pi]_{0^{++}}\,\pi\,S$, $1^{++}\,0^+\,[\pi\pi]_{0^{++}}\,\pi\,P$, and $2^{-+}\,0^+\,[\pi\pi]_{0^{++}}\,\pi\,D$. These three waves use a free parametrization of the dynamical isobar amplitudes for the $J^{PC} = 0^{++}$ isobars according to Eq. (3.67). We denote these freed-isobar amplitudes by $[\pi\pi]_{0^{++}}$. Due to the much larger number of fit parameters, the freed-isobar PWA is performed using only 50 bins

Table 4.2: Set of 88 waves used for the partial-wave decomposition in the first analysis stage. The thresholds define the $m_{3\pi}$ values, below which the respective waves are excluded from the PWA model. The relative intensities are calculated according to Eq. (3.58) using the full analyzed $m_{3\pi}$ and t' range. Waves highlighted in red are included in the resonance model fit (see Sec. 4.1.2). From Ref. [H2].

$J^{PC}\,M^{\varepsilon}$	Isobar	L	Threshold [MeV/c^2]	Rel. int.
$0^{-+}\,0^{+}$	$[\pi\pi]_S$	S	—	8.0 %
$0^{-+}\,0^{+}$	$\rho(770)$	P	—	3.5 %
$0^{-+}\,0^{+}$	$f_0(980)$	S	1200	2.4 %
$0^{-+}\,0^{+}$	$f_2(1270)$	D	—	0.2 %
$0^{-+}\,0^{+}$	$f_0(1500)$	S	1700	0.1 %
$1^{++}\,0^{+}$	$[\pi\pi]_S$	P	—	4.1 %
$1^{++}\,1^{+}$	$[\pi\pi]_S$	P	1100	0.2 %
$1^{++}\,0^{+}$	$\rho(770)$	S	—	32.7 %
$1^{++}\,1^{+}$	$\rho(770)$	S	—	4.1 %
$1^{++}\,0^{+}$	$\rho(770)$	D	—	0.9 %
$1^{++}\,1^{+}$	$\rho(770)$	D	—	0.6 %
$1^{++}\,0^{+}$	$f_0(980)$	P	1180	0.3 %
$1^{++}\,1^{+}$	$f_0(980)$	P	1140	0.1 %
$1^{++}\,0^{+}$	$f_2(1270)$	P	1220	0.4 %
$1^{++}\,1^{+}$	$f_2(1270)$	P	—	0.5 %
$1^{++}\,0^{+}$	$f_2(1270)$	F	—	0.1 %
$1^{++}\,0^{+}$	$\rho_3(1690)$	D	—	0.1 %
$1^{++}\,0^{+}$	$\rho_3(1690)$	G	—	< 0.1 %
$1^{-+}\,1^{+}$	$\rho(770)$	P	—	0.8 %
$2^{++}\,1^{+}$	$\rho(770)$	D	—	7.7 %
$2^{++}\,2^{+}$	$\rho(770)$	D	—	0.3 %
$2^{++}\,1^{+}$	$f_2(1270)$	P	1000	0.5 %
$2^{++}\,2^{+}$	$f_2(1270)$	P	1400	< 0.1 %
$2^{++}\,1^{+}$	$\rho_3(1690)$	D	800	< 0.1 %
$2^{-+}\,0^{+}$	$[\pi\pi]_S$	D	—	3.0 %
$2^{-+}\,1^{+}$	$[\pi\pi]_S$	D	—	0.4 %
$2^{-+}\,0^{+}$	$\rho(770)$	P	—	3.8 %
$2^{-+}\,1^{+}$	$\rho(770)$	P	—	3.3 %
$2^{-+}\,2^{+}$	$\rho(770)$	P	—	0.2 %
$2^{-+}\,0^{+}$	$\rho(770)$	F	—	2.2 %
$2^{-+}\,1^{+}$	$\rho(770)$	F	—	0.3 %
$2^{-+}\,0^{+}$	$f_0(980)$	D	1160	0.6 %
$2^{-+}\,0^{+}$	$f_2(1270)$	S	—	6.7 %
$2^{-+}\,1^{+}$	$f_2(1270)$	S	1100	0.9 %
$2^{-+}\,2^{+}$	$f_2(1270)$	S	—	0.1 %
$2^{-+}\,0^{+}$	$f_2(1270)$	D	—	0.9 %
$2^{-+}\,1^{+}$	$f_2(1270)$	D	—	0.2 %
$2^{-+}\,2^{+}$	$f_2(1270)$	D	—	0.1 %
$2^{-+}\,0^{+}$	$f_2(1270)$	G	—	0.1 %
$2^{-+}\,0^{+}$	$\rho_3(1690)$	P	1000	0.2 %
$2^{-+}\,1^{+}$	$\rho_3(1690)$	P	1300	0.1 %
$3^{++}\,0^{+}$	$[\pi\pi]_S$	F	1380	0.2 %
$3^{++}\,1^{+}$	$[\pi\pi]_S$	F	1380	0.3 %
$3^{++}\,0^{+}$	$\rho(770)$	D	—	0.9 %
$3^{++}\,1^{+}$	$\rho(770)$	D	—	1.0 %
$3^{++}\,0^{+}$	$\rho(770)$	G	—	0.4 %
$3^{++}\,1^{+}$	$\rho(770)$	G	—	0.1 %
$3^{++}\,0^{+}$	$f_2(1270)$	P	960	0.4 %
$3^{++}\,1^{+}$	$f_2(1270)$	P	1140	0.4 %
$3^{++}\,0^{+}$	$\rho_3(1690)$	S	1380	0.4 %
$3^{++}\,1^{+}$	$\rho_3(1690)$	S	1380	0.1 %
$3^{++}\,0^{+}$	$\rho_3(1690)$	I	—	< 0.1 %
$3^{-+}\,1^{+}$	$\rho(770)$	F	—	0.1 %
$3^{-+}\,1^{+}$	$f_2(1270)$	D	1340	< 0.1 %
$4^{++}\,1^{+}$	$\rho(770)$	G	—	0.8 %
$4^{++}\,2^{+}$	$\rho(770)$	G	—	< 0.1 %
$4^{++}\,1^{+}$	$f_2(1270)$	F	—	0.2 %
$4^{++}\,2^{+}$	$f_2(1270)$	F	—	< 0.1 %
$4^{++}\,1^{+}$	$\rho_3(1690)$	D	1700	< 0.1 %
$4^{-+}\,0^{+}$	$[\pi\pi]_S$	G	1400	0.3 %
$4^{-+}\,0^{+}$	$\rho(770)$	F	—	1.0 %
$4^{-+}\,1^{+}$	$\rho(770)$	F	—	0.4 %
$4^{-+}\,0^{+}$	$f_2(1270)$	D	—	0.3 %
$4^{-+}\,1^{+}$	$f_2(1270)$	D	—	0.1 %
$4^{-+}\,0^{+}$	$f_2(1270)$	G	1600	< 0.1 %
$5^{++}\,0^{+}$	$[\pi\pi]_S$	H	—	0.1 %
$5^{++}\,1^{+}$	$[\pi\pi]_S$	H	—	0.1 %
$5^{++}\,0^{+}$	$\rho(770)$	G	—	0.3 %
$5^{++}\,0^{+}$	$f_2(1270)$	F	980	0.1 %
$5^{++}\,1^{+}$	$f_2(1270)$	F	—	0.1 %
$5^{++}\,0^{+}$	$f_2(1270)$	H	—	< 0.1 %
$5^{++}\,0^{+}$	$\rho_3(1690)$	D	1360	< 0.1 %
$6^{++}\,1^{+}$	$\rho(770)$	I	—	< 0.1 %
$6^{++}\,1^{+}$	$f_2(1270)$	H	—	< 0.1 %
$6^{-+}\,0^{+}$	$[\pi\pi]_S$	I	—	0.1 %
$6^{-+}\,1^{+}$	$[\pi\pi]_S$	I	—	0.1 %
$6^{-+}\,0^{+}$	$\rho(770)$	H	—	0.7 %
$6^{-+}\,1^{+}$	$\rho(770)$	H	—	0.1 %
$6^{-+}\,0^{+}$	$f_2(1270)$	G	—	0.1 %
$6^{-+}\,0^{+}$	$\rho_3(1690)$	F	—	< 0.1 %
$1^{++}\,1^{-}$	$\rho(770)$	S	—	0.3 %
$1^{-+}\,0^{-}$	$\rho(770)$	P	—	0.3 %
$1^{-+}\,1^{-}$	$\rho(770)$	P	—	0.7 %
$2^{++}\,0^{-}$	$\rho(770)$	D	—	0.3 %
$2^{++}\,0^{-}$	$f_2(1270)$	P	1180	0.2 %
$2^{++}\,1^{-}$	$f_2(1270)$	P	1300	0.3 %
$2^{-+}\,1^{-}$	$f_2(1270)$	S	—	0.2 %
Flat			—	3.1 %

Table 4.3: Borders of the 11 non-equidistant t' bins, in which the partial-wave analysis is performed using the 88-wave PWA model. The intervals are chosen such that each bin contains approximately 4.6×10^6 events. Only the last range from 0.449 to 1.000 $(\mathrm{GeV}/c)^2$ is subdivided further into two bins. From Ref. [H2].

Bin	1	2	3	4	5	6	7	8	9	10	11	
t' **[(GeV/c)^2]**	0.100	0.113	0.127	0.144	0.164	0.189	0.220	0.262	0.326	0.449	0.724	1.000

in $m_{3\pi}$ and 4 bins in t' for the same analyzed range (see Ref. [H2] for details). The results of the conventional and the freed-isobar PWA are qualitatively in agreement. This validates the parametrizations of the 0^{++} isobars that are employed in the conventional PWA.

The goodness-of-fit of the conventional PWA fit with the 88-wave model is estimated for each $(m_{3\pi}, t')$ cell by generating pseudodata that follow the intensity distribution of the PWA model. This is done by generating events that are uniformly distributed in the three-body phase space using Monte Carlo techniques. The phase-space events are then weighted according to the fit model in Eq. (3.47). Projections of the five-dimensional Monte Carlo distribution are then compared to those of the real data. As is demonstrated in Ref. [H2], the PWA model agrees well with the data over a wide range of the phase space. This is consistent with preliminary results from studies where the regularization approach introduced in Sec. 3.3.7 is used in order to determine the wave set. These studies show that the 88-wave set captures most of the waves contained in the data [115, 116].

The relative intensities of the 88 waves in the conventional PWA fit are listed in Table 4.2. They are calculated by applying Eq. (3.58) to the full analyzed range in $m_{3\pi}$ and t'. The relative intensities of all 88 waves in the PWA model sum up to 105.3 % instead of 100 %. Thus the net effect of the interference of the all amplitudes is slightly destructive. Waves with negative reflectivity, which correspond to unnatural-parity exchange processes, contribute together only 2.2 % to the total intensity. This is consistent with the expected Pomeron dominance. Also the flat wave is small with a relative intensity of only 3.1 %. The by far most dominant wave is the $1^{++}\,0^+\,\rho(770)\,\pi\,S$ wave, which contributes 32.7 % to the total intensity. This wave therefore plays a special role in particular in the resonance-model fit performed in the second analysis stage. The 88-wave set includes waves with spin-exotic $J^{PC} = 1^{-+}$ and 3^{-+} quantum numbers. These waves have small relative intensities, which are, however, significantly different from zero. They contribute 1.8 % and 0.1 %, respectively, to the total intensity. The $1^{-+}\,1^+\,\rho(770)\,\pi\,P$ wave and its resonance content are discussed in detail in Sec. 4.2.5.

4.1.2 Stage II: resonance-model fit

The input for the resonance-model fit are the spin-density matrices $\varrho^{\varepsilon}_{ab}$ as defined in Eq. (3.45). They have been extracted from the data in the first analysis stage by performing the partial-wave decomposition independently in 1100 $(m_{3\pi}, t')$ cells, i.e., 100 bins in $m_{3\pi}$ and 11 bins in t', using the 88-wave PWA model discussed in Sec. 4.1.1.

The goal of the resonance-model fit is to study isovector resonances of the a_J and π_J families with masses up to about $2\,\mathrm{GeV}/c^2$. Unfortunately, with the currently available theoretical models and computing resources, a complete description of the $m_{3\pi}$ and t' de-

pendence of the full 88×88 spin-density matrix is not possible. We therefore have to select a subset of waves that is included in the resonance-model fit. Out of the 88 waves in the PWA model, we select waves that exhibit clear signals of well-known resonances, i.e., resonance peaks that are associated with phase motions. If possible, we include waves that represent different decay modes and different M states of these resonances. These waves are intended to act as reference amplitudes, against which the resonant amplitudes in more interesting waves can interfere. The latter waves exhibit signals of less well-known excited states or have controversial resonance content such as the spin-exotic $1^{-+}\,1^{+}\,\rho(770)\,\pi\,P$ wave.

Table 4.4 lists the 14 waves selected for the resonance-model fit. Compared to previous analyses of the 3π final state, this is the by far largest wave set that is consistently described in a single resonance-model fit. The selected waves contain signals of the well-known resonances $a_1(1260)$, $a_2(1320)$, $\pi_2(1670)$, $\pi(1800)$, $\pi_2(1880)$, and $a_4(2040)$, which appear as peaks in the respective partial-wave intensities and as phase motions in the relative phases of these waves. In addition, the selected wave set includes a clear resonance-like signal of the novel $a_1(1420)$, which was discovered in an earlier analysis of the same COMPASS data in Ref. [H1]. In this analysis, the same 88-wave PWA fit was used but the resonance model included only three partial waves. The set of 14 waves also contains signals of the less well-known or even disputed states $\pi_1(1600)$, $a_1(1640)$, and $a_2(1700)$. The $\pi_1(1600)$ is particularly interesting, because it has spin-exotic $J^{PC} = 1^{-+}$ quantum numbers. It turns out that the data require a third π_2 resonance, the $\pi_2(2005)$, which according to the PDG requires confirmation [13]. In total, the resonance model contains 11 resonances, which are all described using Breit-Wigner amplitudes. With the exception of the $a_1(1260)$ and the $a_2(1320)$, for which we use mass-dependent widths (see Sec. IV A 1 in Ref. [H3] for details), the Breit-Wigner amplitudes of the other resonances have constant widths as in Eq. (1.23). In addition to the 11 resonant components, we include for each wave a separate coherent non-resonant component (see Sec. 3.4.1).

Figure 4.2 shows the intensity distributions of the resonant and non-resonant wave components (colored curves) together with the intensity of the coherent sum of the 14 selected partial-wave amplitudes (gray squares) and the total intensity of the PWA model (black points). The coherent sum of the 14 selected partial-wave amplitudes contributes 57.9 % to the total intensity. This is similar to the intensity sum of the 14 waves, which corresponds to 56.8 % of the total intensity. Thus the net effect of the interference between the 14 partial-wave amplitudes is slightly constructive. It is worth noting that the intensities of the wave components cover a large dynamic range of more than three orders of magnitude. The largest contributions to the intensity come from the $a_1(1260)$ and the non-resonant term in the $1^{++}\,0^{+}\,\rho(770)\,\pi\,S$ wave (red curves in Figs. 4.2(a) and 4.2(c)). Since the resonance model contains only waves with positive reflectivity, all wave components, in particular the resonant and non-resonant components, do interfere. For waves with larger intensities, this interference is mostly constructive.

In total, the 14-wave resonance-model fit has 722 real-valued free paramters that are constrained by 76 505 data points within the chosen fit ranges (see Sec. 3.4.1) that enter the sum in Eq. (3.87). The 22 resonance parameters determined by the fit are summarized and compared to the PDG values in Table 4.5. A graphical representation of the fit result is shown in Fig. 4.3.

Due to the highly precise data, the uncertainties of the resonance parameters are completely dominated by systematic effects. We performed extensive systematic studies to

Table 4.4: Resonance model to describe the elements of the spin-density matrix of 14 selected partial waves from six J^{PC} sectors using Eq. (3.85). The relative intensities listed in the second column are the same as in Table 4.2. The third column lists the resonances used to describe the waves. In total, 11 resonances are used. Details about their parametrization can be found in Sec. IV A 1 in Ref. [H3]. The fourth column lists the parametrizations used for the non-resonant components, the last column the fit ranges (see Sec. 3.4.3 for details). From Ref. [H3].

Partial wave	**Relative intensity**	**Resonances**	**Non-resonant component Eq.**	**$m_{3\pi}$ fit range [GeV/c^2]**
$0^{-+}\,0^{+}\,f_0(980)\,\pi\,S$	2.4 %	$\pi(1800)$	(3.78)	1.20 to 2.30
$1^{++}\,0^{+}\,\rho(770)\,\pi\,S$	32.7 %	$a_1(1260)$, $a_1(1640)$	(3.79)	0.90 to 2.30
$1^{++}\,0^{+}\,f_0(980)\,\pi\,P$	0.3 %	$a_1(1420)$	(3.78)	1.30 to 1.60
$1^{++}\,0^{+}\,f_2(1270)\,\pi\,P$	0.4 %	$a_1(1260)$, $a_1(1640)$	(3.78)	1.40 to 2.10
$1^{-+}\,1^{+}\,\rho(770)\,\pi\,P$	0.8 %	$\pi_1(1600)$	(3.79)	0.90 to 2.00
$2^{++}\,1^{+}\,\rho(770)\,\pi\,D$	7.7 %	$a_2(1320)$, $a_2(1700)$	(3.79)	0.90 to 2.00
$2^{++}\,2^{+}\,\rho(770)\,\pi\,D$	0.3 %		(3.78)	1.00 to 2.00
$2^{++}\,1^{+}\,f_2(1270)\,\pi\,P$	0.5 %		(3.78)	1.00 to 2.00
$2^{-+}\,0^{+}\,\rho(770)\,\pi\,F$	2.2 %	$\pi_2(1670)$, $\pi_2(1880)$, $\pi_2(2005)$	(3.79)	1.20 to 2.10
$2^{-+}\,0^{+}\,f_2(1270)\,\pi\,S$	6.7 %		(3.79)	1.40 to 2.30
$2^{-+}\,1^{+}\,f_2(1270)\,\pi\,S$	0.9 %		(3.78)	1.40 to 2.30
$2^{-+}\,0^{+}\,f_2(1270)\,\pi\,D$	0.9 %		(3.78)	1.60 to 2.30
$4^{++}\,1^{+}\,\rho(770)\,\pi\,G$	0.8 %	$a_4(2040)$	(3.78)	1.25 to 2.30
$4^{++}\,1^{+}\,f_2(1270)\,\pi\,F$	0.2 %		(3.78)	1.40 to 2.30
Intensity sum	**56.8 %**			

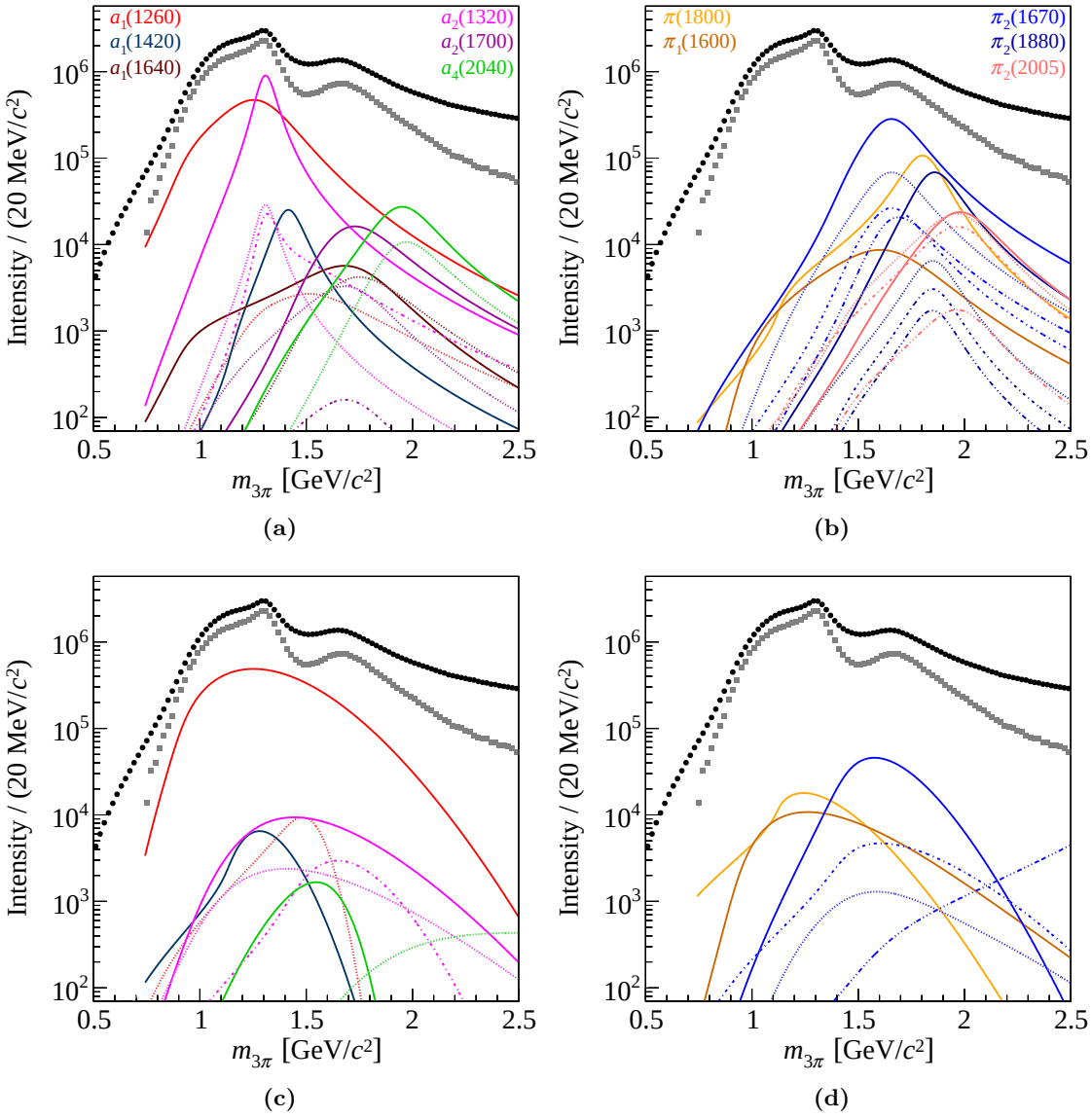

Figure 4.2: Intensity distributions of the wave components in the resonance model (colored curves) compared to the total intensity of the coherent sum of all 88 partial-wave amplitudes in the PWA model (black points) and the intensity of the coherent sum of the 14 partial-wave amplitudes selected for the resonance-model fit (gray squares). (Top row) intensity distributions of the 11 resonances that are included in the resonance model. Different colors encode different resonances. The same resonance may appear in up to four partial waves that correspond to different decay modes. These different decay modes are encoded by different line styles, which are assigned according to the height of the resonance peak. The line shapes of the resonances differ in the various decay modes because of the different phase space. (Bottom row) intensity distributions of the 14 non-resonant components included in the resonance model, one in each wave. Color and line style are defined by the dominant resonance in the respective wave as shown in the top row. From Ref. [131].

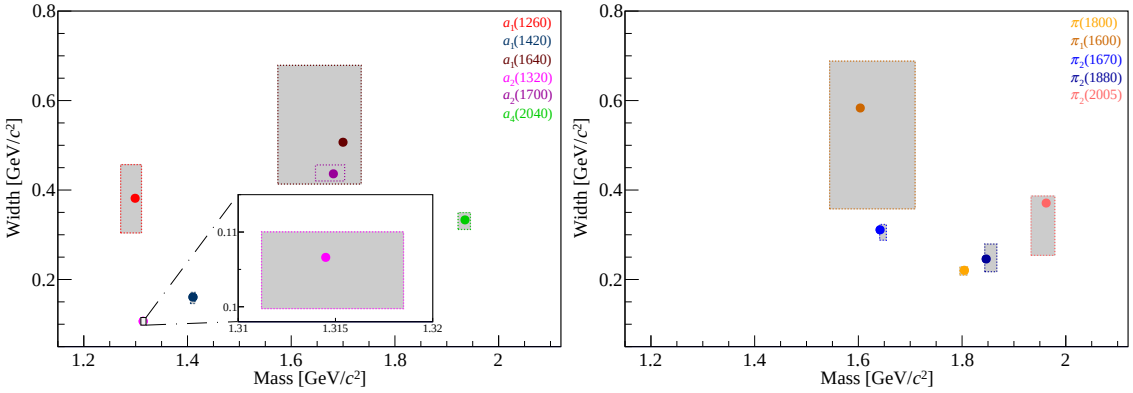

(a) **(b)**

Figure 4.3: Masses and widths of (a) a_J-like and (b) π_J-like resonances extracted in this analysis (points). The systematic uncertainties are represented by the boxes. The statistical uncertainties are at least an order of magnitude smaller than the systematic ones and are hence omitted. Different colors encode different resonances. From Ref. [H3].

estimate the systematic uncertainties. Large effects are observed if we remove the event selection cuts that ensure exclusivity and suppress backgrounds from other physics processes (see Sec. 2.3.1). Also the selection of the waves that enter the resonance-model fit has large effects on some resonance parameters. In addition, the choice of the parametrization of the non-resonant contributions contributes significantly to the systematic uncertainties. The Deck process (see Sec. 3.3.7) is believed to be a dominant source for the non-resonant contributions. In order to study the dependence of our fit result on the parametrization of the non-resonant component, we performed a study, where the shapes of the non-resonant components are determined from a model for the Deck process (see Appendix B in Ref. [H3]). This is done by generating Monte Carlo pseudodata based on the model for the Deck process and by performing the same 88-wave PWA fit as for the real data. Instead of the phenomenological parametrizations for the non-resonant components, we use the square root of the intensity distributions as obtained from the partial-wave decomposition of the Deck Monte Carlo data. We will discuss the results from this study in the sections below. More details of the performed systematic studies are discussed in Sec. V and Appendix D in Ref. [H3].

As is evident from Fig. 4.3, the parameters of the various resonances have vastly different systematic uncertainties. This mainly reflects two aspects of our data: (i) the large dynamic range of the intensities of the resonances in the selected waves as is illustrated in Figs. 4.2(a) and 4.2(b) and (ii) the vastly different strength of the non-resonant components relative to the resonances. As a consequence, we can determine the parameters of the $a_2(1320)$, $a_1(1420)$, $\pi_2(1670)$, $\pi(1800)$, and $a_4(2040)$ with high accuracy. In contrast, the parameters of the $a_1(1260)$, $\pi_1(1600)$, $a_1(1640)$, and $\pi_2(2005)$ have particularly large systematic uncertainties. In the in the following Sec. 4.2, we will discuss selected results from the partial-wave decomposition and the 14-wave resonance-model fit with a focus on candidates for exotic states.

Table 4.5: Resonance parameters with systematic uncertainties as extracted in this analysis. The statistical uncertainties are at least an order of magnitude smaller than the systematic ones and are hence omitted. For comparison, the PDG averages from Ref. [13] are listed. For the $a_2(1320)$, we quote the PDG average for the 3π decay mode. For the two entries marked with a " * " no PDG average exists. The $a_1(1420)$ is listed as "omitted from summary table" and the quoted mass and width values were estimated in an earlier COMPASS analysis based on the same data set that is used here but with only three waves in the resonance-model fit [H2]. The $\pi_2(2005)$ is listed as a "further state" and we quote for comparison the parameters measured by the BNL E852 experiment [132] with the statistical and systematic uncertainties added in quadrature. From Ref. [H3].

(a) a_J-like resonances

		$a_1(1260)$	$a_1(1420)$	$a_1(1640)$	$a_2(1320)$	$a_2(1700)$	$a_4(2040)$
COMPASS	Mass [MeV/c^2]	$1299\,^{+12}_{-28}$	$1411\,^{+4}_{-5}$	$1700\,^{+35}_{-130}$	$1314.5\,^{+4.0}_{-3.3}$	$1681\,^{+22}_{-35}$	$1935\,^{+11}_{-13}$
	Width [MeV/c^2]	380 ± 80	$161\,^{+11}_{-14}$	$510\,^{+170}_{-90}$	$106.6\,^{+3.4}_{-7.0}$	$436\,^{+20}_{-16}$	$333\,^{+16}_{-21}$
PDG	Mass [MeV/c^2]	1230 ± 40	$1414\,^{+15}_{-13}$	1647 ± 22	$1319.0\,^{+1.0}_{-1.3}$	1732 ± 16	$1995\,^{+10}_{-8}$
	Width [MeV/c^2]	250 to 600	$153\,^{+8}_{-23}$ *	254 ± 27	$105.0\,^{+1.6}_{-1.9}$	194 ± 40	$257\,^{+25}_{-23}$

(b) π_J-like resonances

		$\pi(1800)$	$\pi_1(1600)$	$\pi_2(1670)$	$\pi_2(1880)$	$\pi_2(2005)$
COMPASS	Mass [MeV/c^2]	$1804\,^{+6}_{-9}$	$1600\,^{+110}_{-60}$	$1642\,^{+12}_{-1}$	$1847\,^{+20}_{-3}$	$1962\,^{+17}_{-29}$
	Width [MeV/c^2]	$220\,^{+8}_{-11}$	$580\,^{+100}_{-230}$	$311\,^{+12}_{-23}$	$246\,^{+33}_{-28}$	$371\,^{+16}_{-120}$
PDG	Mass [MeV/c^2]	1812 ± 12	$1662\,^{+8}_{-9}$	1672.2 ± 3.0	1895 ± 16	1974 ± 84
	Width [MeV/c^2]	208 ± 12	241 ± 40	260 ± 9	235 ± 34	341 ± 152 *

4.2 Selected results

4.2.1 The $\pi(1800)$

The $\pi(1800)$ has a mass consistent with the second radial excitation of the pion, i.e., the $3\,^3S_1\ |q\bar{q}\rangle$ state. However, the $\pi(1800)$ exhibits a peculiar decay pattern. It decays mostly into 3π and experiments have reported decays via $f_0(500)\,\pi$, $f_0(980)\,\pi$, and $f_0(1370)\,\pi$. This means that for the 3π final state, only decays via $J^{PC} = 0^{++}$ isobars are observed [13]. Surprisingly, the decay into $\rho(770)\,\pi$ is not seen [133]. Also the decay into $f_0(1500)\,\pi$ is not observed in the 3π final state [128], whereas it is seen in the $\eta\eta\pi$ final state [134–136]. However, in the latter final state the $f_0(1370)\,\pi$ decay is not observed [136].

In the COMPASS data, we observe the cleanest $\pi(1800)$ signal in the $f_0(980)\,\pi$ wave, which contributes about 2.4 % to the total intensity. Figure 4.4(a) shows the intensity distribution of the $0^{-+}\,0^+\,f_0(980)\,\pi\,S$ wave in the lowest t' bin, which exhibits a pronounced peak at $1.8\,\mathrm{GeV}/c^2$ that is accompanied by a rapid phase motion (see Fig. 4.4(b)). Although in the $0^{-+}\,0^+\,f_0(980)\,\pi\,S$ wave all final-state particles are in relative S-waves, the amplitude of this wave is reliably extracted from the data and is robust against changes of the PWA model. The t' spectrum of the $\pi(1800)$, which is shown as blue lines in Fig. 4.4(c), has an approximately exponential behavior with a slope parameter value of $8.8\,^{+0.7}_{-0.3}\,(\mathrm{GeV}/c)^{-2}$, which is consistent with a resonance. We obtain resonance parameters of $m_{\pi(1800)} = 1804\,^{+6}_{-9}\,\mathrm{MeV}/c^2$ and $\Gamma_{\pi(1800)} = 220\,^{+8}_{-11}\,\mathrm{MeV}/c^2$. Our measurement of the $\pi(1800)$ parameters is the so far most accurate and in good agreement with the PDG world average [13].

The resonant nature of the $f_0(980)$ isobar in the $\pi(1800)$ decay is confirmed by the results of the freed-isobar PWA (see Sec. 3.3.8). Figure 4.5(a) shows the correlation of the $m_{\pi^-\pi^+}$ intensity distribution of the freed-isobar amplitude with $J^{PC} = 0^{++}$ quantum numbers in the $0^{-+}\,0^+\,[\pi\pi]_{0^{++}}\,\pi\,S$ wave with the $m_{3\pi}$ intensity distribution of this wave. The distribution exhibits a clear peak at $m_{3\pi} \approx 1.8\,\mathrm{GeV}/c^2$ and $m_{\pi^-\pi^+} \approx 1.0\,\mathrm{GeV}/c^2$. In addition, a circular resonance structure appears in the highlighted $f_0(980)$ region in the Argand diagram shown in Fig. 4.5(b). However, there is a second circular resonance structure in the highlighted $f_0(1500)$ region. The $m_{3\pi}$ intensity distribution in the $f_0(1500)$ region shown in Fig. 4.5(c) exhibits a clear $\pi(1800)$ peak (cf. Fig. 4.4(a)). This result is consistent with the $\pi(1800)$ peak observed in the $0^{-+}\,0^+\,f_0(1500)\,\pi\,S$ wave in the conventional PWA using the 88-wave PWA model (see Fig. 4.6(a)). Hence our results show that the $\pi(1800)$ decays into $f_0(1500)\,\pi$ also in the 3π final state as it is expected based on the observation in the $\eta\eta\pi$ final state.

It is worth noting, that the Argand diagram in Fig. 4.5(b) shows no sign of the $f_0(1370)$, which was claimed as a 3π decay mode of the $\pi(1800)$ by previous experiments [13]. This discrepancy could be due to the fact that branching fractions for $f_0(500)$ and $f_0(1370)$ isobars depend strongly on the PWA model, in particular on the parametrizations employed for the 0^{++} isobars. Our result from the freed-isobar PWA, which is model-independent with respect to the parametrization of the 0^{++} isobars, puts doubts on the existence of the $f_0(1370)$ as a $\pi\pi$ resonance and hence as a possible decay mode for the $\pi(1800)$.

Our results confirm the strong dominance of 0^{++} isobars in the $\pi(1800)$ decays to 3π and also the small branching fraction for $\rho(770)\,\pi$. The latter can be seen in Fig. 4.6(b), which shows the intensity of the $0^{-+}\,0^+\,\rho(770)\,\pi\,P$ wave. The intensity distribution exhibits a small structure in the $1.8\,\mathrm{GeV}/c^2$ region, which could be due to the $\pi(1800)$, but the

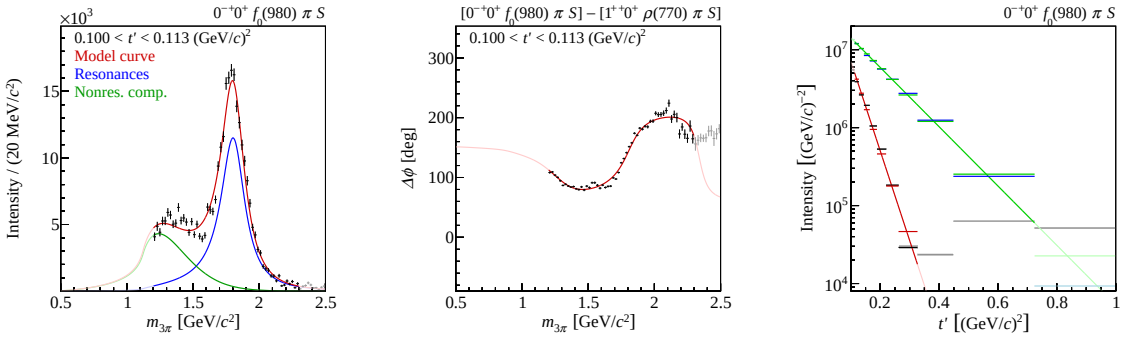

Figure 4.4: (a) intensity distribution of the $0^{-+}\,0^{+}\,f_0(980)\,\pi\,S$ wave; (b) phase of this wave with respect to the $1^{++}\,0^{+}\,\rho(770)\,\pi\,S$ wave, both in the lowest t' bin. The data points represent the result of the partial-wave decomposition in the first analysis stage (see Secs. 3.3 and 4.1.1). The red curve represents the result of the resonance-model fit (see Secs. 3.4 and 4.1.2). The model is the coherent sum of two wave components: $\pi(1800)$ resonance (blue curve) and non-resonant contribution (green curve). The extrapolations of the model and the wave components beyond the fit range are shown in lighter colors. (c) t' spectra of the two components in the $0^{-+}\,0^{+}\,f_0(980)\,\pi\,S$ wave as given by Eq. (3.81). In each t' bin, the horizontal line indicates the central value and the horizontal extent of the line the width of the t' bin. The statistical uncertainty is represented by the height of the shaded box around the central value (invisibly small for most bins). The $\pi(1800)$ component is shown as blue lines and light blue boxes, and the non-resonant component as black lines and gray boxes. The red and green curves represent fits using Eq. (3.82). The red and green horizontal lines represent the integrals of the model function over the t' bins and can be directly compared to the data. Extrapolations of the model beyond the fit range are shown in lighter colors. From Ref. [H3].

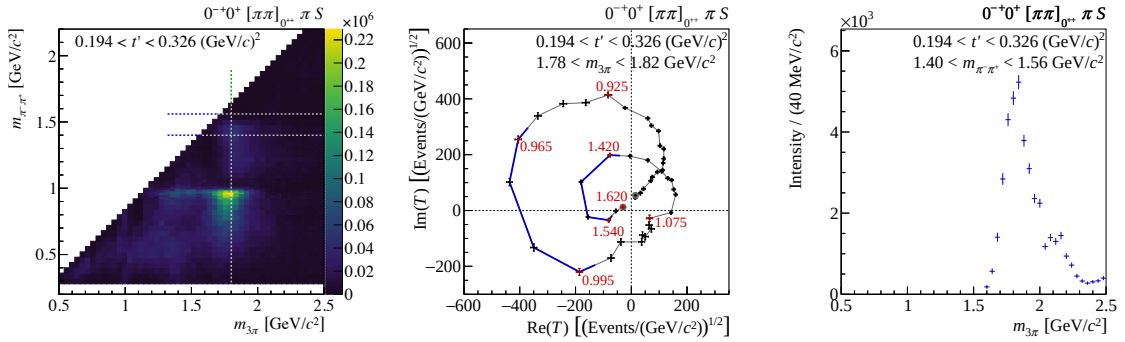

Figure 4.5: Amplitude of the $0^{-+}\,0^{+}\,[\pi\pi]_{0^{++}}\,\pi\,S$ wave with the freed-isobar amplitude $[\pi\pi]_{0^{++}}$ in an intermediate t' bin. (a) two-dimensional representation of the intensity of this wave as a function of $m_{\pi^-\pi^+}$ and $m_{3\pi}$. (c) same as Fig. 4.1(b), but showing the Argand diagram of the freed-isobar amplitude for the $m_{3\pi}$ bin at the $\pi(1800)$ mass that is indicated by the vertical dashed line in (a). (c) intensity as a function of $m_{3\pi}$ summed over a selected $m_{\pi^-\pi^+}$ interval around the $f_0(1500)$ that is indicated by the pair of horizontal dashed lines in (a). From Ref. [H2].

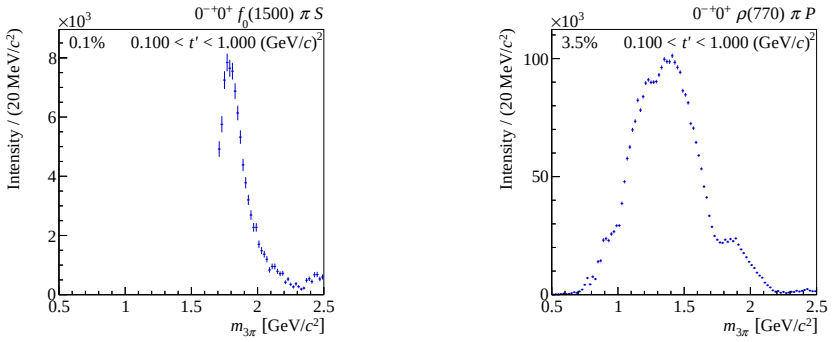

(a) **(b)**

Figure 4.6: Intensity distribution, summed over the 11 t' bins, of (a) the $0^{-+}\,0^{+}\, f_0(1500)\, \pi\, S$ wave and (b) the $0^{-+}\,0^{+}\, \rho(770)\, \pi\, P$ wave. From Ref. [H2].

spectrum is dominated by a broad peak around $1.4\,\mathrm{GeV}/c^2$. First attempts to describe this wave in a resonance-model fit failed, because the model is not able to reproduce the observed intensity distribution. Improving the resonance model is the topic of future research.

In order to explain the peculiar decay pattern of the $\pi(1800)$ it was proposed that the $\pi(1800)$ is a hybrid state [67, 137] or that the peak at $1.8\,\mathrm{GeV}/c^2$ contains actually two states: a conventional $|q\bar{q}\rangle$ state and a hybrid state [138]. A hybrid state in the $1.8\,\mathrm{GeV}/c^2$ region would also be consistent with lattice QCD calculations (see Fig. 1.9). A measurement of the $\rho(770)\,\pi$ and $f_2(1270)\,\pi$ branching fractions of the $\pi(1800)$ in the 3π COMPASS data could help to distinguish between the models. As mentioned above, this requires further development of the resonance model.

4.2.2 The $\pi_2(1880)$

Although the $\pi_2(1880)$ is an established state, the PDG currently does not list any 3π decay modes of the $\pi_2(1880)$ [13]. The 14-wave resonance-model fit contains four 2^{-+} waves. We observe a strong $\pi_2(1880)$ signal only in the $2^{-+}\,0^{+}\, f_2(1270)\,\pi\, D$ wave. In the $\rho(770)\,\pi$ F-wave and the two $f_2(1270)\,\pi$ S-waves with $M = 0$ and 1, the $\pi_2(1880)$ component is small. The intensity distribution of the $f_2(1270)\,\pi$ D-wave is shown in Fig. 4.7(a) and exhibits a peak at about $1.8\,\mathrm{GeV}/c^2$ that is described mostly by the $\pi_2(1880)$ component. The non-resonant contribution is small. There is, however, considerable destructive interference of the $\pi_2(1880)$ with the $\pi_2(1670)$ and the $\pi_2(2005)$. As is shown in Fig. 4.7(b), the peak is associated with a rapid phase motion. In our resonance model, the coupling amplitudes of the $\pi_2(1880)$ in the three 2^{-+} waves with $M = 0$ are constrained by Eq. (3.77). Therefore, the t' spectra of the $\pi_2(1880)$ are very similar in these three waves. As an example, Fig. 4.7(c) shows the t' spectrum of the $\pi_2(1880)$ in the $2^{-+}\,0^{+}\, f_2(1270)\,\pi\, S$ wave. The spectrum is approximately exponential and has a slope parameter value of $7.8\,^{+0.5}_{-0.9}\,(\mathrm{GeV}/c)^{-2}$, which is typical for resonances.

In our resonance-model fit, we find the resonance parameters $m_{\pi_2(1880)} = 1847\,^{+20}_{-3}\,\mathrm{MeV}/c^2$ and $\Gamma_{\pi_2(1880)} = 246\,^{+33}_{-28}\,\mathrm{MeV}/c^2$. While our width value is compatible with the PDG world average of $\Gamma_{\pi_2(1880)} = 235 \pm 34\,\mathrm{MeV}/c^2$, we find a mass value that is $48\,\mathrm{MeV}/c^2$ smaller than the PDG value of $m_{\pi_2(1880)} = 1895 \pm 16\,\mathrm{MeV}/c^2$ [13]. The four measurements listed by the PDG for the $\pi_2(1880)$ fall into two subsets: (i) two measurements with lower masses $m_{\pi_2(1880)} \leq 1880\,\mathrm{MeV}/c^2$ and smaller widths $\Gamma_{\pi_2(1880)} \leq 255\,\mathrm{MeV}/c^2$ [132, 135] that are

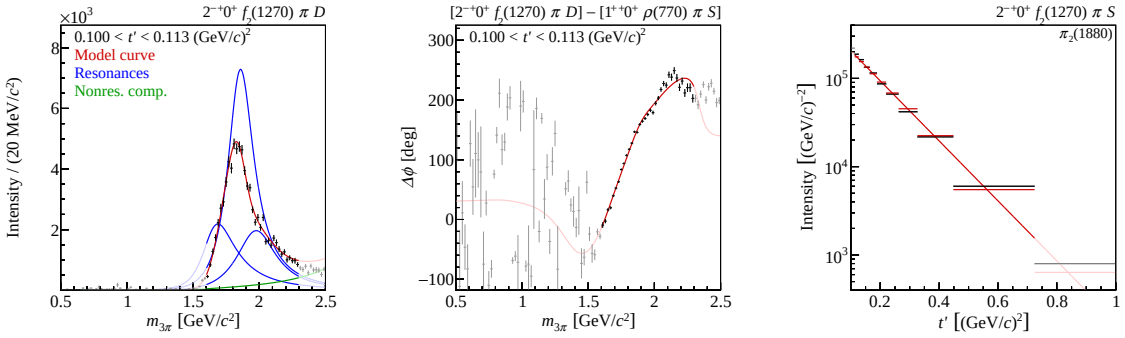

(a) **(b)** **(c)**

Figure 4.7: (a) intensity distribution of the $2^{-+}\,0^+\,f_2(1270)\,\pi\,D$ wave; (b) phase of this wave with respect to the $1^{++}\,0^+\,\rho(770)\,\pi\,S$ wave, both in the lowest t' bin. The curves represent the result of the resonance-model fit. The model and the wave components are represented as in Fig. 4.4. The dominant resonant component is the $\pi_2(1880)$; the contributions from $\pi_2(1670)$ and $\pi_2(2005)$ are smaller. (c) similar to Fig. 4.4(c), but showing the t' spectrum of the $\pi_2(1880)$ in the $2^{-+}\,0^+\,f_2(1270)\,\pi\,S$ wave. From Ref. [H3].

compatible with our estimate of the $\pi_2(1880)$ parameters, and (ii) two measurements with larger masses $m_{\pi_2(1880)} \geq 1929\,\text{MeV}/c^2$ and larger widths $\Gamma_{\pi_2(1880)} \geq 306\,\text{MeV}/c^2$ [136,139] that are better compatible with our estimates for the $\pi_2(2005)$ parameters (see Table 4.5).

In the freed-isobar PWA (see Sec. 3.3.8), we also studied the 2^{-+} wave with a freed dynamical amplitude for the 0^{++} isobars. Figure 4.8(a) shows the correlation of the $m_{\pi^-\pi^+}$ intensity distribution of the freed-isobar amplitude with $J^{PC} = 0^{++}$ quantum numbers in the $2^{-+}\,0^+\,[\pi\pi]_{0^{++}}\,\pi\,D$ wave with the $m_{3\pi}$ intensity distribution of this wave. In this distribution, we observe a clear peak slightly below $m_{3\pi} = 1.9\,\text{GeV}/c^2$ and at $m_{\pi^-\pi^+} \approx 1.0\,\text{GeV}/c^2$. The $\pi_2(1880)$ peak is also clearly visible in the $m_{3\pi}$ intensity distribution in the $f_0(980)$ region that is shown in Fig. 4.8(b). The $m_{\pi^-\pi^+}$ intensity distribution at the $\pi_2(1880)$ peak position is shown in Fig. 4.9(a) and exhibits a narrow peak of the $f_0(980)$. The resonant nature of this peak is confirmed by the corresponding highlighted circular structure in the Argand diagram in Fig. 4.9(b). However, the Argand diagram exhibits an additional smaller circular structure in the highlighted $f_0(1500)$ region, which corresponds to a small peak in the $m_{\pi^-\pi^+}$ intensity distribution. Our freed-isobar PWA result hence establishes two additional 3π decay modes of the $\pi_2(1880)$, namely $f_0(980)\,\pi$ and $f_0(1500)\,\pi$. The latter one is consistent with the $f_0(1500)\,\pi$ decay mode seen in the $\eta\eta\pi$ final state [135].

The $\pi_2(1880)$ is an interesting state, because its mass is too close to that of the $\pi_2(1670)$ ground state in order to be the radial excitation of the latter, i.e., the $2\,^1D_2$ state. The $\pi_2(2005)$ is a much more plausible candidate for the $2\,^1D_2$ state. Hence the $\pi_2(1880)$ could be a supernumerary state. The authors of Refs. [137,138] propose it as a hybrid candidate. This is also consistent with the predictions from lattice QCD calculations (see Fig. 1.9). The authors of Ref. [67] predict for a hybrid meson that the $f_2(1270)\,\pi$ D-wave decay mode is strongly suppressed with respect to the $f_2(1270)\,\pi$ S-wave decay. It is therefore interesting to compare the $\pi_2(1880)$ signals in the $2^{-+}\,0^+\,f_2(1270)\,\pi\,S$ and $2^{-+}\,0^+\,f_2(1270)\,\pi\,D$ waves. Although the interference pattern of the model components in the $f_2(1270)\,\pi$ D-wave is strongly model-dependent and hence the $\pi_2(1880)$ yield not well determined, we can still conclude that the $\pi_2(1880)$ signal in the $f_2(1270)\,\pi$ S-wave is suppressed with respect to

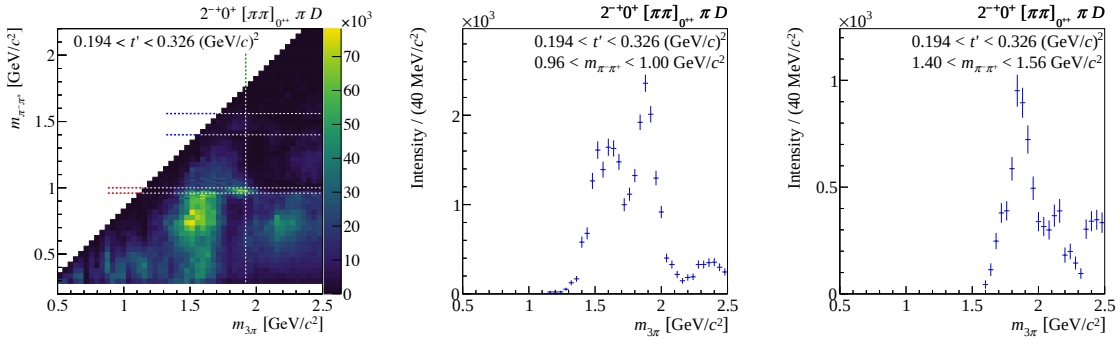

(a) **(b)** **(c)**

Figure 4.8: Amplitude of the $2^{-+}\,0^{+}\,[\pi\pi]_{0^{++}}\,\pi\,D$ wave with the freed-isobar amplitude $[\pi\pi]_{0^{++}}$ in an intermediate t' bin. (a) two-dimensional representation of the intensity of this wave as a function of $m_{\pi^-\pi^+}$ and $m_{3\pi}$. (b) and (c) intensity as a function of $m_{3\pi}$ summed over selected $m_{\pi^-\pi^+}$ intervals around (b) the $f_0(980)$ and (c) the $f_0(1500)$ that are indicated by the pairs of horizontal dashed lines in (a). From Ref. [H2].

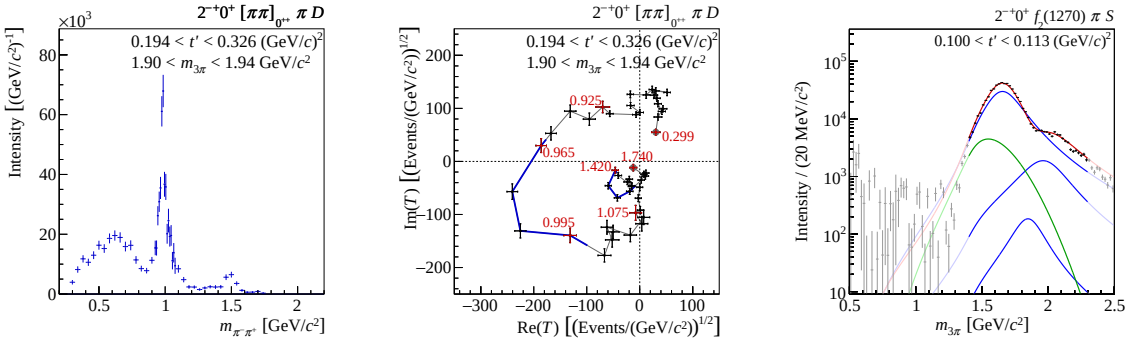

(a) **(b)** **(c)**

Figure 4.9: (a) and (b) amplitude of the $2^{-+}\,0^{+}\,[\pi\pi]_{0^{++}}\,\pi\,D$ wave with the freed-isobar amplitude $[\pi\pi]_{0^{++}}$ in an intermediate t' bin. (a) intensity as a function of $m_{\pi^-\pi^+}$. (b) same as Fig. 4.1(b), but showing the Argand diagram of the freed-isobar amplitude for the $m_{3\pi}$ bin at the $\pi_2(1880)$ mass that is indicated by the vertical dashed line in Fig. 4.8(a). (c) intensity distribution of the $2^{-+}\,0^{+}\,f_2(1270)\,\pi\,S$ wave in the lowest t' bin. The curves represent the result of the resonance-model fit. The model and the wave components are represented as in Fig. 4.4. From Ref. [H2].

the one in the D-wave by about an order of magnitude (see Fig. 4.9(c)). This means that the observed decay pattern is exactly opposite to the one predicted in Ref. [67] for a hybrid state. Our results therefore challenge the hybrid interpretation of the $\pi_2(1880)$.

4.2.3 The $a_1(1260)$

The $a_1(1260)$ is the isovector $J^{PC} = 1^{++}$ ground state and its existence is well established. The PDG lists 23 measurements of the $a_1(1260)$ mass and 26 of the $a_1(1260)$ width,[a] the earliest one being more than 40 years old [13]. Still, the parameters of the $a_1(1260)$ are not well known. Depending on the analyzed process and the employed parametrizations, the values of the $a_1(1260)$ parameters differ substantially [140]. The reported values for the $a_1(1260)$ parameters cover wide ranges. The mass values range from $1041 \pm 13\,\text{MeV}/c^2$ [141] to $1331 \pm 10\,(\text{stat.}) \pm 3\,(\text{sys.})\,\text{MeV}/c^2$ [142] and the width values from $230 \pm 50\,\text{MeV}/c^2$ [141] to $814 \pm 36\,(\text{stat.}) \pm 13\,(\text{sys.})\,\text{MeV}/c^2$ [142]. Due to these large spreads, the PDG does not perform an average but provides only an estimate of $m_{a_1(1260)} = 1230 \pm 40\,\text{MeV}/c^2$ and $\Gamma_{a_1(1260)} = 250$ to $600\,\text{MeV}/c^2$ [13].

The $a_1(1260)$ decays mainly to 3π. The $\rho(770)\,\pi$ S-wave decay mode is the most dominant one with a branching fraction of 60.19 % [142]. The branching fractions into $\sigma\,\pi$ and $f_0(1370)\,\pi$ are also large, whereas those into $\rho(770)\,\pi$ D-wave and $f_2(1270)\pi$ are small. This is consistent with our data, where the $a_1(1260)$ in the $1^{++}\,0^+\,\rho(770)\,\pi\,S$ wave is the by far largest resonance signal (see Fig. 4.10(a)). Hence the $1^{++}\,0^+\,\rho(770)\,\pi\,S$ wave plays a special role in the 14-wave resonance-model fit. Due to the extremely small statistical uncertainties of the $1^{++}\,0^+\,\rho(770)\,\pi\,S$ amplitude, the resonance model has difficulties to describe all details of the data. This applies in particular to the peak region in the intensity distribution as shown in Fig. 4.10(b). The intensity distributions of the $\rho(770)\pi$ S-wave in the 11 t' bins and the real and imaginary parts of the interference terms of this wave contribute together already about 25 % to the total χ^2 value of the model (see Eq. (3.87)). These deviations of the model from the data induce a multi-modal behavior of the minimization procedure and large systematic uncertainties on the resonance parameters of the $a_1(1260)$ and other resonances.

One of the challenges in describing the $1^{++}\,0^+\,\rho(770)\,\pi\,S$ intensity distribution is that the peak in the $a_1(1260)$ region changes its position and shape as a function of t'. This behavior is illustrated in Figs. 4.11(a) and 4.11(b). At low t', the peak sits at about $1.15\,\text{GeV}/c^2$ and shifts to higher masses with increasing t' up to about $1.30\,\text{GeV}/c^2$ in the highest t' bin. In addition, the peak narrows significantly. This demonstrates the necessity to perform a t'-resolved analysis. It is also a sign that the contribution from non-resonant processes to this partial-wave amplitude is large. Indeed, the fit finds a non-resonant component that is comparable in strength to the $a_1(1260)$ in the low and intermediate t' range and even dominant at high t'. The t' spectrum of the $a_1(1260)$ in the $1^{++}\,0^+$ $\rho(770)\,\pi\,S$ wave exhibits an approximately exponential dependence on t' (see Fig. 4.11(c)). However, the slope parameter has a value of $11.8\,^{+0.9}_{-4.2}\,\text{GeV}/c^2$, which is larger than what one would expect for a resonance. The value is similar to the slope parameter value of the non-resonant component in the $\rho(770)\,\pi$ S-wave. This might be a hint that the model is not able to completely separate the $a_1(1260)$ from the non-resonant component.

Since the $1^{++}\,0^+\,\rho(770)\,\pi\,S$ wave has a large contribution from non-resonant processes, the fit result depends strongly on the parametrization employed for the non-resonant

[a] Values from reviews of previous data were excluded from this counting.

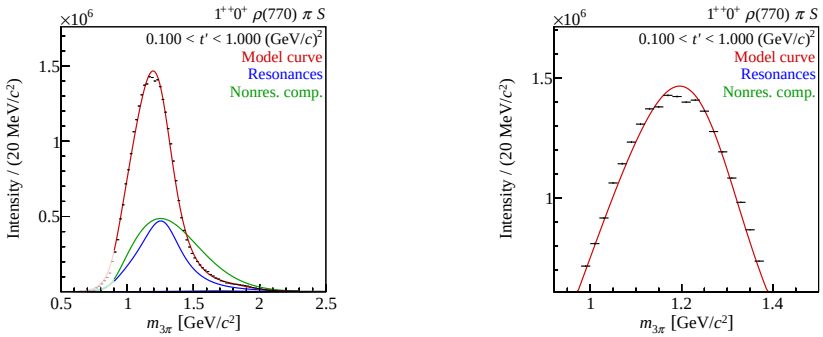

Figure 4.10: Intensity distribution of the $1^{++}\,0^+\,\rho(770)\,\pi\,S$ wave summed over the 11 t' bins. The curves represent the result of the resonance-model fit. The model and the wave components are represented as in Fig. 4.4. The dominant resonant component is the $a_1(1260)$; the $a_1(1640)$ is barely visible. (b) shows a zoomed view of (a). From Ref. [H3].

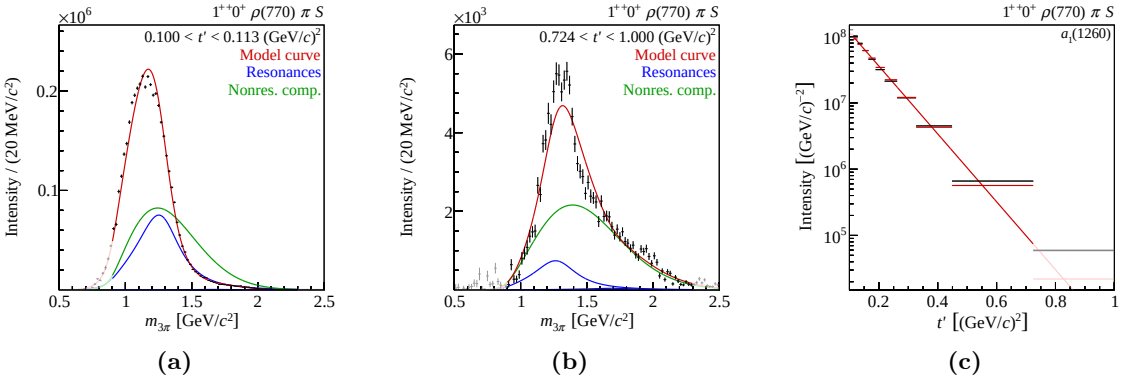

Figure 4.11: Intensity distribution of the $1^{++}\,0^+\,\rho(770)\,\pi\,S$ wave (a) in the lowest and (b) in the highest t' bin. The curves represent the result of the resonance-model fit. The model and the wave components are represented as in Fig. 4.4. The dominant resonant component is the $a_1(1260)$; the $a_1(1640)$ is barely visible. (c) similar to Fig. 4.4(c), but showing the t' spectrum of the $a_1(1260)$ in the $1^{++}\,0^+\,\rho(770)\,\pi\,S$ wave. From Ref. [H3].

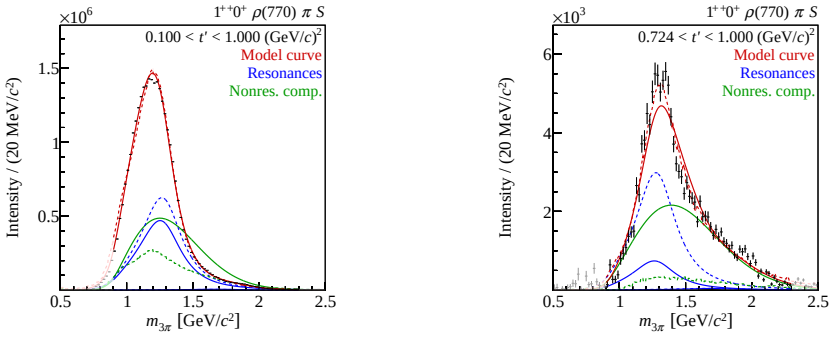

(a) **(b)**

Figure 4.12: Similar to Figs. 4.11(a) and 4.11(b). The dashed curves represent the result of a resonance-model fit where the parametrization of the non-resonant components is replaced by the square root of the intensity distribution as obtained from the partial-wave decomposition of Deck Monte Carlo data. From Ref. [H3].

component. We study this model dependence by performing a resonance-model fit, where the parametrization of the non-resonant components is replaced by the square root of the intensity distribution as obtained from the partial-wave decomposition of Deck Monte Carlo data (see Sec. 4.1.2). The result of this fit is shown as dashed curves in Fig. 4.12. The model describes the $1^{++}\,0^+\,\rho(770)\,\pi\,S$ intensity distributions well. At high t', the peak is described even better than in the main fit with the empirical parametrization of the non-resonant component (see Fig. 4.12(b)). The shapes of the non-resonant component in the various t' bins are similar to those in the main fit, but the yields are much smaller. In turn, the $a_1(1260)$ yields are significantly larger, in particular at high t'.

From the fit, we extract the resonance parameters $m_{a_1(1260)} = 1299\,^{+12}_{-28}\,\text{MeV}/c^2$ and $\Gamma_{a_1(1260)} = 380 \pm 80\,\text{MeV}/c^2$. The large systematic uncertainties are mostly due to the issues discussed above. Our mass value is compatible with the PDG estimate and our width value lies close to the center of the range estimated by the PDG.

4.2.4 The $a_1(1420)$

The $a_1(1420)$ is a surprising resonance-like signal that we discovered in the $1^{++}\,0^+\,f_0(980)\,\pi\,P$ wave [H1]. This is a peculiar decay mode. Only few light mesons are known to decay into $f_0(980)$, among them only two isovector mesons, the $\pi(1800)$ and the $\pi_2(1880)$ [13] (see Secs. 4.2.1 and 4.2.2). Hence the 88-wave PWA model includes only four waves with an $f_0(980)$ isobar (see Table 4.2), two of which, the $0^{-+}\,0^+$ and the $1^{++}\,0^+$ wave, are included in the resonance-model fit. The coherent sum of the four $f_0(980)$ waves, which have all positive reflectivity, contributes only 3.3 % to the total intensity. Most of this intensity is due to the $0^{-+}\,0^+\,f_0(980)\,\pi\,S$ wave (see Sec. 4.2.1). The $1^{++}\,0^+\,f_0(980)\,\pi\,P$ wave contributes only 0.3 % to the total intensity. This wave exhibits a narrow peak at about $1.4\,\text{GeV}/c^2$ (see Fig. 4.13(b)) that is associated by a rapid phase motion of about 180° with respect to other waves (see, e.g., Fig. 4.13(c)). Both features are robust against changes of the PWA model and other systematic effects (see Sec. IV F and Appendix B in Ref. [H2]).

The $a_1(1420)$ signal also appears in the freed-isobar PWA (see Sec. 3.3.8). Figure 4.14(a) shows the correlation of the $m_{\pi^-\pi^+}$ intensity distribution of the freed-isobar amplitude

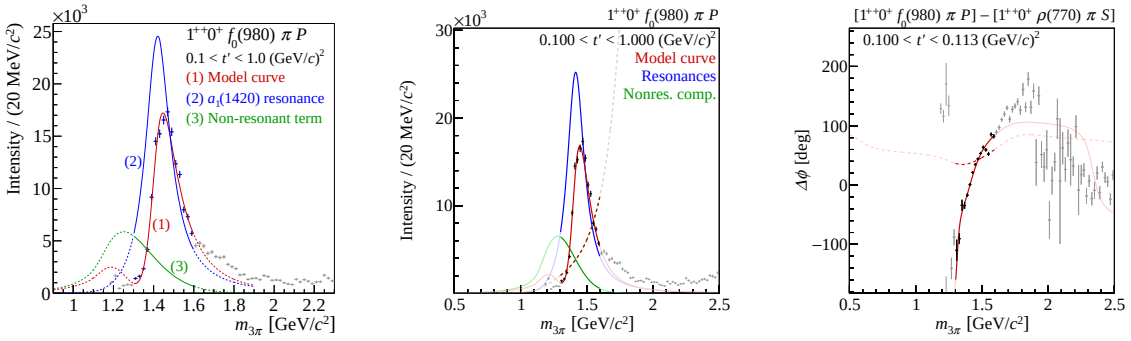

Figure 4.13: (a) and (b) intensity distribution of the $1^{++}\,0^+\,f_0(980)\,\pi\,P$ wave summed over the 11 t' bins; (c) phase of this wave with respect to the $1^{++}\,0^+\,\rho(770)\,\pi\,S$ wave in the lowest t' bin. The curves represent the result of three resonance-model fits. The model and the wave components are represented as in Fig. 4.4 except that the blue curves represent the $a_1(1420)$. (a) shows the result of the 3-wave fit from Ref. [H1], (b) and (c) the result of the 14-wave fit from Ref. [H3] (continuous curves). The dashed curves in (b) and (c) represent the result of a fit, where the $a_1(1420)$ component is removed from the resonance model. The dashed red curves correspond therefore to the non-resonant component. From Ref. [H3].

with $J^{PC} = 0^{++}$ quantum numbers in the $1^{++}\,0^+\,[\pi\pi]_{0^{++}}\,\pi\,P$ wave with the $m_{3\pi}$ intensity distribution of this wave. A clear peak is found at $m_{3\pi} \approx 1.4\,\text{GeV}/c^2$ and $m_{\pi^-\pi^+} \approx 1.0\,\text{GeV}/c^2$. The $m_{3\pi}$ intensity distribution in the $f_0(980)$ region, as shown in Fig. 4.14(b), exhibits a clear $a_1(1420)$ peak (cf. Fig. 4.13(b)). The resonant nature of the $\pi^-\pi^+$ subsystem at the $a_1(1420)$ mass is proven by the Argand diagram in Fig. 4.14(c), which exhibits a clear circular resonance structure in the highlighted $f_0(980)$ region. The results from the freed-isobar PWA confirm the $a_1(1420)$ signal and prove in particular that it is not an artificial structure caused by the parametrizations that are used for the $J^{PC} = 0^{++}$ isobars in the conventional 88-wave PWA fit.

The resonance features of the $a_1(1420)$ signal were first established in a much simpler resonance-model fit that included only three waves [H1]. The estimated Breit-Wigner parameters $m_{a_1(1420)} = 1414\,^{+15}_{-13}\,\text{MeV}/c^2$ and $\Gamma_{a_1(1420)} = 153\,^{+8}_{-23}\,\text{MeV}/c^2$ from the 3-wave fit are consistent with the parameters $m_{a_1(1420)} = 1411\,^{+4}_{-5}\,\text{MeV}/c^2$ and $\Gamma_{a_1(1420)} = 161\,^{+11}_{-14}\,\text{MeV}/c^2$ that are obtained in the 14-wave fit. This is illustrated in Figs. 4.13(a) and 4.13(b), which show the intensity distribution of the $1^{++}\,0^+\,f_0(980)\,\pi\,P$ wave summed over the 11 t' bins together with the two fit results. In both cases, the Breit-Wigner amplitude describes the $a_1(1420)$ peak well. This is also true for the observed phase motions of the $1^{++}\,0^+\,f_0(980)\,\pi\,P$ wave (see, e.g., Fig. 4.13(c)). Another feature of the data that supports the resonance interpretation of the $a_1(1420)$ signal is the approximately exponential behavior of its t' spectrum (see Fig. 4.15) with a slope parameter of $9.5\,^{+0.6}_{-1.0}\,(\text{GeV}/c)^{-2}$, which is a value in the range that is expected for resonances.

The interpretation of the $a_1(1420)$ signal is still unclear. It is too close in mass and too narrow in order to be the radial excitation of the ground-state $a_1(1260)$, i.e., the $2\,^3P_1$ state. Also the fact that the $a_1(1420)$ signal is about 20 times smaller than that of the $a_1(1260)$ in the $1^{++}\,0^+\,\rho(770)\,\pi\,S$ wave speaks against a $|q\bar{q}\rangle$ interpretation. It is peculiar that we find the $a_1(1420)$ signal only in the $f_0(980)\,\pi$ decay mode. The $f_0(980)$ is known

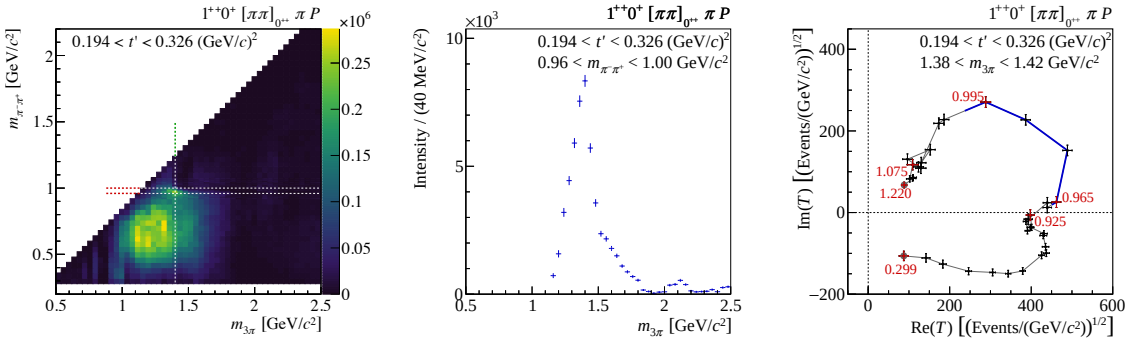

Figure 4.14: Amplitude of the $1^{++}\,0^{+}\,[\pi\pi]_{0^{++}}\,\pi\,P$ wave with the freed-isobar amplitude $[\pi\pi]_{0^{++}}$ in an intermediate t' bin. (a) two-dimensional representation of the intensity of this wave as a function of $m_{\pi^-\pi^+}$ and $m_{3\pi}$. (b) intensity as a function of $m_{3\pi}$ summed over a selected $m_{\pi^-\pi^+}$ interval around the $f_0(980)$ that is indicated by the pair of horizontal dashed lines in (a). (c) same as Fig. 4.1(b), but showing the Argand diagram of the freed-isobar amplitude for the $m_{3\pi}$ bin at the $a_1(1420)$ mass that is indicated by the vertical dashed line in (a). From Ref. [H2].

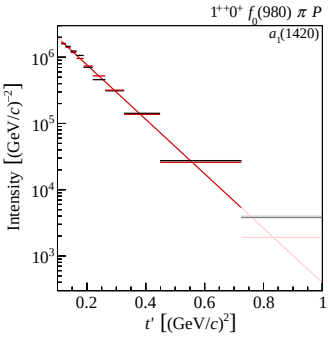

Figure 4.15: Similar to Fig. 4.4(c), but showing the t' spectrum of the $a_1(1420)$ in the $1^{++}\,0^{+}\,f_0(980)\,\pi\,P$ wave. From Ref. [H3].

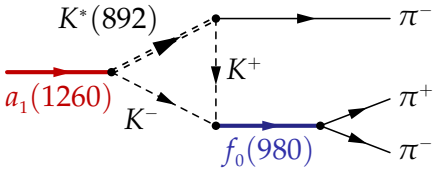

Figure 4.16: Rescattering diagram proposed in Refs. [42, 43] to explain the $a_1(1420)$ signal.

to have a large $s\bar{s}$ component and, as discussed in Sec. 1.6.3, is interpreted by some models as a tetraquark, a molecular state, or a mixture of both [61]. Another interesting aspect of the $a_1(1420)$ is that its mass is suspiciously close to the $K\overline{K}^*$ threshold.

Several interpretations have been proposed for the $a_1(1420)$. It could be the isospin partner of the $f_1(1420)$. This is supported by the mass of the $a_1(1420)$ and by its strong coupling to $f_0(980)$. The much smaller width of the $f_1(1420)$ of only $54.9 \pm 2.6\,\mathrm{MeV}/c^2$ can be explained by its strong coupling to $K\overline{K}^*$, which has a much smaller phase space than the decay $a_1(1420) \to f_0(980)\,\pi$. The molecular model for the $f_1(1420)$ proposed in Ref. [143] could possibly be extended to the isovector case. Isovector $[n\,n]\,[\overline{n}\,\overline{n}]$ and $[n\,s]\,[\overline{n}\,\overline{s}]$ states with $n = u$ or d were predicted in the $1.4\,\mathrm{GeV}/c^2$ mass range in quark-model calculations that include tetraquark states [144]. The $a_1(1420)$ signal has also been described as a mixed state of a $q\bar{q}$ and a tetraquark component [145] and as a tetraquark with mixed flavor symmetry [146]. In addition, calculations based on the AdS/QCD approach find isovector tetraquarks with masses similar to that of the $a_1(1420)$ [147, 148]. The authors of Ref. [149] studied the two-body decay rates for the modes $a_1(1420) \to f_0(980)\pi$ and $a_1(1420) \to K\overline{K}^*(892)$ for four-quark configurations using the covariant confined quark model. They found that a molecular configuration is preferred over a compact diquark-antidiquark state.

In addition to the resonance interpretations discussed above, other explanations do not require an additional a_1 resonance. Basdevant and Berger proposed resonant rescattering corrections in the Deck process as an explanation [150, 151], whereas the authors of Ref. [42] suggested an anomalous triangle singularity in the rescattering diagram for $a_1(1260) \to K\overline{K}^*(892) \to K\overline{K}\pi \to f_0(980)\pi$, which is shown in Fig. 4.16. The results of the latter calculation were confirmed in Ref. [43]. Preliminary studies show that the amplitude for the triangle diagram describes the data equally well as the Breit-Wigner model. In the case of a triangle singularity, the production rate of the $a_1(1420)$ would be completely determined by the production rate of the $a_1(1260)$. Therefore, the slope parameters of the two wave components should be equal. Unfortunately, in our analysis the systematic uncertainties of the slope parameters are too large in order to draw any conclusion.[b] Hence more detailed studies are still needed in order to distinguish between different models for the $a_1(1420)$.

4.2.5 The $\pi_1(1600)$

As mentioned in Sec. 1.6.3, the spin-exotic $\pi_1(1600)$ is a controversial state. The 88-wave set includes one partial wave with $J^{PC} = 1^{-+}$ and positive reflectivity. This $1^{-+}\,1^+\,\rho(770)\,\pi\,P$ wave contributes 0.8 % to the total intensity. As shown in Figs. 4.17(a) and 4.17(b), the shape of the intensity distribution of this wave has a surprisingly strong dependence on t'. At low t', the intensity distribution exhibits a broad structure with a maximum at about $1.2\,\mathrm{GeV}/c^2$ (see Fig. 4.17(a)). This structure becomes narrower with increasing t' and the maximum moves to higher masses, such that a peak emerges at about $1.6\,\mathrm{GeV}/c^2$ in the two highest t' bins (see Fig. 4.17(b)). This t' dependence of the intensity distribution illustrates the necessity for performing the analysis in narrow t' bins. It also indicates that, in addition to potential resonant components, this wave contains large contributions from non-resonant processes. This is consistent with the fact that we do not observe large phase motions with respect to other waves in the $1.6\,\mathrm{GeV}/c^2$ region (see, e.g., Fig. 4.17(c)).

[b] The $a_1(1260)$ in the dominant $1^{++}\,0^+\,\rho(770)\,\pi\,S$ wave has a slope parameter of $11.8\,^{+0.9}_{-4.2}\,(\mathrm{GeV}/c)^{-2}$.

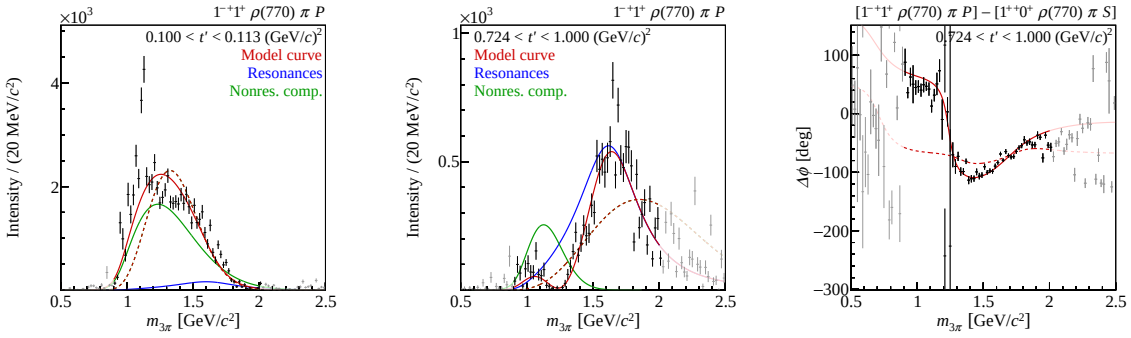

(a) **(b)** **(c)**

Figure 4.17: (a) and (b) intensity distribution of the $1^{-+}\,1^{+}\,\rho(770)\,\pi\,P$ wave in the lowest and highest t' bins, respectively. (c) phase of the this wave relative to the $1^{++}\,0^{+}\,\rho(770)\,\pi\,S$ wave in the highest t' bin. The curves represent the result of two resonance-model fits. The model and the wave components are represented as in Fig. 4.4 except that the blue curves represent the $\pi_1(1600)$. The result of the 14-wave resonance-model fit is represented by the continuous curves. The dashed curves represent the result of a fit, where the $\pi_1(1600)$ component is removed from the resonance model. The dashed red curves correspond therefore to the non-resonant component. From Ref. [H3].

The strong modulation of the shape of the 1^{-+} intensity distribution with t' is successfully reproduced by the resonance model as a t'-dependent interference of a $\pi_1(1600)$ Breit-Wigner amplitude as in Eq. (1.23) and a non-resonant component parametrized using Eq. (3.79). The dashed curves in Fig. 4.17 represent the result of a fit, where the $\pi_1(1600)$ resonance component is omitted from the model so that only the non-resonant component remains in this wave. Although the intensity distribution is still roughly reproduced by the model at low t' (see Fig. 4.17(a)), it fails to reproduce the phases (see, e.g., Fig. 4.17(c)) and the intensity distributions at higher t' (see Fig. 4.17(b)). This demonstrates that the data require a resonant component in the 1^{-+} wave.

The shape of the non-resonant component and its intensity and phase relative to the $\pi_1(1600)$ component change strongly with t'. The latter is illustrated by Fig. 4.18(a), which shows that the coupling phase of the non-resonant component with respect to the $\pi_1(1600)$ (see Eq. (3.83)) changes by more than 180° over the analyzed t' range. In contrast, the coupling phase of the $\pi_1(1600)$ component behaves similar to that of other resonances in the model (see Fig. 4.18(b)).

Due to the large contribution of the non-resonant component to the 1^{-+} intensity, especially at low t', the fit result depends strongly on the parametrization used for the non-resonant component. This model dependence is studied by replacing the parametrizations of the non-resonant components by the square root of the intensity distribution as obtained from the partial-wave decomposition of Deck Monte Carlo data (see Sec. 4.1.2). The result of this study is represented by the dashed curves in Fig. 4.19. Compared to the main fit with the empirical parametrizations of the non-resonant components, the description of the 1^{-+} amplitude is only slightly worse. The non-resonant component has a qualitatively similar dependence on t' and has shapes similar to those in the main fit. Only in the highest t' bin, the non-resonant component has a different, actually more plausible shape than found in the main fit. In the Deck study, the yield of the non-resonant component is significantly lower whereas the yield of the $\pi_1(1600)$ is significantly higher than in the

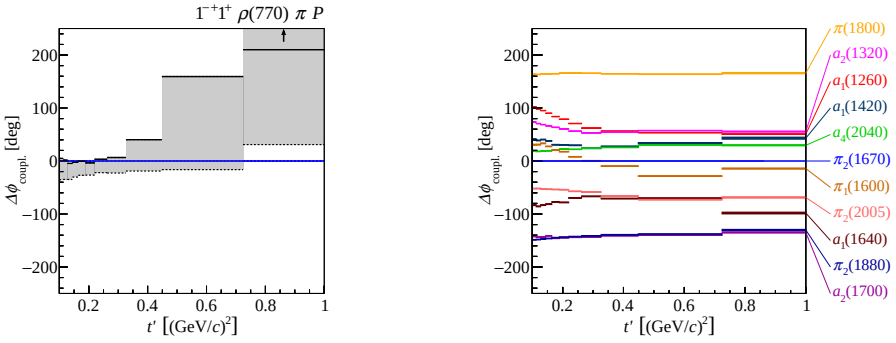

(a) **(b)**

Figure 4.18: (a) t' dependence of the coupling phase of the non-resonant component (black lines) in the $1^{-+}\,1^{+}\,\rho(770)\,\pi\,P$ wave relative to the $\pi_1(1600)$ (see Eq. (3.83)). The magnitude of systematic effects is illustrated qualitatively by two sets of dashed lines with shaded area in between (see Sec. VII A in Ref. [H3]). (b) t' dependence of the coupling phases of the 11 resonance components in the fit model with respect to the $\pi_2(1670)$. The coupling phases are shown for the resonance components in the dominant wave of the respective J^{PC} sector: $0^{-+}\,0^{+}\,f_0(980)\,\pi\,S$, $1^{++}\,0^{+}\,\rho(770)\,\pi\,S$, $1^{-+}\,1^{+}\,\rho(770)\,\pi\,P$, $2^{++}\,1^{+}\,\rho(770)\,\pi\,D$, $2^{-+}\,0^{+}\,f_2(1270)\,\pi\,S$, and $4^{++}\,1^{+}\,\rho(770)\,\pi\,G$. The only exception is the $a_1(1420)$, which appears only in the $1^{++}\,0^{+}\,f_0(980)\,\pi\,P$ wave. The width of the horizontal lines represents the statistical uncertainty. The systematic uncertainty is not shown. From Ref. [H3].

main fit. This shows that in the employed resonance model, the $\pi_1(1600)$ yield has a large systematic uncertainty.

The t' spectrum of the non-resonant component falls steeply with t' and has an exceptionally large slope parameter value of $19.1\,^{+1.4}_{-4.7}\,(\text{GeV}/c)^{-2}$ (black lines in Fig. 4.20(a)). Hence the non-resonant component dominates the 1^{-+} intensity at low t'. Only for $t' \gtrsim 0.3\,(\text{GeV}/c)^2$, the intensity of the $\pi_1(1600)$ component (black lines in Fig. 4.20(a)) becomes larger than that of the non-resonant component. The simple model in Eq. (3.82) is not able to reproduce the downturn of the $\pi_1(1600)$ t' spectrum toward low t'. However, this might be an artificial effect caused by an inappropriate description of the non-resonant component by our parametrizations. It seems that the fit is not be able to completely separate the $\pi_1(1600)$ from the non-resonant component, which dominates at low t'. This hypothesis is supported by the study discussed above, where the shape of the non-resonant component is determined from a model of the Deck process (see Fig. 4.20(b)). In this study, the $\pi_1(1600)$ has a larger yield at low t' so that the resulting t' spectrum of the $\pi_1(1600)$ is well described by the exponential model in Eq. (3.82) and has a slope parameter of $7.3\,(\text{GeV}/c)^{-2}$, which lies in the range expected for resonances.

Not only the yield of the $\pi_1(1600)$ is susceptible to systematic effects but also its Breit-Wigner parameters. The resonance-model fit results in $\pi_1(1600)$ Breit-Wigner parameters of $m_{\pi_1(1600)} = 1600\,^{+110}_{-60}\,\text{MeV}/c^2$ and $\Gamma_{\pi_1(1600)} = 580\,^{+100}_{-230}\,\text{MeV}/c^2$ that have large systematic uncertainties. This mainly reflects the limitations of our current analysis model. While our mass value is compatible with the PDG world average [13]. Our measured width is larger than the PDG value of $241 \pm 40\,\text{MeV}/c^2$.

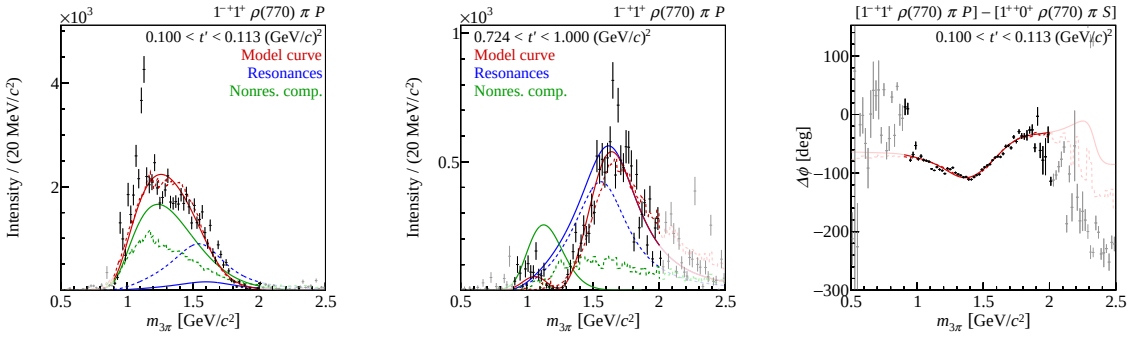

(a) **(b)** **(c)**

Figure 4.19: Similar to Fig. 4.17, except that the phase is shown for the lowest t' bin. Here, the dashed curves represent the result of a resonance-model fit, where the parametrization of the non-resonant components is replaced by the square root of the intensity distribution as obtained from the partial-wave decomposition of Deck Monte Carlo data. From Ref. [H3].

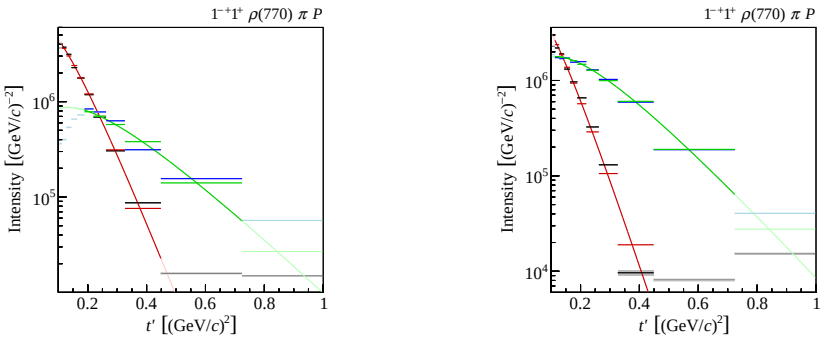

(a) **(b)**

Figure 4.20: Similar to Fig. 4.4(c), but showing the t' spectra of the two components in the $1^{-+}\,1^{+}\,\rho(770)\,\pi\,P$ wave. The $\pi_1(1600)$ component is shown as blue lines and light blue boxes, and the non-resonant component as black lines and gray boxes. (a) result of the main fit. (b) result of a fit, in which the parametrization of the non-resonant amplitude is replaced by the square root of the intensity distribution as obtained from the partial-wave decomposition of Deck Monte Carlo data. From Ref. [H3].

4.2.5.1 Comparison with previous analyses

As already mentioned in Sec. 1.6.3, the $\pi_1(1600)$ is the best established of the three known spin-exotic light-meson candidates. It has been observed by several experiments in various decay modes. The COMPASS, E852, and VES experiments have studied high-energy inelastic scattering reactions of pion beams on nuclear targets and have reported signals in the $\rho(770)\,\pi$ [128,152,153], $\eta'(958)\,\pi$ [154,155], $b_1(1235)\,\pi$ [132,155], and $f_1(1285)\,\pi$ [139,155] decay modes. In an analysis of Crystal Barrel data on the reaction $p\bar{p} \to \omega\pi^+\pi^-\pi^0$, the authors of Ref. [156] also reported evidence for the $\pi_1(1600)$ in the $b_1(1235)\,\pi$ decay mode. The CLEO-c experiment has studied the decays of the charmonium state χ_{c1} to $\eta\pi^+\pi^-$ and $\eta'\pi^+\pi^-$ [157]. They found evidence for an exotic signal in the $\eta'\,\pi$ subsystem consistent with the $\pi_1(1600)$ signal seen in other production mechanisms. A recent summary of all measurements can be found in Ref. [45].

Although $\pi_1(1600)$ signals were claimed in various final states measured by several experiments, in most of these analyses the resonance interpretation of the $\pi_1(1600)$ relies on model assumptions and alternative explanations could not be ruled out completely. Hence the experimental situation is actually rather unclear. Particularly controversial is the $\pi_1(1600)$ signal in the $\rho(770)\,\pi$ channel. The BNL E852 experiment used an $18\,\text{GeV}/c$ pion beam incident on a proton target and was the first to claim a signal for $\pi_1(1600) \to \rho(770)\,\pi$ with $m_{\pi_1(1600)} = 1593 \pm 8\,(\text{stat.})\,^{+29}_{-47}\,(\text{sys.})\,\text{MeV}/c^2$ and $\Gamma_{\pi_1(1600)} = 168 \pm 20\,(\text{stat.})\,^{+150}_{-12}\,(\text{sys.})\,\text{MeV}/c^2$ based on a PWA performed in the kinematic range $0.1 < t' < 1.0\,(\text{GeV}/c)^2$ [128, 152]. The VES experiment used a $37\,\text{GeV}/c$ pion beam on a solid-beryllium target and performed the PWA in the kinematic range $0.03 < t' < 1.0\,(\text{GeV}/c)^2$ [158]. They also observed significant intensity in the $1^{-+}\,1^+\,\rho(770)\,\pi\,P$ wave (see Fig. 4.21(a)). However, they found that the intensity distribution in this wave depends significantly on the PWA model and hence concluded that the wave is contaminated by intensity that leaks from the dominant 1^{++} waves into the 1^{-+} wave. They neither excluded nor claimed the existence of the $\pi_1(1600)$. However, a later analysis of a BNL E852 data sample that was about an order or magnitude larger than the one used in Refs. [128, 152] came to the conclusion that there is no $\pi_1(1600)$ signal in the $\rho(770)\,\pi$ channel [159]. The authors of Ref. [159] performed systematic studies to find the optimal wave set and found that in the original BNL E852 analysis in Refs. [128, 152] a number of important waves were missing in the PWA model. When they included these waves in the PWA model, the peak at about $1.6\,\text{GeV}/c^2$ in the $1^{-+}\,1^+\,\rho(770)\,\pi\,P$ wave disappeared. However, the slow phase motions with respect to other waves remained. This is shown in Fig. 4.21(c) for the kinematic range $0.18 < t' < 0.23\,(\text{GeV}/c)^2$, where the "low wave" points are the result of a PWA fit performed with the smaller wave set from Refs. [128,152] and the "high wave" points are the result of a PWA fit performed with the larger wave set from Ref. [159]. Based on this observation, the authors of Ref. [159] concluded that there is no evidence for a $\pi_1(1600)$ in this wave. For the discussion below it is important to note that this conclusion was based on a PWA performed in the range $t' < 0.53\,(\text{GeV}/c)^2$. In contrast, the first analysis of data from the COMPASS experiment using a $190\,\text{GeV}/c$ pion beam on a solid-lead target showed again evidence for a $\pi_1(1600)$ signal with $m_{\pi_1(1600)} = 1660 \pm 10\,(\text{stat.})\,^{+0}_{-64}\,(\text{sys.})\,\text{MeV}/c^2$ and $\Gamma_{\pi_1(1600)} = 269 \pm 21\,(\text{stat.})\,^{+42}_{-64}\,(\text{sys.})\,\text{MeV}/c^2$ [153] although the PWA model contained even more partial waves than the one used in Ref. [159] (see Fig. 4.21(e)).

The results from our analysis as presented in Sec. 4.2.5 explain the seemingly contradictory experimental findings of the BNL E852, VES, and COMPASS experiments concerning

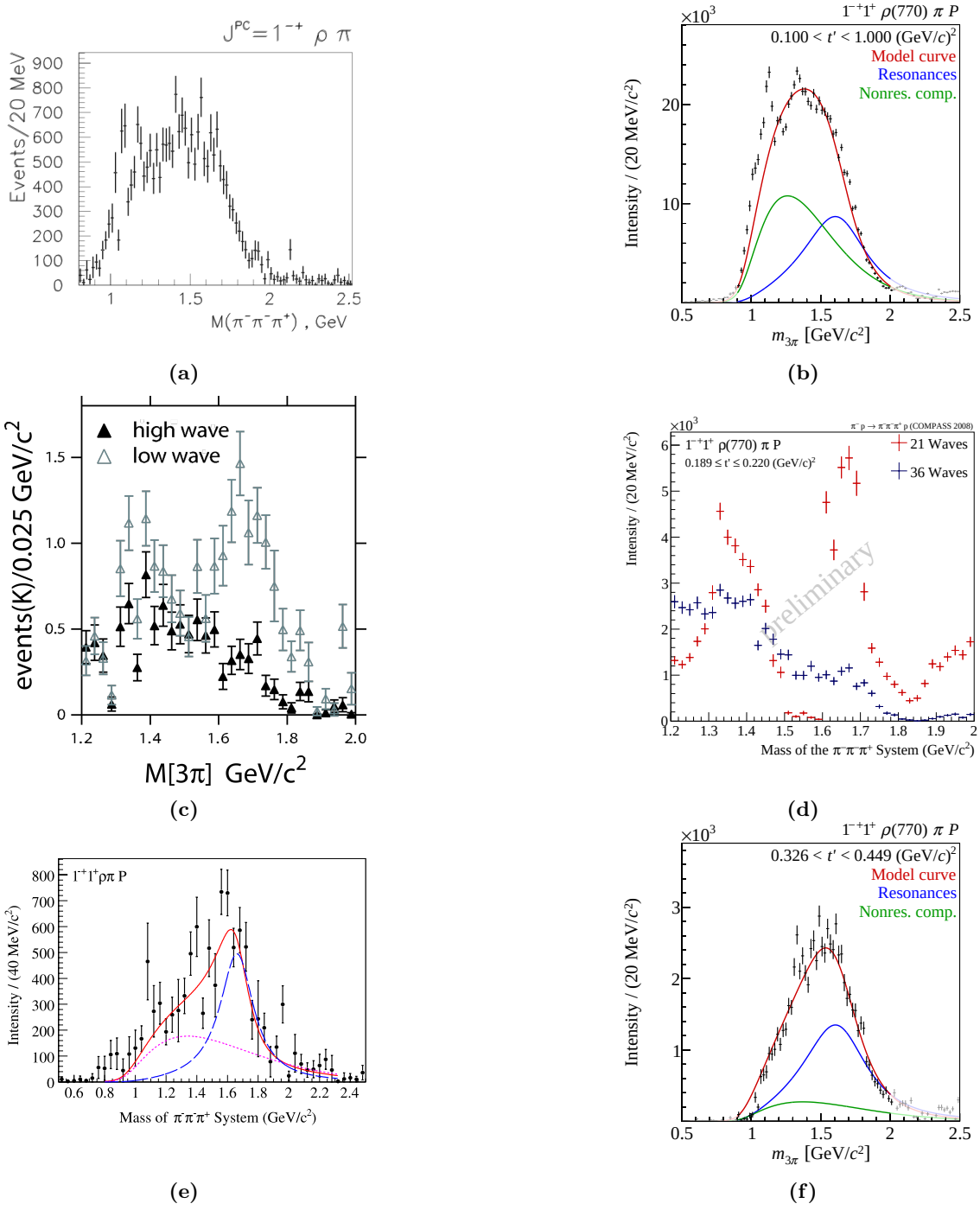

Figure 4.21: Comparison of intensity distributions of the $1^{-+}\,1^+\,\rho(770)\,\pi\,P$ wave obtained by different experiments measuring the diffractive dissociation of a pion beam into 3π. (a) result from an analysis of VES data. From Ref. [158]. (b) result from an analysis of COMPASS data using a proton target; intensity summed over the 11 t' bins. From Ref. [H3]. (c) results from an analysis of BNL E852 data using two different PWA models. From Ref. [159]. (d) results from an analysis of COMPASS proton-target data using the same two PWA models as in (c). The 21-wave set corresponds to "low wave", the 36-wave set to "high wave". From Ref. [73]. (e) and (f) results from analyses of COMPASS data (e) using a solid-lead target and integrating over $0.1 < t' < 1.0\,(\mathrm{GeV}/c)^2$ (from Ref. [153]) and (f) using a proton target, second highest t' bin (from Ref. [H3]).

the existence of a $\pi_1(1600)$ resonance in the $\rho(770)\,\pi$ P-wave. Figure 4.21(b) shows that our intensity distribution of the $1^{-+}\,1^+\,\rho(770)\,\pi\,P$ wave summed over the 11 t' bins is very similar to the one found in the VES analysis [158] (cf. Fig. 4.21(a)). In Fig. 4.21(d), we show the intensity of the $1^{-+}\,1^+\,\rho(770)\,\pi\,P$ wave in the range $0.18 < t' < 0.23\,(\mathrm{GeV}/c)^2$ that is obtained if we perform the PWA using the same two wave sets as in Ref. [159]. The similarity of the results with Fig. 4.21(c) confirms that the $\pi_1(1600)$ signal in the original BNL E852 analysis in Refs. [128, 152] was mostly an artificial structure caused by leakage of intensity from 2^{-+} waves that were missing from the PWA model. We also confirm the finding of Refs. [128, 152] that in the region $t' \lesssim 0.5\,(\mathrm{GeV}/c)^2$ there is only weak evidence for the $\pi_1(1600)$. However, our data show that a resonance-like signal is required to describe the data in the region $t' \gtrsim 0.5\,(\mathrm{GeV}/c)^2$ (see Figs. 4.17(b) and 4.17(c)). This t' region was excluded from the analysis in Ref. [159]. In the COMPASS data taken with a solid-lead target, the contribution of the non-resonant component is much smaller than in the proton-target data. The t'-integrated lead-target data actually resemble the high-t' region of the proton data (compare Figs. 4.21(e) and 4.21(f)). So far, no explanation has been found for this effect.

Another mystery is that the $\pi_1(1600)$ does not seem to be produced in photon-induced reactions. The CLAS experiment did not observe a $\pi_1(1600)$ signal in the charge-exchange reaction $\gamma + p \to \pi^+\pi^+\pi^- + (n)_{\mathrm{miss}}$ [160, 161] (see Fig. 4.22(a)). This finding is supported by an analysis of COMPASS data of the reaction $\pi^- + \mathrm{Pb} \to \pi^-\pi^-\pi^+ + \mathrm{Pb}$ at reduced squared four-momentum transfer $t' < 10^{-3}\,\mathrm{GeV}^2$, where photon exchange is dominant [162] (see Fig. 4.22(b)). In both processes, the dominant underlying reaction is $\gamma + \pi^- \to \pi^-\pi^-\pi^+$. Since we observe the $\pi_1(1600)$ to decay into $\rho(770)\,\pi$, it should couple to $\gamma\,\pi$ via vector-meson dominance. In addition, the $\pi_1(1600)$ is a hybrid candidate and is compatible with the lightest 1^{-+} hybrid state predicted by lattice QCD (see Sec. 1.6.3 and Fig. 1.9). However, the production of hybrids is believed to be enhanced in photo-induced reactions [163, 164]. This is mainly because the photon fluctuates into a quark-antiquark pair with $J^{PC}_{q\bar{q}} = 1^{--}$ quantum numbers. Lattice QCD (see Sec. 1.6.3) and also many models predict that the lowest excitation of the gluon field in a hybrid meson has $J^{PC}_g = 1^{+-}$ quantum numbers. Hence the $q\bar{q}$ pair and the gluonic excitation can directly couple to spin-exotic $J^{PC} = 1^{-+}$ quantum numbers, which is not the case for pion-induced reactions. An interesting feature of the photo-production data is that the intensity vanishes nearly completely in the $1.6\,\mathrm{GeV}/c^2$ region. This could be a sign of destructive interference of a $\pi_1(1600)$ with non-resonant components. This hypothesis could be verified by performing a resonance-model fit on the existing data. In the future, much more precise photo-production data from the GlueX experiment at JLab will help to clarify the situation.

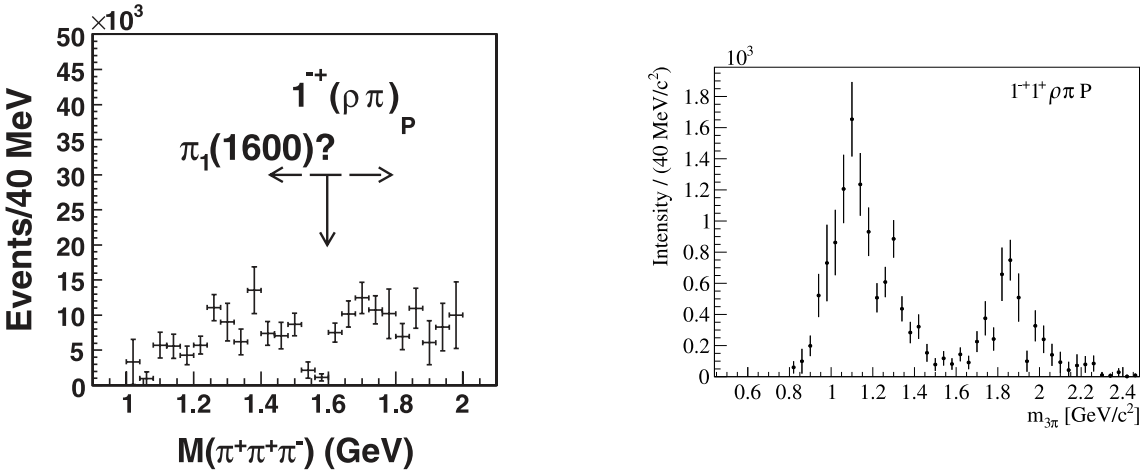

(a) (b)

Figure 4.22: Intensities of the $1^{-+}\,1^{+}\,\rho(770)\,\pi\,P$ wave produced in $\gamma + \pi^- \to \pi^-\pi^-\pi^+$ reactions. (a) result from the CLAS experiment, where the process is embedded into $\gamma + p \to \pi^+\pi^+\pi^- + (n)_{\text{miss}}$. From Ref. [160]. (b) result from the COMPASS experiment, where the process is embedded into $\pi^- + \text{Pb} \to \pi^-\pi^-\pi^+ + \text{Pb}$. From Ref. [162].

Chapter 5

Conclusions and outlook

In this work, we have performed the so far most comprehensive and most detailed partial-wave analysis of the 3π final state. The analysis is based on the currently largest $\pi^-\pi^-\pi^+$ data sample of 46×10^6 exclusive events of the diffractive dissociation reaction $\pi^- + p \to \pi^-\pi^-\pi^+ + p$ that was acquired by the COMPASS experiment.

The analysis was performed in two stages. In the first stage, the data are decomposed into partial-wave amplitudes with well-defined quantum numbers. This decomposition is based on a PWA model with 88 partial waves: 80 waves with positive reflectivity, 7 with negative reflectivity, and one incoherent wave that is isotropic in the phase space and represents uncorrelated three pions (see Table 4.2). This is the largest wave set used so far in a PWA of 3π final states. The partial-wave decomposition is performed independently in 100 bins of the $\pi^-\pi^-\pi^+$ invariant mass $m_{3\pi}$ in the range $0.5 < m_{3\pi} < 2.5\,\mathrm{GeV}/c^2$. Each $m_{3\pi}$ bin is subdivided further into 11 bins of the reduced squared four-momentum transfer t' in the range $0.1 < t' < 1.0\,(\mathrm{GeV}/c)^2$.

In the second stage of the analysis a Breit-Wigner resonance-model fit was performed for a subset of 14 selected partial waves with $J^{PC} = 0^{-+}$, 1^{++}, 2^{++}, 2^{-+}, 4^{++}, and spin-exotic 1^{-+} quantum numbers. The 14 waves are described simultaneously using 11 resonances taking into account all mutual interference terms. Compared to previous analyses of the 3π final state, this is the by far largest wave set that is consistently described in a single resonance-model fit. We have measured the masses and widths of the a_J-like resonances: $a_1(1260)$, $a_1(1640)$, $a_2(1320)$, $a_2(1700)$, $a_4(2040)$, and of the resonance-like $a_1(1420)$ (see Fig. 4.3(a) and Table 4.5); and those of the π_J-like resonances: $\pi(1800)$, $\pi_2(1670)$, $\pi_2(1880)$, $\pi_2(2005)$, and the spin-exotic $\pi_1(1600)$ (see Fig. 4.3(b) and Table 4.5). Extensive studies were performed in order to estimate the systematic uncertainties.

The parameters of $a_1(1420)$, $a_2(1320)$, $a_4(2040)$, $\pi(1800)$, and $\pi_2(1670)$ are reliably extracted with comparatively small uncertainties. The consistency of the $a_1(1420)$ signal with a Breit-Wigner amplitude is confirmed. The $a_1(1420)$ parameter values are consistent with those from a simpler analysis of the same data in Ref. [H1], but have smaller uncertainties. The $a_2(1320)$ and $\pi(1800)$ parameter values are consistent with previous measurements. The measured values of the $a_4(2040)$ mass and width are the most accurate so far. We find a lower $a_4(2040)$ mass and a larger width than some of the previous experiments. The decay of the $\pi_2(1880)$ into 3π is demonstrated for the first time. The $\pi_2(1880)$ is found to decay into $f_2(1270)\,\pi$ D-wave, $f_0(980)\,\pi$ D-wave, and $f_0(1500)\,\pi$ D-wave. Its coupling to the $\rho(770)\,\pi$ P-wave and $f_2(1270)\,\pi$ S-wave decay modes is found to be small. The

measured $\pi_2(1880)$ width is consistent with the world average, the mass is found to be smaller.

The data require a spin-exotic resonance, the $\pi_1(1600)$, in the $1^{-+}\,1^+\,\rho(770)\,\pi\,P$ wave. The t'-resolved analysis allows us to establish for the first time that a significant $\pi_1(1600)$ signal appears only for $t' \gtrsim 0.5\,(\mathrm{GeV}/c)^2$, whereas at low t' the intensity of the spin-exotic wave is saturated by Deck-like non-resonant contributions. The $\pi_1(1600)$ parameters have large uncertainties. The measured width is significantly larger than that observed in previous experiments including our own result from the data taken with a solid-lead target, but it has a large systematic uncertainty toward smaller values. In the future, it would be interesting to study potential $\pi_1(1600)$ signals in COMPASS data in the $\pi^-\pi^0\pi^0$, $\pi^-\,\eta$, $\pi^-\,\eta'(958)$, $\pi^-\pi^0\omega(782)$, and $\pi^-\,f_1(1285)$ final states.

The resonance-model fit is based on a novel approach, which, for the first time, takes into account the different t' dependences of the amplitudes of the resonant and non-resonant wave components in a model-independent way. This is achieved by performing the resonance-model fit simultaneously in the 11 t' bins, so that the t' dependence of the amplitude of each wave component is extracted from the data. This t'-resolved analysis approach allows us to study the production mechanism of resonances in unprecedented detail in terms of the t' spectra of the wave components and the t' dependences of relative phases between the wave components. The latter ones are measured for the first time. Most resonances, including the $a_1(1420)$, are produced with a phase that is approximately independent of t', which is expected if the production mechanism is the same over the analyzed t' range. With the t'-resolved approach, we also take into account the change of the shape of the $m_{3\pi}$ intensity distributions of the partial waves with t', which for some waves is very pronounced. Hence our approach avoids the potential broadening of resonance peaks and the artificial incoherences between the waves and the wave components that may have lead to dilutions and distortions of resonance signals in previous analyses. Our approach not only avoids these issues but also exploits the generally different t' dependences of the resonant and non-resonant wave components in order to better disentangle the two.

Due to the highly precise COMPASS data, the analysis results are dominated by systematic uncertainties. We pursue two strategies in order to reduce these uncertainties: (i) by reducing the model dependence and (ii) by employing more advanced models that incorporate more physical constraints.

In case of the resonance-model fit, one would actually like to extract resonance poles on the second Riemann sheet of the scattering amplitude in the complex s plane instead of model- and process-dependent Breit-Wigner parameters. This requires amplitudes that adhere to the principles of the relativistic S-matrix, in particular analyticity and unitarity. Such amplitudes are currently developed, for example, by the members of the Joint Physics Analysis Center (JPAC) [165–167]. A first successful application of such a model to the $\eta\pi$ D-wave intensity distribution extracted from COMPASS data yielded pole positions for the $a_2(1320)$ and $a_2(1700)$ [168]. Another significant source of systematic uncertainty in the resonance-model fit is the parametrization of the non-resonant components. Hence the development of improved models for double-Regge processes, such as the Deck effect, is also a topic of current research.

In order to reduce the model dependence of the partial-wave decomposition in the first analysis stage, we developed the novel freed-isobar PWA method. With this method, we are able to extract the dynamical amplitudes of two-body subsystems with well-defined J^{PC} quantum numbers in a given three-body partial wave also with well-defined quantum

numbers. We applied this method to the COMPASS data in order to study the isoscalar $J^{PC} = 0^{++}$ $\pi^-\pi^+$ isobars, i.e., f_0 states, in the $\pi^-\pi^-\pi^+$ system. Comparing the result of the freed-isobar PWA with the one of the conventional PWA, where the 0^{++} isobars are described by fixed parametrizations, we found good qualitative agreement. This shows that the parametrizations employed in the conventional analysis do not strongly deviate from the data and do not cause artificial resonance-like structures in the extracted partial-wave amplitudes. This is in particular true for the novel $a_1(1420)$ signal, which is confirmed by the freed-isobar PWA. With this method, we also establish for the first time the decay modes $\pi(1800) \to f_0(1500)\,\pi \to 3\pi$, $\pi_2(1880) \to f_0(980)\,\pi \to 3\pi$, and $\pi_2(1880) \to f_0(1500)\,\pi \to 3\pi$.

The freed-isobar approach actually marks a paradigm shift in how multi-body PWAs are performed. Instead of constructing a PWA model, where one has to decide which isobar resonances to include and which parametrizations and resonance parameters to use, one can now extract these information from the data. This reduces not only the model dependence drastically but also the dependence on external information from other experiments. This allows, for example, to study decay modes that proceed via radially excited isobar states, such as the $f_0(1500)$ in our analysis. One can also measure isobar parameters and branching fractions. In addition, one can study the effect of final-state interactions. The interaction of the isobar with the bachelor pion may lead to measurable distortions of the $\pi^-\pi^+$ amplitudes. With the freed-isobar PWA, these effects can be studied as a function of $m_{3\pi}$ and t' and models of final-state interactions can be tested more directly. In first studies using simple Breit-Wigner amplitudes to describe isobar resonances, a dependence of the Breit-Wigner parameters on $m_{3\pi}$ was found [118]. These studies included not only f_0-like 0^{++} isobars, but also $\rho(770)$-like 1^{--} and f_2-like 2^{++} isobars.

In freed-isobar fits with many freed waves, the PWA model may exhibit mathematical ambiguities at the amplitude level. However, these ambiguities can be identified and resolved [94]. The freed-isobar method is hence a universal tool that is directly applicable to any three-body decay. The only limitation is that large data samples are required. The method is in particular applicable to three-body decays of heavy mesons. Due to the ambiguity issue, it has been used up to now only for single isobars and mostly as a verification tool to prove the resonant nature of interesting signals. Examples of such analyses are the discovery of two pentaquark-like states $P_c(4380)$ and $P_c(4450)$ [169] (see Fig. 5.1) and the observation of the flavor-exotic four-quark-like state $Z_c(4430)^-$ [170], both by the LHCb experiment. Since the ambiguities can now be identified and resolved, the freed-isobar approach can now be used to extract quantitative information while at the same time making the analysis more model-independent. This could improve in particular analyses that search for CP violation in three-body decays of heavy mesons. Concerning our freed-isobar PWA of the COMPASS $\pi^-\pi^-\pi^+$ data, it would be highly interesting to compare our results to a corresponding analysis of, for example, $D \to 3\pi$ or $\tau \to 3\pi\,\nu_\tau$. Such a comparison would allow to better separate the effects from final-state interaction of the three final-state pions from the effects that are caused by the non-resonant contributions because the latter ones are basically absent in the D and τ decays. A comparison of these processes would also help to better understand the $a_1(1260)$ resonance, which is one of the largest sources of systematic uncertainty in our analysis.

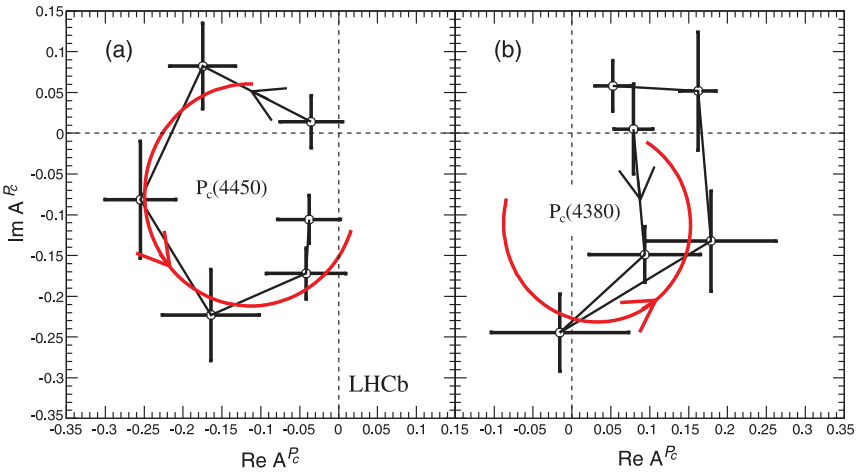

Figure 5.1: Argand diagram of the freed-isobar amplitude for the $J/\psi\, p$ subsystem (a) with $J^P = 5/2^+$ and (b) with $3/2^-$ in $\Lambda_b^0 \to J/\psi K^- p$ decays (similar to Fig. 4.1(b)). The red curves are predictions from Breit-Wigner amplitudes with mass and width values as obtained in the conventional Dalitz-plot analysis. From Ref. [169].

Own contributions

All the work presented in this thesis originated in the COMPASS collaboration, of which I am a member since 1999. For the three articles [H1–H3] that this thesis is based on, I was one of the principal contributors, the main editor, and the head of the drafting committee.

Reference [H2] is based on the results from the PhD theses by Florian Haas [73] and by Fabian Michael Krinner [118], whom I both supervised. I worked with Florian Haas in particular on the development of the 88-wave PWA model, the extension of the PWA method to a two-dimensional binning in $m_{3\pi}$ and t', and on the interpretation of the results. The analysis of Fabian Michael Krinner is based on the ROOTPWA software framework [171], of which I am a co-author. I also contributed to the development of the freed-isobar method and to the interpretation of the results.

Reference [H1] is based on the results from the Master's thesis by Stephan Schmeing [172], who was supervised by me. The 3-wave mass-dependent fit uses the results of the partial-wave decomposition from Ref. [H2]. Together with Stephan Schmeing, I developed a method to reliably find the best physical solution for the multi-modal resonance-model fit in an automatized way and without introducing parameter limits. I co-developed the novel t'-resolved analysis approach, co-developed the fit model in order to extract the novel $a_1(1420)$, and devised a strategy to estimate the systematic uncertainties.

Reference [H3] is based on the results from the Master's theses by Stephan Schmeing [172] and by Stefan Wallner [173]. Using the result of the partial-wave decomposition from Ref. [H2], the resonance model was extended significantly from the 3-waves in Ref. [H1] to 14-waves making it the most comprehensive analysis of its kind. Together with Stephan Schmeing and Stefan Wallner, I developed the fit model, improved and refined the method to find the best physical solution, and devised the systematic studies to estimate the systematic uncertainties.

I also contributed to the development of model-selection techniques for the partial-wave decomposition in the PhD thesis by Karl Alexander Bicker [114] and in the Master's theses by Oliver Johann Drotleff [115] and by Florian Markus Kaspar [116]. All three theses were supervised by me. Although the results are not included in the articles [H1–H3] they were an important confirmation of the 88-wave PWA model used in Ref. [H2].

Acknowledgments

Experimental particle physics is a team sport. Thus the research presented in this work would not have been possible without the help and support from many people.

Most of all I would like to thank Stephan Paul for giving me the opportunity to pursue my Habilititation. Many thanks, Stephan, also for your continuous support, for creating such a pleasant, lively, and stimulating research environment, and for being a great mentor!

My thanks go also to the members of my Fachmentorat, Ulrike Thoma and Norbert Kaiser. I very much appreciate your efforts and support!

A big thank you goes out to the diploma, Master, and PhD students that I had the pleasure to advise and work with over the last years (in alphabetical order): Alexander Austregesilo, Karl Bicker, Christian Dreisbach, Oliver Drotleff, Florian Haas, Florian Kaspar, Fabian Krinner, Stephan Schmeing, Sebastian Uhl, and, last but certainly not least, Stefan Wallner. Extra thanks to Stefan and Fabian for their corrections!

I also would like to express my special gratitude to Suh-Urk Chung and Dmitri Ryabchikov. You taught (not just) me how to do partial-wave analysis. Thank you for all your contributions over the years and for all the enlightening discussions!

It is a pleasure to acknowledge the help and suggestions I got from Vincent Mathieu, Wolfgang Ochs, Jose Pelaez, Mike Pennington, and Adam Szczepaniak. Many thanks for all the inspiring discussions!

I am also very grateful to my colleagues in the COMPASS collaboration. I would like to thank the members of the hadron analysis subgroup, in particular Bernhard Ketzer and Mikhail Mikhasenko, for their contributions. Thanks go also to the COMPASS analysis group, in particular to the analysis coordinators Claude Marchand, Jan Friedrich, Yann Bedfer, and Bakur Parsamyan, for their support and constructive criticism, which helped to improve our analyses. I am particularly indebted to the members of the drafting committee of the three papers that this thesis is based on: Yann Bedfer, Suh-Urk Chung, Wolfgang Dünnweber, Martin Faessler, Wolf-Dieter Nowak, Stephan Paul, Dmitri Ryabchikov, and, again last but not least, Stefan Wallner. Together, we plowed through nearly 140 journal pages and passed all the review hurdles. Thank you for your constructive and diligent work! I always enjoyed our meetings. Thanks go to all collaboration members for all their efforts that made it possible to acquire this treasure trove of data!

Last but not least, big thanks go to the good folk here at E18. I very much enjoyed the friendly and collegial atmosphere and the good company. Special thanks go to Karin Frank. Without your help, I would have ended up “lost in administration”.

Publications included in this cumulative habilitation thesis

[H1] C. Adolph *et al.*, [COMPASS Collaboration], "Observation of a New Narrow Axial-Vector Meson $a_1(1420)$," *Phys. Rev. Lett.* **115** (2015) 082001, arXiv:1501.05732 [hep-ex].

Cited on pp. 3, 4, 78, 90, 91, 101, and 105.

[H2] C. Adolph *et al.*, [COMPASS Collaboration], "Resonance production and $\pi\pi$ S-wave in $\pi^- + p \to \pi^-\pi^-\pi^+ + p_{\text{recoil}}$ at 190 GeV/c," *Phys. Rev. D* **95** (2017) 032004, arXiv:1509.00992 [hep-ex]. Supplemental material at http://journals.aps.org/prd/supplemental/10.1103/PhysRevD.95.032004.

Cited on pp. 3, 4, 19, 32, 35, 37, 38, 39, 46, 63, 73, 74, 75, 76, 77, 82, 84, 85, 87, 90, 92, and 105.

[H3] M. Aghasyan *et al.*, [COMPASS Collaboration], "Light isovector resonances in $\pi^- p \to \pi^-\pi^-\pi^+ p$ at 190 GeV/c," *Phys. Rev. D* **98** (2018) 092003, arXiv:1802.05913 [hep-ex].

Cited on pp. 3, 4, 39, 67, 68, 69, 71, 72, 73, 78, 79, 81, 82, 84, 86, 89, 90, 91, 92, 94, 95, 96, 98, and 105.

Bibliography

[1] S. Bethke, G. Dissertori, and G. P. Salam, [Particle Data Group], "Quantum chromodynamics," *Chin. Phys. C* **40** (2016) 132–150. http://pdg.lbl.gov/2016/reviews/rpp2016-rev-qcd.pdf.

Cited on pp. 5 and 7.

[2] D. J. Gross and F. Wilczek, "Ultraviolet Behavior of Nonabelian Gauge Theories," *Phys. Rev. Lett.* **30** (1973) 1343–1346.

Cited on p. 7.

[3] H. D. Politzer, "Reliable Perturbative Results for Strong Interactions?," *Phys. Rev. Lett.* **30** (1973) 1346–1349.

Cited on p. 7.

[4] L. B. Okun, "The theory of weak interaction," in *Proceedings of the 11th International Conference on High-Energy Physics (ICHEP '62), CERN, Geneva, Switzerland, Jul 4–11, 1962*, pp. 845–866. https://inspirehep.net/record/1341922/files/C62-07-04-p845.pdf.

Cited on p. 8.

[5] E. Eichten, K. Gottfried, T. Kinoshita, K. D. Lane, and T.-M. Yan, "Charmonium: The Model," *Phys. Rev. D* **17** (1978) 3090–3117. [Erratum: *Phys. Rev. D* **21** (1980) 313].

Cited on p. 8.

[6] F. Bissey, A. I. Signal, and D. B. Leinweber, "Comparison of gluon flux-tube distributions for quark-diquark and quark-antiquark hadrons," *Phys. Rev. D* **80** (2009) 114506, arXiv:0910.0958 [hep-lat].

Cited on p. 9.

[7] G. S. Bali, "QCD forces and heavy quark bound states," *Phys. Rept.* **343** (2001) 1–136, arXiv:hep-ph/0001312 [hep-ph].

Cited on p. 9.

[8] R. Alkofer and J. Greensite, "Quark Confinement: The Hard Problem of Hadron Physics," *J. Phys. G* **34** (2007) S3–S21, arXiv:hep-ph/0610365 [hep-ph].

Cited on p. 8.

[9] Clay Mathematics Institute, "Millennium Problem: Yang-Mills and Mass Gap." https://www.claymath.org/millennium-problems/yang%E2%80%93mills-and-mass-gap. [Online; accessed 08-August-2018].

Cited on p. 9.

[10] J. R. Andersen *et al.*, "Discovering Technicolor," *Eur. Phys. J. Plus* **126** (2011) 81, arXiv:1104.1255 [hep-ph].

Cited on p. 9.

[11] G. Panico and A. Wulzer, "The Composite Nambu-Goldstone Higgs," *Lect. Notes Phys.* **913** (2016) 1–316, arXiv:1506.01961 [hep-ph].

Cited on p. 9.

[12] A. V. Manohar, C. T. Sachrajda, and R. M. Barnett, [Particle Data Group], "Quark masses," *Chin. Phys. C* **40** (2016) 793–800. http://pdg.lbl.gov/2016/reviews/rpp2016-rev-quark-masses.pdf.

Cited on p. 10.

[13] C. Patrignani *et al.*, [Particle Data Group], "Review of Particle Physics," *Chin. Phys. C* **40** (2016) 100001.

Cited on pp. 10, 30, 78, 82, 83, 85, 88, 90, and 95.

[14] A. W. Thomas and W. Weise, *The Structure of the Nucleon*. WILEY-VCH, Berlin, 2001.

Cited on p. 10.

[15] J. Gasser, H. Leutwyler, and M. E. Sainio, "Sigma-term update," *Phys. Lett. B* **253** (1991) 252–259.

Cited on p. 10.

[16] J. Gasser, H. Leutwyler, and M. E. Sainio, "Form factor of the σ-term," *Phys. Lett. B* **253** (1991) 260–264.

Cited on p. 10.

[17] S. Scherer and M. R. Schindler, "A Primer for Chiral Perturbation Theory," *Lect. Notes Phys.* **830** (2012) 1–338.

Cited on p. 10.

[18] G. Aad *et al.*, [ATLAS Collaboration], "Observation of a new particle in the search for the Standard Model Higgs boson with the ATLAS detector at the LHC," *Phys. Lett. B* **716** (2012) 1–29, arXiv:1207.7214 [hep-ex].

Cited on p. 10.

[19] S. Chatrchyan *et al.*, [CMS Collaboration], "Observation of a new boson at a mass of 125 GeV with the CMS experiment at the LHC," *Phys. Lett. B* **716** (2012) 30–61, arXiv:1207.7235 [hep-ex].

Cited on p. 10.

[20] M. Gell-Mann, "The Eightfold Way: A Theory of strong interaction symmetry." CTSL-20, 1961. https://www.osti.gov/servlets/purl/4008239.

Cited on p. 11.

[21] Y. Ne'eman, "Derivation of strong interactions from a gauge invariance," *Nucl. Phys.* **26** (1961) 222–229.

Cited on p. 11.

[22] M. Gell-Mann, "A Schematic Model of Baryons and Mesons," *Phys. Lett.* **8** (1964) 214–215.

Cited on pp. 11 and 24.

[23] G. Zweig, "An SU_3 model for strong interaction symmetry and its breaking." CERN-TH-401, 1964. https://cds.cern.ch/record/352337/files/CERN-TH-401.pdf.

Cited on p. 11.

[24] G. Zweig, "An SU_3 model for strong interaction symmetry and its breaking II," in *Developments in the Quark Theory of Hadrons: A Reprint Collection. 1964–1978, Vol. 1*, D. B. Lichtenberg and S. P. Rosen, eds., pp. 22–101. Hadronic Press, 1980. https://cds.cern.ch/record/570209/files/CERN-TH-412.pdff. CERN-TH-412.

Cited on p. 11.

[25] Trassiorf, Wikimedia Commons, "Meson-octet.svg," 2007. https://commons.wikimedia.org/wiki/File:Meson-octet.svg. [Online; accessed 09-August-2018].

Cited on p. 11.

[26] Trassiorf, Wikimedia Commons, "Baryon-octet-small.svg," 2007. https://commons.wikimedia.org/wiki/File:Baryon-octet-small.svg. [Online; accessed 09-August-2018].

Cited on p. 11.

[27] Trassiorf, Wikimedia Commons, "Baryon-decuplet-small.svg," 2007. https://commons.wikimedia.org/wiki/File:Baryon-decuplet-small.svg. [Online; accessed 09-August-2018].

Cited on p. 11.

[28] S. Gasiorowicz and J. L. Rosner, "Hadron Spectra and Quarks," *Am. J. Phys.* **49** (1981) 954–984.

Cited on p. 12.

[29] J. L. Rosner, "Quark Models," in *Techniques and Concepts of High-Energy Physics*, T. Ferbel, ed., NATO Advanced Study Institutes Series (Series B. Physics), vol. 66, pp. 1–141. Springer, Boston, MA, 1981.

Cited on p. 12.

[30] C. Amsler, T. DeGrand, and B. Krusche, [Particle Data Group], "Quark model," *Chin. Phys. C* **40** (2016) 279–289. http://pdg.lbl.gov/2016/reviews/rpp2016-rev-quark-model.pdf.

Cited on pp. 12, 13, 14, and 21.

[31] K. A. Olive *et al.*, [Particle Data Group], "Review of Particle Physics," *Chin. Phys. C* **38** (2014) 090001.

Cited on pp. 15 and 32.

[32] D. Ebert, R. N. Faustov, and V. O. Galkin, "Mass spectra and Regge trajectories of light mesons in the relativistic quark model," *Phys. Rev. D* **79** (2009) 114029, arXiv:0903.5183 [hep-ph].

Cited on pp. 15 and 20.

[33] K. Götzen, "Meson Spectroscopy—Methods, Measurements & Machines," in *3rd European Nuclear Physics Conference (EuNPC2015), Groningen, The Netherlands, Aug 31–Sep 04, 2015*. http://indico.gsi.de/event/2598/session/13/contribution/56.

Cited on p. 15.

[34] D. Asner, C. Hanhart, and E. Klempt, [Particle Data Group], "Resonances," *Chin. Phys. C* **40** (2016) 565–569. http://pdg.lbl.gov/2016/reviews/rpp2016-rev-resonances.pdf.

Cited on pp. 15, 19, and 72.

[35] G. Breit and E. Wigner, "Capture of Slow Neutrons," *Phys. Rev.* **49** (1936) 519–531.

Cited on p. 17.

[36] J. Blatt and V. Weisskopf, *Theoretical Nuclear Physics*. John Wiley & Sons, New York, 1952.

Cited on p. 18.

[37] F. von Hippel and C. Quigg, "Centrifugal-Barrier Effects in Resonance Partial Decay Widths, Shapes, and Production Amplitudes," *Phys. Rev. D* **5** (1972) 624–638.

Cited on p. 18.

[38] V. N. Gribov, *The Theory of Complex Angular Momenta: Gribov Lectures on Theoretical Physics*. Camb. Monogr. Math. Phys. Cambridge University Press, 2007.

Cited on pp. 19, 29, and 69.

[39] S. M. Flatté, "Coupled-channel analysis of the $\pi\eta$ and $K\bar{K}$ systems near $K\bar{K}$ threshold," *Phys. Lett. B* **63** (1976) 224.

Cited on p. 19.

[40] I. J. R. Aitchison, "The K-matrix formalism for overlapping resonances," *Nucl. Phys. A* **189** (1972) 417–423.

Cited on p. 19.

[41] S. U. Chung, J. Brose, R. Hackmann, E. Klempt, S. Spanier, and C. Strassburger, "Partial wave analysis in K-matrix formalism," *Annalen Phys.* **4** (1995) 404–430.

Cited on p. 19.

[42] M. Mikhasenko, B. Ketzer, and A. Sarantsev, "Nature of the $a_1(1420)$," *Phys. Rev. D* **91** (2015) 094015, arXiv:1501.07023 [hep-ph].

Cited on pp. 19, 92, and 93.

[43] F. Aceti, L. R. Dai, and E. Oset, "$a_1(1420)$ peak as the $\pi f_0(980)$ decay mode of the $a_1(1260)$," *Phys. Rev. D* **94** (2016) 096015, arXiv:1606.06893 [hep-ph].

Cited on pp. 19, 92, and 93.

[44] E. Klempt and A. Zaitsev, "Glueballs, hybrids, multiquarks: Experimental facts versus QCD inspired concepts," *Phys. Rep.* **454** (2007) 1–202, arXiv:0708.4016 [hep-ph].

Cited on pp. 20 and 25.

[45] C. A. Meyer and E. S. Swanson, "Hybrid Mesons," *Prog. Part. Nucl. Phys.* **82** (2015) 21–58, arXiv:1502.07276 [hep-ph].

Cited on pp. 20, 25, and 97.

[46] S. Hashimoto, J. Laiho, and S. R. Sharpe, [Particle Data Group], "Lattice quantum chromodynamics," *Chin. Phys. C* **40** (2016) 310–320. http://pdg.lbl.gov/2016/reviews/rpp2016-rev-lattice-qcd.pdf.

Cited on p. 20.

[47] C. Gattringer and C. B. Lang, "Quantum chromodynamics on the lattice," *Lect. Notes Phys.* **788** (2010) 1–343.

Cited on p. 20.

[48] R. A. Briceño, J. J. Dudek, and R. D. Young, "Scattering processes and resonances from lattice QCD," *Rev. Mod. Phys.* **90** (2018) 025001, arXiv:1706.06223 [hep-lat].

Cited on pp. 20, 22, and 23.

[49] K. G. Wilson, "Confinement of Quarks," *Phys. Rev. D* **10** (1974) 2445–2459.

Cited on p. 20.

[50] S. Borsanyi *et al.*, "Ab initio calculation of the neutron-proton mass difference," *Science* **347** (2015) 1452–1455, arXiv:1406.4088 [hep-lat].

Cited on p. 21.

[51] S. Perantonis and C. Michael, "Static potentials and hybrid mesons from pure SU(3) lattice gauge theory," *Nucl. Phys. B* **347** (1990) 854–868.

Cited on p. 21.

[52] G. S. Bali and K. Schilling, "Static quark-antiquark potential: Scaling behavior and finite-size effects in SU(3) lattice gauge theory," *Phys. Rev. D* **46** (1992) 2636–2646.

Cited on p. 21.

[53] S. Necco and R. Sommer, "The $N_f = 0$ heavy quark potential from short to intermediate distances," *Nucl. Phys. B* **622** (2002) 328–346, arXiv:hep-lat/0108008 [hep-lat].

Cited on p. 21.

[54] A. S. Kronfeld, "Twenty-first Century Lattice Gauge Theory: Results from the QCD Lagrangian," *Ann. Rev. Nucl. Part. Sci.* **62** (2012) 265–284, arXiv:1203.1204 [hep-lat].

Cited on p. 21.

[55] J. J. Dudek, R. G. Edwards, P. Guo, and C. E. Thomas, [Hadron Spectrum Collaboration], "Toward the excited isoscalar meson spectrum from lattice QCD," *Phys. Rev. D* **88** (2013) 094505, arXiv:1309.2608 [hep-lat].

Cited on pp. 22 and 26.

[56] M. Lüscher, "Volume Dependence of the energy spectrum in massive quantum field theories: II. Scattering states," *Commun. Math. Phys.* **105** (1986) 153–188.

Cited on p. 23.

[57] M. Lüscher, "Two-particle states on a torus and their relation to the scattering matrix," *Nucl. Phys. B* **354** (1991) 531–578.

Cited on p. 23.

[58] D. J. Wilson, R. A. Briceno, J. J. Dudek, R. G. Edwards, and C. E. Thomas, "Coupled $\pi\pi$, $K\bar{K}$ scattering in P-wave and the ρ resonance from lattice QCD," *Phys. Rev. D* **92** (2015) 094502, arXiv:1507.02599 [hep-ph].

Cited on p. 23.

[59] M. R. Shepherd, J. J. Dudek, and R. E. Mitchell, "Searching for the rules that govern hadron construction," *Nature* **534** (2016) 487–493, arXiv:1802.08131 [hep-ph].

Cited on pp. 23, 25, and 26.

[60] C. Amsler and C. Hanhart, [Particle Data Group], "Non-$q\bar{q}$ Mesons," *Chin. Phys. C* **40** (2016) 1494–1499. http://pdg.lbl.gov/2016/reviews/rpp2016-rev-non-qqbar-mesons.pdf.

Cited on pp. 24 and 25.

[61] C. Amsler and N. A. Törnqvist, "Mesons beyond the naive quark model," *Phys. Rept.* **389** (2004) 61–117.

Cited on pp. 25 and 93.

[62] V. Crede and C. A. Meyer, "The Experimental Status of Glueballs," *Prog. Part. Nucl. Phys.* **63** (2009) 74–116, arXiv:0812.0600 [hep-ex].

Cited on p. 25.

[63] C. A. Meyer and Y. V. Haarlem, "Status of exotic-quantum-number mesons," *Phys. Rev. C* **82** (2010) 025208, arXiv:1004.5516 [nucl-ex].

Cited on pp. 25 and 26.

[64] W. Ochs, "The Status of Glueballs," *J. Phys. G* **40** (2013) 043001, arXiv:1301.5183 [hep-ph].

Cited on p. 25.

[65] N. Brambilla, S. Eidelman, P. Foka, S. Gardner, A. S. Kronfeld, *et al.*, "QCD and strongly coupled gauge theories: challenges and perspectives," *Eur. Phys. J. C* **74** (2014) 2981, arXiv:1404.3723 [hep-ph].

Cited on p. 25.

[66] F.-K. Guo, C. Hanhart, U.-G. Meißner, Q. Wang, Q. Zhao, and B.-S. Zou, "Hadronic molecules," *Rev. Mod. Phys.* **90** (2018) 015004, arXiv:1705.00141 [hep-ph].

Cited on p. 25.

[67] P. R. Page, E. S. Swanson, and A. P. Szczepaniak, "Hybrid meson decay phenomenology," *Phys. Rev. D* **59** (1999) 034016, arXiv:hep-ph/9808346 [hep-ph].

Cited on pp. 26, 85, 86, and 88.

[68] P. D. B. Collins, *An Introduction to Regge Theory and High-Energy Physics*. Cambridge Monographs on Mathematical Physics. Cambridge University Press, Cambridge, UK, 1977.

Cited on p. 29.

[69] E. Levin, "Everything about Reggeons. Part 1: Reggeons in "soft" interaction," arXiv:hep-ph/9710546 [hep-ph].

Cited on pp. 29 and 31.

[70] S. Donnachie, H. G. Dosch, O. Nachtmann, and P. Landshoff, "Pomeron physics and QCD," *Camb. Monogr. Part. Phys. Nucl. Phys. Cosmol.* **19** (2002) 1–347.

Cited on pp. 29 and 30.

[71] P. Abbon *et al.*, [COMPASS Collaboration], "The COMPASS experiment at CERN," *Nucl. Instrum. Methods Phys. Res., Sect. A* **577** (2007) 455–518, arXiv:hep-ex/0703049 [hep-ex].

Cited on p. 31.

[72] P. Abbon *et al.*, [COMPASS Collaboration], "The COMPASS setup for physics with hadron beams," *Nucl. Instrum. Methods Phys. Res., Sect. A* **779** (2015) 69–115, arXiv:1410.1797 [physics.ins-det].

Cited on p. 31.

[73] F. Haas, "Two-Dimensional Partial-Wave Analysis of Exclusive 190 GeV $\pi^- p$ Scattering into the $\pi^-\pi^-\pi^+$ Final State at COMPASS (CERN)," PhD thesis, Technische Universität München, 2014. http://cds.cern.ch/record/1662589/. CERN-THESIS-2013-277.

Cited on pp. 35, 75, 98, and 105.

[74] C. Zemach, "Three pion decays of unstable particles," *Phys. Rev.* **133** (1964) B1201.

Cited on p. 39.

[75] A. McKerrell, "Relativistic two and three-particle states," *Nuovo Cimento* **34** (1964) 1289–1305.

Cited on p. 39.

[76] J. D. Jackson, "Particle and polarization angular distribution for two and three-body decays," in *Physique des Hautes Energies: Proceedings, Ecole d'Eté de Physique Théorique, Les Houches, France*, pp. 325–366. 1965.

Cited on p. 39.

[77] S. M. Berman and M. Jacob, "Spin and parity analysis in two-step decay processes." SLAC-R-043, 1965. https://inspirehep.net/record/48740/files/slac-r-043.pdf.

Cited on p. 39.

[78] S. M. Berman and M. Jacob, "Systematics of Angular and Polarization Distributions in Three-Body Decays," *Phys. Rev.* **139** (1965) B1023–B1038.

Cited on p. 39.

[79] S. U. Chung, "Spin Determination for Boson Resonances," *Phys. Rev.* **138** (1965) B1541–B1545.

Cited on p. 39.

[80] S. U. Chung, "Spin-Parity Analysis for Boson Resonances," *Phys. Rev.* **169** (1968) 1342–1352.

Cited on p. 39.

[81] M. Ademollo, R. Gatto, and G. Preparata, "Tests for Spin and Parity of the B Meson," *Phys. Rev. Lett.* **12** (1964) 462–465.

Cited on p. 39.

[82] M. Ademollo, R. Gatto, and G. Preparata, "Spin Tests for Bosons," *Phys. Rev.* **139** (1965) B1608–B1618.

Cited on p. 39.

[83] G. Ascoli, D. V. Brockway, H. B. Crawley, B. I. Eisenstein, R. W. Hanft, M. L. Ioffredo, and U. E. Kruse, "Partial-Wave Analysis of the 3π Decay of the A_2," *Phys. Rev. Lett.* **25** (1970) 962.

Cited on pp. 39 and 56.

[84] G. Ascoli *et al.*, "Spin-Parity Analysis of the A_3," *Phys. Rev. D* **7** (1973) 669–686.

Cited on pp. 39 and 56.

[85] S.-U. Chung, "Spin Formalisms — Updated Version III." BNL-76975-2006-IR, 2013. http://cds.cern.ch/record/1561144. updated version of CERN-71-08, 1971.

Cited on pp. 39 and 44.

[86] R. J. Cashmore and A. J. G. Hey, "Description for the Reactions $a + b \to c + d + e$," *Phys. Rev. D* **6** (1972) 1303.

Cited on p. 39.

[87] J. D. Hansen, G. T. Jones, G. Otter, and G. Rudolph, "Formalism and assumptions involved in partial-wave analysis of three-meson systems," *Nucl. Phys.* **B81** (1974) 403.

Cited on pp. 39, 41, and 59.

[88] D. Herndon, P. Söding, and R. J. Cashmore, "Generalized isobar model formalism," *Phys. Rev. D* **11** (1975) 3165.

Cited on pp. 39 and 41.

[89] J. B. Dainton and A. J. G. Hey, eds., *Three particle phase shift analysis and meson resonances production*, Daresbury Study Weekend no. 8, DL-R34. 1975.

Cited on p. 39.

[90] M. Daumens, G. Massas, and P. Minnaert, "Spin tests from angular correlations in sequential decays," *Phys. Rev. D* **12** (1975) 291–295.

Cited on p. 39.

[91] J. D. Richman, "An Experimenter's Guide to the Helicity Formalism." CALT-68-1148, 1984. http://lib-extopc.kek.jp/preprints/PDF/1984/8409/8409198.pdf.

Cited on pp. 39 and 44.

[92] D. Aston, T. A. Lasinski, and P. K. Sinervo, "The SLAC three-body partial wave analysis system." SLAC-R-287, 1985. https://inspirehep.net/record/218334/files/slac-r-287.pdf.

Cited on p. 39.

[93] C. W. Salgado and D. P. Weygand, "On the partial-wave analysis of mesonic resonances decaying to multiparticle final states produced by polarized photons," *Phys. Rep.* **537** (2014) 1–58, arXiv:1310.7498 [nucl-ex].

Cited on p. 39.

[94] F. Krinner, D. Greenwald, D. Ryabchikov, B. Grube, and S. Paul, "Ambiguities in model-independent partial-wave analysis," *Phys. Rev. D* **97** (2018) 114008, arXiv:1710.09849 [hep-ph].

Cited on pp. 39, 63, 65, and 103.

[95] J. D. Jackson and D. R. Tovey, [Particle Data Group], "Kinematics," *Chin. Phys. C* **40** (2016) 560–564. http://pdg.lbl.gov/2016/reviews/rpp2016-rev-kinematics.pdf.
Cited on pp. 39 and 40.

[96] S. J. Lindenbaum and R. M. Sternheimer, "Isobaric Nucleon Model for Pion Production in Nucleon-Nucleon Collisions," *Phys. Rev.* **105** (1957) 1874–1879.
Cited on p. 41.

[97] M. Jacob and G. C. Wick, "On the general theory of collisions for particles with spin," *Annals Phys.* **7** (1959) 404–428.
Cited on p. 44.

[98] A. D. Martin and T. D. Spearman, *Elementary Particle Theory*. North-Holland Publishing Co., Amsterdam, 1st ed., 1970.
Cited on p. 44.

[99] E. P. Wigner, *Gruppentheorie und ihre Anwendungen auf die Quantenmechanik der Atomspektren*. Vieweg, Braunschweig, 1931.
Cited on p. 45.

[100] E. P. Wigner, *Group Theory and its Application to the Quantum Mechanics of Atomic Spectra*. Academic Press, New York, 1959. Translated into English by J. J. Griffin.
Cited on p. 45.

[101] M. E. Rose, *Elementary Theory of Angular Momentum*. John Wiley & Sons, New York, 1957.
Cited on p. 45.

[102] S. U. Chung and T. L. Trueman, "Positivity conditions on the spin density matrix: A simple parametrization," *Phys. Rev. D* **11** (1975) 633.
Cited on pp. 50, 51, and 52.

[103] A. Donnachie, H. G. Dosch, P. V. Landshoff, and O. Nachtmann, *Pomeron Physics and QCD*. Cambridge University Press, Cambridge, UK, 1st ed., 2002.
Cited on p. 50.

[104] K. Gottfried and J. D. Jackson, "On the connection between production mechanism and decay of resonances at high energies," *Nuovo Cim.* **33** (1964) 309–330.
Cited on p. 52.

[105] G. Cohen-Tannoudji, P. Salin, and A. Morel, "A simple formulation of high-energy exchange models in terms of direct-channel amplitudes," *Nuovo Cim. A* **55** (1968) 412–422.
Cited on p. 52.

[106] R. A. Fisher, "On the Mathematical Foundations of Theoretical Statistics," *Philos. Trans. Royal Soc. A* **222** (1922) 309–368.
Cited on p. 55.

[107] J. Orear, "Notes on statistics for physicists." UCRL-8417, 1958. http://cds.cern.ch/record/104881.
Cited on p. 56.

[108] J. Orear, "Notes on statistics for physicists, revised." CLNS-82-511, 1982. http://pages.physics.cornell.edu/p510/w/images/p510/6/62/Notes_on_Statistics_for_Physicists.pdf.

Cited on p. 56.

[109] R. J. Barlow, "Extended maximum likelihood," *Nucl. Instrum. Methods Phys. Res., Sect. A* **297** (1990) 496–506.

Cited on p. 56.

[110] R. T. Deck, "Kinematical Interpretation of the First π-ρ Resonance," *Phys. Rev. Lett.* **13** (1964) 169–173.

Cited on p. 60.

[111] X. Pan, "Study of the model dependence of the partial-wave analysis of the three-pion final state," Bachelor's thesis, Technische Universität München, 2018.

Cited on p. 61.

[112] B. Guegan, J. Hardin, J. Stevens, and M. Williams, "Model selection for amplitude analysis," *JINST* **10** (2015) P09002, arXiv:1505.05133 [physics.data-an].

Cited on p. 62.

[113] R. Tibshirani, "Regression Shrinkage and Selection via the Lasso," *J. Royal Stat. Soc. B* **58** (1996) 267–288. http://www.jstor.org/stable/2346178.

Cited on p. 62.

[114] K. A. Bicker, "Model Selection for and Partial-Wave Analysis of a Five-Pion Final State at the COMPASS Experiment at CERN," PhD thesis, Technische Universität München, 2016. http://wwwcompass.cern.ch/compass/publications/theses/2016_phd_bicker.pdf.

Cited on pp. 62 and 105.

[115] O. J. Drotleff, "Model Selection for Partial-Wave Analysis of $\pi^- + p \to \pi^-\pi^+\pi^- + p$ at the COMPASS Experiment at CERN," Master's thesis, Technische Universität München, 2015. http://wwwcompass.cern.ch/compass/publications/theses/2015_dpl_drotleff.pdf.

Cited on pp. 62, 77, and 105.

[116] F. M. Kaspar, "Application and Verification of Model-Selection Techniques for Diffractively Produced Three-Pion Final States," Master's thesis, Technische Universität München, 2017.

Cited on pp. 62, 77, and 105.

[117] E. M. Aitala *et al.*, [E791 Collaboration], "Model-independent measurement of S-wave $K^-\pi^+$ systems using $D^+ \to K\pi\pi$ decays from Fermilab E791," *Phys. Rev. D* **73** (2006) 032004, arXiv:hep-ex/0507099 [hep-ex].

Cited on p. 63.

[118] F. M. Krinner, "Freed-Isobar Partial-Wave Analysis," PhD thesis, Technische Universität München, 2018.

Cited on pp. 63, 65, 103, and 105.

[119] A. B. Kaidalov, "Diffractive Production Mechanisms," *Phys. Rep.* **50** (1979) 157–226.
Cited on p. 67.

[120] C. Adloff *et al.*, [H1 Collaboration], "Inclusive measurement of diffractive deep inelastic ep scattering," *Z. Phys. C* **76** (1997) 613–629, arXiv:hep-ex/9708016 [hep-ex].
Cited on p. 67.

[121] F. Abe *et al.*, [CDF Collaboration], "Measurement of small angle $\bar{p}p$ elastic scattering at $\sqrt{s} = 546$ GeV and 1800 GeV," *Phys. Rev. D* **50** (1994) 5518–5534.
Cited on p. 67.

[122] N. A. Törnqvist, "Understanding the scalar meson $q\bar{q}$ nonet," *Z. Phys. C* **68** (1995) 647–660, arXiv:hep-ph/9504372 [hep-ph].
Cited on p. 68.

[123] V. N. Gribov, *Strong Interactions of Hadrons at High Energies: Gribov Lectures on Theoretical Physics*, vol. 27 of *Camb. Monogr. Part. Phys. Nucl. Phys. Cosmol.* Cambridge University Press, 2008.
Cited on p. 69.

[124] M. L. Perl, *High Energy Hadron Physics*. Wiley-Interscience Publication. Wiley, 1974.
Cited on p. 69.

[125] K. Pearson, "On the criterion that a given system of deviations from the probable in the case of a correlated system of variables is such that it can be reasonably supposed to have arisen from random sampling," *Philos. Mag. Ser. 5* **50** no. 302, (1900) 157–175.
Cited on p. 71.

[126] F. James and M. Roos, "Minuit: A System for Function Minimization and Analysis of the Parameter Errors and Correlations," *Comput. Phys. Commun.* **10** (1975) 343–367.
Cited on p. 71.

[127] F. James and M. Winkler, "MINUIT home page," 2008. http://www.cern.ch/minuit. [Online; accessed 28-May-2018].
Cited on p. 71.

[128] S. U. Chung *et al.*, [E852 Collaboration], "Exotic and $q\bar{q}$ resonances in the $\pi^+\pi^-\pi^-$ system produced in $\pi^- p$ collisions at 18 GeV/c," *Phys. Rev. D* **65** (2002) 072001.
Cited on pp. 73, 83, 97, and 99.

[129] K. L. Au, D. Morgan, and M. R. Pennington, "Meson dynamics beyond the quark model: Study of final-state interactions," *Phys. Rev. D* **35** (1987) 1633.
Cited on p. 74.

[130] F. M. Krinner and D. Ryabchikov. Private communication, 2018.
Cited on p. 74.

[131] S. Wallner. Private communication, 2018.
Cited on p. 80.

[132] M. Lu *et al.*, [E852 Collaboration], "Exotic Meson Decay to $\omega\pi^0\pi^-$," *Phys. Rev. Lett.* **94** (2005) 032002, arXiv:hep-ex/0405044 [hep-ex].

Cited on pp. 82, 85, and 97.

[133] G. Bellini *et al.*, "Evidence for New 0^- S Resonances in the $\pi^+\pi^- pi^-$ Systems," *Phys. Rev. Lett.* **48** (1982) 1697–1700.

Cited on p. 83.

[134] D. V. Amelin, E. B. Berdnikov, S. I. Bityukov, G. V. Borisov, Y. P. Gouz, *et al.*, "Study of diffractive reaction $\pi^- A \to \eta\eta\pi^- A$ at the momentum $p(\pi^-) = 37\,\text{GeV}/c$," *Phys. Atom. Nucl.* **59** (1996) 976–981.

Cited on p. 83.

[135] A. V. Anisovich, C. A. Baker, C. J. Batty, D. V. Bugg, V. A. Nikonov, *et al.*, "Study of $\overline{p}p \to \eta\eta\pi^0\pi^0$ in flight," *Phys. Lett. B* **500** (2001) 222–231, arXiv:1109.6433 [hep-ex].

Cited on pp. 83, 85, and 86.

[136] P. Eugenio *et al.*, [E852 Collaboration], "Observation of the $\pi(1800)$ and $\pi_2(1880)$ mesons in $\eta\eta\pi^-$ decay," *Phys. Lett. B* **660** (2008) 466–470.

Cited on pp. 83 and 86.

[137] F. E. Close and P. R. Page, "The Production and decay of hybrid mesons by flux-tube breaking," *Nucl. Phys.* **B443** (1995) 233–254, arXiv:hep-ph/9411301 [hep-ph].

Cited on pp. 85 and 86.

[138] T. Barnes, F. E. Close, P. R. Page, and E. S. Swanson, "Higher quarkonia," *Phys. Rev. D* **55** (1997) 4157–4188, arXiv:hep-ph/9609339 [hep-ph].

Cited on pp. 85 and 86.

[139] J. Kuhn *et al.*, [E852 Collaboration], "Exotic meson production in the $f_1(1285)\pi^-$ system observed in the reaction $\pi^- p \to \eta\pi^+\pi^-\pi^- p$ at $18\,\text{GeV}/c$," *Phys. Lett. B* **595** (2004) 109–117, arXiv:hep-ex/0401004 [hep-ex].

Cited on pp. 86 and 97.

[140] S. Eidelman, [Particle Data Group], "The $a_1(1260)$ and $a_1(1640)$," *J. Phys. G* **33** (2006) 575–576. http://pdg.lbl.gov/2006/listings/m010.pdf.

Cited on p. 88.

[141] P. Gavillet *et al.*, [Amsterdam-CERN-Nijmegen-Oxford Collaboration], "Backward production of a spin parity 1^+ $\rho\pi$ Enhancement at 1.04 GeV," *Phys. Lett. B* **69** (1977) 119.

Cited on p. 88.

[142] D. M. Asner *et al.*, [CLEO Collaboration], "Hadronic structure in the decay $\tau^- \to \nu_\tau\pi^-\pi^0\pi^0$ and the sign of the tau-neutrino helicity," *Phys. Rev. D* **61** (1999) 012002, arXiv:hep-ex/9902022 [hep-ex].

Cited on p. 88.

[143] R. S. Longacre, "$E(1420)$ meson as a $K\overline{K}\pi$ molecule," *Phys. Rev. D* **42** (1990) 874–883.

Cited on p. 93.

[144] J. Vijande, A. Valcarce, F. Fernandez, and B. Silvestre-Brac, "Nature of the light scalar mesons," *Phys. Rev. D* **72** (2005) 034025, arXiv:hep-ph/0508142 [hep-ph].

Cited on p. 93.

[145] Z.-G. Wang, "Light axial-vector tetraquark state candidate: $a_1(1420)$," arXiv:1401.1134 [hep-ph].

Cited on p. 93.

[146] H.-X. Chen, E.-L. Cui, W. Chen, T. G. Steele, X. Liu, and S.-L. Zhu, "$a_1(1420)$ resonance as a tetraquark state and its isospin partner," *Phys. Rev. D* **91** (2015) 094022, arXiv:1503.02597 [hep-ph].

Cited on p. 93.

[147] T. Gutsche, V. E. Lyubovitskij, and I. Schmidt, "Tetraquarks in holographic QCD," *Phys. Rev. D* **96** (2017) 034030, arXiv:1706.07716 [hep-ph].

Cited on p. 93.

[148] M. Nielsen and S. J. Brodsky, "Hadronic superpartners from a superconformal and supersymmetric algebra," *Phys. Rev. D* **97** (2018) 114001, arXiv:1802.09652 [hep-ph].

Cited on p. 93.

[149] T. Gutsche, M. A. Ivanov, J. G. Körner, V. E. Lyubovitskij, and K. Xu, "Test of the multiquark structure of $a_1(1420)$ in strong two-body decays," *Phys. Rev. D* **96** (2017) 114004, arXiv:1710.02357 [hep-ph].

Cited on p. 93.

[150] J.-L. Basdevant and E. L. Berger, "The twofold emergence of the a_1 axial vector meson in high energy hadronic production," arXiv:1501.04643 [hep-ph].

Cited on p. 93.

[151] J.-L. Basdevant and E. L. Berger, "Peak Locations and Relative Phase of Different Decay Modes of the a_1 Axial Vector Resonance in Diffractive Production," *Phys. Rev. Lett.* **114** (2015) 192001, arXiv:1504.05955 [hep-ph].

Cited on p. 93.

[152] G. S. Adams *et al.*, [E852 Collaboration], "Observation of a New $J^{PC} = 1^{-+}$ Exotic State in the Reaction $\pi^- p \to \pi^+\pi^-\pi^- p$ at 18 GeV/c," *Phys. Rev. Lett.* **81** (1998) 5760–5763.

Cited on pp. 97 and 99.

[153] M. Alekseev *et al.*, [COMPASS Collaboration], "Observation of a $J^{PC} = 1^{-+}$ Exotic Resonance in Diffractive Dissociation of 190 GeV/c π^- into $\pi^-\pi^-\pi^+$," *Phys. Rev. Lett.* **104** (2010) 241803, arXiv:0910.5842 [hep-ex].

Cited on pp. 97 and 98.

[154] E. I. Ivanov *et al.*, [E852 Collaboration], "Observation of exotic meson production in the reaction $\pi^- p \to \eta'\pi^- p$ at 18 GeV/c," *Phys. Rev. Lett.* **86** (2001) 3977–3980, arXiv:hep-ex/0101058 [hep-ex].

Cited on p. 97.

[155] D. V. Amelin, Y. G. Gavrilov, Y. P. Gouz, V. A. Dorofeev, R. I. Dzhelyadin, *et al.*, "Investigation of hybrid states in the VES experiment at the Institute for High Energy Physics (Protvino)," *Phys. Atom. Nucl.* **68** (2005) 359–371.

Cited on p. 97.

[156] C. A. Baker, C. J. Batty, K. Braune, D. V. Bugg, N. Dzhaoshvili, *et al.*, "Confirmation of $a_0(1450)$ and $\pi_1(1600)$ in $\bar{p}p \to \omega\pi^+\pi^-\pi^0$ at rest," *Phys. Lett. B* **563** (2003) 140–149.

Cited on p. 97.

[157] G. S. Adams *et al.*, [CLEO Collaboration], "Amplitude analyses of the decays $\chi_{c1} \to \eta\pi^+\pi^-$ and $\chi_{c1} \to \eta'\pi^+\pi^-$," *Phys. Rev. D* **84** (2011) 112009, arXiv:1109.5843 [hep-ex].

Cited on p. 97.

[158] A. Zaitsev, [VES Collaboration], "Study of exotic resonances in diffractive reactions," *Nucl. Phys.* **A675** (2000) 155–160.

Cited on pp. 97, 98, and 99.

[159] A. R. Dzierba, R. Mitchell, E. Scott, M. R. Shepherd, P. Smith, M. Swat, *et al.*, "Partial wave analysis of the $\pi^-\pi^-\pi^+$ and $\pi^-\pi^0\pi^0$ systems and the search for a $J^{PC} = 1^{-+}$ meson," *Phys. Rev. D* **73** (2006) 072001, arXiv:hep-ex/0510068 [hep-ex].

Cited on pp. 97, 98, and 99.

[160] M. Nozar *et al.*, [CLAS Collaboration], "Search for the Photoexcitation of Exotic Mesons in the $\pi^+\pi^+\pi^-$ System," *Phys. Rev. Lett.* **102** (2009) 102002, arXiv:0805.4438 [hep-ex].

Cited on pp. 99 and 100.

[161] P. Eugenio and C. Bookwalter, [CLAS Collaboration], "Search for exotic mesons in photoproduction at JLab CLAS," *AIP Conf. Proc.* **1560** (2013) 421–423.

Cited on p. 99.

[162] S. Grabmüller, "Cryogenic Silicon Detectors and Analysis of Primakoff Contributions to the Reaction $\pi^-\text{Pb} \to \pi^-\pi^-\pi^+\text{Pb}$ at COMPASS," PhD thesis, Technische Universität München, 2012. https://cds.cern.ch/record/1492155/files/CERN-THESIS-2012-170.pdf. CERN-THESIS-2012-170.

Cited on pp. 99 and 100.

[163] A. Afanasev and P. R. Page, "Photoproduction and electroproduction of $J^{PC} = 1^{-+}$ exotics," *Phys. Rev. D* **57** (1998) 6771–6777, arXiv:hep-ph/9712388 [hep-ph].

Cited on p. 99.

[164] A. P. Szczepaniak and M. Swat, "Role of photoproduction in exotic meson searches," *Phys. Lett. B* **516** (2001) 72–76, arXiv:hep-ph/0105329 [hep-ph].

Cited on p. 99.

[165] Joint Physics Analysis Center. http://jpac.jlab.org. [Online; accessed 14-September-2018].

Cited on p. 102.

[166] A. Jackura, M. Mikhasenko, and A. Szczepaniak, [JPAC Collaboration], "Amplitude analysis of resonant production in three pions," *EPJ Web Conf.* **130** (2016) 05008, arXiv:1610.04567 [hep-ph].

Cited on p. 102.

[167] M. Mikhasenko, A. Jackura, B. Ketzer, and A. Szczepaniak, [COMPASS and JPAC Collaborations], "Unitarity approach to the mass-dependent fit of 3π resonance production data from the COMPASS experiment," *EPJ Web Conf.* **137** (2017) 05017.

Cited on p. 102.

[168] A. Jackura *et al.*, [JPAC and COMPASS Collaborations], "New analysis of $\eta\pi$ tensor resonances measured at the COMPASS experiment," *Phys. Lett. B* **779** (2018) 464–472, arXiv:1707.02848 [hep-ph].

Cited on p. 102.

[169] R. Aaij *et al.*, [LHCb Collaboration], "Observation of $J/\psi p$ Resonances Consistent with Pentaquark States in $\Lambda_b^0 \to J/\psi K^- p$ Decays," *Phys. Rev. Lett.* **115** (2015) 072001, arXiv:1507.03414 [hep-ex].

Cited on pp. 103 and 104.

[170] R. Aaij *et al.*, [LHCb Collaboration], "Observation of the Resonant Character of the $Z(4430)^-$ State," *Phys. Rev. Lett.* **112** (2014) 222002, arXiv:1404.1903 [hep-ex].

Cited on p. 103.

[171] B. Grube, S. Neubert, *et al.*, "ROOTPWA." http://github.com/ROOTPWA-Maintainers/ROOTPWA. [Online; accessed 16-September-2018].

Cited on p. 105.

[172] S. Schmeing, "Resonance Extraction in Diffractive 3π Production using 190 GeV/c π^- at the COMPASS Experiment (CERN)," Master's thesis, Technische Universität München, 2014. http://wwwcompass.cern.ch/compass/publications/theses/2014_dpl_schmeing.pdf.

Cited on p. 105.

[173] S. Wallner, "Extraction of Resonance Parameters of Light Meson Resonances in the Charged Three-Pion Final State at the COMPASS Experiment (CERN)," Master's thesis, Technische Universität München, 2015. http://wwwcompass.cern.ch/compass/publications/theses/2015_dpl_wallner.pdf.

Cited on p. 105.